Microstructural stability of a nickel-based alloy overlay on a 2.25Cr1Mo steel substrate

Hassan Saghafifar, M.Sc.

Thesis submitted for the degree of

Doctor of Philosophy

Department of Mechanical, Materials, and Manufacturing Engineering

The University of Nottingham

July 2011

Abstract

Ni-based superalloy weld overlays are widely used in electricity generating plants to significantly reduce high temperature corrosion problems of ferritic steel components under service conditions. Welding a nickel alloy similar to IN625 onto the outer bore of a 2.25Cr1Mo steel tube enhances its service life as a superheater tube in the highly corrosive environment of a Waste-to-Energy boiler. For the purposes of studying the effects of high temperature service on the microstructure of this laid tube with a weld overly, a series of thermal exposure tests at 650˚C was performed for different times from 1 day up to 128 days. The microstructural evolution was studied using a combination of analytical techniques along with changes in hardness profile across the interface. Changes in the microstructure were examined using OM, SEM, EPMA, EBSD and FIB-STEM.

Hardness survey results indicate significant changes in the interfacial region during ageing. Formation of a soft zone ~300 μm wide and its subsequent re-hardening was observed in the steel side while the hardness of the bulk steel remained unchanged. Development of a hard band ~30 μm wide adjacent to the interface in the weld overlay region and hardening of the bulk overlay material occurs in the early stages of ageing and remained unchanged with ageing time. Thermodynamic calculations were performed using Thermo-Calc software and TCFE6 and TTNI7 databases to aid interpretation of experimental data.

Microstructural evolution in the steel region is related to the carbide transformation process and carbon migration. In the bulk of the steel tube, the bimodal microstructure is stable and in the tempered martensite/bainite areas, the initial M_3C transform to $M_{23}C_6$ through a series of metastable carbides while in the ferrite grains, M_2C carbide precipitates and transforms directly to the equilibrium carbide. The main process for supply of carbon atoms is transformation of carbides and the rates of transformation are related to the as-welded microstructure. On the steel side of interfacial region where bainite was formed after welding, the stability of metastable carbides is related to the carbon content. Long term ageing causes Mo replenishment in the coexisting ferrite and fine grains have formed in this region following long term ageing.

Experimental observations confirmed that a network of alloyed $M_{23}C_6$ carbide precipitates was formed at the interface in the steel side which are believed to interrupt the carbon migration across the interface. Moreover, there is a carbide precipitation region within ~100 μm from the interface in the weld overlay. Beyond this region intermetallic phases like Mo-rich μ and Nb-rich δ were formed in the interdendritic regions and along the grain boundaries. Hard band formation is related to precipitation of the σ phase.

Contents

Acknowledgements

I would like to express my deepest gratitude to Professor Graham McCartney and Professor Phillip Shipway for their continued support and guidance during my PhD studies. Their attitude, enthusiasm, patience and encouragement regarding my research are greatly appreciated.

I would like to thank the technical staff in Advanced Materials Group. Special thanks to Mr Keith Dinsdale and Dr Nigel Neate for their constant help and expertise using SEM and TEM. I would like to thank Mr Thomas Buss and Mr Martin Roe for their assistance using different characterization techniques. I would also like to thank Mr Graham Malkinson for help in samples preparation and thermal exposure. Finally, I am very grateful for the help from Dr Deen Zhang.

I would like to take this opportunity to thank the University of Nottingham International Office for the funding my Ph.D. programme.

Very special thanks to Hoda, the one and only, who I love deeply, for taking very good care of me during this period of time, for her unconditional love, support, understanding, patience, and for encouraging me to follow my Ph.D. program.

List of abbreviations

CCT	Continues - Cooling - Transformation
EDS	Energy Dispersive X-Ray Spectrometry
G. B.	Grain Boundary
IPF	Inverse Pole Figure
ISE	Ion beam induced Secondary Electron
S.D.	Standard Deviation
SIMS	Secondary Ion Mass Spectrometry
TCP	Topological - Close - Pack
TIG	Tungsten – Inert - Gas
TM/B	Tempered Martnesite and or Bainite
TTT	Time – Temperature – Transformation
Tγ	Transformed Austenite (γ)

Chapter 1

Introduction

In the 21st century, the world faces an important challenge of providing plentiful, cheap energy to meet the needs of growing global demands. It is believed that a strong set of electricity generation technologies and fuels including fossil fuels and renewable sources should be developed to assure adequate supplies. One of the renewable energy sources is waste [1] and conversion of all kinds of it, including municipal solid waste (MSW) and biomass to energy in waste-to-energy (WtE) plants is recognized globally as one of the means for electricity supply [2]. In order to improve the thermal efficiency of the WtE plants, it is essential to raise the operation temperature of the boiler [3].

Conventionally, the chromium-molybdenum series of ferritic steels such as 2.25Cr1Mo steel is used widely in the power generation and process industries because of their high strength at elevated service temperature, combined with

microstructural stability [4, 5]. However, ferritic steels do not provide adequate resistance in high temperature corrosive environments such as WtE boilers. It should be noted that the typical life time of components in a power station is about 200,000 hours [6] and thus the cost and performance of materials for this kind of application should be optimised [7].

Optimisation of cost and performance suggests a surface engineering approach using a Ni-based alloy with high Cr content as a coating on the candidate ferritic steel. Coatings can be produced by several methods such as co-extrusion, diffusion treatment, thermal spraying, laser cladding and weld overlaying [8]. Good bond integrity, heat transfer and corrosion resistance are the essential characteristics for a coating. Among various methods of cladding, there is a growing interest in weld overlays because of the intermixing and metallurgical bonding of the weld metal to the substrate [9].

Alloy 625 is a nickel based alloy with alloying elements such as Cr, Mo and Nb and is one such material which is commonly used for cladding processes [10]. There is large body of work on the microstructural evolution of Alloy 625 with different microstructures (wrought and as-cast) at elevated temperatures and it has concluded that chemical composition and initial microstructure are critical parameters.

In addition, the microstructural changes in 2.25Cr1Mo steel after long term service have been extensively reported in the literature (see section 2-3-2). Moreover, there are some papers regarding effects of welding on the as-welded microstructure and its evolution at high temperature (see section 2-3-3). However, little detailed work has been undertaken on the microstructural

evolution of Alloy 625 weld overlay on a 2.25Cr1Mo substrate and their reciprocal effects.

Nevertheless, there are a number of studies which are devoted to microstructural analysis of dissimilar material weld joints at high temperatures. It has been concluded that alloying elements such as carbon diffuse across the interface according to their chemical potential gradient. The carbon migration process is a well known process in the many dissimilar weld joints and it occurs from the low alloy side of interface to the high alloy side. There are many important factors which affect the carbon diffusion process such as time and temperature and also the type of stable phases in each material.

The stable phases in multicomponent materials such as steels and nickel-based alloys can be predicted by using thermodynamic calculation software such as Thermo-Calc. Knowing the stable phases in each system helps the systematic analysis of the effects of chemical composition changes on the microstructural evolution in the complex systems.

Therefore, the aim of this investigation is to understand the effects of service conditions at temperatures above 600˚C on the microstructure of the 2.25Cr1Mo steel/nickel-based alloy weld overlay system. The following objectives are set up to reach this aim:

1) To clearly characterize the microstructure and chemical composition of weld overlay and 2.25Cr1Mo steel and the compositional variation at the weld interface in the as-welded condition.

2) To evaluate microstructural changes in both materials following elevated temperature exposure of samples at 650°C and investigate the effects of this treatment on the hardness of both materials.

3) To better understand carbon diffusion during high temperature exposure and its effects on the microstructure and determine the important parameters affecting carbon diffusion in both materials and develop a model for the microstructural changes.

4) To analyse the stable phases in both materials by performing thermodynamic calculations using Thermo-Calc software and to understand the effects of intermixing during welding and carbon migration during thermal exposure on the stable phases which are related to microstructural evolution.

Chapter 2

Literature review

2-1- Introduction

This chapter provides the context for the themes explored within this thesis. The underlying aspects are materials for boiler applications and their properties are presented and in particular, the use of weld overlay as a corrosion barrier is discussed. Emphasis is placed upon microstrucutral features of 2.25Cr1Mo steel and Alloy 625 and their stabilities in high temperature service. In particular, focus is given to carbide transformation in the 2.25Cr1Mo steel and solidification behaviour of an Alloy 625 weldment and its secondary phase formation at high temperatures.

Work on different types of dissimilar weld joints is presented and their microstructural evolution discussed. The most important issue in these systems is carbon diffusion between dissimilar materials. The reactions and

phase transformation at the interface are presented. Finally, a thermodynamic calculation method and its application in prediction of stable phases in the multi component systems is presented in the final section.

2-2- General Background

2-2-1- Energy challenges and WtE plants

Energy may be the most important factor that will influence the shape of society in the 21st century. The cost and availability of energy significantly impacts our quality of life, the health of national economies, the relationships between nations, and the stability of our environment. Biomass and waste are renewable energy sources in the modern world [1].

Today's Waste-to-Energy (WtE) plants are power plants that utilize municipal solid waste as their fuel rather than coal, oil or natural gas. WtE plants recover the thermal energy contained in the waste in boilers that generate steam that can then be sold directly to industrial customers, or used on-site to drive turbines for electricity production [3].

The use of fossil fuels for electricity generation poses a unique set of challenges. On the one hand, this kind of fuel is plentiful and available at low cost in much the world. On the other hand, traditional methods of fuel combustion emit pollutants and CO_2 at high levels relative to other energy-generation options [11]. Environmental concerns are a great challenge in modern power generation and it is claimed that in addition to reduction of waste materials, WtE plants produce electricity from waste with less environmental impact than landfill process of waste[12].

The principle of WtE technology is feeding the waste material to an incinerator and producing thermal energy by combusting it. In order to improve the thermal efficiency of these plants, there is a need to raise the steam temperature and pressure. The main technology is the development of high temperature materials with sufficient resisitance to the aggressive environment. Extensive research and development programmes have resulted in numerous high strength alloys with sufficient corrosion resistance for the boiler tubing [2, 3, 13-15].

2-2-2- Materials requirements for boiler in WtE plants

Low alloy ferritic steels are used extensively in modern power generation for components which operate at temperature less than 550˚C and steam pressure less than 35 MPa where creep deformation limits the service life which is about 200,000 h [16-18]. Creep is an important design consideration for steam tubes operating at temperatures in excess of 400˚C. The chromium–molybdenum series of steels are used widely in both power plant and process industries because they offer high strength at ambient and elevated temperature, combined with adequate toughness. The availability of these low alloy steels makes them economically attractive [5].

These steels contain chromium from 0.5 wt.% to 12 wt.% and some molybdenum, usually up to a maximum of 1 wt.%. Other strong carbide formers such as vanadium and niobium may also be added. The 2.25Cr1Mo steel is one of the most important steels in this group [4]. Metallurgical changes occur when creep-resisting steels are used at elevated temperature

because their properties largely depend on the precipitation and stability of alloy carbides. The initial microstructure of the steel is also important and some factors such as grain size, solid solution hardening, type of structure, precipitation or dispersion hardening and segregation at structural discontinuities such as grain boundaries are important too.

As waste has a variable composition, the combustion gas from waste incineration furnaces fluctuates both in gas temperature and composition. Therefore, corrosion in WtE plants is a more challenging issue than it is in conventional power plants. Corrosive gases such as hydrogen chloride (HCl) combined with fly ash (dust) contained in the combustion gas result in a severe high temperature corrosive environment [8, 19-21]. Low alloy steels suffer from severe corrosion in chlorine-containing environments; however, nickel-based alloys are significantly more resistant than steels, as the steels mass change in a corrosive environment is about 6.5 times compared to that of the Inconel 625 in the similar environment [1]. The presence of Cr and Mo in the nickel alloys are very important in corrosion resistance [22].

2-2-3- Surface engineering for boiler components and weld overlay

There has been an increasing interest in the need to optimise the cost and performance of materials with appropriate corrosion resistance and mechanical properties for boiler components. Materials having both attributes are very scarce and therefore in many applications, bimetallic systems are necessary.

Materials with satisfactory corrosion resistance must be highly alloyed in nickel, chromium and molybdenum; thus they are expensive. Moreover there are many difficulties in utilizing these materials since the mechanical properties of these alloys may not meet the requirements of structural components. There is thus a need for surface engineering, using a protective surface layer to protect the structural components against corrosion and/or erosion. This allows the structural components to meet the codes and standards in terms of strength while relying on the surface protective layer to protect against corrosion. This protective layer can be produced by several methods such as: weld overlaying; co-extrusion [7]; diffusion bonding [9]; thermal spraying [23]; and laser cladding [24]. The protective layer needs to exhibit good bond integrity, high heat transfer, good corrosion resistance, and low porosity, since these are the essential characteristics that provide optimum life of boiler components.

Among all the cladding processes, there is a growing interest in weld overlaying in light of the metallurgical bonding between the weld metal and substrate, providing strong adhesion and reducing the possibility of crack propagation along the interface. Welding processes can be automated to yield large output at a reduced cost. The durability of weld overlay cladding is higher than that of a protective layer produced by other methods, since a dense coating layer that is chemically bonded with the base metal and as thick as several millimetres can be produced by this method [25].

Commercially available nickel-based superalloys have been used for weld overlays [26, 27]. In order to achieve the maximum high-temperature

corrosion protection with these alloys, there is a need to maintain the lowest possible dilution from the underlying steel in the overlay. Excessive dilution in welding that may result up to 20 wt% iron content in the nickel-based superalloy weld overlay is known to reduce the resistance to high temperature chloride attack to half compared to un-diluted alloy [28].

It is also important that overlay welding does not result in embrittlement or degradation in the mechanical properties of the overlaid component. Nickel alloy weld overlays on steel have been found to exhibit similar mechanical properties to ferritic steel [10]. Furthermore, tests on the components after long term service have indicated that nickel alloys increased resistance of the overlaid boiler components to overheating and to falling clinker [10].

2-2-4- Alloy 625 weld overlay and welding processes

Alloy 625 is a nickel-based superalloy with corrosion resistance and high strength at temperature above 500˚C [29]. It contains about 22 wt% Cr, about 9 wt% Mo, less than 5 wt% Fe and about 3.5 wt% Nb. Welding and overlaying with Alloy 625 filler metal is common in many industrial plants in the oil and gas industries [30]. These welding products closely match the coefficient of expansion of many ferritic steels, accept iron dilution without cracking, weld readily with dissimilar metals and possess the corrosion properties inherent of bulk Alloy 625 [31]. Since this nickel-based alloy has a long established reputation for its resistance to highly corrosive environments, it has been used in WtE environments [32, 33]. The bimetallic Alloy 625/steel system is also a good candidate for many other applications such as offshore

and onshore components [30] and black liquor recovery boilers, and for some waste heat recovery systems in steel making, such as basic oxygen furnace (BOF) hoods and electric arc furnace (EAF) hoods [10].

The welding process allows successful use of a number of specific deposition techniques which can be chosen according to application. For each application, there is a need to compromise between deposit thicknesses, surface chemical composition, deposition rate, and welding parameters. Some argue that one of the most successful processes for weld overlaying Alloy 625 is the submerged- arc-welding (SAW) process [34]. However, there are others applications where the automatic gas-metal-arc-welding (GMAW) is used as a standard process for applying Alloy 625, such as production of boiler water-walls. The pulsed-gas-metal-arc-welding (PGMAW) process has a wide range of use in overlay applications too, since this process has the lowest dilution level which is related to lower heat input compared to other processes [30]. Figure 2-1 shows a schematic diagram of weld overlay application on a water wall of the WtE boiler.

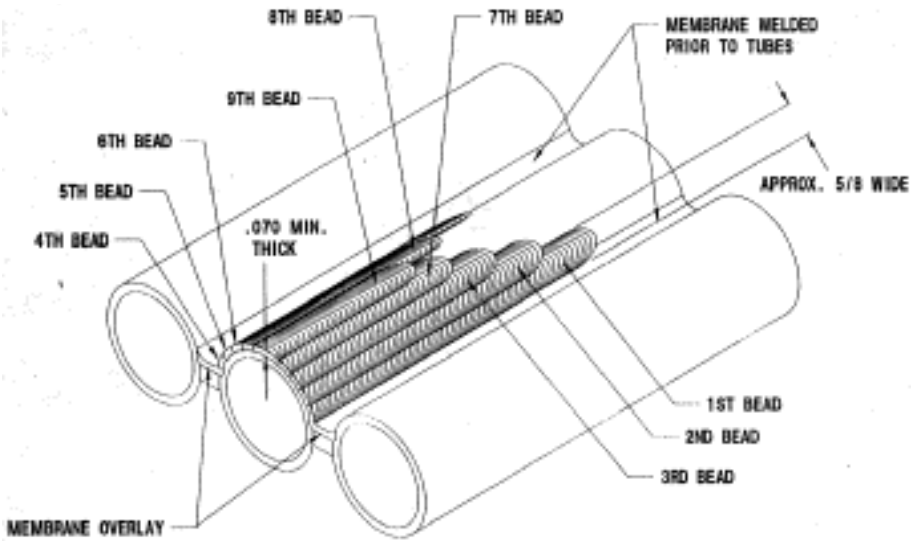

Figure 2-1. Schematic diagram of weld overlay beads to cover the tube-membrane water-wall in the WtE boilers [10].

There are some parts in the boiler such as the superheater which is constructed from individual tubes and therefore the weld overlay should be applied by a spiral mode. The spiral weld overlay can be applied with a low energy input which will only influence the microstructure of the substrate within a limited depth [35], so that its strength will not change significantly. A superheater spiral weld overlaid tube is shown schematically in Figure 2-2.

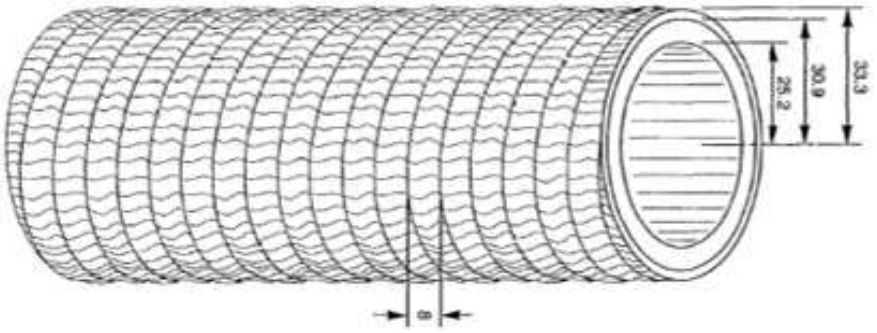

Figure 2-2. Schematic diagram of spiral weld overlaid tube [36].

2-3- 2.25Cr1Mo steel

A Cr-Mo low alloy ferritic steel used extensively in modern power generation has a nominal composition of 0.1 wt.% carbon, 1.9 to 2.6 wt.% chromium and 0.8 to 1.13 wt.% molybdenum. This steel is known as 2.25Cr1Mo steel or T22 [37] and 10CrMo910 [38] in the literature. Its popularity is due to its excellent mechanical and creep properties as well as good resistance to oxidation and hydrogen embrittlement at elevated temperatures. In spite of these excellent properties, a number of problems such as temper embrittlement and creep embrittlement have often been associated with it use [39].

2-3-1- Physical metallurgy of 2.25Cr1Mo steel

2.25Cr1Mo steel is a low carbon ferritic steel which has been successfully used in non-nuclear elevated temperature applications for a number of years. The amount of chromium in this steel confers increased oxidation resistance, so allowing it to be used at 550 to 600°C. The molybdenum content of this steel is known to be about the optimum level to give the required creep resistance. The presence of chromium in the range of 2.25 wt.% counteracts the embrittling tendency caused by presence of molybdenum [40]. This steel is normally regarded as the best low alloy creep resisting steel with an optimum combination of properties with widespread application [5].

The mechanical and corrosion resistance of Cr-Mo steels depend upon their microstructure [41] which can be predicted using knowledge of their TTT and CCT diagrams. Figure 2-3 presents these diagrams for 2.25Cr1Mo steel. Large amounts of 2.25Cr1Mo steel enter service in either the quenched and tempered condition, or the normalized condition.

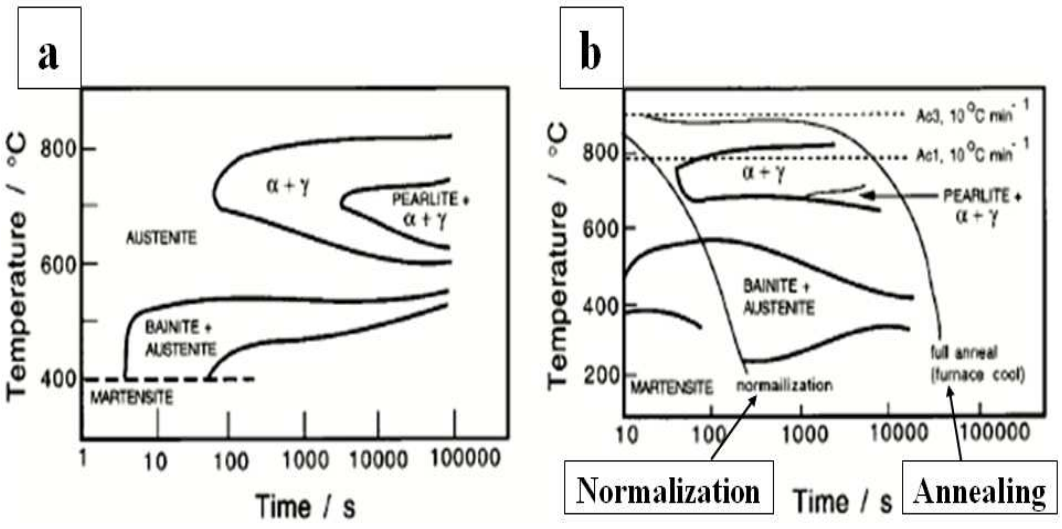

Figure 2-3. Corresponding (a) TTT and (b) CCT diagrams for a 2.25Cr1Mo steel. The CCT diagram shows the terminology used in describing air-cooling form the austeniteisation (i.e. normalizing) and furnace cooling (i.e. annealing) [42].

Some believe that in former case, the microstructure usually consists of tempered martensite and/or bainite, while in the later case it contains a mixed microstructure of ferrite and very fine pearlite [43]. However, others argue that in the air cooled and tempered condition, the microstructure is largely bainitic with varying amounts of ferrite depending on the cooling rate of product after tempering [5].

For power plant applications, this steel is usually air cooled after austenitisation [42]. The initial microstructure has a great effect on the service life of this steel. By increasing the bainite content to about 50-60%, the creep resistance of this steel can be maximized [44]. The tempering temperature for this steel depends on the desired mechanical properties at elevated temperatures, and it is in the range of 650-750°C.

The major metallurgical advantage of this steel is that it will transform to a fully bainitic microstructure over a wide range of temperatures. Thus the tempered microstructure contains many carbide precipitates which act as dispersion hardening particles. The precipitates present in this state are spheroidsed carbides originally present in the bainite, predominantly M_3C (M=Cr, Fe, Mo) and the smaller incoherent Mo_2C needles [42].

2-3-2- Carbide transformation in 2.25Cr1Mo microstructure at high temperature

During tempering or service at high temperature, the morphology, distribution and type of carbides in the 2.25Cr1Mo steel will change depending on the time and temperature [45]. This transformation depends on the initial microstructure of the steel and its grain size as well as the applied stress and

temperature of service. Moreover, the carbon content has a critical influence on the ageing behaviour of this steel [46]. There is a large body of research which analysed the carbides in this steel after long term service [39, 43, 44, 47, 48]. However, some of the assessments of carbide transformation in this steel are based on the extrapolation of accelerated thermal ageing tests [49] or the creep rupture data obtained from laboratory tests [50-52]. The validity of such an approach is thought to be justified since the accelerated ageing tests have shown to produce carbides whose chemical compositions are comparable to those of the carbides which precipitate under actual service exposure conditions [53].

The initial microstructure of 2.25Cr1Mo steel contains numerous, finely dispersed carbides embedded in the matrix which undergo changes in composition and shape during service. Therefore, these changes can be used to form a time-temperature recorder which can be used in remanent life assessments [54]. The carbide transformation sequences occurring during the tempering of this steel, proposed by different researchers are very different. The first and widely referenced work is that by Baker and Nutting [55]. They and some other researchers [5] argue that the equilibrium carbide in this steel is M_6C and that there are different sequences in either bainite or ferrite for carbide transformation as follows:

In bainite: $\mathcal{E} - carbide\ M_3C \rightarrow M_3C + M_2C \rightarrow M_{23}C_6 \rightarrow M_6C$

$\downarrow$

$M_7C_3 \rightarrow M_6C$

In ferrite: $M_2C \rightarrow M_6C$

It should be noted that the ageing temperature and time has a great influence on these sequences. For example, it is noted that thermal ageing at 850 K to 900 K for durations less than 10,000 hours could not lead the transformation of metastable carbides to the equilibrium carbide [56].

Further experiments showed that M_6C and $M_{23}C_6$ are stable carbides after long term thermal ageing at elevated temperatures [57]. The sequences of carbide transformation are shown in Figure 2-4. This diagram shows that increasing exposure time at temperature above 650˚C results in $M_{23}C_6$ growth at the expense of cementite and Mo_2C in addition to Cr_7C_3 precipitates. Therefore it causes a decrease in the number of particles in the microstructure.

The final carbides are shown to be $M_{23}C_6$ and M_6C; however, some researchers have argued that two carbides cannot coexist at equilibrium in the 2.25Cr1Mo steel. Therefore, it is suggested that the equilibrium carbide should be one of the Mo-rich M_6C and the Cr-rich $M_{23}C_6$.

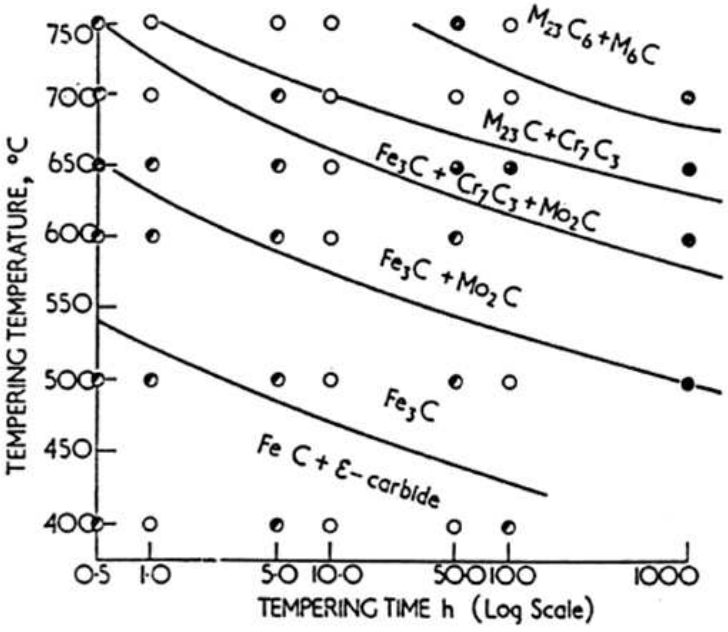

Figure 2-4. Summary of carbide transformation sequence [58].

It is found that the nucleation and growth of carbides is sensitive to the presence of minor alloying additions [59]. Finally, there is some recent researches which shows that in silicon-containing steels, the transformation sequence in the bainitic regions is given as [58]:

$$\mathcal{E} - carbide\ M_3C \rightarrow Fe_3C \rightarrow Mo_2C \rightarrow M_6C \rightarrow M_7C_3 \rightarrow M_{23}C_6$$

While in ferrite grains the sequence is given as [43]:

$$M_2C \rightarrow M_{23}C_6$$

Moreover, carbide transformation sequences have different rates in the various microstructures. These changes occur at a slower rate in a mixed microstructure of bainite and allotrimorphic ferrite when compared with a fully bainitic microstructure [60, 61].

2-3-3- Effects of welding on the 2.25Cr1Mo microstructure

The low alloy ferritic steels, (especially 2.25Cr1Mo steel) are used in as-manufactured and as-welded conditions in service. Welding processes alter the microstructure in the near-weld region and produce a complex microstructure leading to sharp variations in service behaviour [62]. The weldability of this steel is good, although reheat cracking and cold cracking in the heat affected zone (HAZ) and in the fusion zone are sometimes observed [63]. The difficulties related to welding can be minimized by preheating or by using low heat inputs, such as multi-pass welding, in order to reduce austenite grain growth and to increase the amount of fine grained bainitic microstructure [64].

The microstructure of the weld metal and HAZ is dependent on the heat input, the welding procedure and the post weld heat treatment. It is claimed [64] that the microstructure of the 2.25Cr1Mo steel weld metal is largely bainitic, consisting of packets of elongated and outlined platelets. These are interpreted as individual bainitic ferrite platelets outlined by retained carbon-enriched austenite. Carbides may possibly also be present between platelets.

Metallographic analysis of the HAZ adjacent to the fusion boundary [63, 65] reveals a bainitic structure consisting of laths of ferrite with aligned carbide precipitates between the laths. There is limited information about the types of carbide in the HAZ of 2.25Cr1Mo steel and it is reported that Mo_2C and M_6C carbides are not seen in this region [66]. As the heat input increases, this microstructure becomes coarser. Pro-eutectoid ferrite was never observed in this zone. It is reported that the austenite grain size differs across the HAZ; adjacent to the fusion boundary there is a prior coarse grain region which changes to a fine grain region as the distance from the fusion boundary increases [66, 67] .

The number of carbides in the fine-grained zone is higher than in other regions and these carbides tend to be coarser [63]. Therefore, the microstructural evolution in these two regions is different during post weld heat treatment (PWHT) or during service life. This is considered to be consequence of differences in the austenite grain size, bainite morphology and carbide size distribution governed by cooling rate and chemical composition. These differences all affect carbide transformation during PWHT or service life [68].

2-4- Alloy 625, a nickel based super alloy

For evaluation of the weld overlay characteristics, it is necessary to have a good knowledge of the standard Alloy 625. The solidification behaviour of Alloy 625 is presented since this is relevant to work addressing a weld deposit of this material. Moreover, phases which precipitate during high temperature service are identified and described. This information aids understanding of the relationship between the phases and their stabilities in the microstructure during high temperature exposure.

The development of Alloy 625 was started in the 1950s to meet the then-perceived demand for a high-strength main steam-line piping material [69]. Alloy 625 has been among the most successful nickel based alloys for long term engineering applications as it is a solid-solution strengthened alloy. Although the alloy was originally designed as a solid solution strengthened alloy, it has been shown that some secondary phases form during solidification [70] or precipitate during ageing treatment or service at temperatures in the range of 600 to 750˚C [71].

2-4-1- Solidification of Alloy 625 and weld deposit of Alloy 625

To be termed Alloy 625, the composition has to fall within certain limits which are mentioned in 2-2-4. However, variations within this range can affect the microstructure and thus properties. In cases such as hard-facing [72] and weld cladding [73] where Alloy 625 is used as weld deposit, the composition will be affected by substrate dilution. It is suggested that solidification reactions in such diluted compositions will be different to those

of pure Alloy 625 and consequently phase formation processes will differ. Moreover, solidification during welding is an inherently non-equilibrium process and the microstructures generated during welding are often not those predicted by applying equilibrium considerations to existing phase diagrams [74].

Phase formation during solidification of nickel alloys has been widely presented in the literature, and provides a foundation for the discussion of phase formation process during solidification in a weld overlaid Alloy 625 on the steel substrate. The effects of the following issues on the formation of these solidified microstructures are then presented.

1) Increase in the cooling rate which cause changes to the equilibrium condition

2) Changes in the composition due to mixing with steel

2-4-1-1- Solidification of Alloy 625

In order to investigate phase formation during solidification, the sequence of solidification reactions is of prime importance. Alloy 625 is considered as a modified version of alloy 718 [71]. This assumption is helpful for understanding the solidification behaviour of Alloy 625. The dominating solidification reaction in these nickel alloys is the enrichment of the remaining interdendritic liquid in niobium as the γ dendrites form from the liquid. This causes formation of niobium-rich Laves and/or niobium carbide in those regions during the final stages of solidification [71]. Another way of illustrating the solidification is a pseudo ternary equilibrium diagram which is

shown in Figure 2-5. This schematic presentation is based on the alloy 718 data [75] and is modified for Alloy 625 [71]. As shown in Figure 2-5, the C/Nb ratio dictates the solidification path from three available paths and affects the resultant microstructure. Path 1 is related to the high C/Nb ratios and leads to the formation of γ+NbC with no Laves phase. Path 2 is for intermediate C/Nb ratios and firstly forms γ+NbC, followed by Laves phase formation at the end of solidification. At low C/Nb ratios (path 3) γ+Laves phase forms with no NbC. Examination of microstructures in typical heats of Alloy 625 reveal the Path 1 (γ + NbC) or Path 2 (γ + NbC + Laves) microstructures [71].

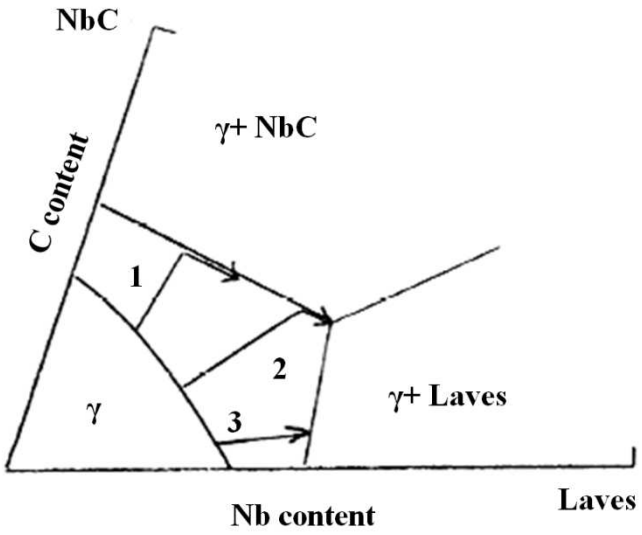

Figure 2-5. Schematic view of solidification paths in Alloy 625 [71]

The F.C.C. structure of the nickel matrix has a high solubility for many substitutional alloying elements, but commercial nickel alloys often contain a large number of minor phase particles such as carbides, nitrides, borides and intermetallic compounds in their as-solidified condition [76]. This reflects the fact that the solidification rate and other alloying elements such as N and B also affect microstructure.

There are a few publications describing phase formation during solidification and important factors which affect formation of Nb-rich phases in Alloy 625 [70, 71]. Differential thermal analysis (DTA) was performed to establish approximate equilibrium solidus and liquidus temperatures of Alloy 625 with different Nb, Si and C contents. These DTA results reveal that the presence of these elements decreases liquidus temperature from 1406˚C to 1352˚C and solidus temperature from 1380˚C to 1275˚C which causes an increase of the melting range (ΔT) and formation of minor phases during the final stages of solidification.

Microstructural examination of as-solidified Alloy 625 revealed that there are two different types of elemental segregation during solidification of Alloy 625. The continuous segregation pattern within the primary austenite (γ) dendrites causes the liquid solubility to be exceeded during the terminal stages of solidification, promoting another segregation between austenite (γ) and the various minor phases [70]. Therefore, it is found that solidification of Alloy 625 terminates by a eutectic-like reaction of enriched remaining liquid phase forming a solid solution alloy (γ) and various niobium-rich phases such as NbC, M_6C and Laves phase, the details of which depend on the chemical composition. The solidification reaction in Alloy 625 with a levels of Nb=3.53 wt%, C= 0.035 wt%, Si=0.46 wt% is as follows [70]:

$$L + \gamma \rightarrow L + \gamma + NbC \rightarrow L + \gamma + NbC + Laves \rightarrow \gamma + NbC + Laves$$

The amount of eutectic-type constituents can be calculated, at least semi-quantitatively, from DTA thermo-grams. Using this technique, it has been found that the minor phases to matrix ratio is about 3% to 5% and depends on

the carbon and silicon contents [70]. The important factors affecting the final microstructure are carbon to niobium ratio (C/Nb) as well as iron and silicon contents. The higher C/Nb ratio results in more carbide while the higher iron and silicon contents promote more Laves phase in the microstructure.

2-4-1-2- Solidification of weld deposit of Alloy 625

Work by Cieslak [77] describes the solidification of gas tungsten arc (GTA) weld deposit of Alloy 625 as a function of composition and determined the fundamental melting/solidification parameters such as liquidus and solidus temperatures. In his research, he correlated the solidification microstructure and weldability of Alloy 625 as a function of chemical composition, along with sequences of solidification reactions leading to the formation of the as-welded microstructure.

The DTA results obtained from re-melting weld deposits showed that the important alloying elements (i.e. Nb, C and Si) decreased the liquidus from 1354˚C to 1333˚C and the solidus temperature from 1250˚C to 1158˚C which caused an increase in the melting range (ΔT). The melting temperature range was related to the presence of a eutectic-type constituent which increased hot cracking susceptibility. These possible eutectic phases are identical to those of the as- solidified Alloy 625 [77], the dominant phase depending on the weld wire characteristics [78] .

In research relating to Alloy 625 overlay deposits on a nickel-based material produced by plasma transferred arc welding (PTAW), it is argued that the C/Nb ratio is the primary factor controlling the secondary phase formation

[79]. As the C/Nb ratio decreased from 0.024 to 0.016, the content of γ/NbC eutectic constituent also decreased from 1.25 to 0.77 vol%, but the content of γ/Laves eutectic constituent increased from 1 to 2.5 vol%, resulting in a total content of eutectic constituents being increased from 2.25 to 3.27 vol% [79]. Formation of the Laves phase increases the tendency for hot cracking during welding [77] and reduces the ductility in as cast material [71]. Moreover, the corrosion resistance decreases due to spatial inhomogeneity in the composition [80].

2-4-1-3- Effect of heat input during welding and cooling rate

In the industrial application of Alloy 625 as a weld metal, other phases such as sigma (σ) and P phases appear as a result of non-equilibrium solidification [81]. The appearance of these phases in the microstructure can be related to local segregation. During non-equilibrium solidification, the thermodynamic driving force for formation of these phases is achieved by a sufficient local segregation.

In a weld overlay structure, heat input during the welding is an important parameter which can affect the resultant microstructure, and metallographic examination has indicated that the formation of secondary phases in Alloy 625 weld overlays depends on the heat input [33]. It is claimed that the lower heat input would result in more rapid cooling and less time being available for segregation. Rapid cooling would promote a lower degree of segregation of the alloy constituents, a finer dendrite spacing and finer dispersion of the terminal phase.

Moreover, it is shown that the phase fraction of secondary phases found in Alloy 625 weldment decreased from about 3 % to about 1% as the cooling rate increased from 0.1 to 10^4 K/s. This can be explained as a consequence of interaction between solute atoms and the trapped vacancies in the solid [82]. It should be noted that increasing the cooling rate has no effect on the type of carbides formed, but it is observed that the distribution of carbide particles changes from relatively few large particles to many fine precipitates as the cooling rate is increased [83].

2-4-1-4- Effect of dilution

Dilution of the overlaid material with substrate material occurs during welding processes. This dilution results in a variation of chemical composition in an overlay and thus there is a variation in the solidification behaviour and microstructure since these are sensitive to chemical composition. In general, during welding of an Alloy 625 on a steel substrate, the content of Fe, C and Si increases in the Alloy 625 overlay composition. It has been shown that addition of Fe up to 6 wt.% to Alloy 625 did not change the solidification behaviour. Moreover, the C-enriched alloy solidification behaviour is identical to pure Alloy 625 [84]. In both of them, molybdenum and niobium have been shown to exhibit strong tendencies to segregate to interdendritic regions and their segregation was balanced by inverse segregation of nickel and iron to dendrites cores [84].

It is believed that the Laves phase fraction increases with an increase in the content of Fe and Si alloying elements in Alloy 625. The formation of Laves phase and NbC particles in the interdendritic regions decreases the toughness

of weld metal. The impact energy at room temperature of the weld metal made with a standard (Fe = 3.19 wt%, Si = 0.22 wt%) filler wire is about 42.3 J. This value increased to about 152.7 J in a weld made with the low Fe and Si wire (Fe = 0.80 wt.%, Si = 0.08 wt.%) [71]. In addition, it has been shown that addition of iron caused alteration in the Laves phase composition. The more iron in the Alloy 625 (increasing from 2 wt% to 6 wt%), the larger the iron concentration in the Laves phase (increasing form ~1 wt% to 4 wt%) in the as-solidified sample [84].

2-4-2- Phase precipitation during high temperature exposure in Alloy 625

The main aim of this section is to describe phase changes that occur at high temperature in Alloy 625. It is clear that solid-state transformation or phase precipitation during high temperature exposure relies on the initial microstructure. Therefore, in order to understand the precipitation of secondary phases in a weld microstructure of Alloy 625 during high temperature exposure, the available information concerning precipitation processes in the wrought Alloy 625 can be used as a guideline.

Alloy 625 was not originally developed as a precipitation hardened alloy [85] but in the 1970's, a long time ageing study showed that there are various phase transformations that can take place in this material as a function of time and temperature [86]. It should be noted that secondary phases which are precipitated during production processes can significantly influence the microstructure of the wrought Alloy 625 products [87]. Different carbides and inter-metallic compounds can precipitate in Alloy 625 after thermal exposures

at temperatures in the range of 600 - 1000˚C. Due to its high content of molybdenum, chromium and niobium, Alloy 625 exhibits complex precipitation behaviour [88]. The precipitation behaviour in the wrought alloy is also dependent upon the carbon content and final annealing treatment [89].

A large amount of research has been carried out to correlate the properties and precipitation behaviour of wrought Alloy 625 [71, 88-93]. In order to simplify this, the following categories can be considered:

1) Precipitation of hardening phases

2) Carbides and carbo-nitrides

3) Topologically closed-packed (TCP) phases

2-4-2-1- Precipitation Hardening Phases

The efforts for identification of these phases in Alloy 625 go back to early stages of its application. Comprelli and Wolff [94] noted that in Alloy 625 material and other researchers found in weld metal of Alloy 625 [95] , there is an increase in hardness (from ~270 to ~370 Vickers) after ageing at 700˚C. Moreover, tensile strength increases (form ~880 to ~1000 $N.mm^{-2}$) and a significant decrease of elongation (form 32 % to 20 %) occurred after ageing at 700˚C.It was assumed that this was due to the precipitation of a coherent phase (γ') with formula [Ni_3(Nb, Al, Ti)] as seen in other nickel alloys [96]. However, research work of Bohm [97] showed that the increase in the hardness at temperatures above 750˚C is caused by the precipitation of a stable incoherent orthorhombic phase with formula [Ni_3(Nb,Mo)].

The long term ageing study was carried out and the mechanical properties of Alloy 625 were determined for samples exposed 8,000 hours at 649˚C, 760˚C and 871˚C [86]. It was found that an increase in tensile strength was observed after exposure at 649˚C (812.2 Mpa compared to 456.4 Mpa in mill annealed condition) but that tensile strength dropped significantly to about 671.6 Mpa in samples aged at 760˚C and further decreasing happen to about 439.2 Mpa at 871˚C. The reported X-ray diffraction results of this study showed that two M_6C phases and a Ni_3Nb phase were present in the material aged at 871˚C, but the increased strength at 649˚C was not explained by the X-ray data [87].

Further investigations in this regard showed that strengthening at intermediate temperatures (between 600 to 700˚C) in Alloy 625 occurred by precipitation of the metastable γ" phase. This phase has a body centred tetragonal $D0_{22}$ structure while the equilibrium intermetallic phase is the δ phase with $D0_a$ structure. It is believed that the metastable γ" phase [$Ni_3(Nb,X)$] forms on ageing at temperatures above 600˚C and transforms to the orthorhombic δ phase [$Ni_3(Nb,Mo)$] upon prolonged ageing[98].

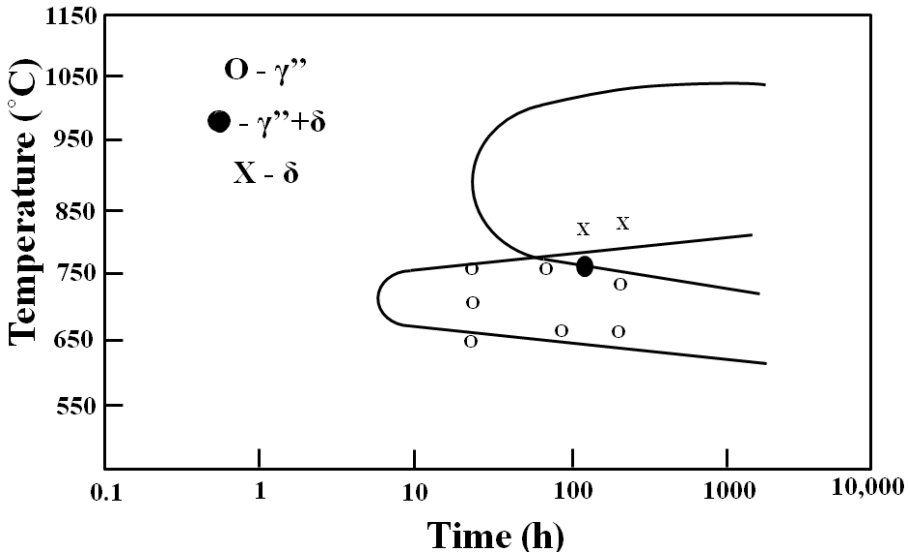

Figure 2-6. Time-Temperature-Precipitation (TTP) diagram corresponding to γ" and δ precipitation in Alloy 625 [98].

Moreover, it was shown that δ phase [$Ni_3(Nb,Mo)$] formation is possible directly from the supersaturated solid solution at higher temperatures [99]. It is claimed that the equilibrium phase (δ) often nucleates at grain boundaries during thermal exposure while dislocations act as effective nucleation sites for precipitation of the γ'' phase [98, 100]. Time-temperature-precipitation (TTP) curves corresponding to the formation of these phases are presented in Figure 2-6, while their micrographs are shown in Figure 2-7.

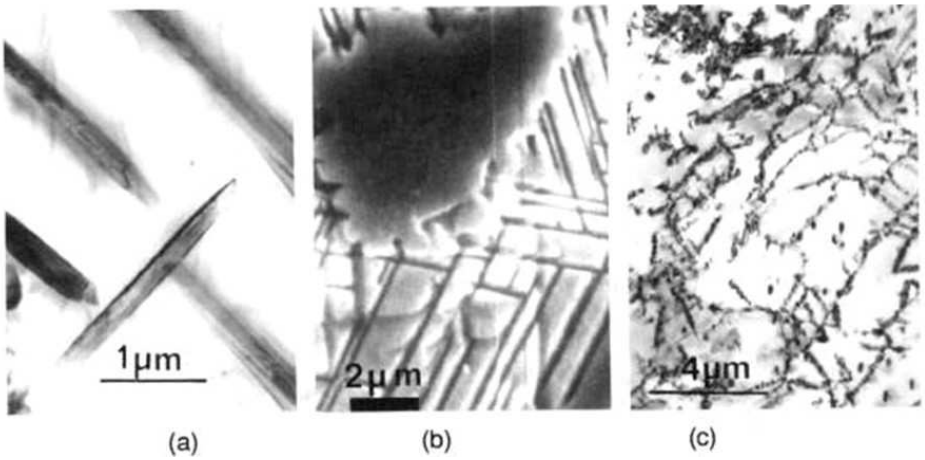

Figure 2-7. Different precipitates found in Alloy 625; (a) δ precipitates formed after ageing at 820˚C for 200 hours, (b) plates of δ phase growing from a NbC precipitate, and (c) γ'' precipitates formed after ageing at 675˚C for 100 hours [93].

2-4-2-2- Carbides and carbo-nitrides

NbC carbides with B1 structure [82] form in this alloy during the final stages of solidification; these are generally termed primary NbC particles [71]. In the solution annealed condition (above 1100˚C), all the phases, except primary NbC, have been put into solid solution and further carbide precipitation in Alloy 625 during ageing has been observed from 650˚C onwards [101]. It has been reported that three different carbides i.e. MC, M_6C and $M_{23}C_6$ are present in the temperature range from as low as ~600˚C to as high as ~1050˚C[102].

Others have argued that the temperature range is more limited being in the range of 760-980˚C [103].

The type of carbide formed during heat treatment depends upon the temperature. At higher temperatures, roughly from 870˚ to 1040˚C, the carbides are both MC (NbC) as thin grain boundaries films, and M_6C, where M is principally Ni, Cr, and Mo. At temperatures in the 700˚C - 870˚C range, the grain boundary carbides are primarily $M_{23}C_6$ where M is almost entirely Cr. After intermediate temperature heat treatments, all three carbides can usually be found [103, 104].

However, Muzyka [105] has reported that the primary MC carbides decompose during annealing on prolonged exposure at elevated temperatures into M_6C and $M_{23}C_6$ [106]. Many researchers report precipitation of all carbides on grain boundaries [71]. It should be noted that the chemical composition of MC with intergranular precipitation is different from intragranular primary MC precipitates with irregular shape [107, 108]. The lattice parameter of the primary MC carbide was found to lie between the reported lattice parameter of NbC and TiC phases [101]. The thin film on the grain boundaries is reported to be mainly NbC [71]. Two different morphologies for intergranular MC have been reported, namely the diamond shape and dendritic form [93].

The M_6C and $M_{23}C_6$ carbides commonly have blocky, irregular shapes and form as series of separate, discrete grain boundary particles. Figure 2-8 shows TEM micrographs of these types of carbides. The MC carbide formed in the early stages of heat treatment (after 1 hour) at 900˚C while the $M_{23}C_6$ carbide

was formed after a prolonged heat treatment (100 hours) at lower temperature (800˚C). The M_6C carbide precipitates after 1 hour at higher temperature (1025˚C). The stability of different carbides in solutionized Alloy 625 forged bar has been reported by Vernotloier and Cortial [109, 110] who mentioned that fine $M_{23}C_6$ carbides precipitated along austenite grain boundaries in a sample heat treated for 8 h at 700˚C, whereas a sample heat treated for 8 h at 800˚C contained M_6C carbide, and the sample heat treated at 1050˚C contained only MC carbide. The precipitation of the M_6C carbide at 800˚C caused degradation of mechanical properties (reduction of yield stress ~150 $N.mm^{-2}$) [109] and corrosion resistance (3 times) [110] of Alloy 625.

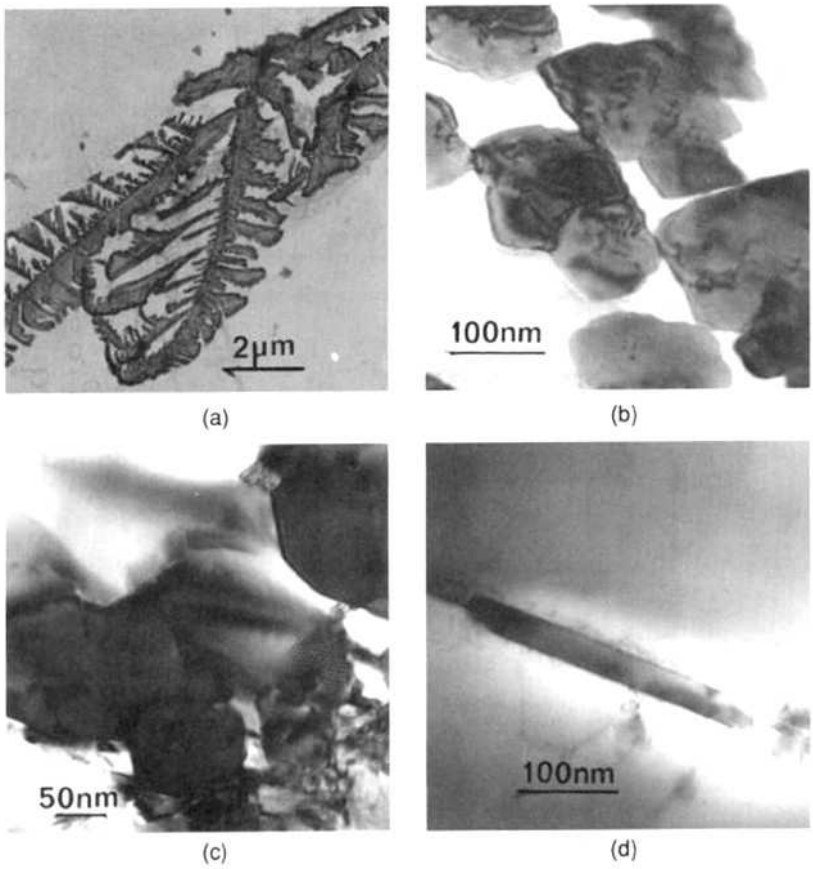

Figure 2-8. Images of different intergaranular carbides; (a) dendritic MC (900˚C, 1 h), (b) diamond shaped MC (900˚C, 1 h), (c) $M_{23}C_6$ blocky shape (800˚C, 100 h), (d) M_6C needle shape (1050˚C, 1h) [93].

Moreover, slight changes in the chemical composition resulted in different type of carbides [111]. Table 1 summarizes the crystal structures and typical compositions of the carbides types which found to be present in the microstructure of wrought Alloy 625 [71].

Table 1.Structures and typical compositions of the carbide precipitates [71].

Phase	Structure	Location	Typical Composition
M C	Cubic , Fm3m a_0= variable	Matrix	$(Ti_{0.07}\ Cr_{0.04}\ Fe_{0.02}\ Ni_{0.09}\ Nb_{0.75}\ Mo_{0.03})C$
			$(Ti_{0.53}\ Cr_{0.03}\ Ni_{0.04}\ Nb_{0.39}\ Mo_{0.01})C$
	a_0=0.43nm	Grain Boundaries	$(Ti_{0.15}\ Cr_{0.04}\ Fe_{0.01}\ Ni_{0.12}\ Nb_{0.67}\ Mo_{0.01})C$
M_6C	Cubic , Fd3m a_0=1.13nm	Grain Boundaries	$(Cr_{0.21}\ Fe_{0.02}\ Ni_{0.37}\ Nb_{0.08}\ Mo_{0.24}\ Si_{0.08})_6\ C$
$M_{23}C_6$	Cubic , Fm3m a_0=1.08nm	Grain Boundaries	$(Cr_{0.85}\ Fe_{0.01}\ Ni_{0.07}\ Mo_{0.07})_{23}\ C_6$

2-4-2-3- Topologically Closed Packed (TCP) phases

The last group of precipitates are intermetallic compounds commonly known as topologically-close-packed (TCP) phases because of their characteristic crystal structures [91, 92]. These can be listed as follows:

1) Laves Phase
2) Sigma (σ) Phase
3) Mu (μ) Phase
4) Ni_2M Phase

Laves phase: Laves phase is a hexagonal A_2B compound that can be found in number of binary alloys [112]. In more complex alloys, Laves phase can contain significant amounts of other alloying or impurity elements, and depart considerably in composition from a simple A_2B type chemistry. In Alloy 625,

the Laves phase has noticeable compositional variations that reflect the differences in processing history of the alloy in which the particles were formed [71]. Irrespective of processing, Laves phase is generally found to be significantly enriched in Nb (12 to 27 wt%), Mo (12 to 23 wt%), and Si (2 to 9 wt%) while the Fe, Cr levels are 3 to 5 wt% and 13 to 22 wt% respectively which are not noticeably different compared to the nominal Alloy 625 composition [33, 77].

Sigma (σ) phase: this phase typically appears in Fe-Cr alloys that contain more than 20 wt% of Cr, and in these alloys and it has the approximate composition of FeCr. Sigma (σ) phase has a complex, tetragonal layered structure and tends to nucleate from $M_{23}C_6$ carbides to which it is structurally and compositionally related. Although sigma (σ) phase formation is not common in Ni-Cr systems, it can form in nickel based alloys that contain about 10 wt% Mo and more than 15 wt% Fe and other alloying elements that tend to stabilize sigma (σ) phase including Si and W [113].

Mu (μ) phase: Some researchers [92] believe that the Mu (μ) phase has a A_6B_7 type composition where A is Mo and/or W and B is Fe and/or Co. It has a hexagonal close-packed structure and $D8_5$ crystal system. Others claim that Mu (μ) phase has a complex, rhombohedral structure, which occurs in Cr containing alloys with large amounts of Mo and W and stabilized by Fe [113]. Mu (μ) phase particles tend to nucleate on M_6C carbides which are structurally and compositionally (Mo-rich) similar. For a certain Ni-Cr-Mo-Fe alloy, the Mu (μ) phase is reported to have a composition as follows [92]:

$$(Ni_{0.36}Cr_{0.16}Fe_{0.04}Co_{0.02})\ (Mo_{0.39}W_{0.03})$$

Ni_2M: This intermetallic compound with Pt_2Mo-type structure is reported to precipitate in Alloy 625 after prolonged service at temperatures close to but less than 600˚C [114, 115]. This phase is known as Ni_2M or Ni_2 (Cr, Mo) and has six variants and precipitates in the austenite grains. These particles exhibit a snowflake-like morphology and are uniformly distributed in the matrix [106]. There are other minor phases in the Alloy 625 matrix [116]; however, due to their negligible fractions, further discussion is not necessary for the purpose of this work.

2-4-3- TTT diagrams for wrought Alloy 625

It has been shown that different phases precipitate in Alloy 625 depending upon temperature and duration of ageing [117] and TTT diagram is a helpful tool in analysing of the precipitation behaviour in this alloy. Several TTT diagrams have been presented for Alloy 625 which differ in certain aspects from each other. There are several possible reasons for these differences; the first is variation in composition within the ranges given for Alloy 625. The second source of variability is related to the techniques which are used to identify the phase transformations.

With these facts in mind, a TTT diagram for commercial Alloy 625 was first published by E. Schanbel and co-workers [88] and is presented in Figure2-9. It is clear that heat treatment of the material during its processing can significantly change the TTT diagram; for example by solution annealing, the precipitation behaviour of Alloy 625 is changed. Crum and co-workers [88] have published a revised TTT diagram which is shown in Figure2-10.

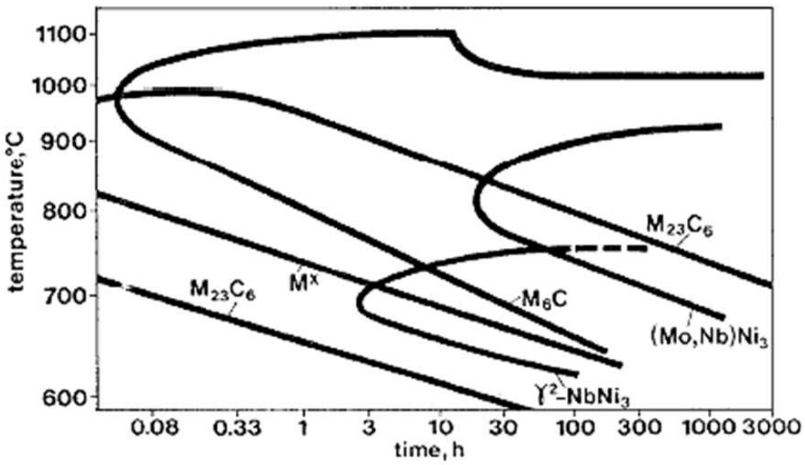

Figure2-9. Time-Temperature-Transformation diagram for Alloy 625 [88].

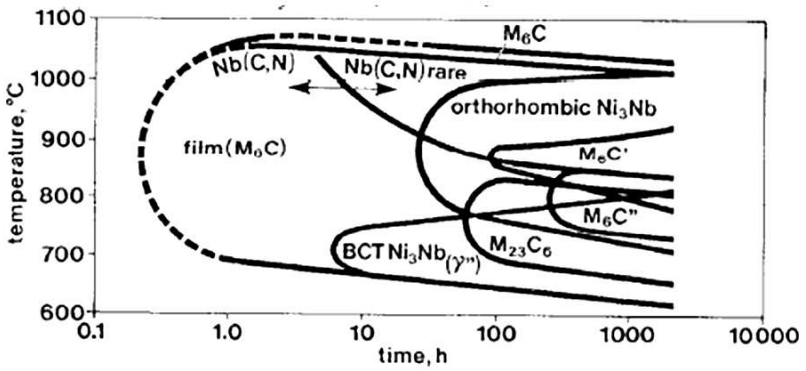

Figure2-10. TTT diagram for solution treated Alloy 625 [88].

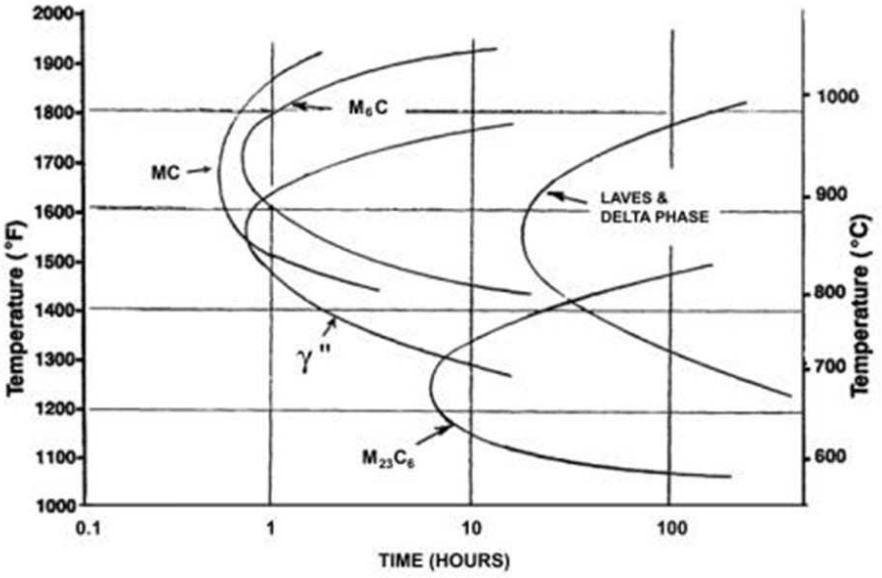

Figure 2-11. Approximate TTT diagrams for phase formation at high temperatures in nominal Alloy 625 [71].

Finally, Floreen [71] presented an approximate TTT diagram for nominal (as defined by Floreen) heats of wrought Alloy 625 (see Figure 2-11). Carbo-nitrides are not indicated on the Floreen diagram due to wide difference in the composition of nominal heats; however, the main intermetallic phase i.e. Laves phase is identified in this diagram. Although the precipitation of δ and γ'' are similar in all of these diagrams, carbide precipitation curves are different in terms of temperature and time. Additionally, the TTT diagram for the specific solution treated alloy (see Figure2-10) contains different variants of M_6C carbide while there is only one variant in the diagram shown in Figure 2-11; these variations are related to differences in the chemical composition. In addition to these differences, the Ni_2M phase, which was experimentally detected in Alloy 625, was not present in the TTT diagrams referred to in the literature [118]. Additionally, Figure2-9 and 2-10 have features inconsistent with the basic principles of TTT diagrams.

2-4-4- Precipitation behaviour of weld deposit

Thermal exposure also can markedly change the microstructure of a weld deposit. However, there are issues in the application of TTT diagrams for prediction of precipitation behaviour of Alloy 625 with an as-welded microstructure. For example, even if care is taken to avoid Laves phase in the as-welded structure, the enrichment of Nb in the interdendritic regions will lead to accelerated precipitation reactions in the ageing experiments.

Figure 2-12 shows an example of a TTT diagram for Delta (δ) precipitation in GTA deposited Alloy 625 weld metal compared to wrought Alloy 625 [71]. As seen, the time for Delta (δ) formation was reduced by a factor of 50

compared to that of the wrought material. It is reported by Cortial [95, 119] that in the rough-welded condition with TIG, the minor phases are present in the interdendritic regions, which is normal for any metal in the as-solidified state. Different interdendritic phases have been identified which are Laves phases, MC and M_6C carbides. This indicates that the M_6C carbide was formed during the non-equilibrium conditions associated with welding. It is reported that the corrosion resistance of the as-solidified IN625 is reduced due to several microstructural changes which occur during rapid solidification. Phase formation during the re-solidification of laser melted surface and/or solidification of the weld overlay has been shown to be a source of high corrosion rate under severe conditions [26, 80].

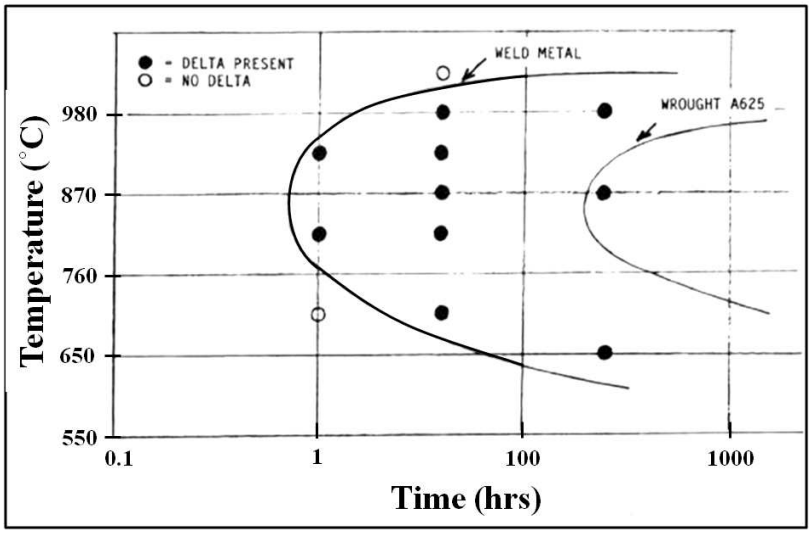

Figure 2-12. TTT diagram showing thermal exposure conditions for formation of Delta in weld metal compared to wrought Alloy 625 [71].

2-5- Cladding and dissimilar metal welding

There is a large body of research addressing dissimilar welding and their results may be relevant to this work which is concerning microstructural evolution in a weld overlay/substrate system. The effects of the welding process and inter-diffusion of elements across the interface during post weld

heat treatment (PWHT) and service can be used as a guide for understanding of the weld overlay/steel substrate system.

Dissimilar metal welds are widely used in high temperature applications in industrial plants and are generally fusion welded. There are different types of dissimilar weld joints such as joints between steels of different phase type (austenitic-ferritic joints) and/or steels of differing substitutional alloy content (primarily ferritic-ferritic joints). Moreover, there are weld joints between different types of steel and nickel alloys. The weldability, compatibility, and long term microstructural and mechanical stability of the welded joints, are of the highest importance in the analysis of dissimilar weld joints.

2-5-1- Interface and its different regions

When a dissimilar metals joint enters service at high temperatures, microstructural changes and elemental redistribution may occur with these changes being most marked close to the fusion boundary. The weld interface of the weldment is classically defined as the interface between the liquid metal and the heat affected zone.

However, microstructural examination on a finer scale reveals a more complicated metallurgical condition at the fusion boundary. Savage [120] has presented a schematic illustration of the various regions of the weld which is shown in Figure 2-13. As presented, there are two additional zones between the melted weld metal and heat affected zone. These are the unmixed zone and the partially melted zone, with the apparent interface being between these two regions.

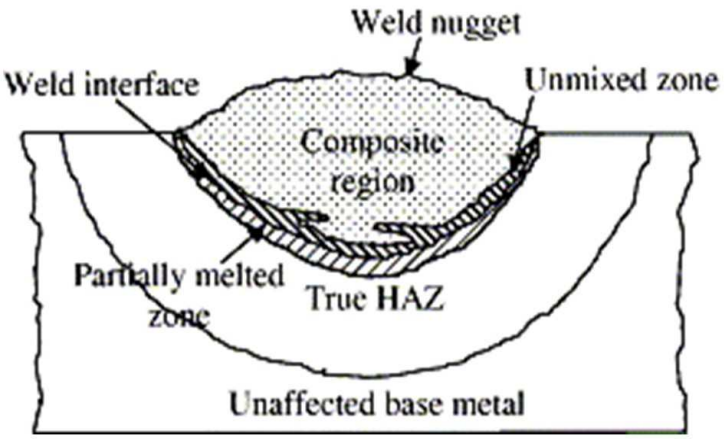

Figure 2-13. Schematic illustration showing different regions of a heterogeneous weld and the proposed terminology of these regions [120].

Usually, all the material in the so called HAZ is regarded as remaining solid right up to the boundary of the fully molten region. However, metallographic examination at high magnifications reveals significant localized melting within this zone near to the fusion boundary. It has become apparent, therefore, that the definition of the fusion boundary is dependent upon both the magnification and metallographic technique used to examine this region.

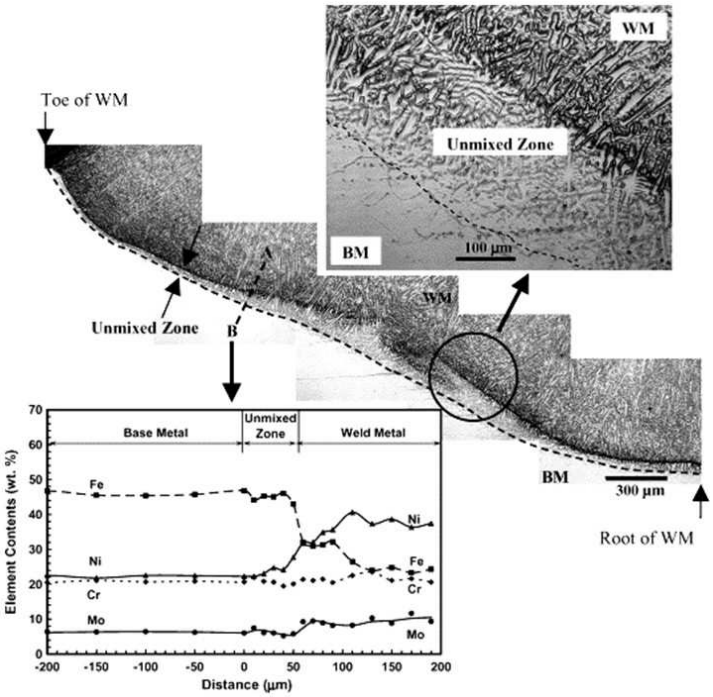

Figure 2-14. Showing photomicrographs of the welding interface indicates identification of unmixed zone with elemental profile [121].

In dissimilar weld joints, an important issue is the difference in chemical composition of the materials which are being welded together. The interface can be identified by the point where the elemental profiles start to change such as shown in Figure 2-14. As seen, a clear layer of unmixed zone exists between the weld metal and substrate. However, there are different materials in this region and therefore this zone is actually the inter-mixing zone.

2-5-2- Interface and Diffusion

Dissimilar joints are prone to migration of alloying elements across the interface during their service at elevated temperature. This occurs owing to wide difference between chemical compositions of materials. The main factors that influence the stability of the welded joint are the phase nucleation, element diffusion, and the rate of phase transformation. These factors depend significantly on temperature and the diffusion path which is related to the structure of the interface; secondary phases have been found to nucleate in an area near to the interface.

The microstructural transformation in a treated weld joint is usually a complicated issue when diffusion between two different materials occurs at the interface. In such cases, several mutually influencing phase transformations can often be observed. The rate of phase transformation is dependent on the temperature and chemical composition of the materials. Changes in the chemical potentials of the elements can cause phase precipitation, phase dissolution, and/or interface replacement in the diffusion zone along the welded interface [122, 123].

2-6- Microstructural evolution in dissimilar weld joints

The mechanical performance of dissimilar weld joints is dependent on the microstructural changes taking place in the interface region at high temperature. Owing to differences between the two materials, transport of elements across the interface occurs, which could potentially result in either dissolution or precipitation of phases such as intermetallics and carbides. The formation of phases is dependent on the heat treatments which are applied during welding (including post weld heat treatment) as well as the service condition.

2-6-1- Different Cr-content steels and formation of soft and hard zones

In all dissimilar steel joints, it is known that carbon migration across the weld interface occurs from the low-alloy steel to the more highly alloyed austenitic [123-128] or ferritic steels [67, 129-135]. This happens generally during post weld heat treatment (PWHT) or subsequent service at elevated temperature. As a result of this migration, a carbon depleted zone (soft zone) is formed in the heat affected zone (HAZ) of the low alloy steel and a carbon enriched zone (hard zone) is formed in the highly alloyed steel [128, 133, 136]. Since the solubility of carbon in ferrite is extremely low, the partitioning of carbon involves the dissolution of carbides on the low alloy side of the weld, and the precipitation of carbides on the high alloy side of the weld. The precipitation of carbides at temperatures where the joints enter service begins with the

formation of cementite, followed by a number of alloy carbides as the system tends towards equilibrium [131, 137-139].

2-6-2- Steel/nickel alloys and formation of carbide arrays

There is a wide body of research regarding the development of the interfacial structure in steel/nickel alloy weld joints [6, 140-147]. The low Cr ferritic steels include 2.25Cr1Mo, AISI 4130 and T11 while nickel alloys include Inconel 625, Inconel 182 (Ni-15% Cr-10% Fe-8% Mn-2% Nb), Hastelloy G (Ni-22% Cr-20% Fe-7% Mo-2% Co-2% Cu-2% W) and Alloy 800 (Fe-30% Ni-20% Cr-1% Mn-0.5% Ti).

Moreover, other different types of steels including stainless steels such as SS310 [141, 145, 147] and high Cr ferritic steels such as 9Cr1Mo [146, 148] are welded to nickel alloys. These dissimilar weld joints are used very frequently in the welding of power plant components, since it is claimed that failures which occur by low ductility circumferential cracking in Cr steel weld joints can be resolved by using nickel alloys as the weld metal [143].

However, the joint made with a nickel-based weld is not immune to failure. It is claimed that nickel-based joints after failure or long-term service exposure contain arrays of particles, mainly $M_{23}C_6$ and M_6C in the ferritic steel, parallel and very close (~1μm) to the weld interface. The precipitates show two general morphologies; the most frequent is a single plane of precipitates with mean size >0.5 μm, and the other is a wide band of finer precipitates (>100 nm). These morphologies are classified as types I and II respectively [6, 140].

It is reported that during welding of 2.25Cr1Mo steel with different nickel alloy fillers, a band of martensite ~0.5 to 50 μm wide forms between the steel and the weld metal due to dilution of steel into the weld metal [6, 143]. The interface between the steel and the martensite band acts as a site for precipitation of coarse carbides during ageing, and a line of these particles grow on the narrow martensite band. It is believed that microscopic cracking is generally associated with these precipitates [6].

These precipitates develop during long-term high temperature service exposure and in the particular system (2.25Cr1Mo steel/ Inconel 182) it is reported that interfacial precipitation can be accelerated by laboratory ageing at 630-700˚C and precipitates and hardness profile in a sample aged at 630˚C for 6000 h are similar to those after long term service [6]. However, above 657˚C, extended laboratory ageing on multi-bead weld samples can cause interfacial precipitate dissolution and gross decarburization of some regions in the weld metal, which are not typical features in the ex-service joints [140].

2-6-3- Phase transformation at 2.25Cr1Mo steel and Alloy 625 weld overlay

There are two publications which address the 2.25Cr1Mo steel substrate and Alloy 625 weld overlay system [149, 150]. One of them addresses phase transformation at the interfacial region and evaluation of microstructural characteristics which could affect the mechanical properties and corrosion resistance of weld overlay. In this research, the interface microstructure of different cladding methods were evaluated [149]. The other paper relates to dilution of steel in the weld overlay and its subsequent solidification

behaviour [150]. There are some differences in the nature of the systems examined, including the iron content of the weld overlay and the interdiffusion structure and width. Moreover, different secondary phases in the weld overlay were reported.

Ayer [149] reported that SIMS images of the interface between 4130 steel and Alloy 625 for chromium and nickel exhibited a sharp change at the interface. However, the iron image indicated a somewhat greater movement of iron into the Alloy 625 cladding which is about 20 μm. He found that these images are similar for 2.25Cr1Mo steel/IN625. The overall composition measured by EDS in a TEM with a 40 nm microprobe demonstrated that transition occurred over approximately a 5 μm distance. The composition of the ferritic steel was modified only by moving ~1 μm away from the interface while the composition in the Alloy 625 side was modified to less than 10 wt.% Fe over a 4 μm distance.

Nevertheless, DuPont [150] has found that the process of weld cladding can be visualized to consist of the melting of a small region of the steel surface by the molten Alloy 625 weld pool. The elements from this melted region of the steel are homogenized in the liquid phase which provides a greater intermixing and minimizes the gradient of compositional profile. The transition region was seen to be ≈20 μm and beyond this transition region there is no systematic variation in composition with distance. Thus, the weld metal composition was shown to be homogeneous on a macroscopic scale with 27.2 ± 5.8 wt.% Fe content.

These researchers have reported different secondary phases in the weld overlay material which may be associated with the differences in compostion and welding process. Ayer [149] reported that grain boundary precipitates were either M_6C or NbC carbides. The stoichiometry of M_6C carbides was determined to be as follows:

$$(Mo_{0.4}\ Ni_{0.36}\ Cr_{0.16}\ Fe_{0.08})_6\ C$$

In contrast, DuPont [150] has reported that secondary phase formation and microsegregation behaviour of the main alloying elements (Fe, Ni, Cr, Mo and Nb) are very similar to those for Alloy 718. The Laves phase formed in a eutectic-type morphology with γ at final stages of solidification as follows:

$$L \rightarrow L + \gamma \rightarrow L + \gamma + Laves \rightarrow \gamma + Laves$$

Ayer [149] has reported that, as in conventional welding, HAZ was observed in the steel and the grain size of the steel had been modified over a major portion of the HAZ. Some interesting microstructural features were also observed at the interfacial region. At the interface between the FCC austenite and BCC ferrite regions, a thin zone of un-tempered martensite was observed. The thickness of the martensite region varied in the range of 0.2 to 0.5 μm. In addition to martensite, precipitation of particles was also observed at the boundary between the un-tempered martensite and ferrite. The particles were identified to be $M_{23}C_6$ carbides.

Formation of these carbides is dependent upon the carbon content of this region. The ferrite is changed to austenite during the welding and the carbon solubility is enhanced. Upon cooling the cladding to room temperature, a

small region of the steel in the interface region is transformed to austenite or austenite + $M_{23}C_6$ carbide region. This reversion is the result of the presence of alloying elements in the area near to interface (such as nickel) which stabilise austenite to lower temperatures.

2-7- Evaluation of microstructural evolution using thermodynamic calculation

The understanding of microstructural evolution in a dissimilar weld joint between nickel alloy and steel system is based on the depth of knowledge of the phase equilibria of both materials in this system. An accurate knowledge of phase fields and transformation temperatures in the steel and the nickel alloy is therefore vital for successful studies of microstructural evolution during thermal exposure. As both of the materials are considered to be multicomponent, so the thermodynamic calculations in each of them would be an important approach in understanding the changes in the microstructure of the system.

The CALPHAD (CALculation PHAse Diagram) method has proved to be an efficient tool for solving various problems in the field of materials research and thermochemistry [151]. In recent years, significant progress has been made in the application of thermodynamic methods to the calculation of multicomponent phase diagrams in steels [152-154], nickel based superalloys [155-158] and other Ni-Cr-Mo alloys [159]. An important reason for employing thermodynamic methods is that they offer a means of systematising and modelling the behaviour of one interesting phase such as a carbide in complex systems like nickel superalloys. This allows the phase relations of

multi-component, multiphase systems to be modelled from those of their subsystems.

Various computer-based thermodynamic models such as Thermo-Calc [160] (used during this research) and MTDATA [58, 161] are commercially available for the calculation of multiphase, multicomponent equilibria as a function of pressure and temperature in conjunction with appropriate thermodynamic property databases. The thermodynamic databases contain assessed Gibbs energy parameters for the thermodynamic models for individual phases. The databases are then linked to software for the calculation of phase equilibria for the practical applications of interest. The success of the CALPHAD technique depends upon the reliability of these databases.

2-7-1- Thermo-Calc software

Thermo-Calc is a software and database package for all kinds of phase equilibrium, phase diagram and phase transformation calculations and thermodynamic assessments. Moreover, many types of process simulations can be performed using this programme. It has been developed for complex heterogeneous interaction systems with strongly non-ideal solution phases and can be applied to any thermodynamic system in different fields like metallurgy, alloy development, semiconductors etc. depending on the kind of database it is connected to [160].

The underlying methodology of this programme is usually a Gibbs free energy minimization process and Thermo-Calc makes use of a very general algorithm to find the equilibrium state of a system. The development of Thermo-Calc started at the Royal Institute of Technology in Stockholm [162] . This

technique allows much more flexibility for the user setting the external conditions for the equilibrium state than any other thermodynamic software. For example, Thermo-Calc is the only software that allows explicit conditions on individual phase compositions or configuration whereas most software can handle conditions on the overall composition only. For example, activities and chemical potentials of the components, volumes, enthalpies, entropies etc. can also be set as conditions. Many quantities that must be calculated by so called "target calculations", i.e. a double minimization procedure, with other software can be calculated directly and much faster with Thermo-Calc.

The flexible way to set conditions is particularly useful when Thermo-Calc is used as a subroutine package in application programs, for example in microstructure evolution or process simulations. For phase diagram calculations, the facility that each condition is set separately and that any condition can be used as axis variable means that Thermo-Calc can calculate innumerable types of diagrams. Thermo-Calc was designed originally for multi-component systems and all its facilities are available for systems with up to 40 components [163].

2-7-2- Modelling of microstructure evolution in Ni-based alloys

The design of new or modified nickel based superalloys for high temperature application is an extremely expensive and time consuming process. Therefore thermodynamic calculations are being introduced in attempt to reduce these costs [164]. Thermodynamic simulation using a CALPHAD software like

Thermo-Calc can bring some useful information to aid understanding of the phase transformations in complex multicomponent systems of the nickel based alloys [165]. However, little experimental data are available on the effectiveness of these predictive tools in these systems.

In the case of Ni-based superalloys, interesting data are the liquidus, the solidus, the hardening phase (γ' and/or γ'') solvus i.e. temperature above which no hardening phase exists at equilibrium, and the temperature range for the existence of minor phases like carbides, carbo-nitrides, borides and TCP phases. Amounts and compositions of such phases are also required to be computed. Some of these data which are obtained from the equilibrium phase diagram for Inconel 625 are presented elsewhere [142].

2-7-3- Prediction of microstructural states in Cr-Mo steels

The microstructural changes in the Cr-Mo steels, especially in the dissimilar weld joints, can affect the service life of the component or the properties of the joint. Thus it is of great practical importance to be able to predict structural changes that occur during the thermal histories associated with production, post weld heat treatment and service. This problem has been tackled both experimentally and by application of numerical calculation. Extensive literature is available for the microstructure – property correlations and identification of carbides in a variety of Cr-Mo steels. However, there are a few works which are related to thermodynamic properties of these Cr-Mo steels [166, 167] and 2.25Cr1Mo steel [168].

There are some models developed by Bhadeshia for carbide transformation sequences in power plants steels [169, 170] which are dependent upon the accurate thermodynamic data of the stable carbides in these steels. Moreover, there is a paper which uses phase diagrams to predict the stable phases in the microstructure of these steels [153].

2-7-4- Thermodynamic aspects of carbon migration in dissimilar weld joints

An interesting feature in dissimilar weld joints is the carbon migration. It is important to predict the microstructural changes in these joints during thermal histories in production and service. Computer simulation of diffusion in the multiphase systems has been thoroughly investigated [152, 171, 172]. In order to perform accurate simulations, one needs an accurate thermodynamic description of different materials in the dissimilar weld joint system which is available within the thermodynamic softwares such as Thermo-Calc system.

2-8- Summary

There is a large body of work on the microstructural evolution in the 2.25Cr1Mo steel and Alloy 625 at service temperatures. Moreover, the microstructural evolution in dissimilar weld joints between steels and nickel-based alloys are available. In the current work, the microstructure of the various regions of a Ni-based weld overlay on a 2.25Cr1Mo steel substrate in as-welded condition will be characterised.

High temperature exposure tests will be used to produce a set of simulated service microstructures to allow characterization of the microstructural changes in the different regions with ageing time. This work will examine the microstructural changes that occur in the 2.25Cr1Mo steel and the weld overlay material system and the reciprocal effects on each material due to carbon migration.

Moreover, thermodynamic modelling work has been carried out for the simulation of phase formation during welding and at certain temperature with different carbon contents in each material of this system. This information can then be used as a guide to the long term service performance of weld overlaid components.

Chapter 3

Experimental procedure

3-1- Introduction

The experimental procedure used for the performance of high temperature exposure tests and the microstructural characterization of different samples presented in this thesis will be discussed in this chapter. The first sections concern the starting materials and experimental procedure for thermal exposure tests. The next sections cover the sample preparation for the various chemical and surface techniques used to examine the changes in the microstructure before and after thermal exposure tests. Methods of microstructural examination and characterization are then briefly reviewed in the following sections.

3-2- Materials

The starting material in this work was a weld overlaid tube with 25 mm outside diameter as shown in Figure 3-1(a). The tube consists of a weld overlay layer with approximately 1.7 to 2 mm thickness which is applied by a proprietary spiral welding method on the outer bore of a steel tube with 15 mm internal diameter and about 3.5 mm wall thickness. This tube is designed to be used in a boiler super heater tube in a WtE plant. A wrought IN625 plate was used to compare the characteristics of the weld overlay with Alloy 625.

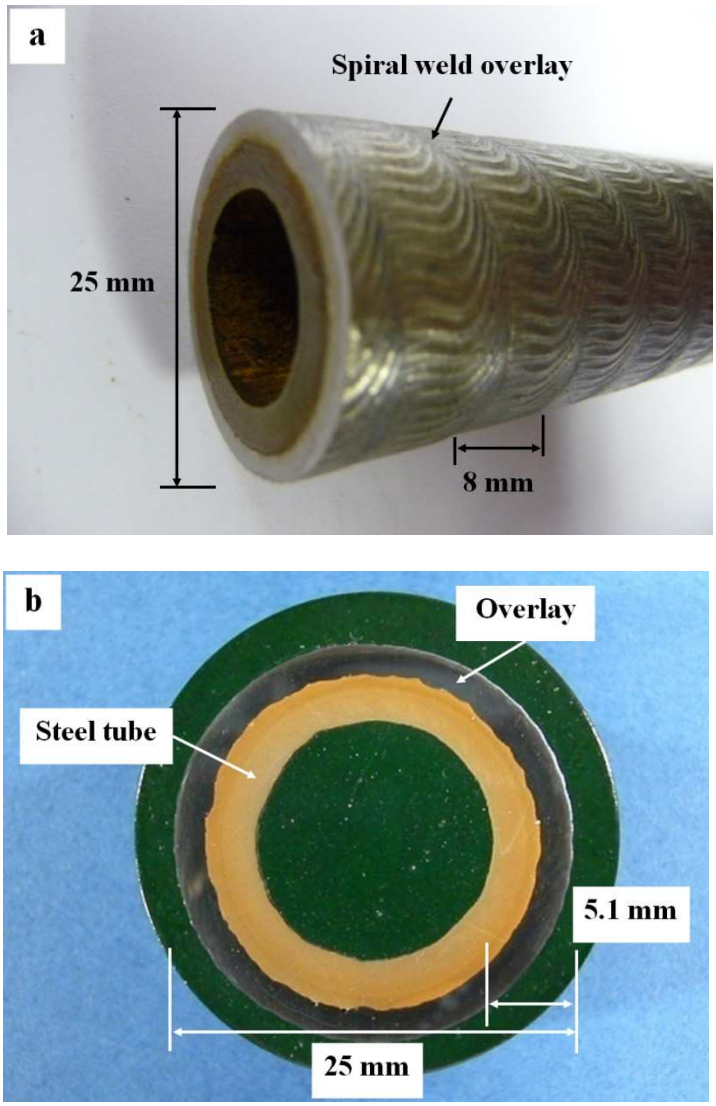

Figure 3-1. Showing (a) the weld overlaid tube and weld bead specifications, (b) the whole cross sectional sample of the tube.

The tube was nominally a 2.25Cr1Mo steel and the weld overlay was a nickel-based alloy similar to IN625. The typical composition ranges of these materials are given in Table 3-1.

Table 3-1.Nominal chemical composition of 2.25Cr1Mo steel and IN 625 alloy (wt.%)

Element	*Steel 2.25Cr1Mo*	*IN625*
C	<0.1	<0.1
Al	-	<0.4
Si	<0.5	<0.5
Ti	-	<0.4
Cr	2-2.5	20-23
Mn	<0.5	<0.5
Fe	Balance	<5
Ni	-	Balance
Nb	-	3.15-4.15
Mo	0.9-1.2	8-10

3-3- High temperature exposure tests and thermal exposed samples

In order to simulate the effects of high temperature service conditions on this overlaid tube, individual samples were produced by cutting sections of tube. The sections were cut with about 7 to 10 mm thickness and each section was subsequently cut into quarters, yielding 4 specimens. Figure 3-2(a) shows a typical cross sectional samples used in this work. The specimen dimensions are suitable for mounting and preparation processes.

The aim of this research is to analyse the evolution of microstructure during high temperature exposure. Referring to previous research, the microstructure of 2.25Cr1Mo ferritic steel undergoes phase changes above 675˚C which are

undesirable for service condition [6, 140]. Therefore, specimens were kept below this temperature. They were heated in a furnace at 650°C for high temperature exposure experiments for various times, from 1 day to 128 days to ensure maximum rates of phase transformations which are applicable for service conditions.

The sample identification represents its exposure time in days and therefore includes "D" e.g. D128 represents a sample which was at elevated temperature for 128 days. All specimens were air cooled after their exposure time. Due to the oxidation of the steel occurring during the high temperature exposure tests in the air, for long term experiments i.e. 64 and 128 day tests, these samples were sealed in evacuated quartz tubes at a residual pressure of 10^{-5} torr before being placed in the furnace and were subsequently air cooled to room temperature. As the main aim was to analyse the phase transformation and precipitation behaviour at this temperature, the use of a vacuum will not affect on the behaviour.

It should be mentioned that for some conditions such as the as-welded and the 128 day conditions, the longitudinally sectioned samples (see Figure 3-2(b)) were examined. These samples were used for analysis of the microstructral features along the length of tube. Moreover, in order to investigate how the nickel alloy microstructure behaves in the absence of the steel substrate, one tube section with about 10 mm length was cut and its steel substrate was removed by machining which is shown in Figure 3-2(c). The thermal effect of machining on the weld overlay material will be negligible after 128 days exposure.

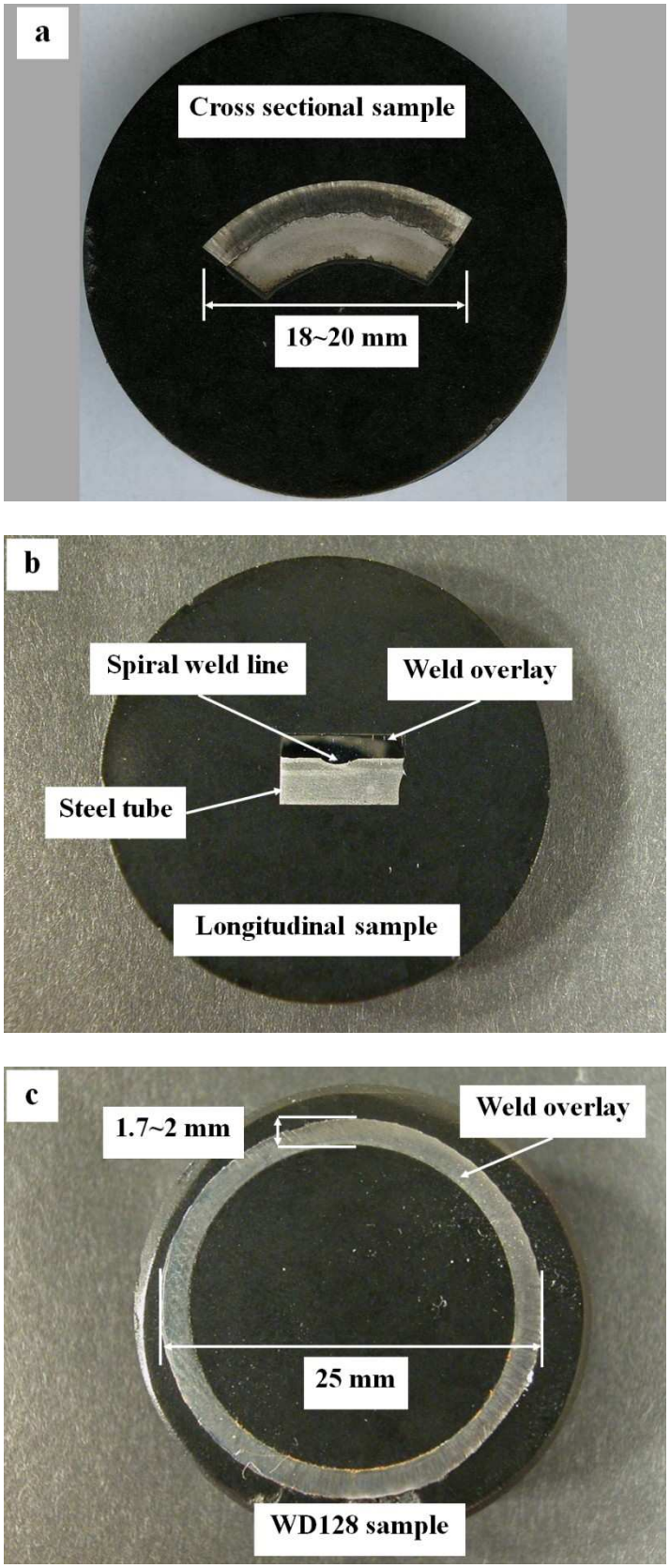

Figure 3-2. Showing (a) the typical cross sectional sample used for high temperature exposure tests, (b) the longitudinal section of the tube used for the analysis of the interface in the as-welded condition and after 128 days, and (c) the free standing of weld overlay (WD128) sample after high temperature exposure and mounting.

Moreover, hardening due to machining should be relieved in the first hours of thermal exposure. It should be noted that three different sets of high temperature exposure tests were carried out in this work which are reported in Table 3-2. In the first set, the exposure time started at 1 day giving the D1 sample. Afterwards, the exposure time was increased by a factor of 2 for the next exposure test, up to a maximum of 128 days.

Based on the results of the first set and in order to obtain a more detailed understanding of microstructural changes during high temperature exposure, a second set of tests were undertaken. In this set, the first sample was exposed for 12 days and the exposure time was increased by four days for the next test; the final sample in the second set has been exposed for 32 days. Because of performing two sets of exposure tests, two samples i.e. D16 and D32 were produced twice, providing a measure of the reproducibility of the tests.

Table 3-2: Sample identification including sample name, its quantity and the exposure time in hours at 650˚C

Sample Name	*Number of samples in each set*			*Time(hours)*
	set1	*set2*	*Set3*	
As-welded	1	0	0	0
D1	1	0	0	24
D2	1	0	0	48
D4	1	0	0	96
D8	1	0	0	192
D12	0	1	0	288
D16	1	1	0	384
D20	0	1	0	480
D24	0	1	0	576
D28	0	1	0	672
D32	1	1	0	768
D64	1	0	0	1536
D128	1	0	0	3072
WD128	0	0	1	3072

In the third set of tests, only the free standing weld overlay sample was exposed. In order to compare its precipitation behaviour with the D128 sample, this sample was exposed for 128 days at 650˚C in the air, as there is no concern about oxidation and is termed WD128 sample. Moreover, the furnace ambient has no effect on the precipitation of the weld overlay material. Comparison of WD128 microstructure with D128 reveals the effect of steel on the weld overlay micorstructural evolution.

3-4- Sample Preparation

3-4-1- Composition analysis using spark emission spectroscopy

This technique was employed to determine chemical composition of both the overlay and tube materials using a FOUNDARY-MASTER instrument. The instrument requires a flat surface of at least 15 X 15 mm and Figure 3-3 shows a mounted cross section of a sample prepared for this experiment.

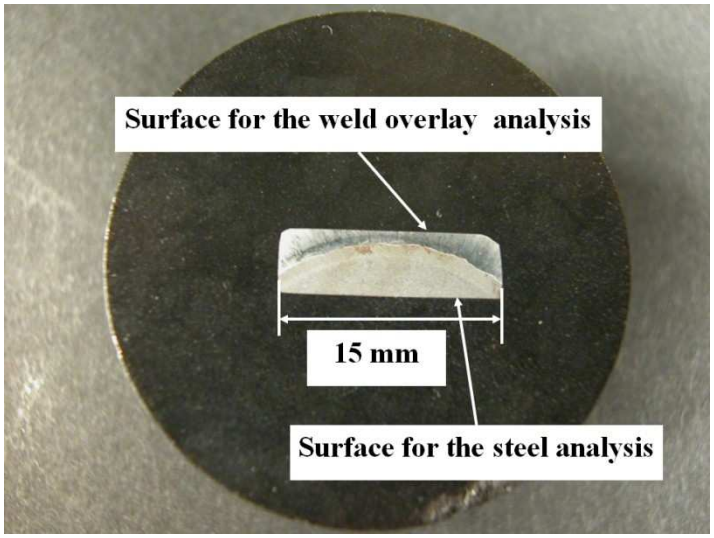

Figure 3-3. Showing a cross section of the flat sample using for chemical composition analysis after mounting

The steel composition was determined from analysis of the surface shown in Figure 3-3. The other side of sample was used for the analysis of the overlay which was performed on two different flat planes. The position of these planes was referenced to the distance from the steel/nickel alloy interface at the midpoint of the sample. The distances were 700 μm and 500 μm respectively.

3-4-2- Sample preparation for optical and SE microscopy

Specimens for the microstructural characterization studies were prepared by conventional mounting, grinding and polishing methods. Because of oxidation and decarburization of steel in the samples during high temperature exposure tests, and to avoid its effects, approximately 1 mm of specimen surface were removed by grinding. The cross sectional samples were firstly hot mounted using different Metprep mounts (conductive and non-conductive) and a Buehler Metaserv automatic mounting press. The mounted samples were ground mechanically to 1200 grit with SiC papers, then polished with 6 microns and 1 micron diamond paste respectively to obtain mirror surface. For some characterization processes such as EBSD, the roughness of surface finished with 1 micron diamond paste was not suitable; in these cases the final polishing was conducted with colloidal silica suspension (Si_2O, 0.1 μm, pH: 9.0).

As a result of the widely dissimilar compositions of weld overlay material and steel substrate in the samples, it was necessary to etch samples sequentially to reveal the microstructure of each part. 2% NITAL solution was used for the steel part and the etching time has a great effect on the microstructure and

after running many tests, it was found that by 30 seconds etching time the best result can be achieved.

The weld overlay region required highly corrosive etch and there are many processes for Alloy 625 etching which is reported in hand books and former researches. In the present investigation, two different methods were used for etching the weld overlay as well as wrought IN625, namely electrolytic etching and etching with AQUA REGIA.

In former method, a solution of 10 wt.% oxalic acid in water, was used with electrode potentials of 2-3 V. The cathode of the device was connected to a stainless steel plate which was suspended in the solution. The anode was connected to the sample with a wire. The desirable etching time in this process depends on electrode potentials and decreases by increasing voltage. The electrolytic etching process required a non-conductive mount which causes limitations for using EDX of the samples in the electron microscopy.

The latter etching method used AQUA REGIA solution which consists of a 25% by volume of HNO_3 and 75% by volume of HCl. It was found that this solution must be heated up to 50°C prior to etching. This reduces the etching time and causes more corrosion rate during etching and protrudes the dendrites after etching. As the AQUA REGIA etchant solution is very corrosive, the etching time is less than 10 seconds.

3-4-3- FIB-TEM sample preparation

The TEM analysis required a thin foil which is electron transparent and the main issue is to prepare a sample and choose a proper thinning process among

different thinning processes. The Focused ion beam (FIB) instrument is a powerful tool in material studies as micromachining for transmission microscope specimen preparation is possible with it. Moreover, it can be used for high resolution imaging process. In this section, the FIB-TEM sample preparation will be outlined.

Because of sputtering action of the ion beam, the FIB can be used to locally remove or mill away material. Therefore, this process can be used for production of the sample from the bulk material and also for its thinning process. The microstructure of the D64 and the D128 samples were studied using the FIB-TEM method in the Department of Materials, Loughborough University. Three specimens were prepared from these samples; the first one was taken from the weld interface and two other samples were taken from ~100 μm and ~500 μm distant from the interface in the steel region.

Figure 3-4(a) shows the locations of the TEM specimens in the D64 sample. TEM specimens were cut form similar locations in the D128 sample. Figure 3-4(b) shows a micro-volume sample for production of a TEM sample using the FIB method. It is clear that material around the micro-volume sample has been removed. Finally, the micro-volume sample has been cut from the bulk with ion beam again.

An Omniprobe micro-manipulator was used to lift out the micro-volume sample. This sample was thinned using FIB to produce a TEM specimen. Finally, a Pt gas injector system is used for local Pt thin film deposition. The TEM specimen with a deposited film of Pt and mounted in the sample holder is shown in Figure 3-4(c).

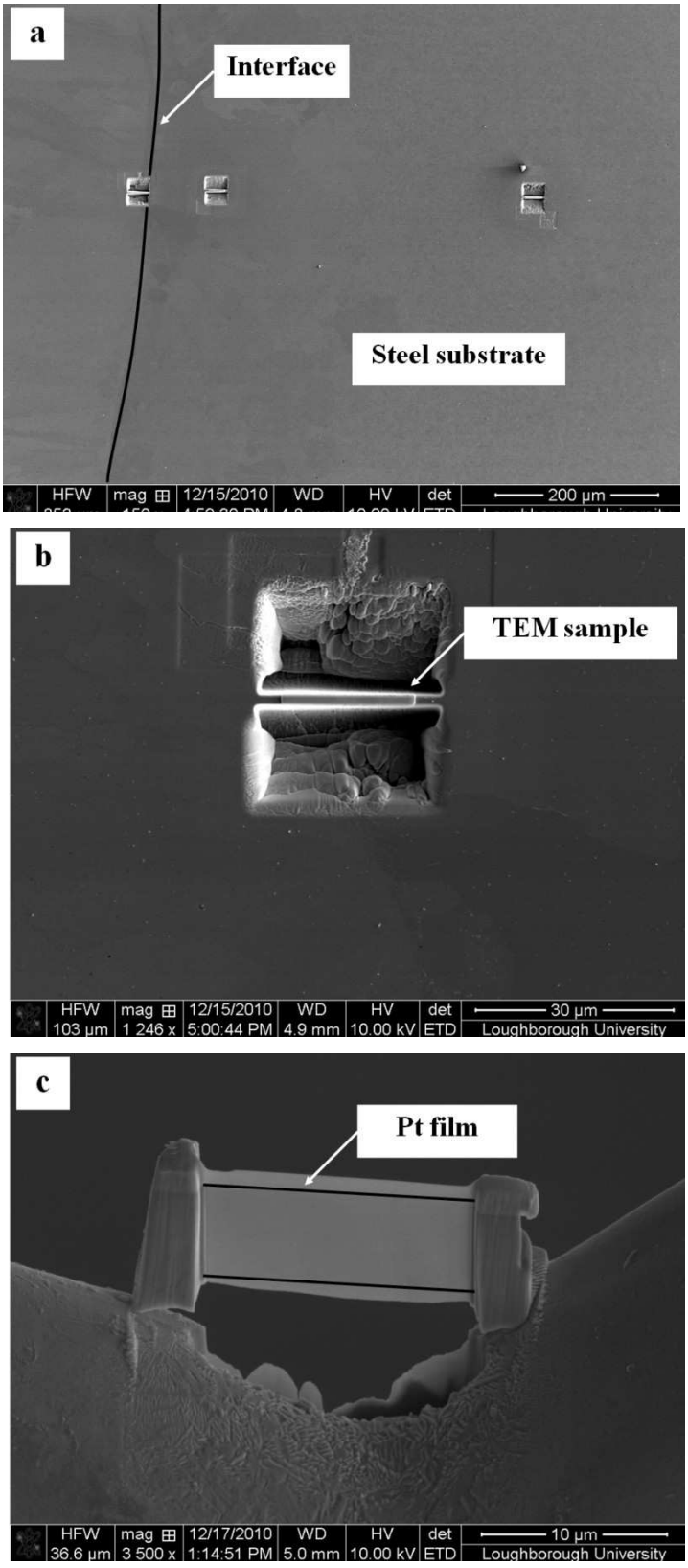

Figure 3-4. Showing (a) TEM specimens locations in the cross sectional sample with different distances from the interface, (b) the micro-volume sample which is used for the TEM thin foil preparation, and (c) the TEM electron transparent specimen in the sample holder which is covered by deposition of Pt films.

3-5- Principles of characterization methods

3-5-1- Optical emission spectroscopy

The chemical composition analysis of the steel substrate and the weld overlay material as well as wrought IN625 were performed using an optical emission spectrometer. The specimen preparation procedure is detailed in section 3-4-1. The optical emission spectrometer determines element concentration via a quantitative measurement of the optical emission from excited atoms.

This high-temperature discharge provides sufficient energy to promote the atoms into high energy levels. The atoms decay back to lower levels by emitting light. Since the transitions are between distinct atomic energy levels, the emission lines in the spectra are narrow. The spectra of samples containing many elements can be very congested, and spectral separation of nearby atomic transitions requires a high-resolution spectrometer. Since all atoms in a sample are excited simultaneously, they can be detected simultaneously using a polychromator with multiple detectors. This ability to simultaneously measure multiple elements is a major advantage of optical emission spectroscopy. In this research, a FOUNDRY-MASTER instrument was used which works with electron discharge in argon atmosphere. Different software was used for analysis of the steel and the nickel alloy. The results of this analysis are presented in appendix No.1.

3-5-2- Optical Microscopy

Optical microscopy is a conventional process for characterisation of the microstructure. In this work, there are some features in the microstructure of

some samples which are only visible with an optical microscope. In other words, the optical microscopy images show distinctive regions compared to the other microscopy methods. In this work, primary microstructural analysis was carried out on the samples using a Nikon model OPTIPHOT microscope. This microscope was equipped with a Nikon digital camera DMX1200F for imaging. Three different objective magnifications were used in this method. For overall images it was 5X while for detailed images it was 40X and finally for high magnification images, it was 100X.

3-5-3- Scanning Electron Microscopy (SEM)

SEM provides valuable information regarding the microstructural features in the cross sectional samples. The SEM characterization was performed on a FEI microscope. This FEI XL30 scanning electron microscope was fitted with a tungsten filament which operates in high vacuum mode. The microscope was primarily operated at an accelerating voltage of 20 kV, spot size of 4-6 and a working distance of 10 mm in both secondary electron (SE) and back scattered electron (BSE) imaging modes.

In a typical SEM system, a stream of electrons generated by the filament of the electron gun is accelerated toward the specimen using a positive electrical potential. This stream is confined and focused using the metal apertures and magnetic lenses into a thin, focused, monochromatic beam. This beam is focused onto the sample using a magnetic lens. This electron beam irradiates the surface of the specimen which in turn produces a signal in the form of either x-ray fluorescence, secondary or back scattered electrons. The signal produced by the secondary electrons is detected and sent to a cathode ray tube

(CRT) image. By changing the width (W) of the electron beam scan, the magnification (M=D/W) can be changed where D is the width of the CRT. Since D is constant, the magnification can be increased by decreasing the width (W).

The secondary electron imaging method was mainly used for analysing the microstructure of samples in the etched condition. However, backscattered electron imaging was used for the analysis of different phases available in samples in the un-etched condition, since the BSE imaging mode relies on the differences in the mean atomic number of the phases. The mean atomic numbers of all the phases which are expected to occur in the 2.25Cr1Mo steel/ nickel alloy system are listed in appendix No.2.

3-5-4- Transmission Electron Microscopy (TEM)

Transmission electron microscopy is powerful imaging tool for detailed crystal structure and observing the fine particles in the matrix as well as other features such as grain boundaries. As mentioned in section 3-4-3, FIB-TEM specimens were produced from different regions of the D64 and the D128 samples. A Philips Tecani F20 FEG-(S)TEM equipped with an Oxford ISIS EDS system and a Fischione high annular dark field detector (HAADAF) was operated at 200 kV in STEM mode for high resolution imaging and analytical studies.

In a STEM, a narrow spot of the focused electron beam scanned over the sample in a raster. The rastering of the beam across the sample makes this mode of TEM suitable for analysis techniques such as mapping with EDS and

annular dark field imaging (ADF). These signals can be obtained simultaneously, allowing direct correlation of image and quantitative data. By using a STEM and a high-angle detector, it is possible to form atomic resolution images.

3-5-5- Ion beam imaging

In the same manner that images are generated in an SEM, the ion beam can rastered over a sample surface and the emitted electrons, particles (atoms and ions), and electromagnetic radiation can be detected. In the FIB instrument, the imaging is based on detecting the low-energy electrons referred to as ion-induced secondary ions (ISEs).

As an alternative to chemical etching, by controlling the FIB, the contrast mechanism for ISE can be changed from channelling which reveals grain microstructure, to a contrast that reveals the phase distribution. In this technique, only surface atoms layers are removed so actual surfaces are remained for the quantification. The ion beam imaging analysis was performed on an FEI Nova 600 Nanolab dual beam system which combines both a FIB and a FEG-SEM in a single instrument.

3-5-6- Energy Dispersive X-ray Analysis (EDX)

Energy dispersive X-ray (EDX) analysis was used together with SEM for local elemental identification. When the incident electron beam interacts with the specimen the bombardment of high energy electrons on the orbiting inner most electron shell of an atom will lead to the escape of high energy electrons

and leave a vacancy. An electron from the outer orbiting shell jumps into the empty electron vacant shell and emits energy. The emitted energy, in the form of X-ray photons is specific for each element in the periodic table. The induced X-ray fluorescence in the sample is energy-analyzed using a cooled semiconductor detector. The element-specific spectral lines are identified to give the elemental composition for the incident area.

This technique employed with an Oxford Instruments Si detector in combination with the SEM in the present work. Data were converted using a standardless ZAF correction procedure. The process is suitable for determining elements with atomic number higher than 12; therefore light elements such as B, C, etc. cannot be quantified.

3-5-7- Electron Probe Micro Analysis (EPMA)

An electron probe micro analyzer (EPMA) is an analytical tool used for determination of chemical composition of small volumes of solid materials. It works similarly to a SEM-EDX but emitted X-rays are wavelength-analysed. The basic measurement in this method is the intensity ratios of X-rays from a sample and a standard which is most conveniently taken to be the pure element [173].

The measured intensities require certain instrumental correction, including subtraction of back-ground, the chief source of which is the continuous X-ray spectrum. The composition at the analysed point is calculated from the corrected intensities by applying ‘matrix corrections’ which take account of the various factors governing the relationship between intensity and

composition. These are commonly applied in the form of 'ZAF correction' with separate correction factors dependent on atomic number, absorption and fluorescence [174].

A JEOL JXA-8200 electron microprobe in Department of Archaeology at University of Nottingham (with thermionic emission from an electron gun fitted with a tungsten 'hairpin' filament which operates at high accelerating voltage under high vacuum mode) was employed to examine the light elements such as carbon distribution in the microstructure of the samples. The micro probe analyser was primarily operated at an accelerating voltage of 20 kV and 10^{-4} Torr or better vacuum. Magnetic lenses are used to focus the beam into a fine probe incident on the surface of the specimen and a probe diameter of 0.2-1 μm is typical. The electron beam current used in this research was about 10 nA which is in the range of typical current (1-100 nA) and working distance of this microprobe analyser is about 11 mm. In microprobe analysis, the X-ray spectrum is recorded with either with 4 wavelength dispersive spectrometers (WDS) or one energy dispersive spectrometer (EDS).

In the current research, the WDS method was used to obtain quantitative information about the composition of different phases in each sample. Prior to quantitative analysis, it was necessary to calibrate each spectrometer using pure metal standards from Micro-Analysis Consultants Ltd. Moreover, the $\varphi\rho Z$ correction method supplied by JEOL was used to obtain quantitative results.

3-5-8- EBSD

Electron backscattered diffraction (EBSD) is a technique which allows crystallographic information to be obtained from the samples in the scanning electron microscope (SEM). In EBSD, a stationary electron beam strikes a tilted crystalline sample and the diffracted electrons form a pattern on a fluorescence screen. This pattern is characteristic of the crystal structure and orientation of the sample region from which it was generated.

The diffraction pattern can be used to measure the crystal orientation, measure grain boundary misorientations, discriminate between different materials, and provide information about local crystalline perfection. When the beam is scanned in a grid across a polycrystalline sample and the crystal orientation measured at each point, the resulting map will reveal the constituent grain morphology, orientations, and boundaries. These data can also be used to show the preferred crystal orientations (texture) present in the material. A complete and quantitative representation of the sample microstructure can be established with EBSD.

An Oxford Instruments HKL Technology Nordlys II EBSD detector fitted to FEI XL-30 and controlled with CHANNEL5 software was used to obtain preliminary EBSD results for the D128 sample. In order to determine the chemical composition and crystallographic nature of observed phases in the D32 and the D64 samples, the combined EBSD and EDS analyses were carried out in Oxford Instruments laboratory. A Nordlys S detector and X-MAX 80 ESD detector from Oxford Instruments installed on a FEG SEM were used for this study. The Flamenco software was used to acquire both

EBSD and EDS data. Tango and Salsa software modules in CHANNEL5 were used for post processing the EBSD data acquired. The EBSD data was obtained with a probe current of 10 nA and an acceleration voltage of 20 kV.

3-6- Hardness measurements

3-6-1- Microhardness method

The Vickers hardness tests were conducted with a LECO-M400 machine and were measured using a 200 gf load on specimens at various locations of samples. The measurements were carried out on the steel and weld overlay regions systematically at various distances from the weld interface. Four sets of measurement were carried out on different locations of a sample which are shown Figure 3-5(a).

In each set, there are different intervals between two successive indents. In the preliminary measurements, the distance is more than ~200 μm, while in the final measurements it was reduced to the standard minimum distance. In the measurements of low hardness regions, and in order to keep the standard minimum distance between two successive indents, the hardness measurements were carried out on an inclined line. The distance from the interface increased by ~100 μm and a ~100 μm horizontal distance is considered between them. Figure 3-5(b) shows a set of these hardness measurements which was carried out on the steel substrate of the D32 sample. On the basis of the preliminary results, the detailed measurements of hardness in the harder regions were carried out by decreasing the intervals between indents to ~20 μm.

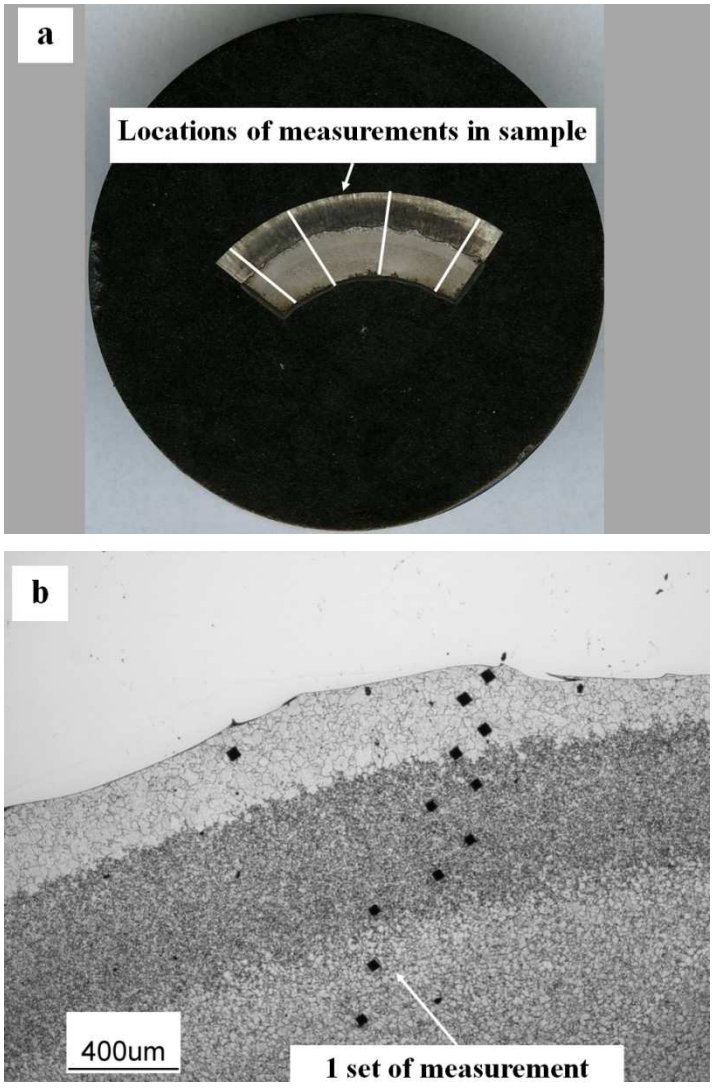

Figure 3-5. Showing (a) four preliminary hardness measurement sets of different regions in a sample, (b) indicates a set of measurement in the steel region of D32 sample.

In order to characterize the boundary of different hardness regions, the hardness measurement has been repeated on the certain areas of the sample between two indents. This process was repeated for 4 different regions of the sample and each time 5 tests were carried out. The hardness values versus the distance from the interface were used to establish the hardness profile of the sample in one location. Based on these results, the comparison between hardness profiles of different samples can be made.

This procedure was applied on the as-welded sample as well as thermally exposed samples for identification of hardness profile. The hardness profile

changes are crucial in this investigation, as they are related to the microstructural evolution during high temperature exposure experiments.

3-6-2- Nanohardness method

A MML Nanotest system manufactured by Micro Materials Ltd was used to carry out the nano-indentation for hardness measurement of the WD128 sample. The indentation experiments were performed using a standard diamond Berkovich indenter. A 5 mN load was used with a 3X10 grid in which indents were approximately 5 μm apart. Due to limitations of microhardness method in the edges, this type of indentation was carried out on two different regions i.e. bulk and edges of polished WD 128 sample in order to reveal the hardness changes in these regions.

Chapter 4

Characterization of the as-welded condition

4-1- Introduction

The material in this project is a weld overlaid tube which has a potential application as a superheater tube in a WtE boiler. The purpose of this chapter is to make an extensive characterization for different regions of this tube in the as-welded (i.e. as-deposited) condition. In the first section, the macrostructure of the tube is reviewed and the chemical composition of different regions is presented.

In the second section, the microstructure of the steel substrate is reported and its different zones are introduced. It should be noted that the substrate is a ferritic steel and the analyses were carried out to evaluate the effects of the

welding on its microstructure. A brief discussion about the interface region is also presented in a following section.

The final section considers the weld overlay of similar composition to IN625 and in this section, characteristics of different zones in this material will be reported. Moreover, secondary phases in this material will be analysed.

4-2- Macrostructural features and chemical composition

The experimental work described here was conducted on the cross section of weld overlaid tube to gain an understanding of the macrostructure. There are two main regions, namely the steel substrate tube and the weld overlay as shown in Figure 4-1. As shown, the overlay region thickness is between 1.7 and 2.0 mm and the steel substrate thickness is about 3.0 to 3.5 mm. The variations in the thicknesses are because of surface roughness of the weld overlay and the wavy interface between the two.

The welding process for cladding on the outer bore of steel tube causes a wavy interface between the weld overlay and substrate. The amplitude of the interface undulations depends on the location. There are large undulations with a few millimetres wavelength and several hundred microns amplitude in some points while there are some parts with smaller wavelength and few microns amplitude.

The results of the chemical composition analysis of the weld overlay are presented in the Table 4-1. The results are from two longitudinal planes parallel to the tube axis but at different distances from the interface (700 μm

and 500 μm). The details of the sample preparation were presented in section 3-4-1.

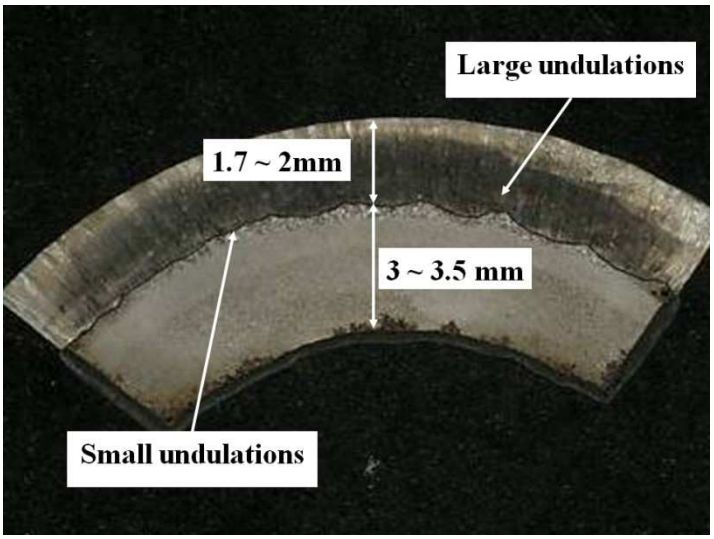

Figure 4-1. Showing typical sample in this project with the thickness of the weld overlay and the steel substrate; the interface undulation is related to welding and alters form point to point.

The chemical composition of a wrought IN625 plate is presented in Table 4-2 for comparison. It is clear from Table 4-1 that the chemical composition of weld overlay is similar to that of alloy IN625. By comparing these tables, it is clear that the weld overlay has significantly more iron and carbon and lower molybdenum and niobium contents. However, the chromium content is about the same in the both materials.

Moreover, it can be seen that some minor elements such as Ti in both materials are in the same range while other minor elements i.e. Cu, Co and Al contents are negligible in the weld overlay material. The higher Fe and C levels in the weld overlay material come from either dilution during cladding or the use of a consumable with higher iron and carbon compared to the standard IN625 or a combination of both.

Table 4-1.Chemical composition of the weld overlay from different planes with 700 µm and 500 µm distance from the interface

Element	*Composition (wt.%)*		*Average (wt.%)*
	at 700µm	*at 500µm*	
C	0.02 to 0.03	0.01 to 0.02	0.02
Ti	0.17 to 0.18	0.18 to 0.19	0.18
Cr	20.6 to 20.7	21.0 to 21.1	20.9
Fe	8.3 to 8.7	7.3 to 7.7	8.0
Ni	Balance	Balance	Balance
Nb	3.1 to 3.2	3.1 to 3.3	3.2
Mo	8.1 to 8.2	8.1 to 8.3	8.2

Table 4-2.Measured chemical composition of the wrought IN625, wt.%

Element	*wt.%*	*Average (wt.%)*
C	0.004 to 0.006	0.005
Al	0.1 to 0.11	0.1
Ti	0.20 to 0.22	0.21
Cr	21.8 22.0	21.9
Fe	3.09 to 3.28	3.18
Co	0.09 to 0.1	0.1
Ni	Balance	Balance
Cu	0.17 to 0.174	0.17
Nb	3.4 to 3.6	3.5
Mo	9.1 to 9.2	9.2

Table 4-3.Measured chemical composition of the steel substrate, wt.%

Element	*wt.%*	*Average (wt.%)*
C	0.09 to 0.11	0.10
Si	0.22 to 0.25	0.24
Cr	2.31 to 2.34	2.33
Mn	0.42 to .44	0.43
Fe	Balance	Balance
Cu	0.10 to 0.11	0.11
Ni	0.9 to 0.1	0.1
Mo	0.91 to 0.92	0.92

The chemical analysis of the steel substrate is presented in Table 4-3. The chromium content is approximately 2.25 wt.%, the molybdenum content is ~ 1 wt.% and the carbon content is ~ 0.1 wt.%. Therefore, it can be assumed that the steel substrate in the overlaid tube is the well known 2.25Cr1Mo steel which is also known by the code 10CrMo910 and T22. The results of the optical emission spectroscopy are presented in the appendix No.1.

4-3- Microstructural characterization of 2.25Cr1Mo steel substrate

Figure 4-2(a) is a low magnification image of the steel region of the tube cross-section. Two different zones in the 2.25Cr1Mo steel microstructure are clearly visible after etching with 2% Nital and are labelled in this image.

1) A HAZ zone close to the interface, about 1 mm wide and with a uniform microstructure.

2) A central zone of the steel region, ~ 2 to 2.5 mm wide and with a bimodal microstructure.

The optical microscopic images of different zones of the steel substrate in the as-welded condition are shown in Figure 4-2(b) and (c). The HAZ can be divided into two regions as follows (see Figure 4-2(b)):

1) A Near-HAZ ~ 300 μm wide with a uniform microstructure

2) A Far-HAZ ~ 700 μm wide with a non-uniform microstructure.

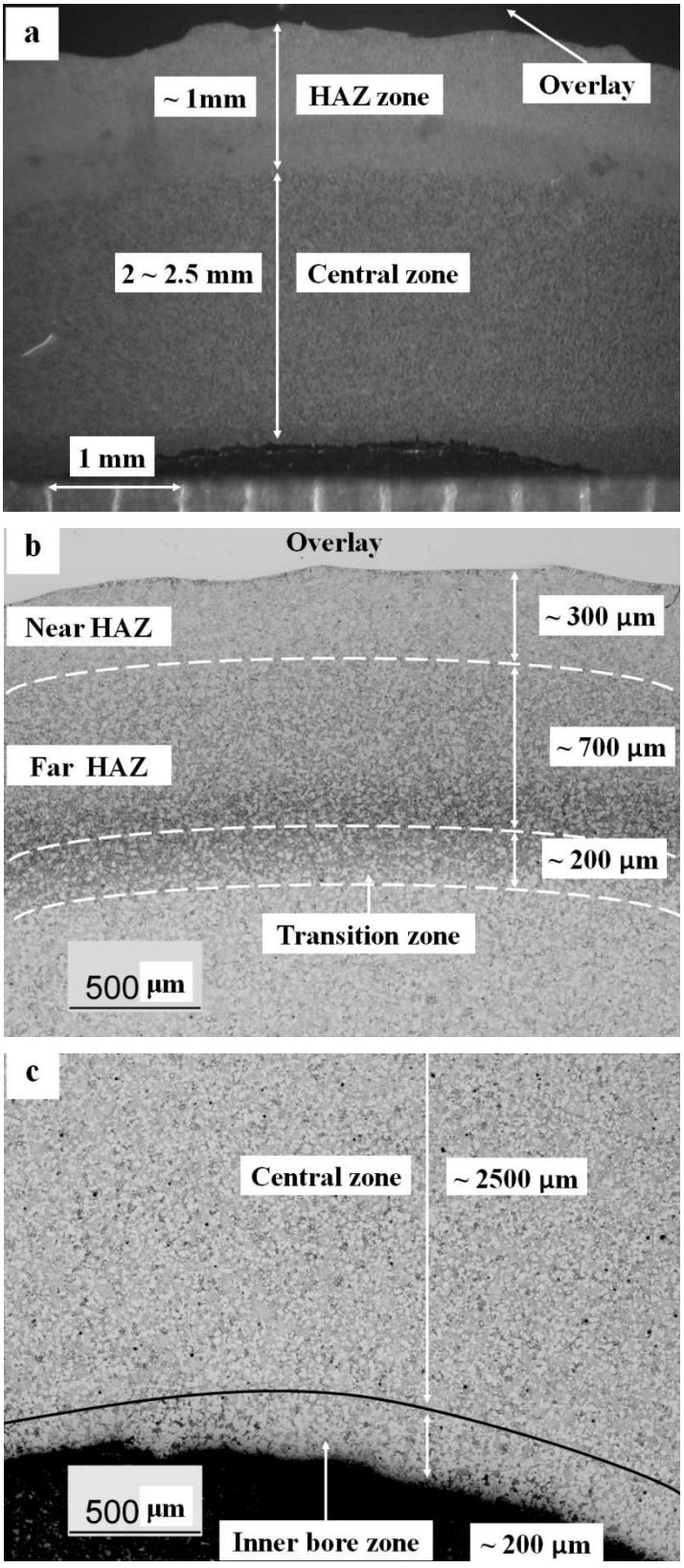

Figure 4-2. Showing different zones in the cross section of the steel substrate in the etched condition; (a) low magnification image indicates the HAZ and the central zones, (b) higher magnification optical microscope image of two zones in the HAZ and the transition zone and (c) higher magnification optical microscope image of the central and inner bore zones.

It is clear that by moving away from the interface, the uniformity of the HAZ zone decreased which is related to the maximum temperature and rate of heating/cooling of the thermal cycle during the welding process. Moreover, there is a zone ~ 200μm wide between the far-HAZ and central zone. The microstructure of the steel has changed gradually from a bimodal structure to a more uniform microstructure in this zone which is termed the transition zone in this thesis.

Figure 4-2(c) shows the inner bore of the tube; further investigation revealed that the steel microstructure close to the inner bore area is slightly different from that in the central zone. This area ~200 μm wide has a higher fraction of ferrite grains compared to the central zone. There are thus five main different zones in the 2.25Cr1Mo steel substrate of the weld overlaid tube with different microstructures, and from the tube's inner bore towards welding interface they are referred as following:

1) An inner bore zone ~150 to 200 μm wide with a higher proportion ferrite grains in the microstructure.

2) A central zone ~ 2000 to 2500 μm wide with approximately equal portions of ferrite and carbide containing regions.

3) A transition zone ~ 200 μm wide which has a transformed two phase microstructure.

4) A far-HAZ zone ~ 700 μm wide with a one phase microstructure; however, the former bimodal structure is still visible.

5) A near-HAZ zone ~ 300 μm wide with a uniform microstructure.

4-3-1- Inner bore microstructure

It is probable that the central and the inner bore zones of the steel were not affected by the thermal cycle of the welding process and therefore they retain their initial microstructures. Figure 4-3 shows different images of these regions. The optical microscope image of the inner bore zone is shown in Figure 4-3(a1) and reveals predominantly ferrite (α-Fe) grains and some small dark etching areas.

The width of this zone varies from point to point and is ~150 to 200 μm wide as indicated in the lower magnification SE micrograph of this region (see Figure 4-3(b1)). The higher magnification SE micrograph of the inner bore zone microstructure is presented in Figure 4-3(c1) and reveals that ferrite (α-Fe) grains have a featureless appearance after etching while the dark optical microscope areas surface have a mottled contrast. It is suggested that bright particles are carbides in a tempered martensite or bainite structure. These areas will be termed TM/B (tempered martensite/bainite) in the rest of the thesis.

4-3-2- Central zone microstructure

The bimodal microstructure of the central zone is seen in the majority of 2.25Cr1Mo steel region and consists of approximately equal proportions of ferrite (α-Fe) grains and TM/B areas. This type of microstructure is seen in the central part of steel tube between the inner bore and the transition zones. The optical microscope image of this zone is presented in Figure 4-3(a2) and shows its main features which are large areas of TM/B and ferrite (α-Fe) grains of different size.

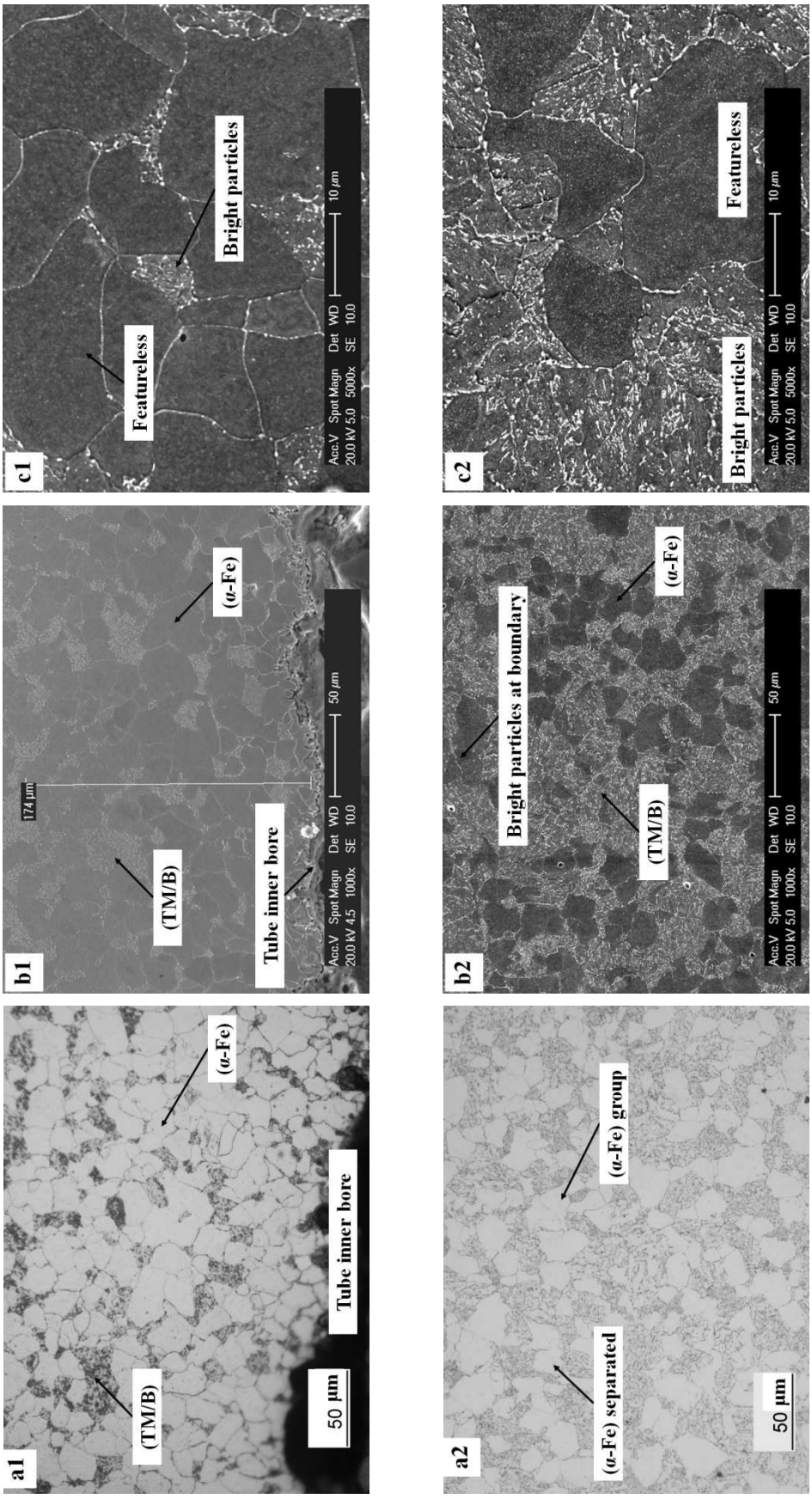

Figure 4-3. Showing microstructure of the inner bore (1) and the central (2) zones in the etched condition; (a1,a2) optical microscope images, (b1,b2) lower magnification SE micrographs and (c1,c2) higher magnification SE micrographs.

As seen in Figure 4-3(b2), there are some locations in the central zone where the TM/B areas can be considered as matrix and small grains of ferrite (α-Fe) are formed in these areas. Nevertheless, there are other locations where a group of ferrite (α-Fe) grains are formed and their grain boundaries are clearly visible. There are some bright particles on the grain boundaries of ferrite grains as labelled in this image. The bright particles are seen more clearly in the higher magnification SE micrograph (see Figure 4-3(c2)) on the boundaries of ferrite grains and in the TM/B areas. Referring to section 2-3, it is believed that these particles are likely to be carbides as a common feature in a tempered martensitic or bainitic structure. It must be noted that the etching process causes relief of carbides on the surface and so carbides are seen as bright in the SE micrographs.

4-3-3- Transition zone microstructure

The transition zone is between the far-HAZ and the central zone. In this zone, the bimodal microstructure including (α-Fe) and TM/B has partially transformed to austenite (γ-Fe) during the welding process. The austenite subsequently transformed to martensite or bainite during the rapid cooling of the weld thermal cycle. The resultant regions after cooling are termed Tγ (transformed γ) in this thesis.

Figure 4-4(a) shows the etched microstructure of the transition zone. In the higher peak temperature parts of this zone (upper parts of Figure 4-4(a)) the microstructure was completely transformed to γ. However, some untransformed ferrite grains are present in the central part and some TM/B areas appear in the lower parts of this image.

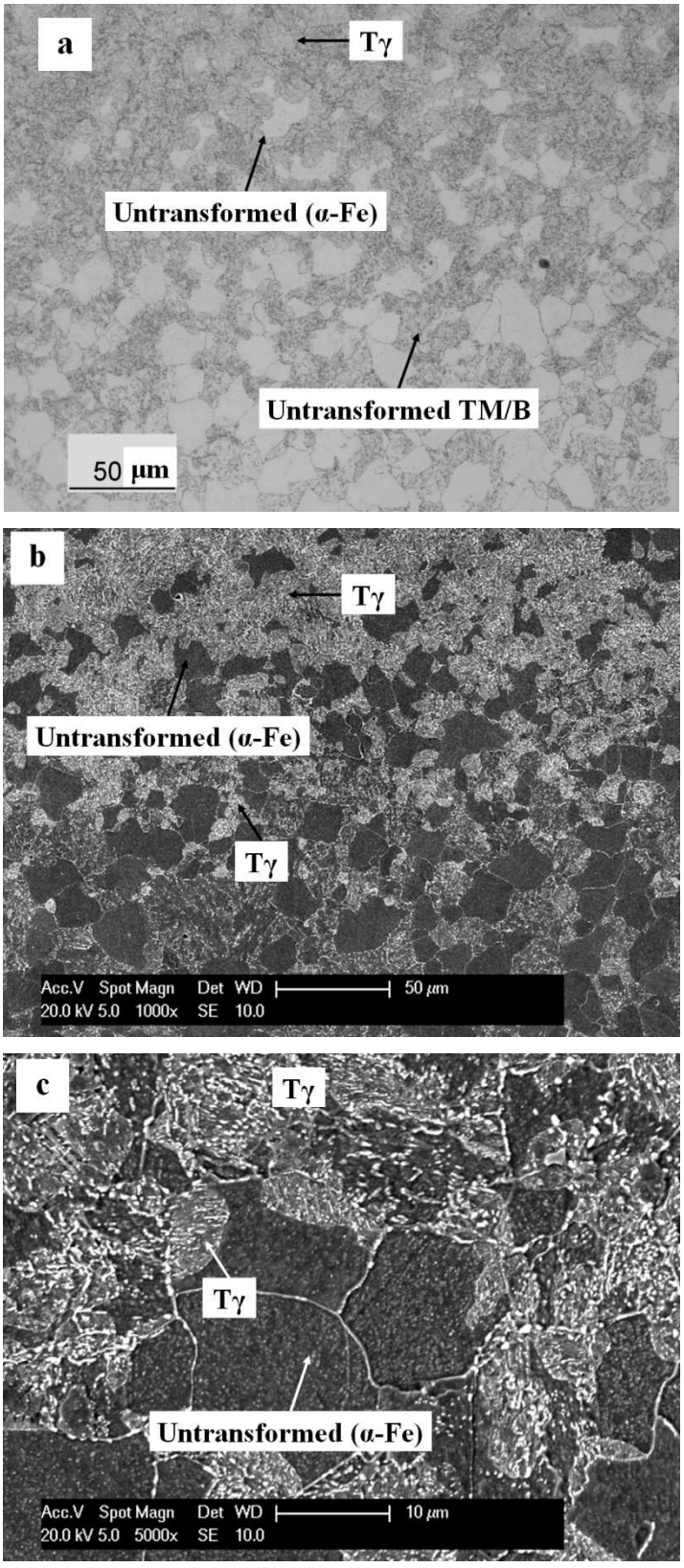

Figure 4-4. Showing microstructure of the transition zone in the etched condition; (a) optical microscope image indicates the untransformed (α-Fe) and the untransformed TM/B as well as the Tγ, (b) lower magnification SE micrograph of the untransformed (α-Fe) and Tγ areas in the transition zone and (c) higher magnification SE micrograph indicates the Tγ structure in the TM/B areas and corners of a ferrite (α-Fe) grain.

The untransformed (α-Fe) grains and TM/B are related to the lower peak temperature during the welding process. In the lower parts of transition zone, only some parts of TM/B areas and the corners of (α-Fe) grains were transformed to the γ during heating up period. Figure 4-4(b) shows a low magnification SE micrograph of the transition zone which is similar to the optical microscope image. The untransformed (α-Fe) grains and TM/B areas are clearly labelled in this image.

The higher magnification SE micrograph of this zone is presented in Figure 4-4(c) and reveals that the Tγ structure is different from the initial microstructure. The edges and corners of ferrite grains convert to Tγ after the welding process while the centre of the grains remains untransformed. In the transition zone, the TM/B areas and the ferrite (α-Fe) grains were transformed to a uniform structure which is the main feature of the HAZ. The transformation process from the initial structure to austenite (γ) at high temperature and then to the Tγ structure is critically dependent on the heating and cooling rates of the thermal cycle of the welding and the peak temperature of the region. Moreover, it is suggested that the TM/B areas were transformed to austenite in a shorter time compared to the ferrite grains.

4-3-4- Far-HAZ zone microstructure

In this work, the HAZ region is divided into a near-HAZ and a far-HAZ. It is suggested that, during welding, the temperature of the steel surface must reach at least to that of IN625 melting temperature. Referring to former research [150], there is a range for IN625 melting temperature which is between approximately 1250 and 1420˚C. Therefore, the regions of the steel adjacent

to the weld overlay were heated above the austenitisation temperature and rapidly cooled afterwards. The region where austenitisation and air cooling led to a uniform lath-like structure is termed near-HAZ.

The uniformity of the austenite phase depends on the carbide dissolution and austenitisation temperature which is a function of distance from the interface. The region where a completely uniform lath-like structure was not seen is termed the far-HAZ. Thus, the area closer to the interface is heated up to a higher temperature, so the austenite in this area is more uniform compared to other areas which are far from the interface. It is suggested that in the far-HAZ zone, the carbide dissolution in the austenite during welding may not have been completed.

Figure 4-5(a) shows an optical microscope image from the area about 500 μm distant from the interface. It is shown in Figure 4-2(b) that the width of the far-HAZ zone is ~700 μm and therefore the image with ~500 μm distance from the interface is showing the central part of the far-HAZ zone. Traces of the initial bimodal microstructure of the central zone are still distinguishable in this image.

A low magnification SE micrograph of this zone, taken from the same region (~500 μm distant from the interface) is presented in Figure 4-5(b). There are some regions with more bright contrast particles compared to the other parts. Therefore, this type of microstructure is called non-uniform Tγ in this thesis. Figure 4-5(c), shows a higher magnification image of this zone. The former TM/B areas and ferrite (α-Fe) grains are labelled in this image.

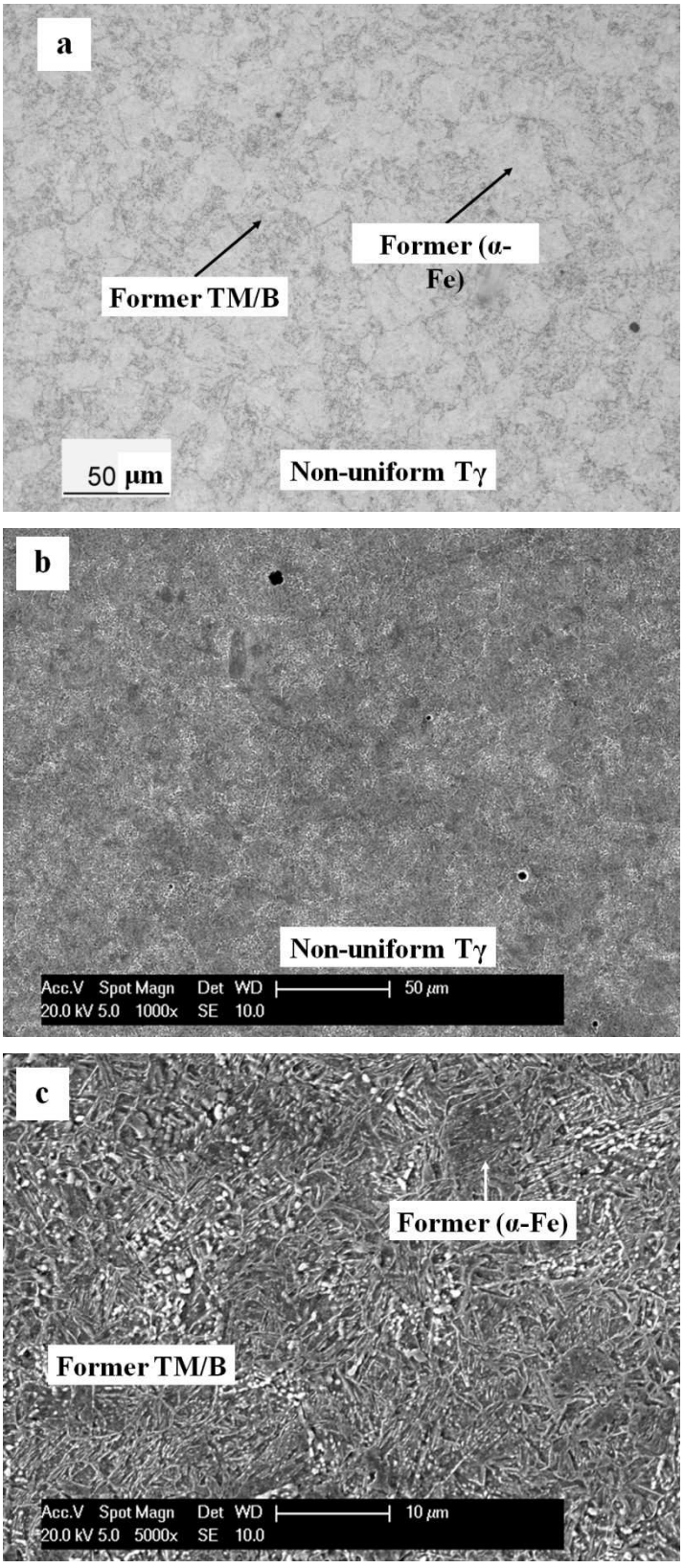

Figure 4-5. Showing microstructure of the area ~500 µm distant from the interface (far-HAZ) zone in the etched condition; (a) optical microscope image indicates former (α-Fe) and TM/B, (b) lower magnification SE micrograph of the non-uniform far-HAZ zone and (c) higher magnification SE micrograph contains blocky carbide particles in the former TM/B area.

The main feature of the far-HAZ zone is the presence of the un-dissolved carbide particles in the former TM/B areas which is related to incomplete austenitisation during heating up period. The un-dissolved carbide particles in the far-HAZ zone (see Figure 4-5(c)) are blocky which are different compared to the initial TM/B area (see Figure 4-3(c2)).

4-3-5- Near-HAZ zone

Figure 4-6(a) shows an optical microscope image of the interfacial region (close to the overlay) in the etched condition. The microstructure of this region (defined as the near-HAZ zone) is uniform without any un-dissolved blocky carbides. A high magnification SE micrograph of the interfacial region is shown in Figure 4-6(b). The lath-like structure is visible in the microstructure close to interface which is the main characteristic of rapidly cooled austenite.

Figure 4-6(c) shows the microstructure of the area about 300 μm distant from the interface. It can be seen that the nature of the uniform Tγ microstructure is also visible in this area. Therefore it is suggested that the width of this zone is ~300 μm which is different from point to point. It can be said that the appearance of the un-dissolved carbides could be considered as the border between the near-HAZ and the far-HAZ zones.

Comparison of Figure 4-6(c) and Figure 4-5(c) reveals the differences between the uniform Tγ and the non-uniform Tγ microstructure.

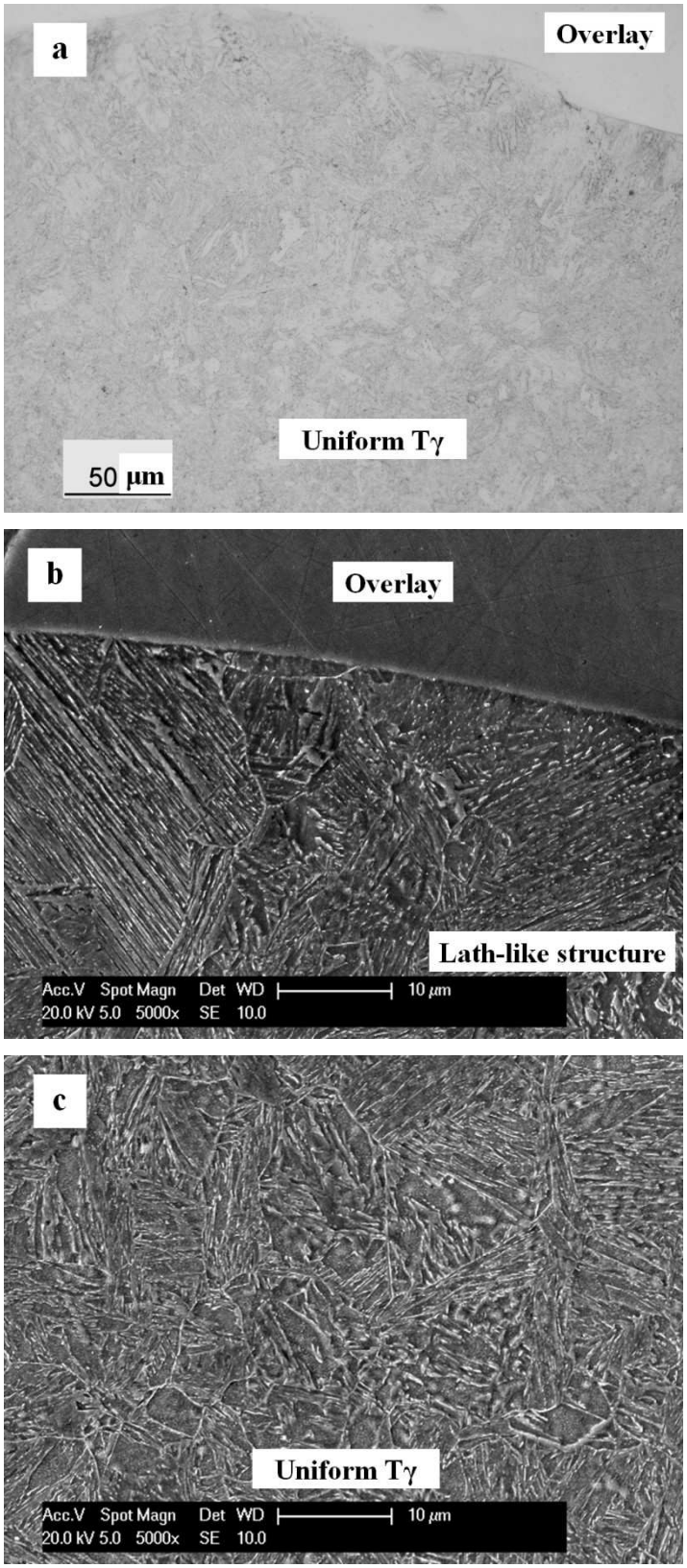

Figure 4-6. Showing microstructure of the near-HAZ zone in the etched condition; (a) optical microscope image shows the microstructure of the uniform Tγ close to interface, (b) higher magnification SE micrograph of the interfacial region illustrates lath-like structure and (c) higher magnification SE micrograph of the area ~300 µm distant from the interface shows uniform Tγ.

It is suggested that at a smaller distance from the interface, un-dissolved blocky carbide particles disappeared from the microstructure and replaced with the lath-like structure. The length of the laths of the Tγ microstructure increased from less than 10 μm in the area away from the interface (see Figure 4-6(c)) to about 30 μm adjacent to interface (see Figure 4-6(b)).

4-4- Interface characterisation

In order to understand the intermixing process of the fusion weld overlay and the steel substrate, a comprehensive investigation on the interface region was carried out. Figure 4-7(a) and (b) show the typical interface in the cross sectional samples in the etched condition. Nital did not affect the weld overlay region; therefore the interface can be clearly identified. EDX line scans across the interface showed the compositional variation in the interfacial region. The composition changes from a Fe-rich to a Ni- rich alloy in less than 5 μm (see Figure 4-7(c)). This profile for different shapes of interface was similar.

Further investigation was carried out on longitudinal sections. Figure 4-8(a) shows a BSE micrograph of the interfacial region in these samples and indicates the semi-melted interface areas. It is clear that during the welding process, some areas of the steel did not fully melt. The semi-melted areas in the interfacial region proved that the interface is not a planar feature between the steel and weld overlay. Figure 4-8(b) shows an un-melted steel part in the weld overlay region. The presence of the semi-melted regions and or un-melted parts in the interfacial region cause an undulating interface and therefore it can be considered as a three dimensional feature.

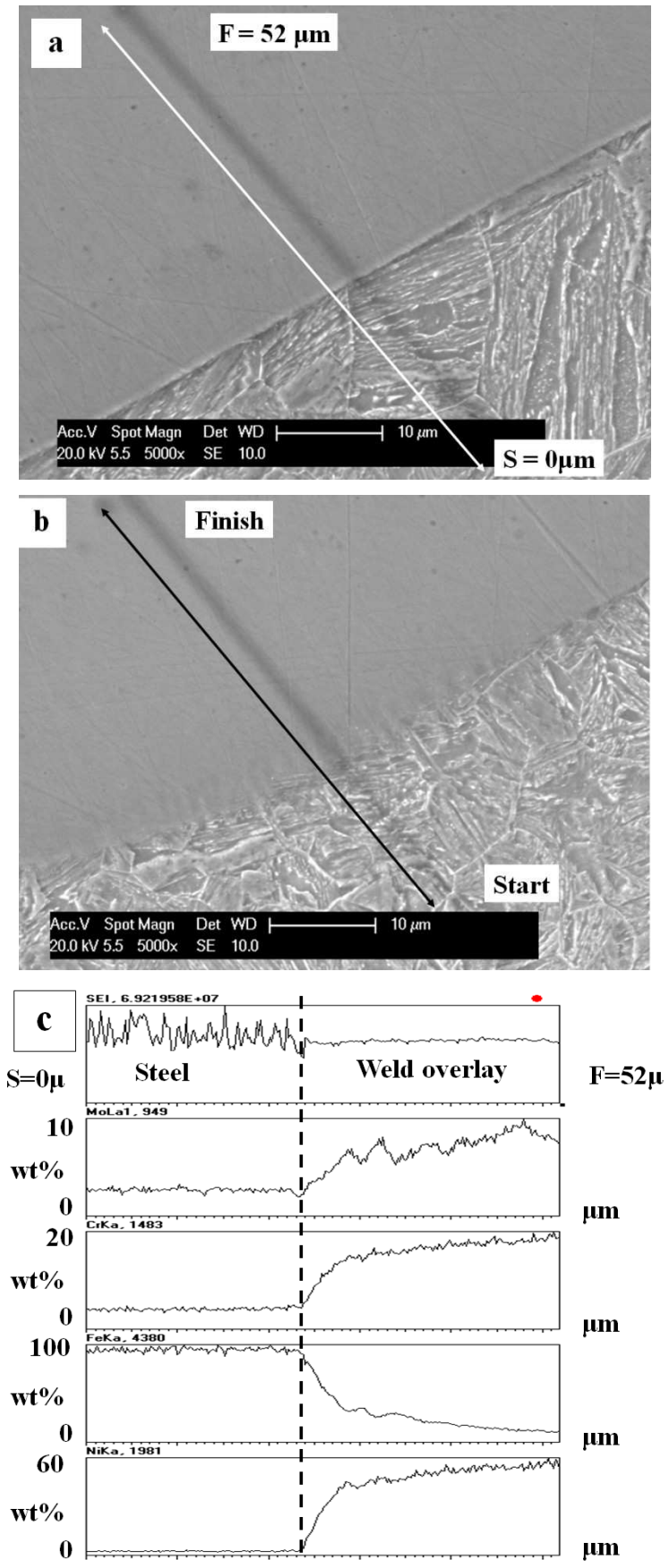

Figure 4-7. Showing the nature of the interface in the weld overlay/substrate system; (a, b) SE micrographs from different locations of interface etched in Nital indicate different interface shapes, (c) compositional profile at the interface shown in figure(a).

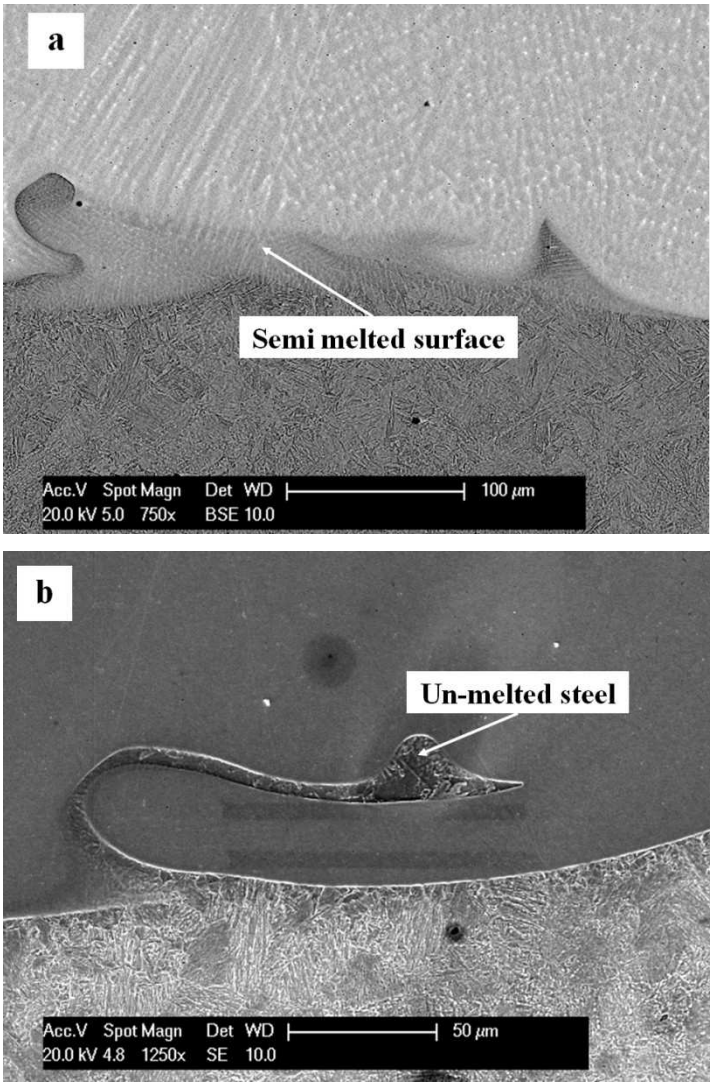

Figure 4-8. Showing the weld overlay/substrate interfacial region, (a) low magnification BSE micrograph from the interfacial region in the longitudinally sectioned sample indicates the semi melted areas, (b) higher magnification SE micrograph form the un-melted steel part in the weld overlay region.

4-5- Microstructural characterization of the weld overlay

Etching samples with Aqua-Regia reagent revealed the weld overlay microstructure. Figure 4-9(a) shows an optical microscope image from the whole region of the weld overlay. One edge of this region is the interface with the steel and the other one is the tube outer surface. The weld overlay microstructure has a dendritic structure which is a characteristic of an as-

solidified material. The columnar dendrites exist through the whole region and show directional solidification aligned with the radial direction.

Figure 4-9(b) shows a higher magnification optical microscope image of the weld overlay close to interface with the steel. There is a region in this image where the columnar dendrites are not visible. Due to partial melting of the steel surface and intermixing with the weld pool during the welding process, the microstructure of this region is different from the other parts. This region of less than 30 μm wide is called the mixing zone in the rest of this thesis. However, other parts of the weld overlay region have a similar structure. Therefore the region beyond the mixing zone is considered as the bulk zone of the weld overlay.

The most important feature in the dendritic microstructure of the bulk weld overlay is inhomogeneity of the chemical composition between the dendrite cores and interdendritic regions. The segregation phenomenon in this region can be seen in the BSE micrograph (BSE signal is sensitive to the mean atomic number) and is shown in Figure 4-9(c).

As seen in this image, there are some bright features which are labelled as interdendritic regions of higher mean atomic number. Moreover, the darker areas can be considered as the cores of dendrites. It means that during solidification, the segregation of higher atomic number elements such as Mo and Nb cause the interdendritic regions to become brighter in contrast compared to that of the dendrite cores.

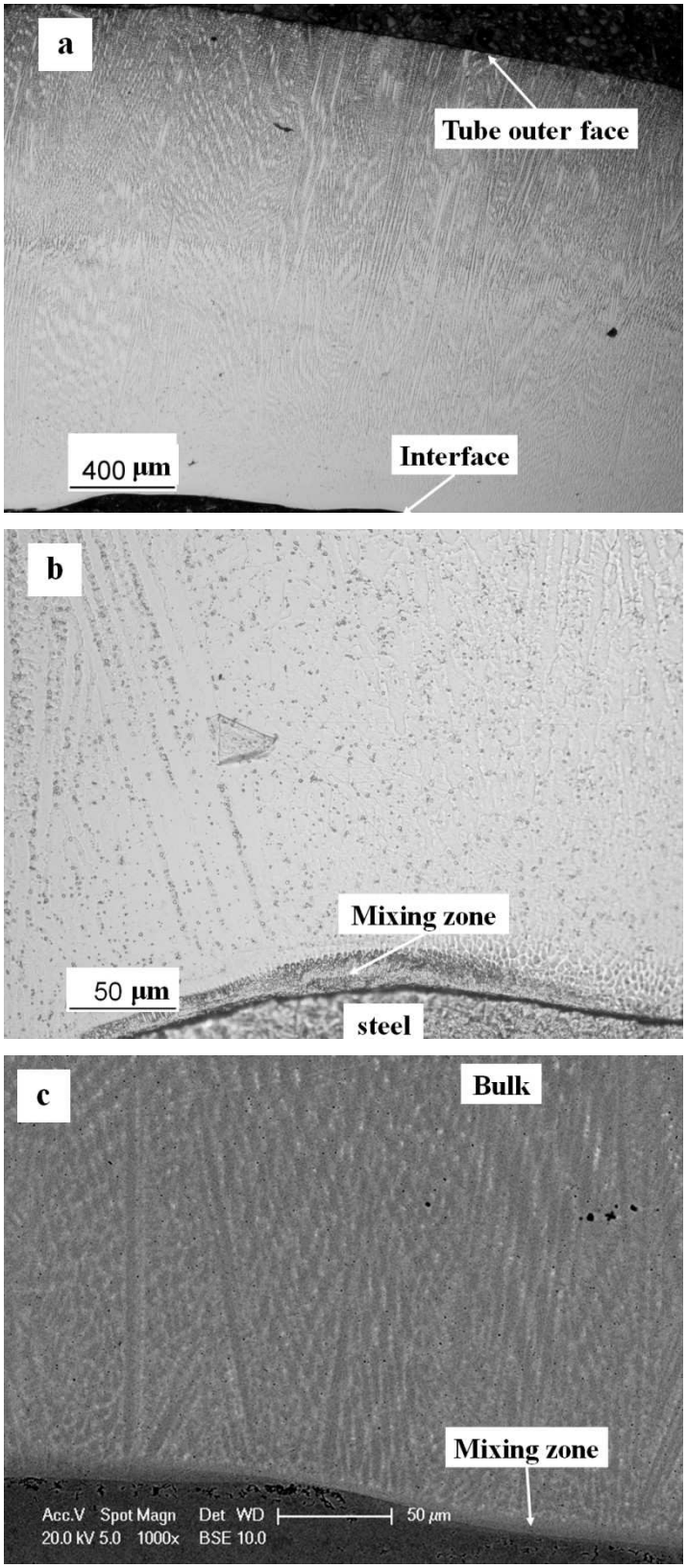

Figure 4-9. Showing microstructure of the weld overlay region; (a) low magnification optical microscope image indicates the edges of the weld overlay region, (b) high magnification optical microscope image of the mixing zone close to interface and (c) BSE micrograph of the weld overlay region indicates inhomogeneity in the microstructure of bulk zone.

EDX analyses, with line scans, were carried out on the different locations of the weld overly region in order to reveal the chemical composition differences between the interdendritic and dendrite core regions. Figure 4-10(a) shows an EDX line scan results from a location in the bulk zone at ~500 µm from the interface. The corresponding location of this analysis is presented in Figure 4-10(b). It can be seen the bright contrast regions match with the higher niobium and molybdenum content regions.

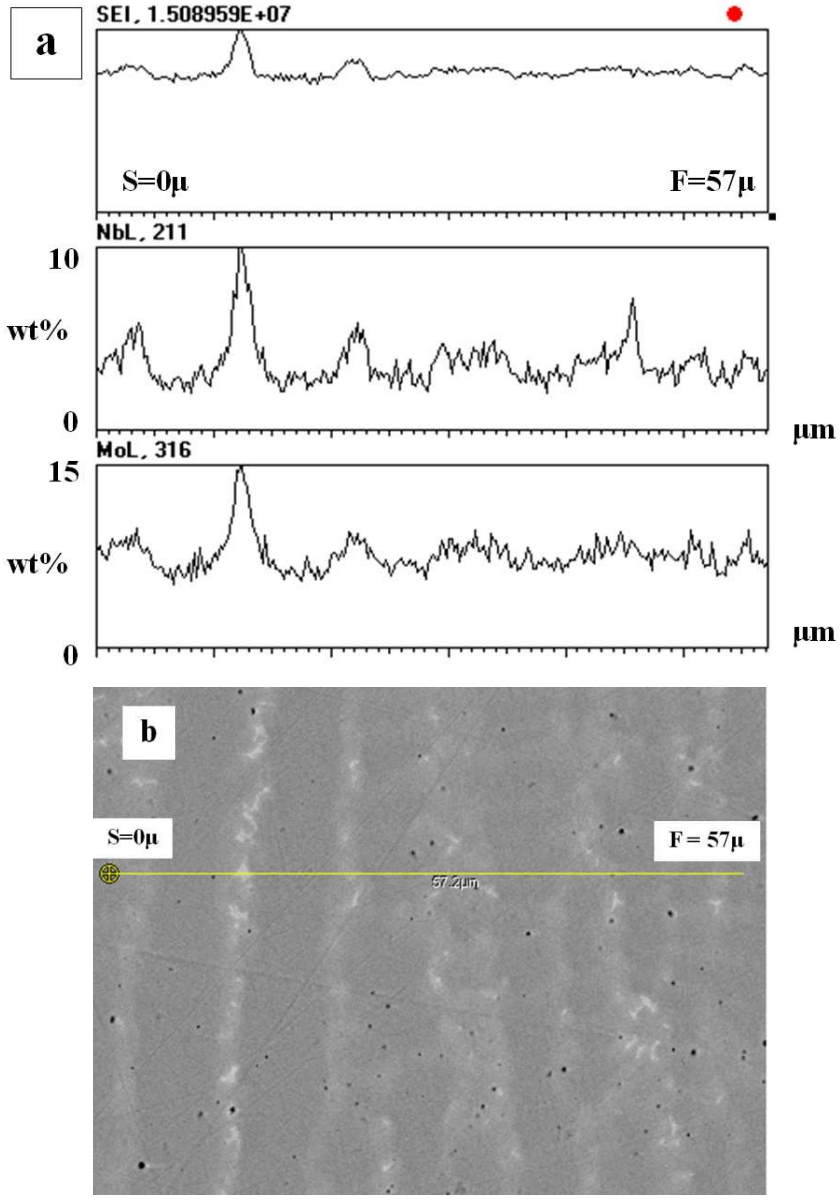

Figure 4-10. Showing inhomogeneity in the bulk zone of the weld overlay (a) EDX analysis results showing concentration profiles of Mo and Nb, (b) location of the line scan indicates the bright regions correspond to the higher Mo and Nb regions.

4-5-1- Chemical composition profile through the weld overlay region

Based on the previously mentioned results, it is suggested that there are two main zones in the weld overlay region as follows:

1) A mixing zone ~ 30 μm wide

2) A bulk zone with a dendritic structure

EDX area analyses were carried out on different locations of these two zones to analyse the differences in their chemical composition. In order to compare the results of different parts, all the EDX analyses were taken in the form of a box 10 μm wide and 100 μm long. EDX analyses were repeated on five or six different locations with the same distance from the interface.

4-5-1-1- Mixing zone

The chemical composition of the mixing zone was determined with two sets of area analyses. The first set was carried out on many different locations at ~1 μm distant from the interface. The schematic diagram of this set of analyses is shown in Figure 4-11 and the results are presented in Table 4-4. This table presents the results from 6 different locations and reveals that the chemical composition in the first 10 μm of weld ovverlay varies significantly.

The second set of analyses was carried out on different locations at ~10 μm distant from the interface (D=10 μm). Table 4-5 shows the results of 5 points of this set of analyses and it seen that by increasing the distance from the interface, the average of iron content decreases while other elements increase.

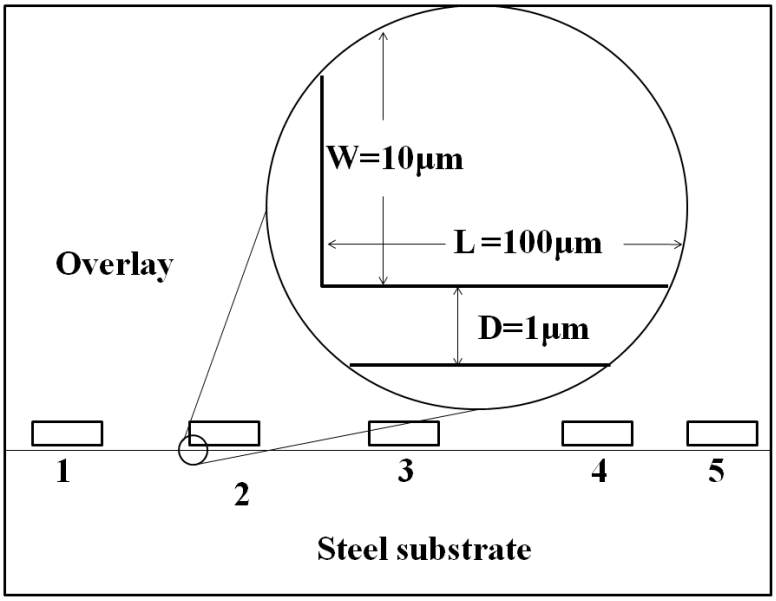

Figure 4-11. Showing schematic of EDX analysis on different locations of the mixing zone with 1 µm distance from the interface

Table 4-4. Chemical composition of the mixing zone in the weld overlay region at different areas 1 µm distant from the interface. (D=1 µm)

Element (wt.%)	*A(1)*	*A(2)*	*A(3)*	*A(4)*	*A(5)*	*A(6)*	*Mean*	*S.D.*
Cr	10.5	13.1	15.4	15.3	15.1	11.3	13.5	2.2
Fe	57.3	44.7	33.4	33.7	36.9	54.5	43.4	10.6
Ni	26.8	35.3	43.2	43.2	40.5	28.5	36.2	7.3
Nb	1.2	1.5	1.9	1.8	1.7	1.5	1.6	0.3
Mo	3.9	5.1	5.8	5.9	5.6	4.1	5.0	0.9

Table 4-5. Chemical composition of the mixing zone in the weld overlay region at different areas 10 µm distant from the interface. (D=10 µm)

Element (wt.%)	*A(1)*	*A(2)*	*A(3)*	*A(4)*	*A(5)*	*Mean*	*S.D.*
Cr	16.2	19.6	18.8	14.8	17.8	17.4	1.9
Fe	30.7	16.1	17.6	36.7	23.1	24.8	8.7
Ni	43.0	53.1	51.5	40.2	48.7	47.3	5.5
Nb	3.2	3.2	3.9	2.2	3.0	3.1	0.6
Mo	6.6	7.7	7.7	5.9	7.3	7.0	0.8

A comparison of the mean values of Fe and Ni in these tables reveals the intermixing of the weld overlay with the steel substrate. The variation in the

chemical composition at a fixed distance from the interface is probably related to the interface undulations. The presence of the semi melted and/or un-melted parts of the steel substrate in the area close to interface causes higher iron content in some locations of the mixing zone.

4-5-1-2- Bulk zone

In order to have a chemical composition profile in the bulk zone, the EDX area analyses were carried out on locations with different distances from the interface. The EDX results for one set of these measurements are shown in Figure 4-12. As variations of high atomic number elements i.e. Mo and Nb are smaller than other elements, their profiles are presented in a separate graph. It is seen that after a distance of ~30 μm from the interface, the composition of the bulk zone is almost uniform through whole region. The border between the mixing and the bulk zones can be defined by the dashed line shown in Figure 4-12.

This type of measurement was repeated on different locations of weld overlay region and the results were very similar. The resultant profiles exhibit a plateau between 20 to 40 μm from the interface. Comparison between the compositions of the bulk zone in different profiles reveals that nickel and iron content vary within a range of 3 wt.%. However, the concentration variation range of other elements in different profiles is less than 1 wt.%. Finally, the composition in the bulk zone is close to the analysis results from the spark emission spectroscopy (see Table 4-1).

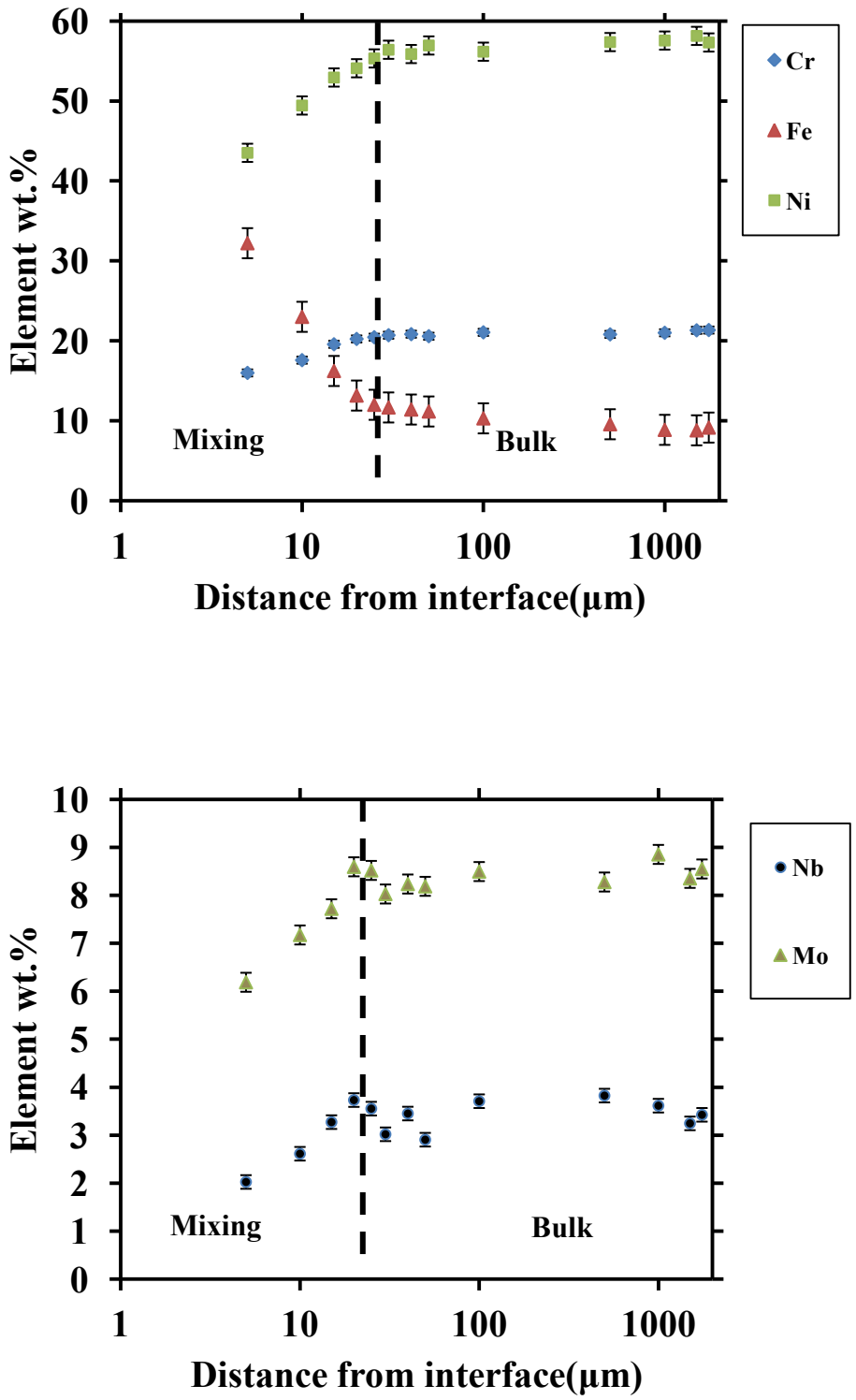

Figure 4-12. Showing typical EDX analysis results for the weld overlay region on logarithmic distance scale; (above) indicates variation of the matrix elements i.e. Cr, Fe and Ni as a function of distance from the interface, (below) shows variation of minor alloying elements i.e. Mo and Nb in the same way.

4-5-2- EPMA results

EPMA analysis using WDX spectrometers was carried out on the interfacial region of a cross sectional sample. The methodology employed is described in section 3-5-7. Figure 4-13 shows elemental colour maps for Cr, C, Nb, Ti, Mo and Fe as well as a backscattered electron image from the interfacial region (with CP in the data bar) between the steel (lower part) and weld overlay (upper part). The concentrations represented by the different colours are shown by the scales to the right of the image.

The mixing zone, previously identified by SEM/EDX, is clearly visible as a ~30 μm wide zone of high Fe and low Ni, Cr, Mo and Nb compared to the bulk of the weld overlay. The levels of these elements away from the mixing zone are also in agreement with the SEM/EDX results. Moreover, EPMA results give more distinct information about distribution of the niobium and molybdenum in the weld overlay region.

As seen, the concentrations of the both of these elements are increased in the mixing zone with increasing distance from the interface (Mo concentration at the interface is ~1 at.% and increases to about 6 at.% while Nb concentration at interface is almost zero and increases to ~2 at.%). However, the Mo distribution in the bulk zone is somewhat different from the Nb distribution. The Mo map appears more uniform whereas the Nb is concentrated in some regions in the bulk zone which are red and visible in Figure 4-13.

It should be noted that most of the Nb-rich points correlate with Ti-rich points. This fact can be related to formation of secondary phases at final stages of

solidification. Presence of Ti and Nb possibly is related to (MC) carbide. Moreover, the carbon concentration range is not valid which is related to its low concentration.

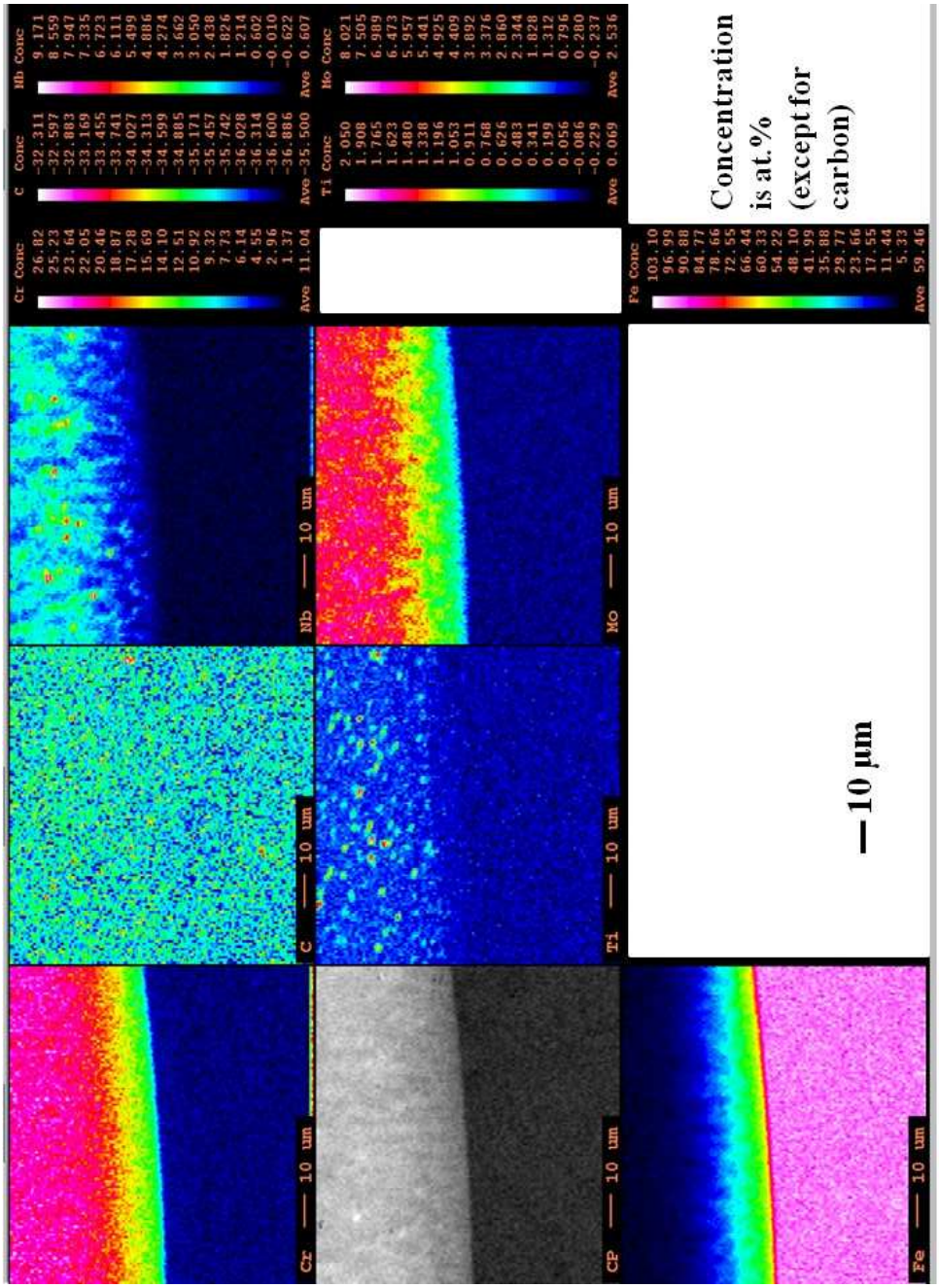

Figure 4-13. Showing different element maps in the interfacial region with the steel at the lower part and weld overlay at the upper part; the variation in chemical composition is visible in the mixing zone. The boundary between the mixing and the bulk zones is clearly visible and some (Nb, Ti)-rich points are present in the bulk zone. The carbon concentration range is not valid and its map did not show anything.

In summary, as a result of the welding of the nickel alloy on the outer bore of the steel tube, following regions are present in the weld overlaid steel tube in the as-welded condition:

1) 2.25Cr1Mo steel substrate

    a) A inner bore region which contains ferrite grains

    b) A central zone region with bimodal microstructure which contains approximately equal portions of ferrite grains and TM/B areas as the main zone

    c) A transition region which shows the extent of austenitisation during the welding

    d) A far-HAZ region ~700 μm wide with a non-uniform microstructure including un-dissolved carbides

    e) A near-HAZ zone region ~300 μm wide with a uniform lath-like microstructure

2) Nickel alloy weld overlay region

    a) A mixing zone ~30 μm wide with high Fe content

    b) A bulk zone with ~9 wt.% Fe content and 0.02 wt.% C which are higher than the standard wrought IN625 which is mentioned in Table 4-2.

Chapter 5

Characterization following high temperature exposure

5-1- Introduction

In order to prevent failures in service, it is necessary to evaluate the effects of service conditions on the microstructure and mechanical properties of the steel tube and the weld overlay, particularly in the interfacial region. In this project, the main focus is on the effect of high temperature exposure on the hardness and microstructure of different regions of the weld overlay and the steel substrate. The weld overlay is a nickel based alloy similar in composition to IN625 but with a higher iron and carbon contents and the substrate is 2.25Cr1Mo ferritic steel.

Due to the differences in the chemical composition of these materials, transport of various elements across the interface is likely to occur during the high temperature exposure. As the results reveal a complex set of interactions, a brief overview will be presented in section 5-2. The aim of this is to provide the reader with a succinct description in which the primary processes in the microstructural evolution are defined. Moreover, schematic diagrams displaying the main features in the microstructure of both materials are outlined.

In the following sections of this chapter, the results of hardness tests and microstructural analysis of the thermally exposed samples are presented. In these sections, evidences about the microstructure evolution in the weld overlay region and different zones of the steel are described in detail. The results are classified by region in terms of the microstructural evolution processes.

5-2- Overview

The hardness and microstructure of samples were analysed in detail (see section 5-3 and 5-4) and changes in the microstructure are classified in the present section. The changes in the microstructure were compared with the as-welded condition. The microstructures of the steel substrate as well as the weld overlay in the as-welded condition are reported in chapter 4. In the as-welded condition, there is a significant variation in the microstructure of the steel from the near-HAZ region to the tube inner bore due to the different thermal cycles experienced.

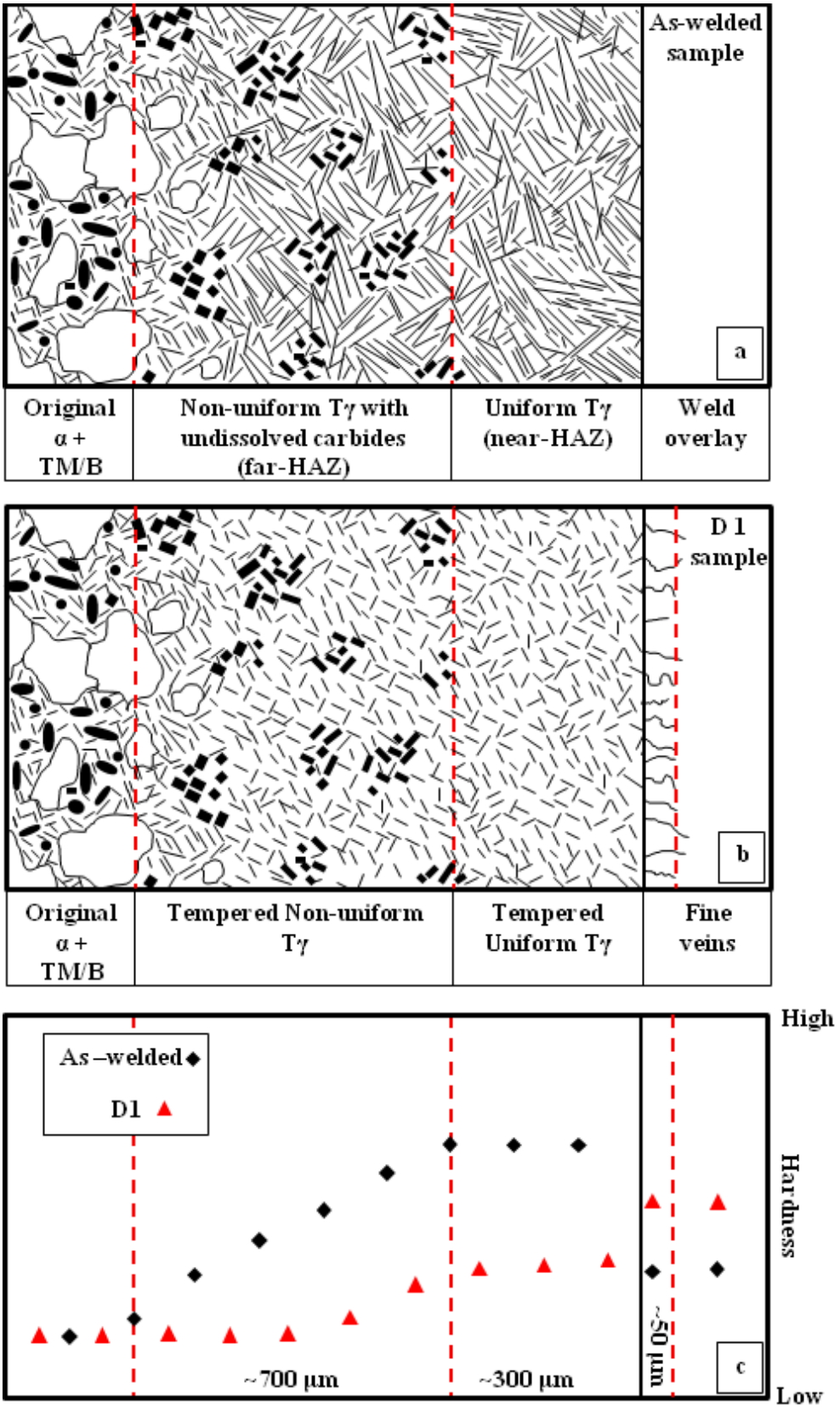

Figure 5-1. Showing (a) schematic diagram of the as-welded sample microstructure, indicates different region in the steel, (b) schematic diagram of the D1 sample microstructure, indicates tempering in the steel and the fine veins formation in the weld overlay, (c) indicate the hardness values of both materials; in the steel due to tempering it is decreased while it is increased for the weld overlay region due to hardening.

Figure 5-1(a) shows the schematic diagram of the as-welded sample. In this steel, the initial microstructure contains ferrite (α-Fe) grains and the TM/B areas. This bimodal structure converts to austenite during welding and then by rapid cooling lath-like structure was formed and termed (Tγ). Due to the gradient in peak temperature during the welding, the uniformity of HAZ microstructure decreases with increasing the distance from the interface (compare the near-HAZ with far-HAZ).

Thermal exposure at 650˚C for 1 day causes tempering of the lath-like Tγ structure in the HAZ region to give a tempered structure with small carbide precipitates. Figure 5-1(b) shows schematically this issue. The hardness drops in the HAZ region as seen in Figure 5-1(c). Thermal exposure causes hardening of the weld overlay, and hardness of the weld overlay in the D1 sample increases compared to the as-welded condition (see Figure 5-1(c)).

Moreover, due to carbon migration across the weld interface at high temperature and presence of carbide former elements, carbide particles are likely to precipitate along the grain boundaries in the weld overlay. Therefore, some features, termed veins, formed in the weld overlay side of interfacial region. These veins ~50 μm long are shown in Figure 5-1(b).

After 8 days exposure (D8 sample), tempering of the steel and a decrease in its hardness continues. This is accompanied by increasing the length of the veins in the weld overlay to about 100 μm. Moreover, the hardness increases up to a depth of 20 μm into the weld overlay. This region is termed a “hard band” which is emphasised as a dark band in Figure 5-2(a). The maximum hardness of this region rises to about 500 kgf mm^{-2}.

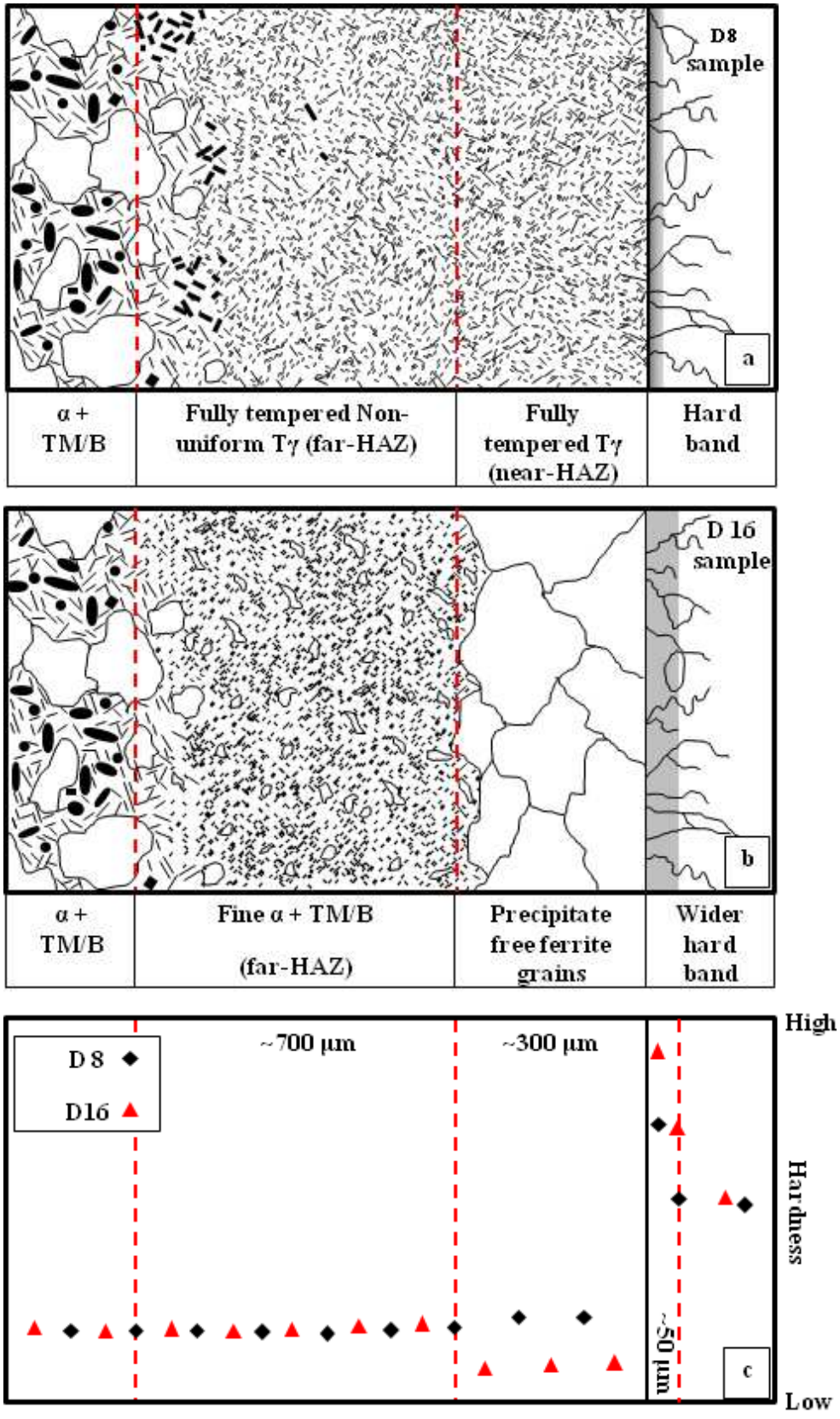

Figure 5-2. Showing (a) schematic diagram of the D8 sample, indicates fully tempered structure in the steel and the vein growth and hard band formation in the weld overlay (b) schematic diagram of the D16 sample, indicates soft zone in the former near-HAZ region and further growth in the veins and wider hard band in the weld overlay and (c) indicates the hardness variation in different parts of two samples.

Further increase in exposure time causes apparently further carbon migration from the steel to the weld overlay and a soft zone forms on the steel side of the interface. This soft zone is first apparent after 12 days exposure and remains even after 32 days of exposure. The microstructure of the D16 sample is shown schematically in Figure 5-2(b). The main characteristics of the soft zone are a large ferrite grain structure and low hardness (see Figure 5-2(c)). The width of the soft zone is ~300 μm which is equivalent to the near-HAZ region. The soft zone is largely free from precipitates.

In the weld overlay region of the D16 sample, the width of the hard band increased to ~50 μm and its maximum hardness increased to ~600 kgf mm^{-2}. The hard band width is correlated to the mixing zone (see section 4-5-1-1) which is a nickel rich region with ~30 at.% iron content material. Moreover, comparison of the D8 and D16 samples indicates that veins become thicker with increasing exposure time at 650˚C.

After 64 days exposure, see Figure 5-3(a), two important changes took place in the near-HAZ region. First, fine particles were precipitated within the large ferrite grains and secondly a network of coarse carbide particles was formed at the interface between the weld overlay and the steel (in the steel side). This has led to a re-hardening of the near-HAZ region (see Figure 5-3(c) compared to Figure 5-2(c)).

Within the weld overlay region, the features termed veins did not extend further into the sample but appeared more distinct, suggesting a coarsening of the precipitates within them (see Figure 5-3(a) compared to Figure 5-2(b)).

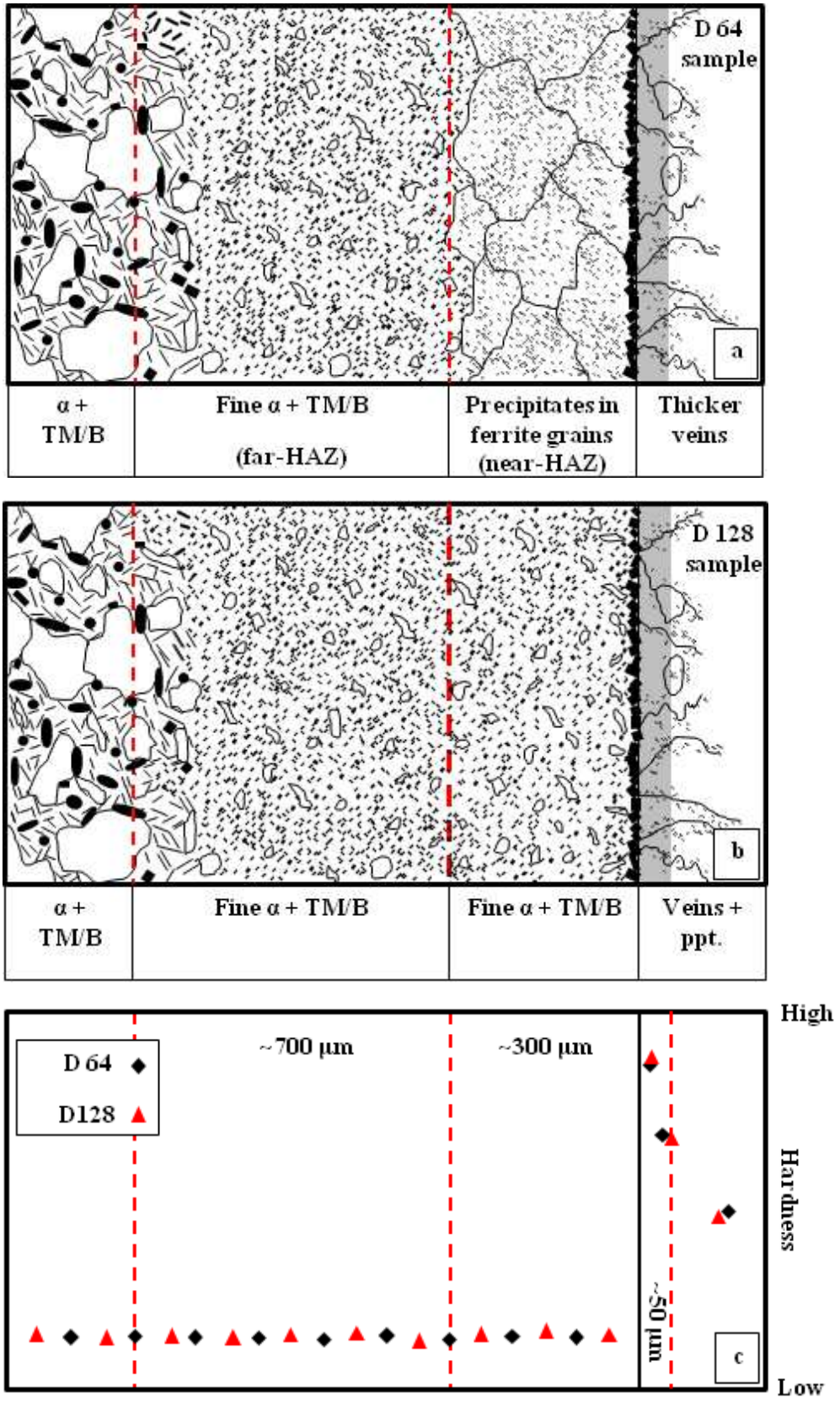

Figure 5-3. Showing (a) schematic diagram of the D64 sample, indicates precipitates within the large ferrite grains and a coarse precipitate network at the interface region, (b) schematic diagram of the D128 sample indicate fine grains of ferrite and TM/B formation in the former near-HAZ region; and (c) indicates the hardness variation of the different regions of two samples.

Finally, after 128 days, the hardness values of the near-HAZ region and the hard band in the weld overlay underwent little further change. However, the grain size of the ferrite in the near-HAZ region decreased very significantly from ~150 μm to less than 10 μm. Also in the bulk zone of the weld overlay region the TCP precipitates become visible (see Figure 5-3(b)).

This overview provides a framework for presenting the detailed experimental results in the following sections. The hardness results are presented in section 5-3 followed by the microstructral observations after different ageing times at 650 ˚C in section 5-4.

5-3- Hardness survey

The microhardness measurements for both materials, the weld overlay (nickel alloy) and steel tube (2.25Cr1Mo) were carried out in the as-welded condition and after each thermal exposure experiment. In this section, the results of hardness tests for different samples are presented. The hardness measurement procedure was described in section 3-6.

It should be noted that several hardness measurements in a sample show similar profiles and in a particular zone, there is ~30 kgf mm^{-2} difference between the maximum and the minimum values. Therefore, for displaying the changes in the hardness profile of different samples, one set of measurements is presented in the diagrams for each sample. The typical ~30 kgf mm^{-2} error bar should be considered in each diagram which represents the difference between values of a certain zone in the sample.

The hardness values of the weld overlay region in the as-welded condition are presented in Figure 5-4(a), and show a range of 220 - 250 kgf mm^{-2} for both zones. The hardness values for the steel region in the as-welded condition are presented in Figure 5-4(b) and show the maximum hardness values are corresponding to the near-HAZ region (~300 μm wide) and are between 430 and 460 kgf mm^{-2}.

The hardness values in the far-HAZ region are in the range of ~200 to ~430 kgf mm^{-2} and decrease with increasing distance from the interface. The hardness values in the central zone are in the range of ~150 to ~180 kgf mm^{-2}. It can be suggested that the hardness profile in the as-welded condition is correlated to the peak temperature during welding.

High temperature exposure has a significant effect on the hardness of both regions (steel and weld overlay). The hardness values for the weld overlay and the steel regions of the D1 sample are presented in Figure 5-4(a) and (b) respectively. As seen, in the weld overlay region, the hardness values increase to the range of ~280 to ~310 kgf mm^{-2}. Moreover, the hardness values in both regions of the HAZ in the D1 sample are decreased compared to those of the as-welded sample. The hardness values in the HAZ region varied in the range of ~220 to ~250 kgf mm^{-2}, which are still higher compared to those of the central zone.

The central zone hardness values range is between ~150 and ~180 kgf mm^{-2}, in the D1 sample, which is similar to that of the as-welded sample. This means that high temperature exposure for 1 day did not affect the hardness values of this zone in the steel region.

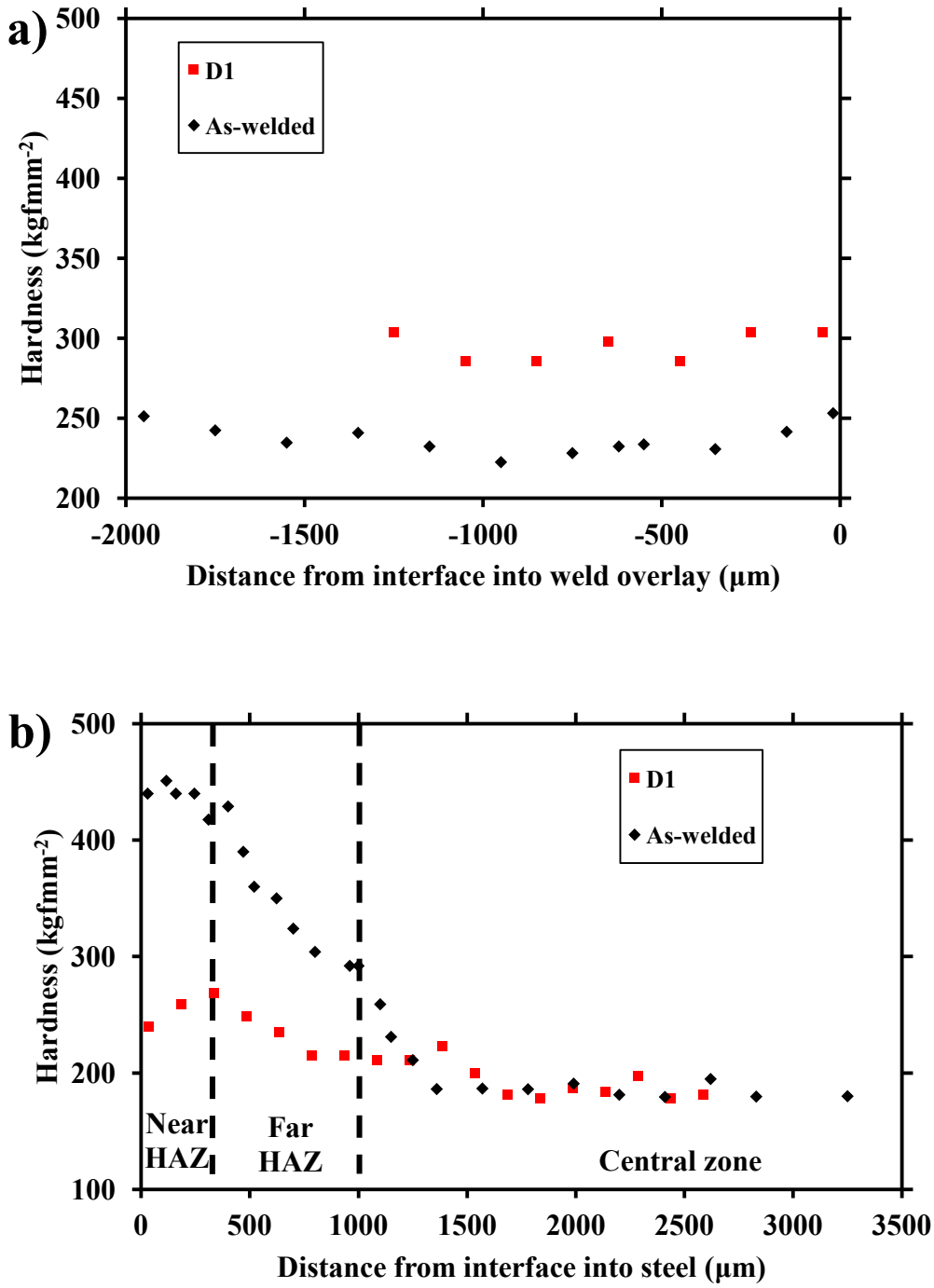

Figure 5-4. Showing (a) hardness profile in the weld overlay region of the as-welded and the D1 samples, (b) hardness profile in the steel region of the as-welded and the D1 samples.

The hardness values of the D4 sample in different regions are shown in Figure 5-5. As seen, increasing the exposure time to four days did not change the hardness profiles significantly in the steel region. However, hardness values in

the weld overly region increased to the range of ~320 to ~350 kgf mm^{-2}, which is higher compared to that of the D1 sample (~280 to ~310 kgf mm^{-2}).

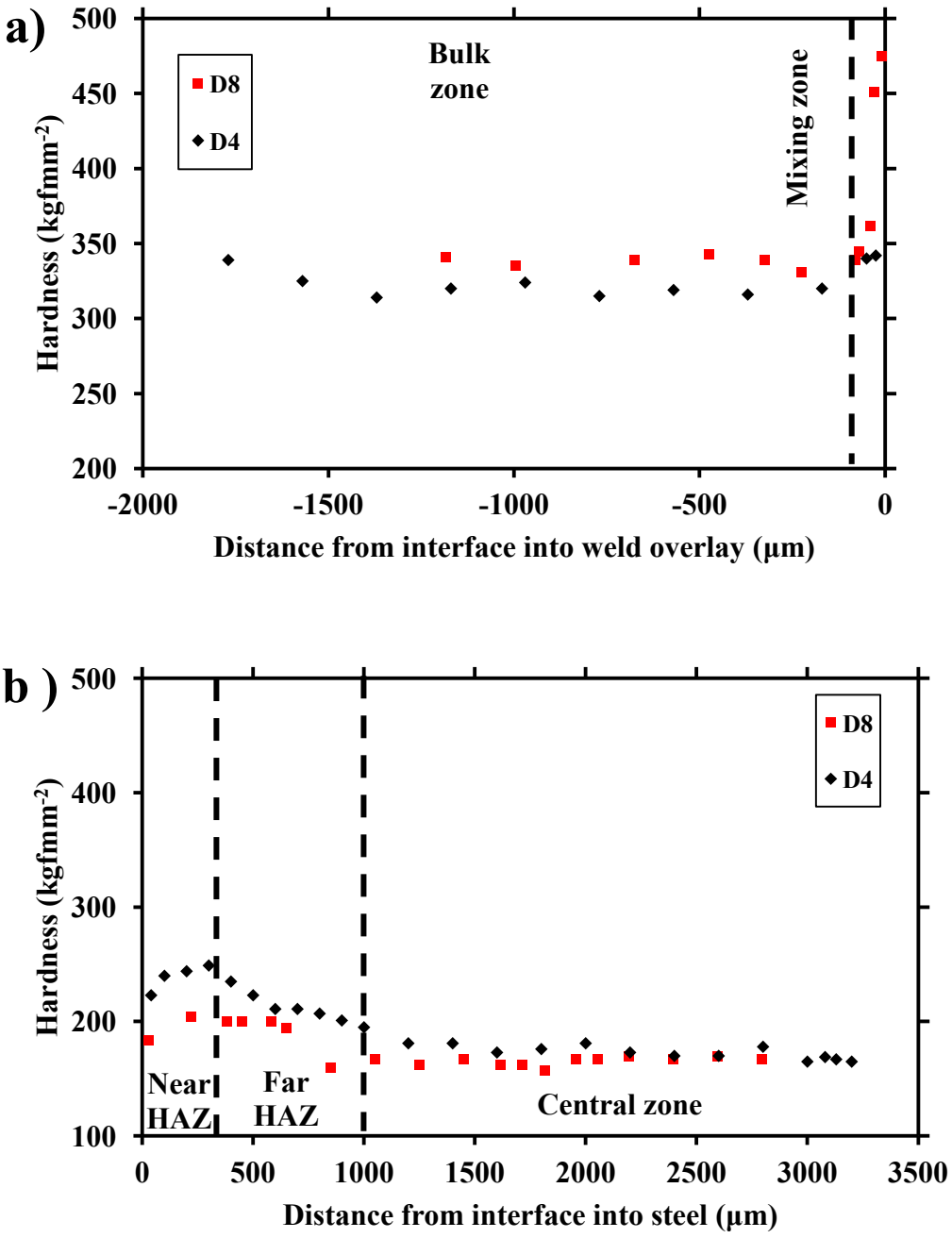

Figure 5-5. Showing (a) hardness profile in the weld overlay of the D4 and the D8 samples indicates hard band formation, (b) hardness profile in the steel region of the D4 and the D8 samples, indicates hardness decreasing in the HAZ region.

Figure 5-5(a) shows the hardness profile in the weld overlay region of the D8 sample. As seen, the hardness of the mixing zone increased significantly to the range of 470 - 500 kg fmm^{-2}. Meanwhile, the hardness values of the bulk zone underwent little changes compared to the D4 sample. In the steel region, as shown in Figure 5-5(b), the hardness values of the HAZ region in the D8 sample decreased to the range of 170 - 200 kgf mm^{-2}; which is very close to the hardness values of the central zone.

A comparison of the hardness profiles in the as-welded sample (see Figure 5-4) and the D8 sample (see Figure 5-5) shows that the hardness profile in the steel region becomes uniform through whole the steel region. Moreover, after 8 days of exposure, the hardness values increased in the mixing zone of the weld overlay region which is called hard band.

Increasing the exposure time to 16 days causes further changes in the hardness profiles of both regions. The weld overlay hardness profile in the D16 sample is presented in Figure 5-6(a) and it is obvious that the maximum hardness in the hard band increases to a range of 590 - 620 kgf mm^{-2}. Moreover, the hard band width increases up to ~50 μm. The hardness values of the bulk zone show little changes compared to those of the D8 sample.

The hardness profile in the steel region of the D16 sample is presented in Figure 5-6(b). The hardness values decrease to a range of 110 - 130 kgf mm^{-2}, in the near-HAZ region. A soft zone (low hardness), ~300 μm wide, formed in all mid-term exposed samples (from 12 to 32 days). However, the hardness values in other regions of the steel show small changes (less than 10 kgf mm^{-2}) compared to those of the D8 sample.

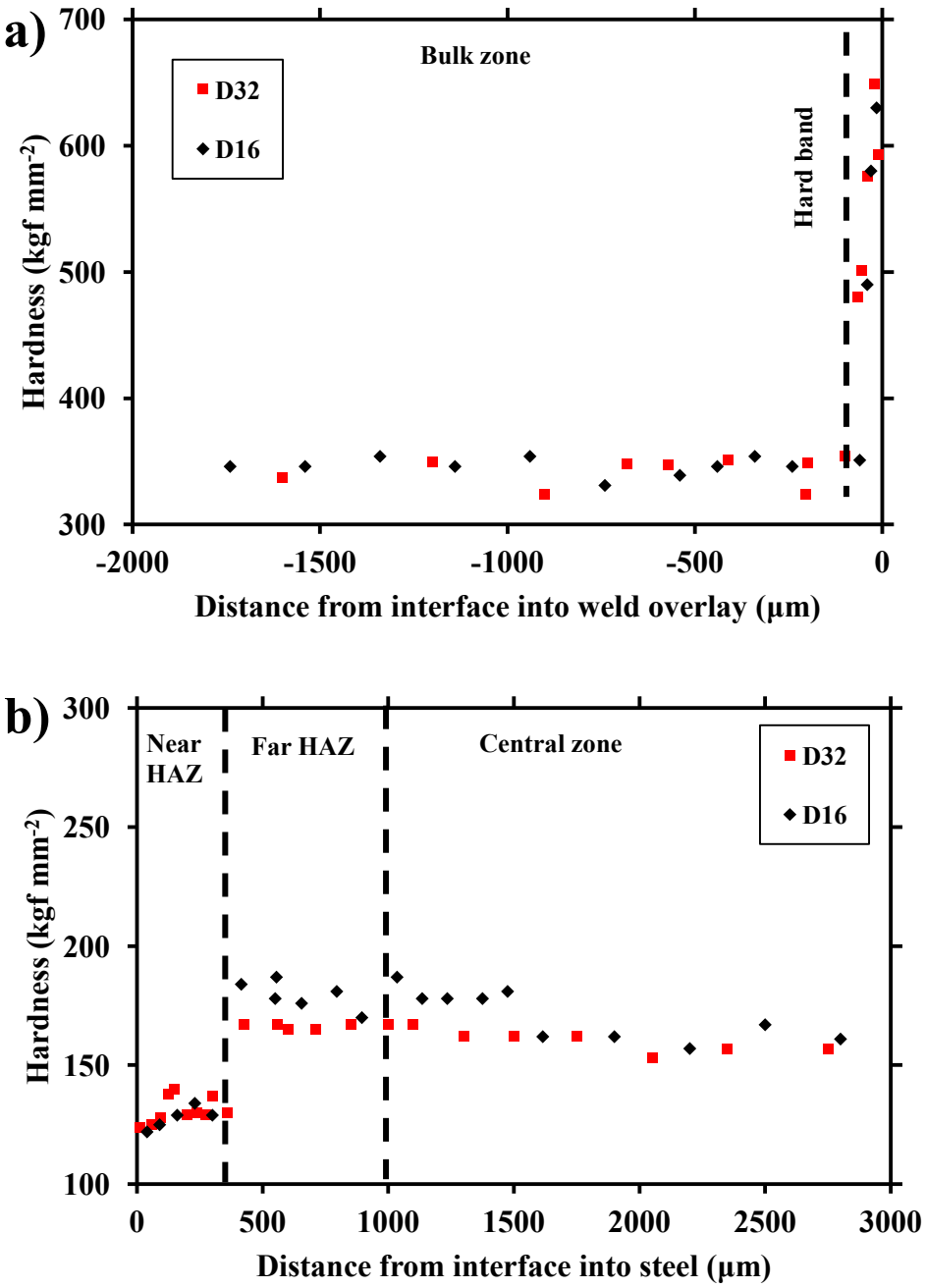

Figure 5-6. Showing (a) hardness profile in the weld overlay of the D16 and the D32 samples indicates formation of hard band, (b) hardness profile in the steel region of the D16 and the D32 samples, indicates formation of soft zone.

Exposure at 650˚C for 32 days did not affect the hardness profiles compared to those of the D16 sample. As shown in Figure 5-6(a), the maximum hardness of the hard band increases to the range of 620 - 650 kgf mm^{-2}, in the D32 sample, while its width is similar to that observed in the D16 sample.

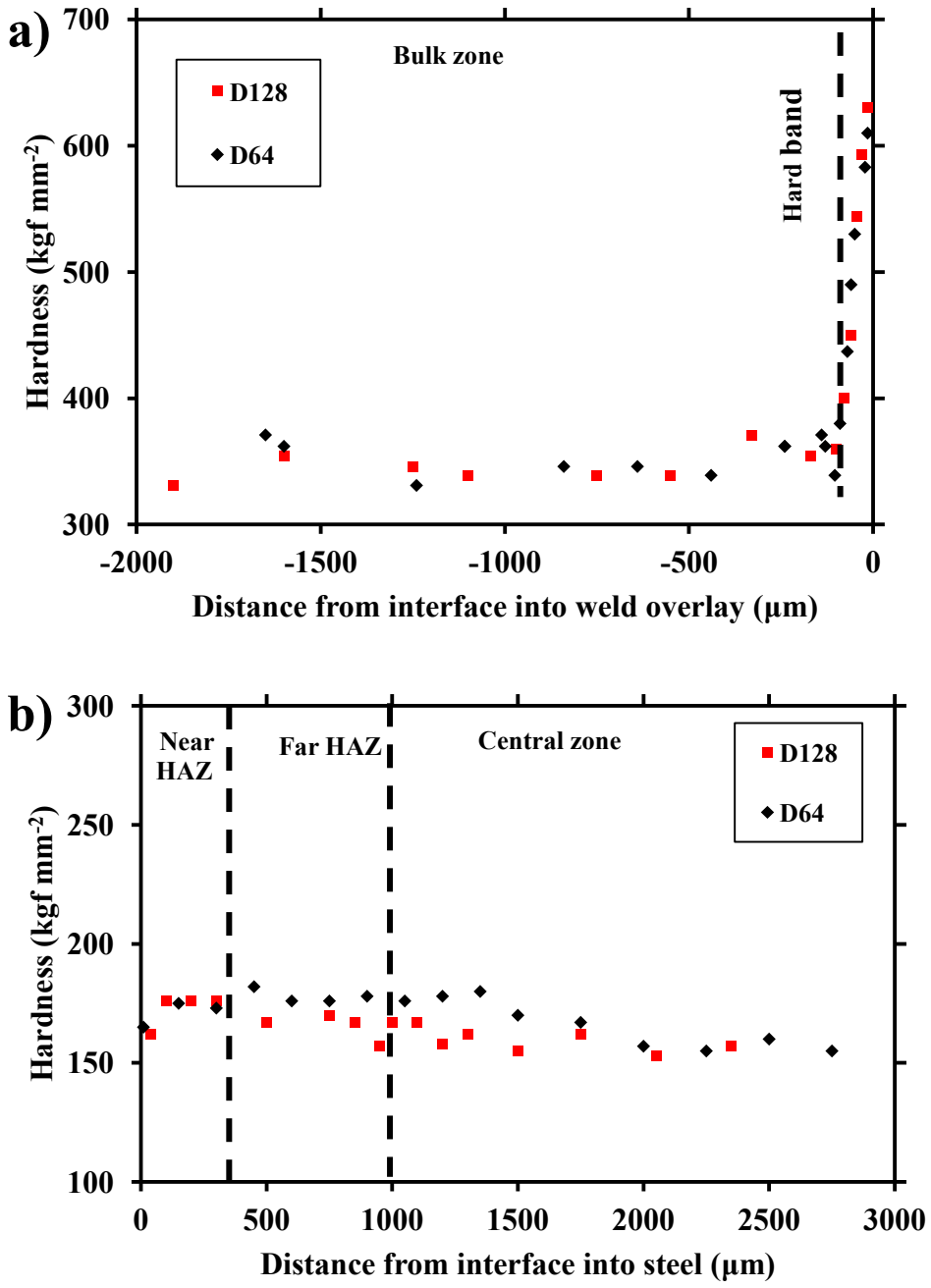

Figure 5-7. Showing (a) hardness profile in the weld overlay of the D64 and the D128 samples, (b) hardness profile in the steel region of the D64 and the D128 samples, indicates re-hardening of the near-HAZ region.

Moreover, the hardness values of the bulk zone in the D32 sample are almost similar to those of the D16 sample. The hardness profile in the steel region of the D32 sample shown in Figure 5-6(b) indicates that the soft zone hardness values and width are similar to those of the D16 sample. The hardness values

of the far-HAZ region in the D32 sample are almost the same as those of the central zone. Further investigations about the hardness profiles in samples of the second set of tests, including D12, D16, D20, D24, D28 and D32 samples, did not reveal any significant changes compared to those presented in Figure 5-6. Therefore, it is suggested that the hardness profiles in this figure are valid for all mid-term exposed samples

The hardness profile of the weld overlay region in the D64 sample, presented in Figure 5-7(a), indicates that increasing the exposure time did not affect the hardness values in this region. However, the hardness profile of the steel region in the D64 sample shows a significant change (about 50 kgf mm^{-2}) in the Near-HAZ region compared to that of the D32 sample. The hardness values of the soft zone have increased to the range of 160 - 180 kgf mm^{-2}. This range is almost the same as that of the central zone (see Figure 5-7(b)).

In other words, increasing the exposure time to 64 days caused re-hardening of the soft zone. Examination of hardness values in the D128 sample did not reveal significant changes in the hardness profiles of both regions compared to those of the D64 sample. These hardness profiles for both regions are presented in Figure 5-7(a) and (b).

WD128 sample hardness survey

The WD128 sample was aged after having had the steel substrate machined away and hardness measurement was carried out on the bulk zone of the WD128 sample using microhardness method and same procedure. The preliminary results did not reveal any significant change in the hardness of the bulk zone in the WD128 sample compared to those of the D128 sample. In

order to investigate the formation of a hard band in this sample, the hardness measurement in the edges of the sample was required.

The refined hardness measurement was done using a nano-indentation method as described in section 3-6-2 at two different locations of the WD128 sample. The hardness values at the edges of sample are reported as 7.7±0.6 GPa. However, the hardness of the bulk zone is reported as 5.4±0.6 GPa. Therefore, it is suggested that a hard band formed even in the absence of solid state diffusion from the steel substrate.

5-4- Microstructural characterization

The microstructure evolution in the weld overlay and the steel regions are linked together but in the following sections, the microstructural changes in the different regions are represented separately. In the next section, the microstructural evolution in the weld overlay region is reported and the microstructural changes in the different zones of the steel region are described in the latter section.

5-4-1- Microstructural evolution in weld overlay region

Microstructural changes occur during the high temperature exposure. For a better understanding of these changes, the thermally exposed samples should be divided into following three categories:

1) Early stages of thermal exposure including samples D1 to D8

2) Mid-term thermally exposed samples including D16, D32 and D64

3) Long term thermally exposed samples including D128 and WD128

5-4-1-1- Microstructural evolution in the early stages of thermal exposure

Examination of the D1 sample reveals that some features named as veins formed in the mixing zone of the weld overlay.

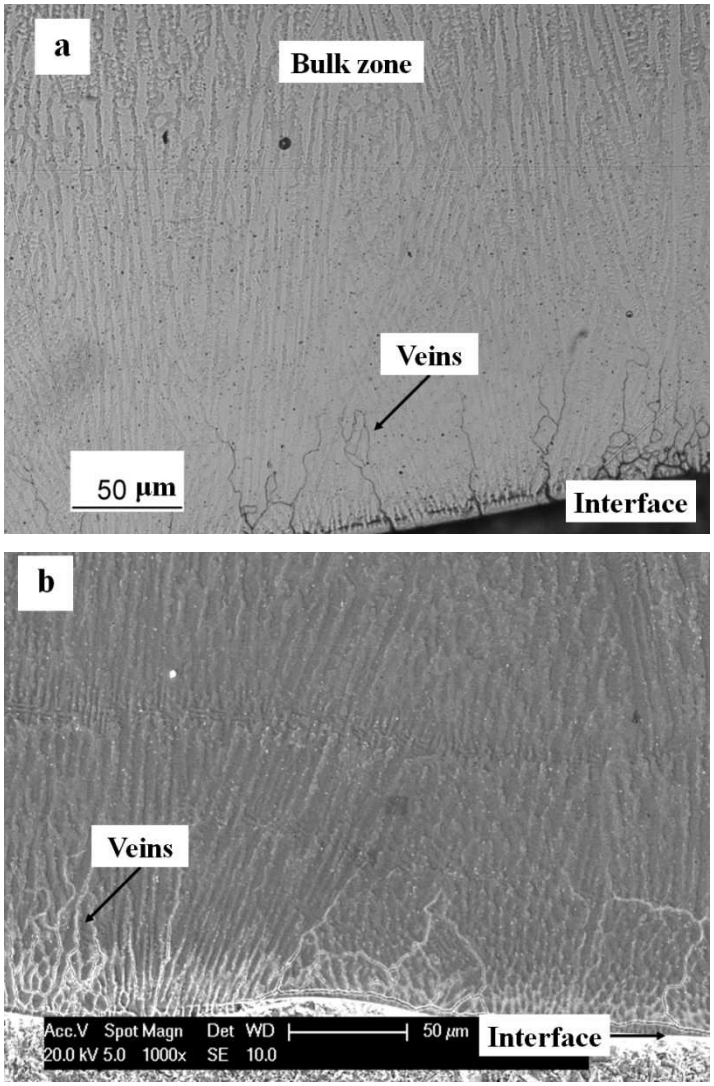

Figure 5-8. Showing overall view of the weld overlay region in the D1 sample; (a) optical microscope image in the etched condition indicates veins ~50 µm long, (b) SE micrograph in the etched condition indicates formation of the veins along the dendrites.

An optical microscope image from the D1 sample in the etched condition shows these veins close to interface (see Figure 5-8(a)). These veins ~50 μm long are the main features in the microstructure of the D1 sample. SE micrograph of the interfacial region in the etched conditions presented in Figure 5-8(b) shows that veins are formed along the dendrites. Moreover, the length and population of these veins vary from point to point. Further investigation confirmed that there is no significant change in the bulk zone of the weld overlay region in the D1 sample compared to that of the as-welded sample.

Figure 5-9(a) shows a BSE micrograph of the interfacial region in the polished condition and indicates a vein ~30 μm long with darker contrast compared to the matrix. It is suggested that veins contain some precipitates with lower mean atomic number compared to that of the matrix. Figure 5-9(b) shows a higher magnification optical microscope image of the veins in the etched condition, indicating formation along the dendrites. Figure 5-9(c) shows a SE micrograph in the etched condition indicating formation of veins with different sizes at the interdendritic regions. Moreover, some fine precipitates are visible in the large veins.

Examination of the D2 sample indicates the growth of veins. An optical microscope image of the D2 sample presented in Figure 5-10(a) shows the veins are ~100 μm long. Further investigations reveal that these veins outline the grain boundaries of weld overlay region. Figure 5-10(b) presents a SE micrograph of the D2 sample in the etched condition and the grain structure of the weld overlay region is clearly visible in this image.

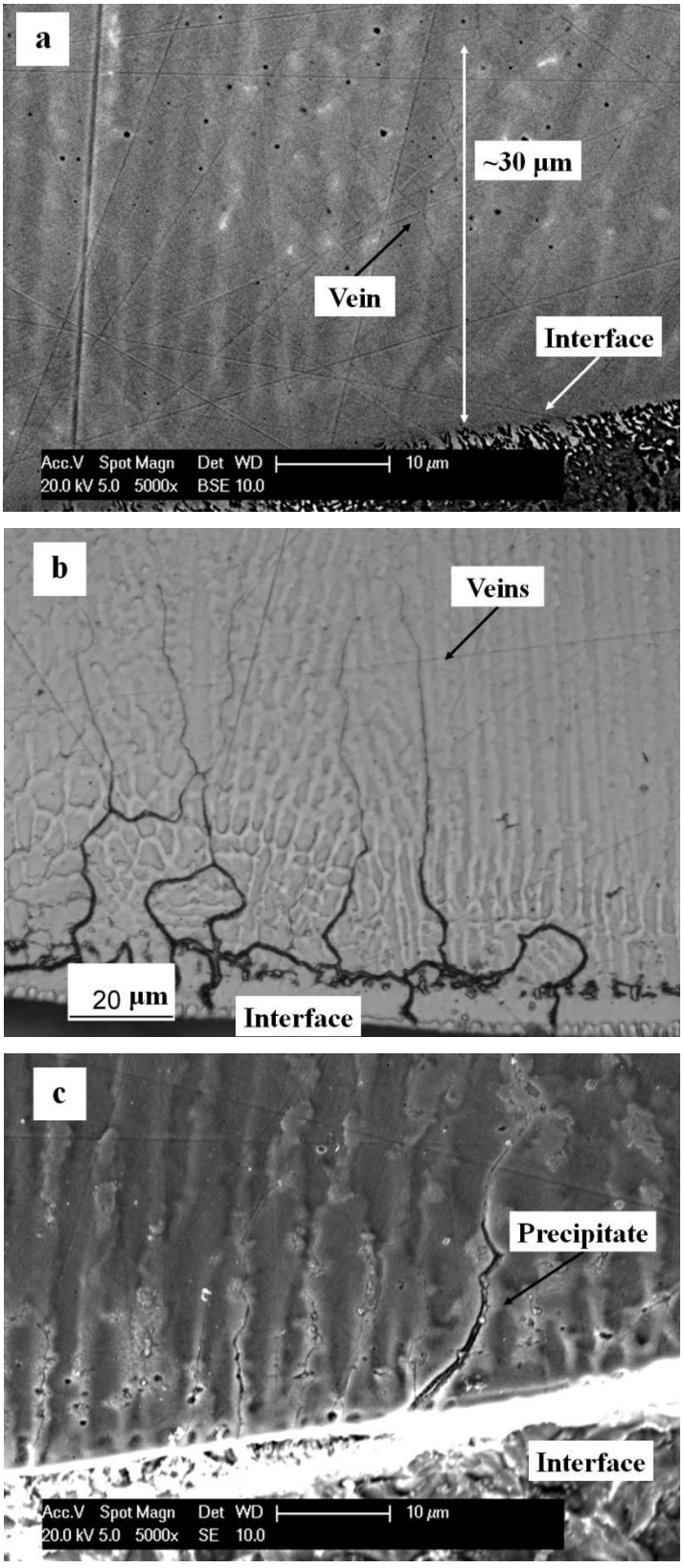

Figure 5-9. Showing different aspects of the veins in the D1 sample; (a) BSE micrograph in the un-etched condition indicates a vein ~30 µm long with darker contrast compared to the matrix, (b) optical microscope image in the etched condition indicates veins locations and (c) SE micrograph in the etched condition indicates different sizes of the veins and precipitates in the larger one.

An EDX line scan across the wide veins (see Figure 5-10(c)) reveals the Cr and Mo concentrations are about 50% higher in veins compared to those of the matrix. Considering higher Cr and Mo content in the veins and their dark contrast in the BSE micrograph (see Figure 5-9(a)), it is suggested that (Cr, Mo)-rich carbide are likely to precipitate along the grain boundaries of the weld overlay region.

The analysis of the D4 sample reveals that growth of the veins in the interfacial region has continued. The optical microscope image of the interfacial region in the D4 sample in the etched condition is shown in Figure 5-10(d). In addition to the veins, some grain boundaries are present in the area ~300 μm away from the interface.

Figure 5-10(e) shows a SE micrograph of the interfacial region in the D4 sample in the etched condition. The veins have formed mostly in the interdendritic regions. These interdendritic regions are protruding from the matrix in the etched condition.

Further investigation with the SEM reveals that fine precipitates are present on the grain boundaries in the area ~300 μm away from the interface. These precipitates on the grain boundaries are shown in Figure 5-10(f). It should be noted that the grain boundaries are present in some parts of the microstructure where the precipitates are large enough to be observed. It is clear that the grain boundaries in the area ~300 μm away from the interface become visible by precipitation of fine particles along them. EDX spot analysis revealed that some of these fine precipitates which are large enough to be analysed, are enriched in Nb, Mo compared to the matrix.

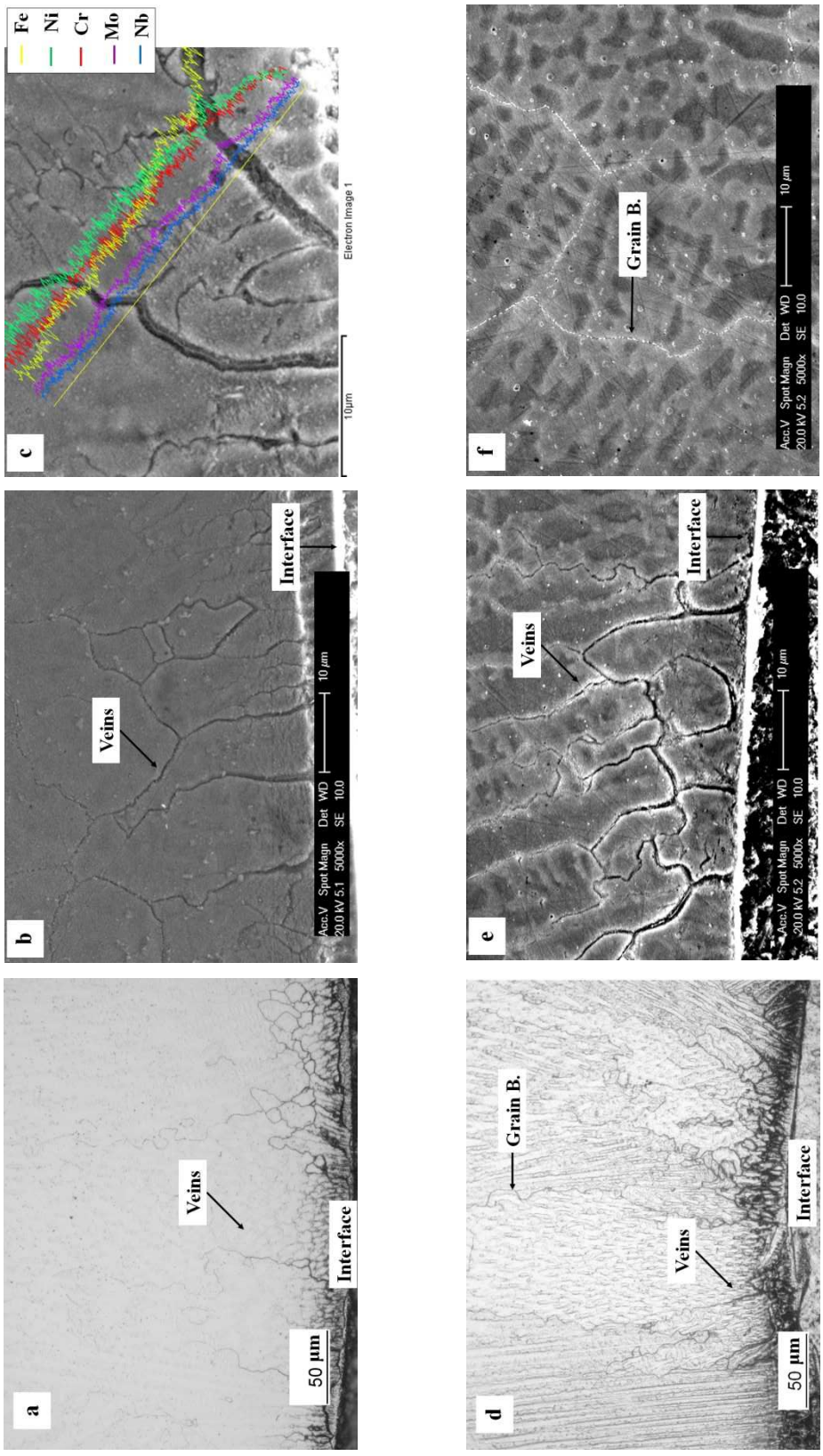

Figure 5-10. Showing microstructure of the D2 and the D4 sample in the etched condition; (a) optical microscope image of the D2 sample, (b) SE micrograph of the veins in the D2 sample and (c) EDX line scan results of a vein in the D2 sample; (d) optical microscope image of the D4 sample, (e) SE micrograph of the veins in the D4 sample and (f) SE micrograph of the grain boundaries in the area ~300 µm from the interface in the D4 sample

Microstructural analysis of the D8 sample in the etched condition, revealed a dark etch band of ~20 μm wide, adjacent to the interface which is shown in Figure 5-11(a). As was indicated in section 5-3, a hard band formed in the interfacial region of the D8 sample which was ~20 μm wide. It is suggested that formation of the dark band is related to hardening of this region. Figure 5-11(b) shows a BSE micrograph of the D8 sample and indicates more distinct darker contrast features compared to the D1 sample (see Figure 5-9(a)). As seen, these features are outlined the grain boundaries.

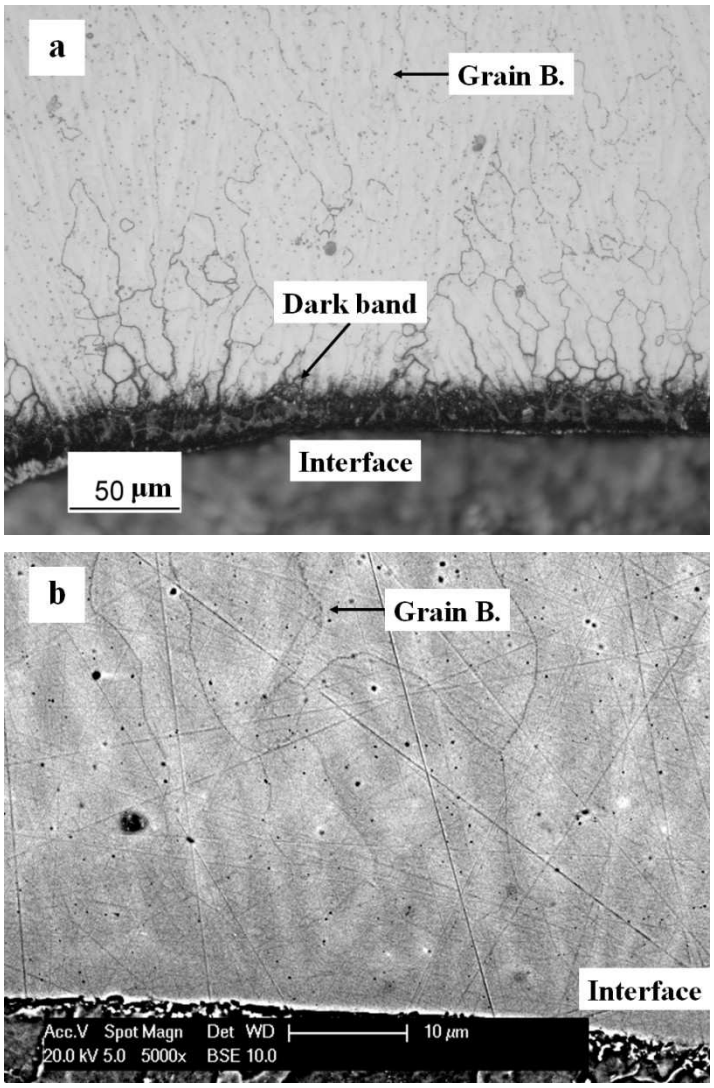

Figure 5-11. Showing the interfacial region of the D8 sample in different conditions; (a) optical microscope image in the etched condition indicates the dark band ~20 μm wide, b) BSE micrograph of interfacial region in the un-etched condition indicates darker contrast grain boundaries in the area close to interface.

Figure 5-12(a1) shows a lower magnification SE micrograph of the interfacial region in the D8 sample in the etched condition while Figure 5-12(a2) shows an area ~300 μm distant from the interface in the same condition. The grain boundary features are present in both of these images. Higher magnification SE micrographs of these features in both regions are shown in Figure 5-12(b1) and (b2) respectively. These images indicate fine precipitates along the grain boundary features.

BSE micrographs of two regions in this sample at different distances from the interface (i.e. ~50 μm and ~300 μm) in the un-etched condition are presented in Figure 5-12(c1) and (c2) respectively. The grain boundary features in the area close to the interface have darker contrast compared to the matrix. Further investigation indicates that dark grain boundaries are present within ~100 μm distance from the interface. However, grain boundaries in the area far from the interface contain bright contrast precipitates. It is suggested that darker precipitates are likely to correspond carbide precipitates in the interfacial region while the bright precipitates in the bulk zone are Mo, Nb enriched precipitates. The changes in the microstructure of the weld overlay region in the early stage of thermal exposure is summarised in the following points:

1) (Cr, Mo)-rich carbide precipitation along the grain boundaries within ~100 μm distance from the interface.

2) (Nb, Mo)-rich precipitates formation along the grain boundaries in the bulk zone.

3) Formation of a dark etch band, ~20 μm in width, adjacent to interface.

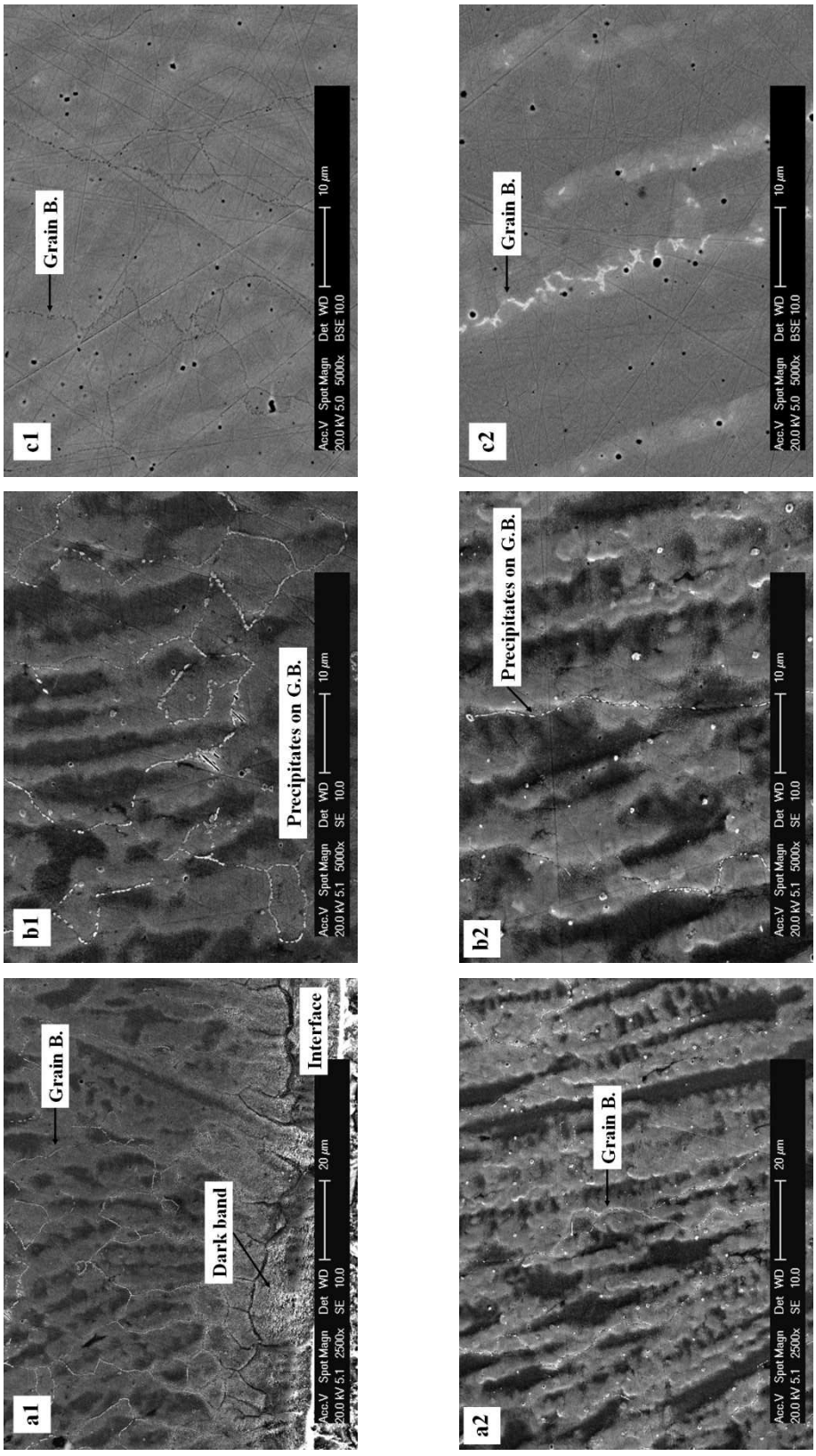

Figure 5-12. Showing micrographs of the interfacial region (1) and the bulk zone (2) in the D8 sample; (a1, a2) lower magnification SE micrographs in the etched condition indicate grain boundary features, (b1, b2) higher magnification SE micrographs indicate fine precipitates and (c1, c2) BSE micrographs in the un-etched condition indicate the dark precipitates in the interfacial region and bright precipitates in the bulk zone.

5-4-1-2- Microstructural evolution in the mid-term thermally exposed samples

In this section, the microstructural evolution in three samples i.e. D16, D32 and D64 are reported. Detailed investigation on the weld overlay microstructure in the etched condition using optical microscope revealed that the dark etch band width was increased to ~50 μm in the D16 sample as indicated in Figure 5-13(a).

However, as seen in this image, the length of the veins in the D16 sample did not change significantly compared to that of the D8 sample and remained at ~100 μm. The appearance of the dark etch band is related to the etching of the weld overlay in Aqua-Regia. For example, electro-etching of this sample results in a different appearance to the interfacial region. A higher magnification image of the interfacial region of the D16 sample in the electro-etched condition is presented in Figure 5-13(b). As seen, the dark etch band region does not appear in this condition. This image indicates that the hard band in the D16 sample has granular structure which is different from the dendritic structure of the bulk zone.

A higher magnification image of the bulk zone (~300 μm distance from the interface) in the D16 sample etched in Aqua-Regia is presented in Figure 5-13(c) and shows the sub grains. It should be noted that an identical microstructure was observed for all of the mid-term thermally exposed samples in the etched condition, for both etching processes. Hence, the corresponding images of the D32 and the D64 samples are not presented here as they are very similar to those of the D16 sample.

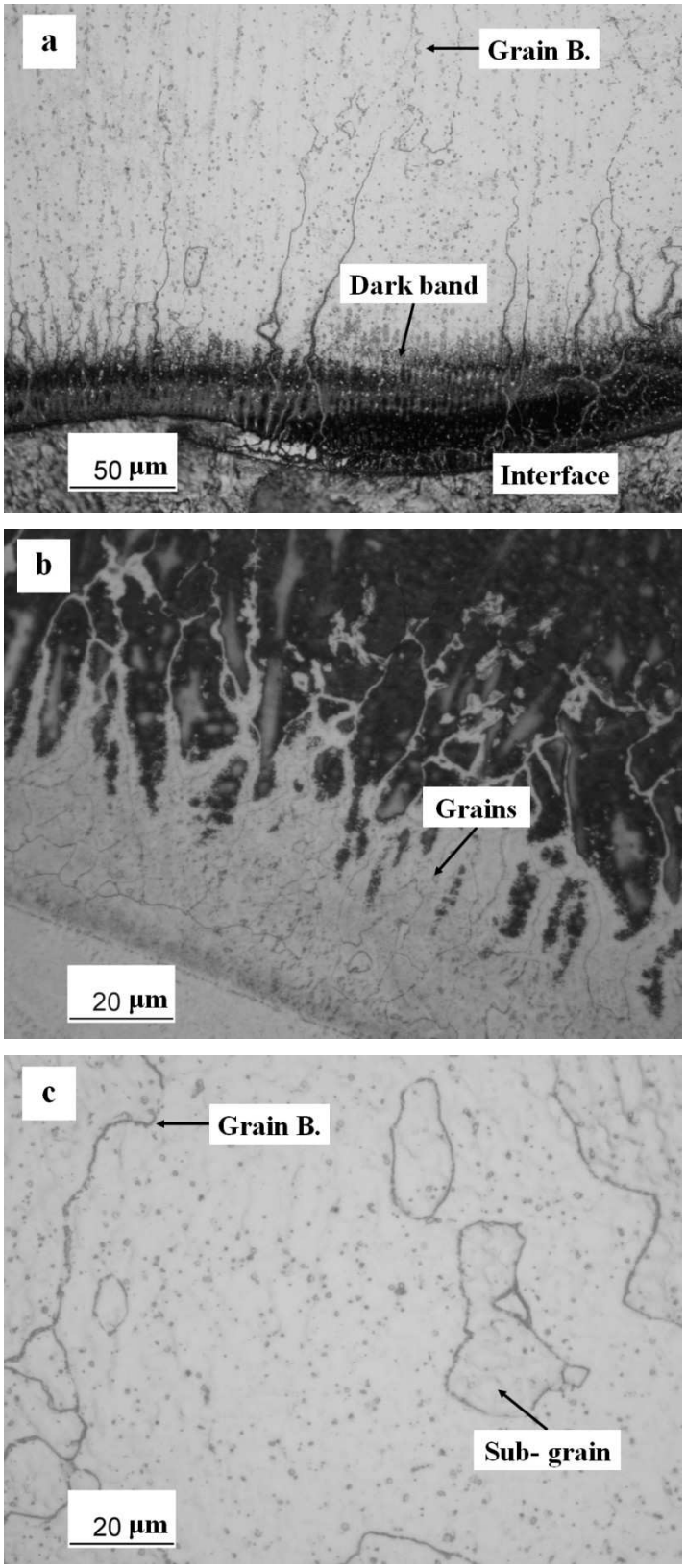

Figure 5-13. Showing optical microscope images of the D16 sample weld overlay region in the etched condition; (a) lower magnification image indicates the dark band and the grain boundaries, (b) higher magnification image of the electro-etched sample indicates grains in the mixing zone and (c) higher magnification image of the bulk zone indicates formation of sub grains.

Further examinations were carried out on the microstructure of the D16 sample in the etched condition using SEM. A SE micrograph of the interfacial region of this sample, presented in Figure 5-14(a1), shows the dark band region and grain boundaries. The EDX area analyses results from the D16 sample have shown that composition of the interfacial region in this sample generally is similar to the as-welded condition (see Figure 5-14(a2)). Therefore, the formation of the hard band is not related to the compositional changes.

A higher magnification SE micrograph of the grain boundaries in the interfacial region is presented in Figure 5-14(b1). The EDX spot analysis of the large particles present along the grain boundaries in this region is shown in Figure 5-14(b2) and indicates higher Cr and Mo compared to the matrix.

As seen in Figure 5-14(c1), fine precipitates in the bulk zone are individual precipitates which are formed in the interdendritic regions. As seen, there are different types of precipitates in this region. There are some larger blocky particles dispersed in the interdendritic regions. EDX spot analysis on these particles indicates higher Nb and Ti content compared to the matrix. Moreover, there are some irregular shape precipitates, which EDX spot analysis on them shows higher Nb and Mo content compared to those of the matrix (see Figure 5-14(c2)).

The microstructure of the weld overlay region in the etched condition in the D32 and the D64 samples are similar to those of the D16 sample. However, there are some minor differences in the interfacial region of the mid-term thermally exposed samples which can be revealed by BSE micrographs.

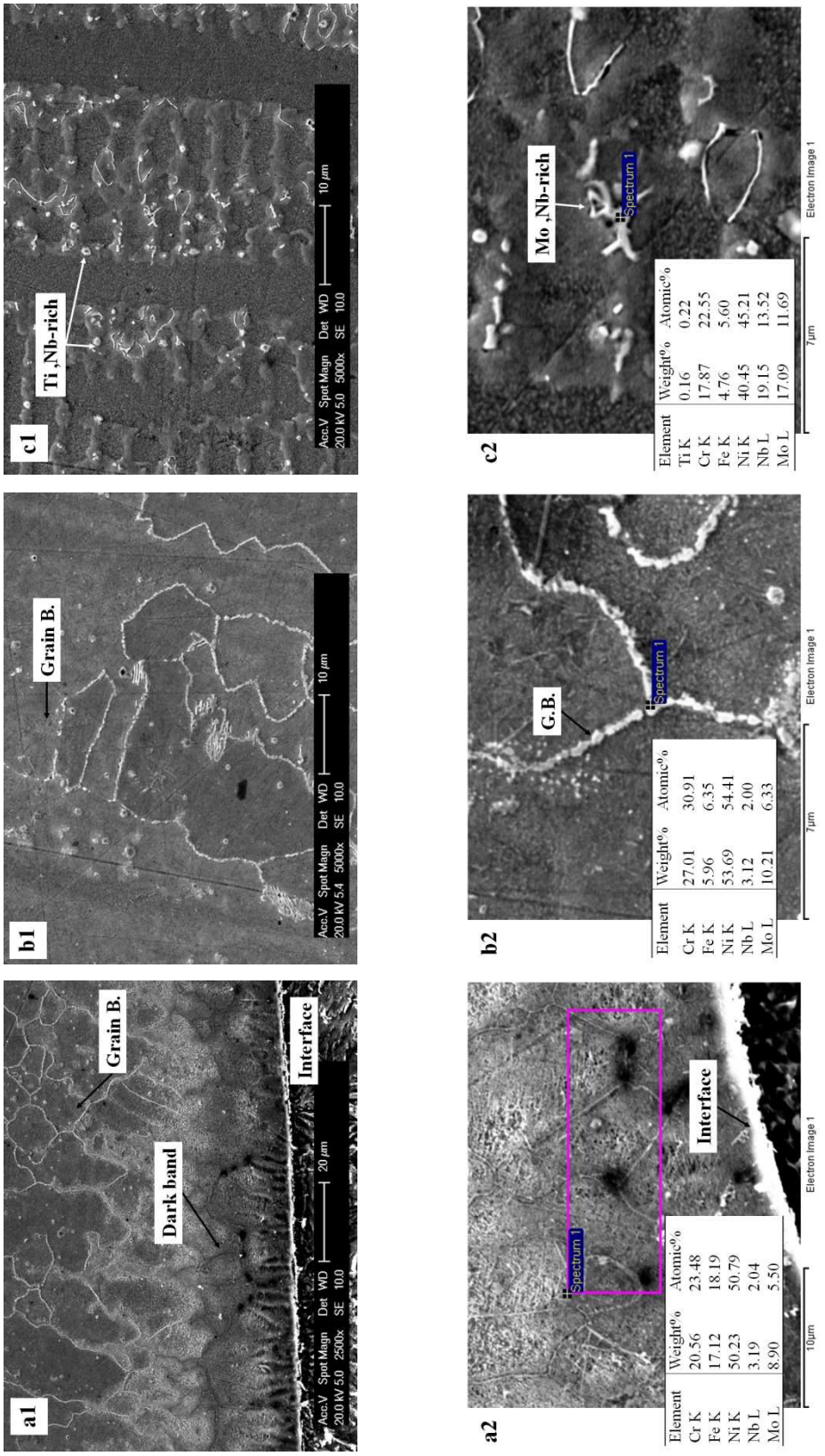

Figure 5-14. Showing SE micrographs (1) and EDX results (2) of the weld overlay region in the etched condition in the D16 sample; (a1) lower magnification image of the interfacial region, (a2) EDX results for the hard band; (b1) higher magnification image of the grain boundaries close to interface, (b2) EDX results for a particle in this region; (c1) higher magnification image from the bulk zone indicates two different particles, (c2) EDX results for a Mo, Nb- rich particle in this region.

Increasing exposure time causes coarsening of the (Cr, Mo)-rich carbide precipitates along the grain boundaries within ~100 μm of the interface. Figure 5-15(a1) shows a higher magnification BSE micrograph from the interfacial region in the D16 sample and dark grain boundaries are hardly visible in this image. In the same region of D64 sample the dark grain boundaries became more distinct at the same magnification (see Figure 5-15(b1)). Figure 5-15(c1) shows the EDX line scan results across these dark grain boundaries in the D64 sample and indicates higher Cr and Mo contents in them.

Figure 5-15(a2) and (b2) show the region at a ~100 μm distance from the interface in the D16 and D64 sample respectively. The dendritic microstructure is visible in D16 sample while in the D64 sample there are some bright precipitates at the end of dark grain boundaries. Figure 5-15(c2) shows the EDX line scan results across the large bright particles in this region of the D64 sample and shows a higher Mo and Nb content in them compared to those of the matrix.

EPMA analysis was carried out on a region at a distance of ~50 μm from the interface in the D64 sample and its results are shown in Figure 5-16. This image shows the elemental colour maps for all elements in the weld overlay region as well as a BSE micrograph of the analysed area (indicated in the image). The dark grain boundary is correlated to the Cr-rich regions in the Cr map. Moreover, the Mo map also shows a band with slightly higher Mo concentration in the regions which are correlated to the grain boundary.

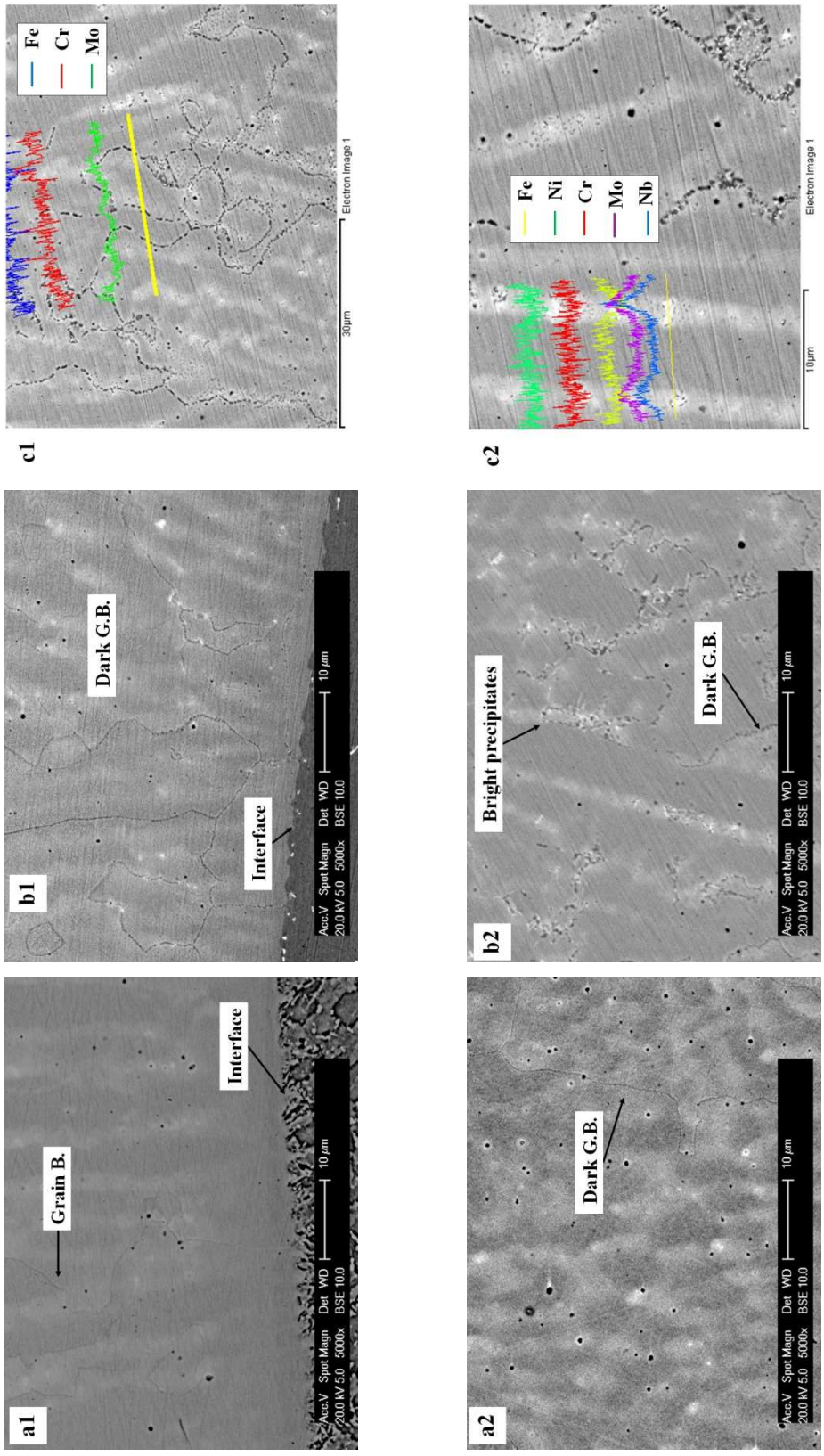

Figure 5-15. Showing microstructural evolution in the interfacial region (1) and the area at a ~100 µm distance from the interface (2) in the mid-term samples; (a1) the interfacial region of the D16 sample (b1) the same region in the D64 sample and (c1) the EDX results of the dark grain boundaries in this region. (a2) the area at a ~100 µm distance from the interface in the D16 sample, (b2) the same region in the D64 sample and (c2) the EDX results of bright precipitates in this region.

Therefore, it is suggested that (Cr, Mo)-rich carbide are likely to precipitate along the grain boundaries in this region. Moreover, there are some bright contrast precipitates in Figure 5-16 which are correlated to higher concentrations of Nb and Mo. It is suggested that these precipitates are related to formation of intermetallic phases. However, it should be noted that some of the Nb-rich points are related to the Ti-rich points too. The average concentrations in (at.%) for the elements except carbon in this region are in the same range compared to those of the D16 sample (see Figure 5-14(a2)).

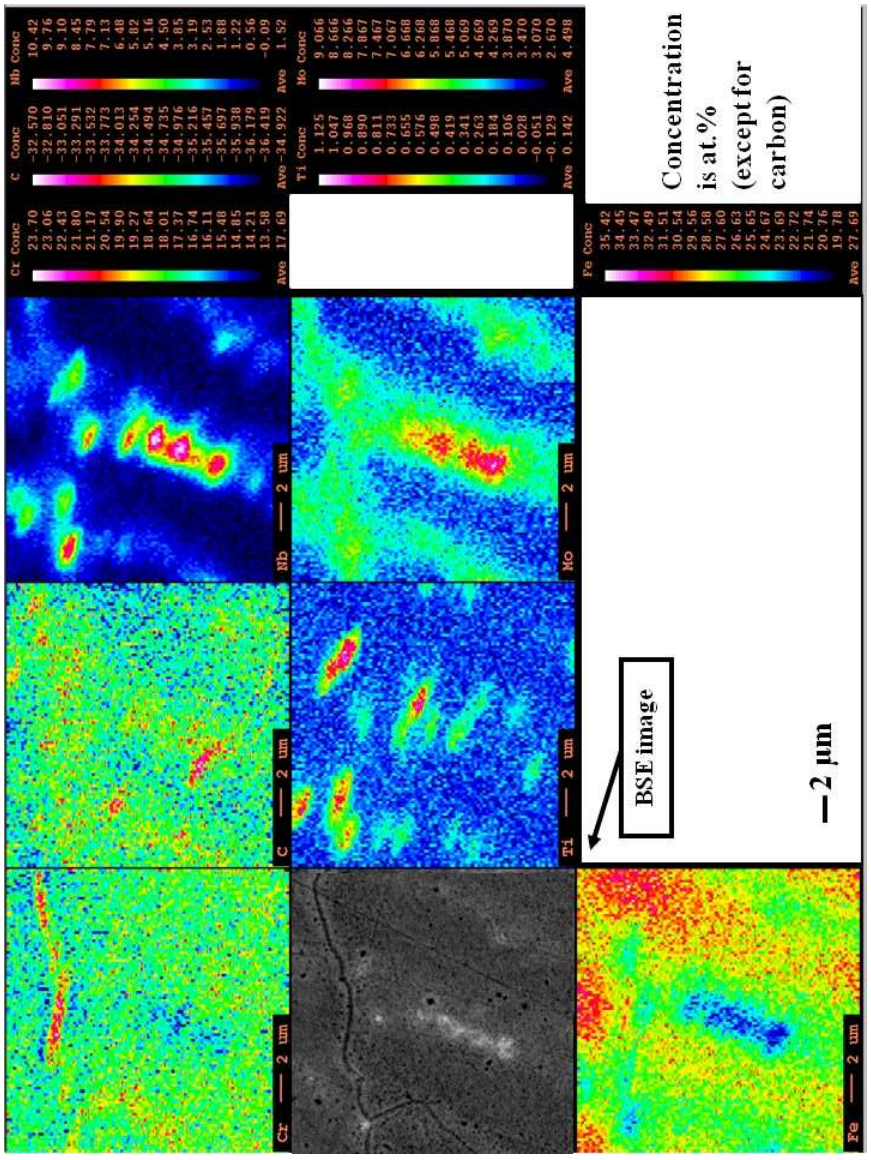

Figure 5-16. Showing EPMA analysis results on the weld overlay region of the D64 sample in the un-etched condition indicates dark and bright precipitates.

EDX line scan results from the interfacial region in the polished condition in D32 and the D64 samples are presented in Figure 5-17(a1) and (a2) respectively and show that the concentration profiles for different elements in this region are very similar to those of the as-welded sample (see Figure 4-12). Further analyses were carried out on the D32 and the D64 samples in order to identify the differences in precipitate population by Oxford-instruments Company. BSE micrographs of an area at ~50 µm distance from the interface in the D32 and the D64 samples are presented in Figure 5-17(b1) and (b2).

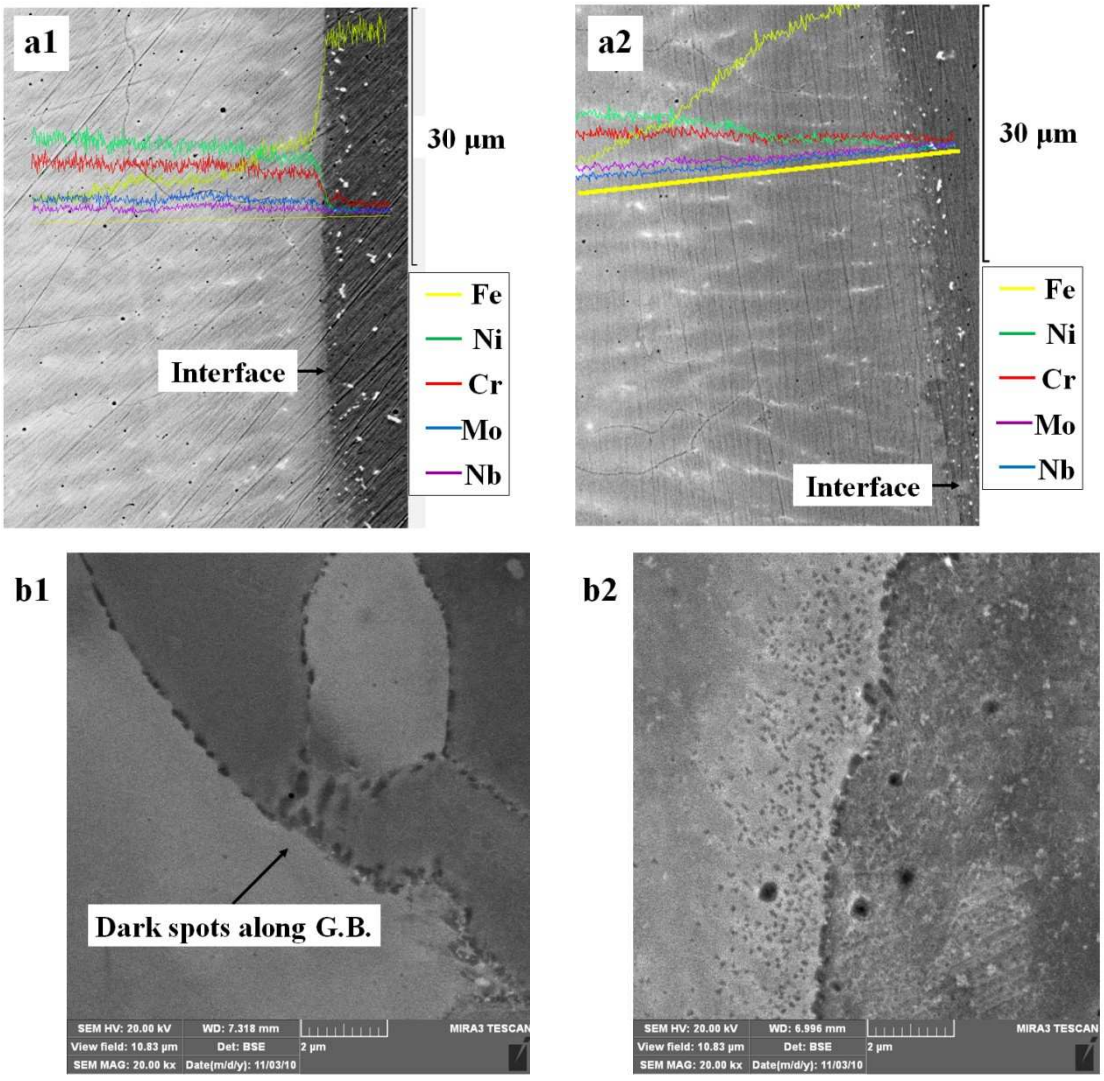

Figure 5-17. Showing different images for midterm exposed samples; (a1) EDX line scan for the interfacial region of the D32 sample, (a2) EDX line scan in the D64 sample; (b1) BSE micrograph of precipitates along the grain boundaries in the D32 sample and (b2) BSE micrograph of precipitates around the grain boundaries in the D64 sample.

A comparison of these images shows that there are more dark precipitates around the grain boundaries in the D64 sample compared to those of the D32 sample. These images indicate that although the length of carbide precipitation region close to interface is constant, the population of these carbides was increased with increasing exposure time.

Evolution processes in the weld overlay region of the mid-term thermally exposed samples, are summarized as following points:

1) Coarsening of the carbide precipitates along the grain boundaries in the interfacial region (within ~100 μm distance from the interface) and formation of some particles around the grain boundaries.

2) Formation of a (Nb, Mo)-rich phase along the grain boundaries beyond ~100 μm distance from the interface and precipitation of (Nb, Ti)-rich in the bulk zone of the weld overlay region.

3) The dark etch band composition is similar to its as-welded condition and formed due to different etching behaviour of the hard band.

5-4-1-3- Microstructural evolution after long term thermal exposure

In this section results of the microstructure evaluation after long term thermal exposure are presented. The experimental observations for the D128 sample are described in the next section. Moreover, in order to understand the effect of steel substrate on the evolution processes, the results of the WD128 sample are shown in the following section.

The D128 sample

Figure 5-18(a) shows an optical microscopic image of the interfacial region in the D128 sample in the etched condition. As seen, the dark etch band width did not change significantly compared to that of the D16 sample (see Figure 5-13). However, due to coarsening of the precipitates along the grain boundaries in the interfacial region, they appear more distinct in this sample compared to those of the mid-term exposed samples.

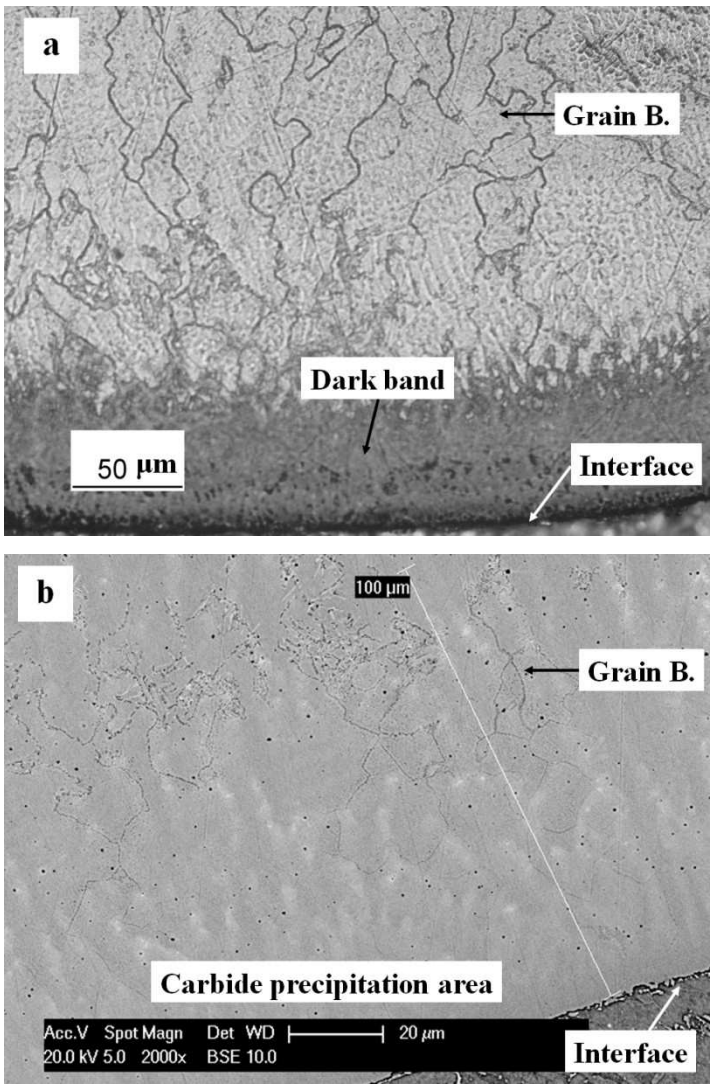

Figure 5-18. Showing the weld overlay region microstructure in the D128 sample; (a) optical microscope image in the etched condition indicates the grain boundaries in the interfacial region, (b) BSE micrograph of the interfacial region in the un-etched condition indicates the carbide precipitation area.

Figure 5-18(b) shows a BSE micrograph of the D128 sample in the un-etched condition and indicates a region ~100 μm wide with carbide precipitates adjacent to interface. It is seen that even after a long term ageing process; the carbides precipitates along grain boundaries did not grow beyond this region. A comparison of Figure 5-18(a) and (b) indicates that grain boundaries in the etched condition beyond ~100 μm from the interface contain different precipitates.

Higher magnification BSE micrographs from different regions in the weld overlay are presented in Figure 5-19 and reveal that some bright precipitates are present beyond the carbide precipitation region. A BSE micrograph from the region at ~250 μm distant from the interface is shown in Figure 5-19(a) and indicates irregular shape bright precipitates adjacent to some dark features in this region. In other words, in this region carbides and precipitates with higher atomic number are present together. These precipitates were probably TCP phase which formed in the interdendritic locations and along the grain boundaries in this region.

Figure 5-19(b) shows a BSE micrograph of the region at ~100 μm distant from the interface. It is seen that at the end of the carbide precipitation region, there is a different morphology for TCP precipitates. There are some acicular precipitates adjacent to carbide precipitates which are different from those observed in the bulk zone of the weld overlay region. Finally, Figure 5-19(c) shows carbide precipitates along grain boundaries in the interfacial region. It is seen that the population of these precipitates adjacent to interface is less than other parts.

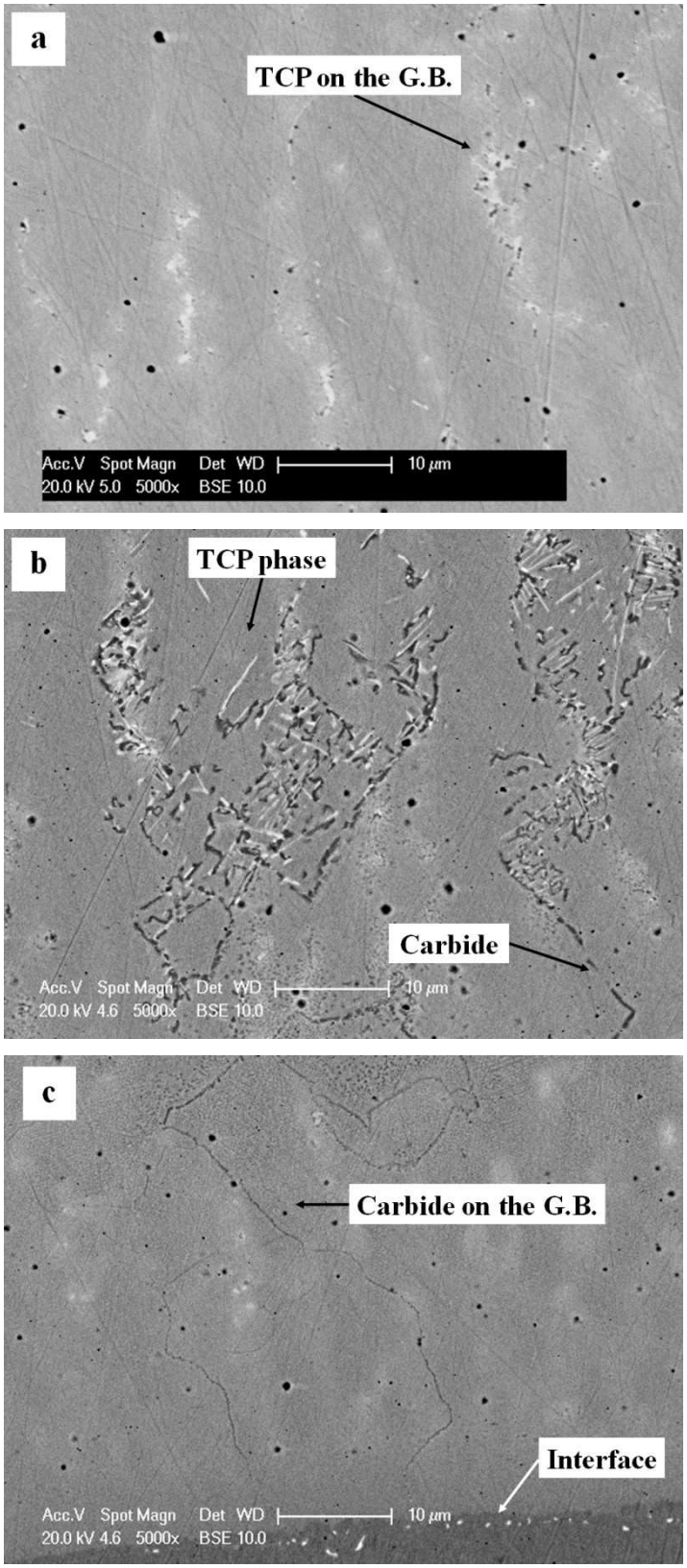

Figure 5-19. Showing different regions of the D128 sample; (a) the BSE micrograph at ~250 µm distant from the interface indicates TCP precipitates along the grain boundaries, (b) the BSE micrograph at ~100 µm distant from the interface indicates different TCP phases in this region and (c) the BSE micrograph from the interfacial region indicates carbide precipitates along the grain boundaries.

EPMA analyses were carried out on the different locations of the weld overlay region in the D128 sample. The average compositions of the mixing and the bulk zone are similar to those of the as-welded sample. Moreover, some elemental mappings were carried out on this sample. The first analysis was carried out on a region at ~50 μm distant from the interface.

Figure 5-20(a) shows a BSE micrograph in this region which indicates the analysed area. Figure 5-20(b) shows the elemental colour maps for this region and due to larger size of carbide precipitates in this sample, the carbon map shows higher concentrations in the regions which are correlated to the grain boundary. Although the Cr map is also showing that grain boundaries are Cr-rich, it is clear that Cr is uniformly distributed in the matrix of this region.

The Mo map shows two different precipitation behaviours; in the regions which are correlated to the grain boundary there are higher concentrations of Mo which is similar to the Cr map. Nevertheless, in the region which is correlated to the bright precipitate there is a higher concentration of Mo which is similar to Nb map. Moreover, there are some isolated, high concentration regions of Ti and Nb which are correlated to the brighter contrast points in the interdendritic regions.

The next EPMA was carried out on the region at ~100 μm distant from the interface in the D128 sample where acicular precipitates are present. The analysed area is shown in Figure 5-21(a) and the corresponding elemental maps are presented in Figure 5-21(b). As seen there are two Mo, Nb-rich points and one Nb, Ti-rich point.

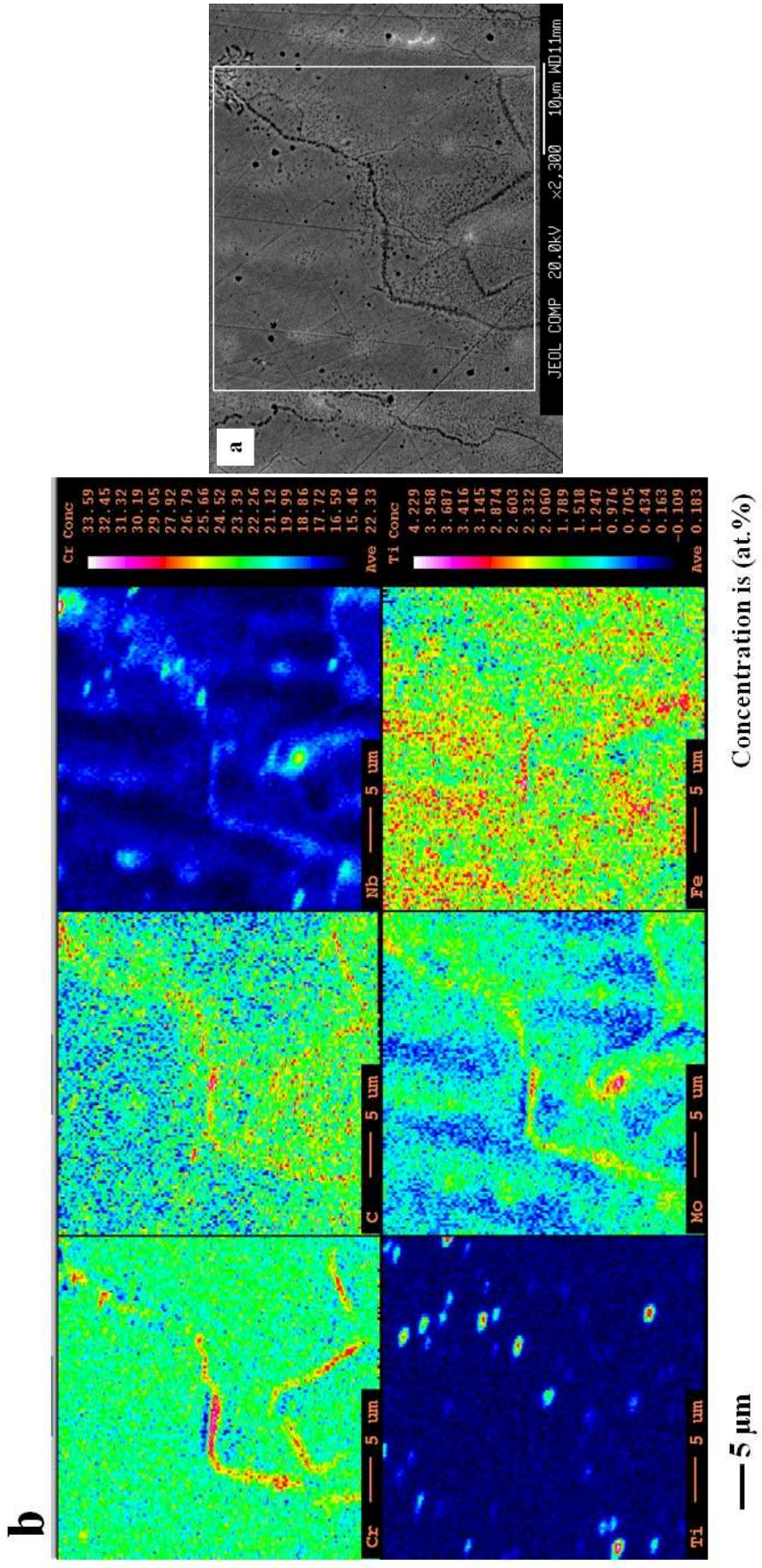

Figure 5-20. Showing EPMA results for a region at ~50 μm distant from the interface in the D128 sample; (a) the BSE micrograph indicates the analysed area, (b) The colour maps for the elements.

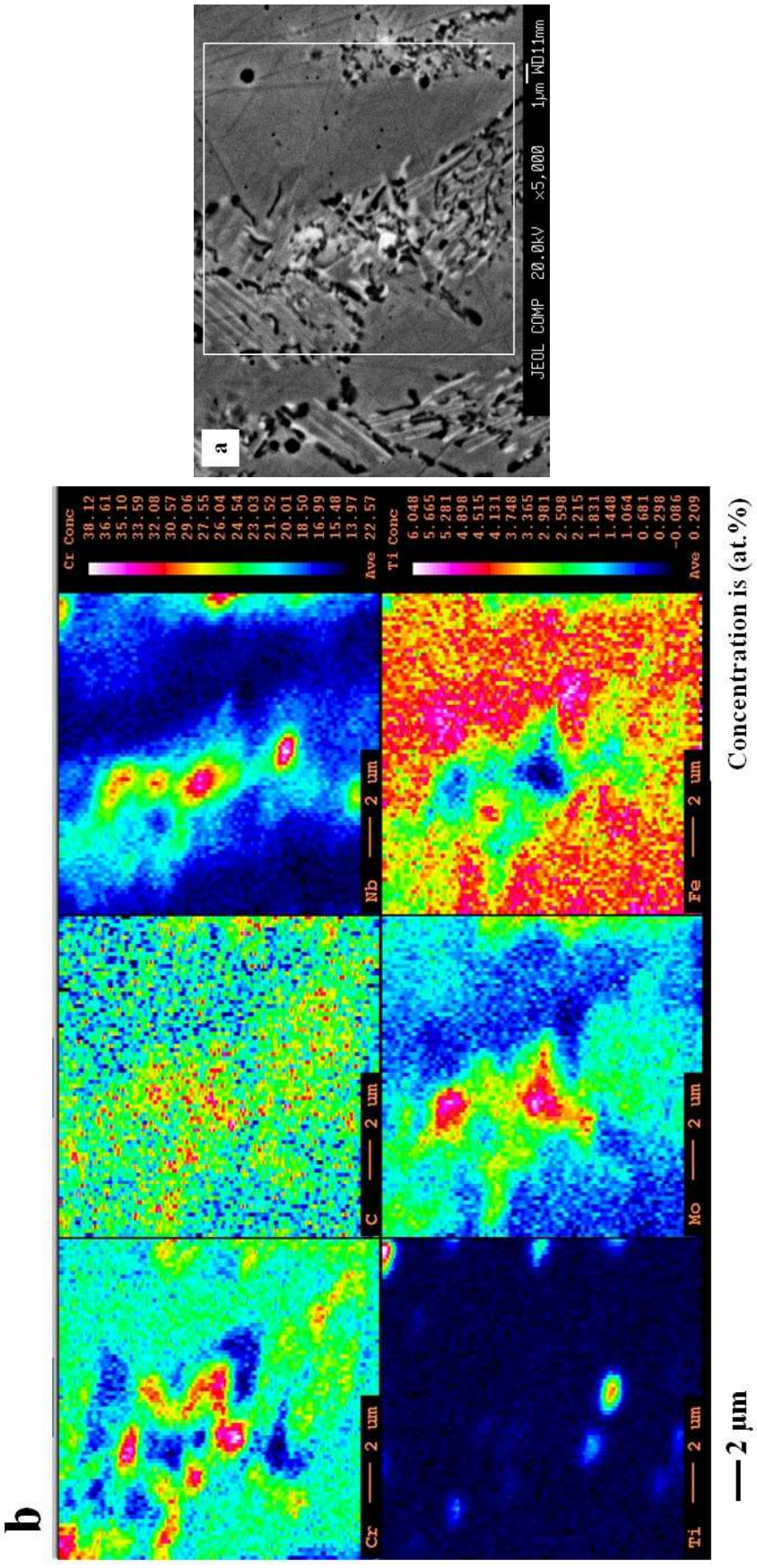

Figure 5-21. Showing EPMA results for a region at ~100 μm distant from the interface in the D128 sample; (a) the BSE micrograph indicates the analysed, (b) The colour maps for the elements.

It is seen that two red points in the Mo map are correlated to the brighter blocky particles in the BSE micrograph. Moreover, evaluation of the Nb map indicates that although the Nb-rich regions are correlated to the Mo-rich regions, the highly Nb-rich points are in different positions compared to those of the Mo-rich points. Moreover, it is observed that some parts of the Mo-rich regions in the bright particles are correlated to the Cr-rich regions. Nevertheless, some of the bright precipitates are corresponding to regions which are enriched in Nb and Ti.

The WD128 sample

Figure 5-22(a) shows an optical microscope image of the WD128 sample in the etched condition which is different compared to that of the D128 microstructure (see Figure 5-18(a)). The dark etch band is not seen adjacent to the interface; however, nano-indention hardness measurement results indicate a higher hardness for the interfacial region compared to the bulk zone in the WD128 sample. The grain boundaries in the interfacial region of the WD128 sample are less distinct compared those of the D128 sample.

An EDX line scan across the grain boundaries in the interfacial region of the WD128 sample (see Figure 5-22(b)) reveals some (Mo, Nb)-rich precipitates along the grain boundaries. Further investigation was carried out in the un-etched condition. A BSE micrograph of the WD128 sample presented in Figure 5-22(c) shows some bright contrast precipitates along the grain boundaries in the interfacial region. There is no evidence for carbide precipitation in this region which is different compared to the D128 sample (see Figure 5-18(b)).

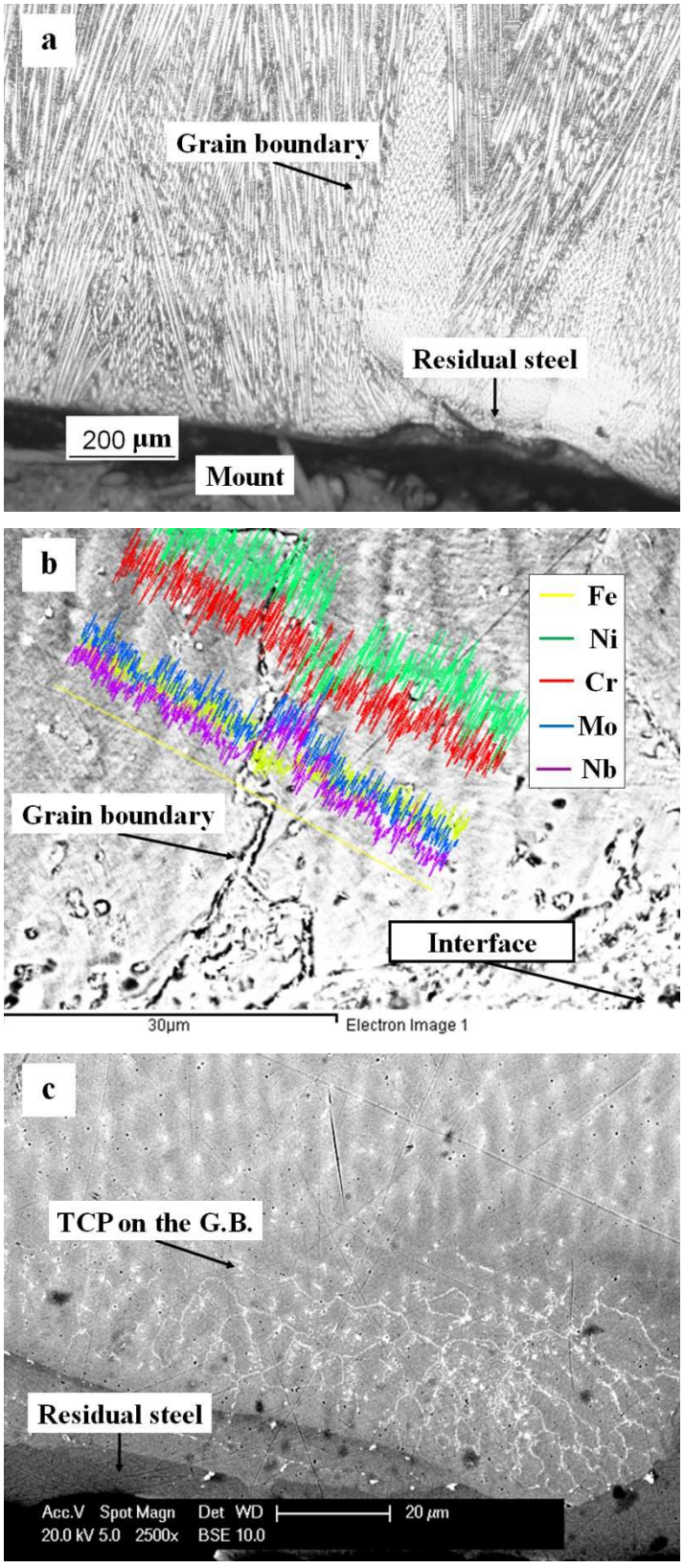

Figure 5-22. Showing the interfacial region in the WD128 sample; (a) an optical microscope image in the etched condition indicates grain boundaries, (b) EDX line scan results for the precipitates along the grain boundaries and (c) a BSE micrograph in the un-etched condition indicates the TCP phase precipitates along the grain boundaries close to the interface.

It is concluded that formation of the hard band is not related to presence of the dark etch band and the steel substrate. A comparison of BSE micrographs for the D128 and the WD128 samples indicates that presence of steel substrate has a great influence on the type of precipitates along the grain boundaries in the interfacial region. In the D128 sample, carbide precipitates are present while TCP precipitates have formed along the grain boundaries in the WD128 sample.

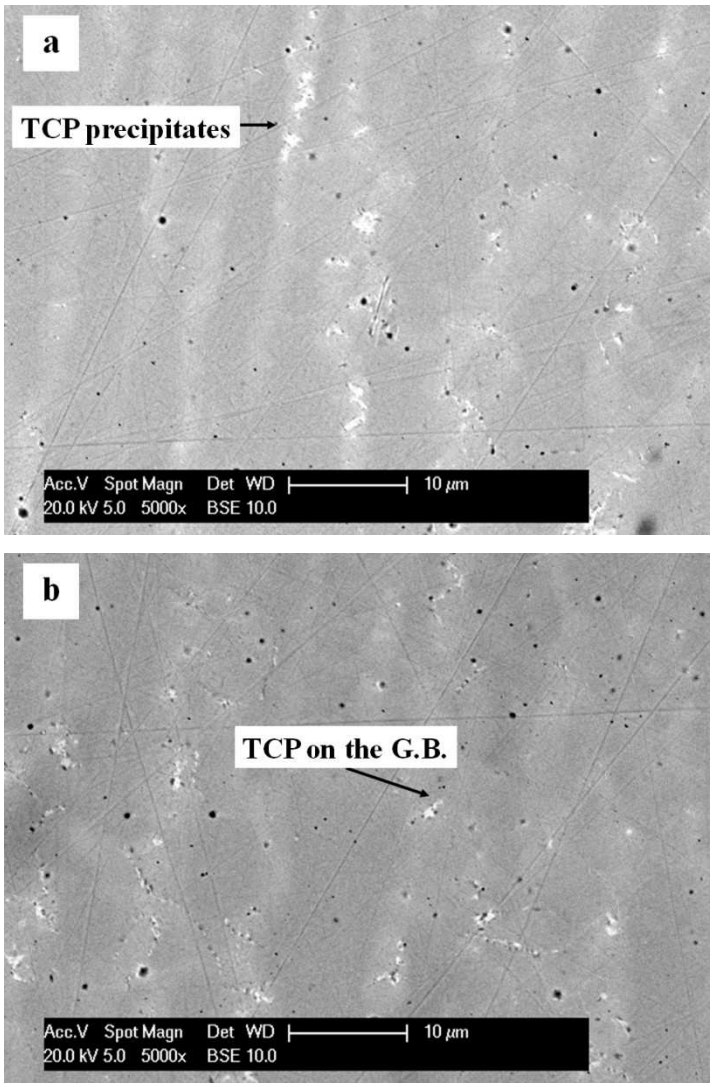

Figure 5-23. Showing different regions in the bulk zone of the WD128 sample in the un-etched condition (a) a BSE micrograph of a region at ~250 µm distant from the interface indicates larger TCP precipitates at interdendritic regions, (b) a BSE micrograph of a region at ~100 µm distant from the interface indicates the smaller TCP precipitates along grain boundaries.

Figure 5-23(a) shows a higher magnification BSE micrograph from a region at ~250 μm distant from the interface and shows the individual bright contrast precipitates (TCP phase) which is similar to the D128 sample (see Figure 5-19(a)). A BSE micrograph from a region at ~100 μm distant from the interface (presented in Figure 5-23(b)) shows some fine bright contrast precipitates (TCP phase) along the grain boundaries which are smaller compared to other regions. Moreover, the acicular bright precipitates did not appear in this sample.

5-4-2- Microstructural evolution in the steel region

As mentioned in chapter 4, there are five regions with different microstructures in the steel region of the as-welded sample. The microstructural evolution in each region is dependent upon the initial microstructure. Three main regions are defined here for investigations of the microstructural changes in the steel region.

The first and the second regions were chosen at ~100 μm and ~500 μm distant from the interface which are in the near-HAZ and the far-HAZ regions respectively. The third region was chosen at a ~1 mm distant from the inner bore of tube which is in the central zone. Different analyses were carried out on the microstructure of these regions to investigate the microstructural evolution in each region. As described in section 5-2, different processes are defined for changes in the microstructure of 2.25Cr1Mo steel region. These processes and related samples are described in the following sections:

1) Tempering of the near-HAZ region is shown by the D1 and the D8 samples microstructure.

2) Soft zone formation is described by presentation of two mid-term thermally exposed samples i.e. the D16 and D32 samples.

3) Re-hardening of the soft zone in the D64 sample and fine grain formation in the D128 sample are shown together.

4) Formation of a network of carbides at the interface with increasing exposure time is shown in the D32, the D64 and the D128 samples.

5-4-2-1- Tempering of the near-HAZ region

Figure 5-24(a1) shows an optical microscope image for the steel region in the D1 sample in the etched condition which is similar to the as-welded sample (see Figure 4-2(b)). Moreover, the locations of the main regions are shown in this image. The optical microscope image of the D8 sample in the etched condition is presented in Figure 5-24(a2). The overall view of the D8 sample in this condition is similar to that of the D1 sample. However there are some white/bright regions adjacent to the interface.

Figure 5-24(b1) and (b2) are SE micrographs from the interfacial region in the D1 and the D8 samples in the etched condition. These images indicate some precipitate free regions adjacent to the interface in the D8 sample. BSE micrographs from the interfacial region of the D1 and the D8 samples in the un-etched condition are shown in Figure 5-24(c1) and (c2) which indicate formation of some fine bright precipitates in the D8 sample.

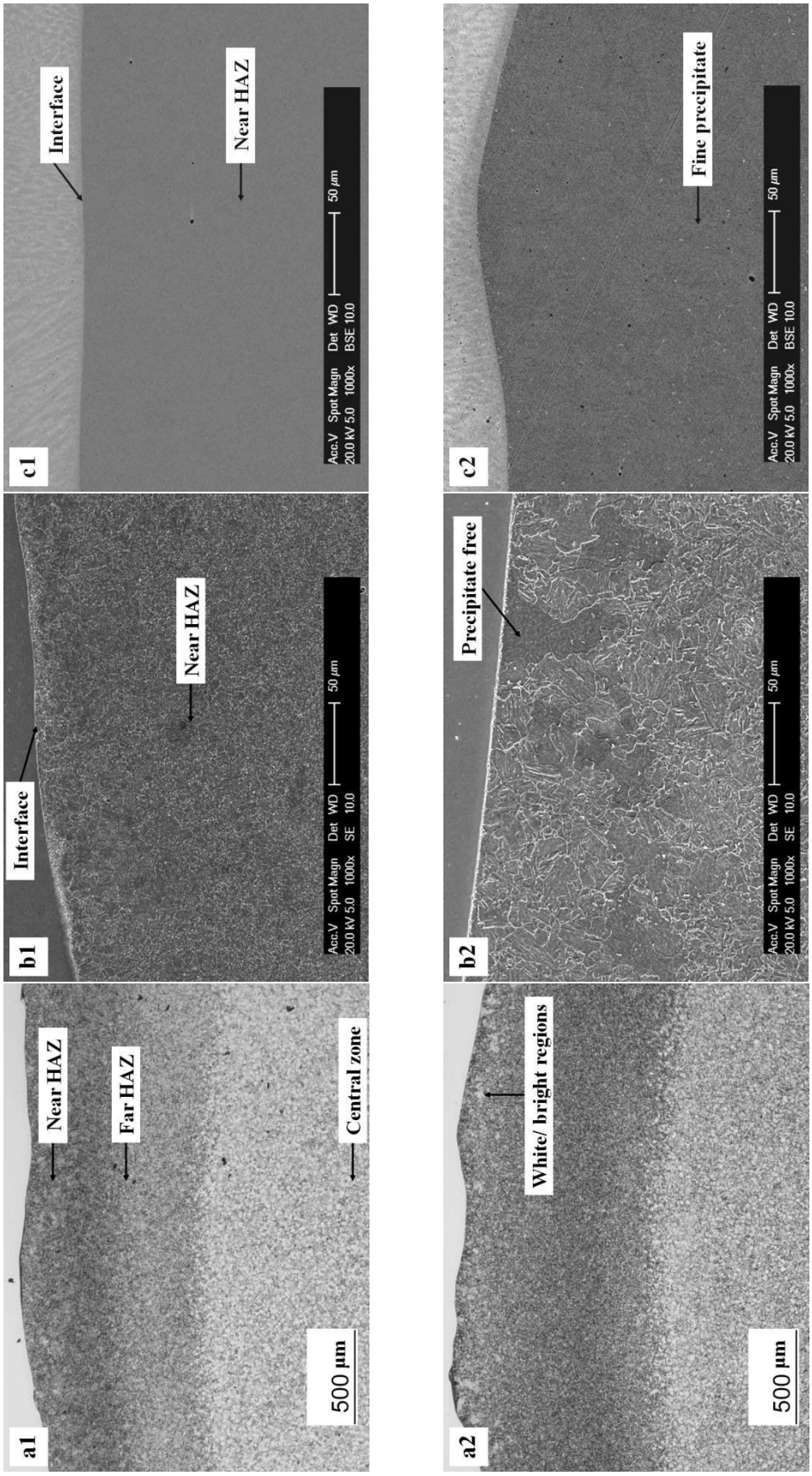

Figure 5-24. Showing different images of the D1 (1) and the D8 (2) samples; (a1, a2) optical microscope images, (b1, b2) SE micrographs indicate the precipitate free regions in the D8 sample and (c1, c2) BSE micrographs in un-etched condition.

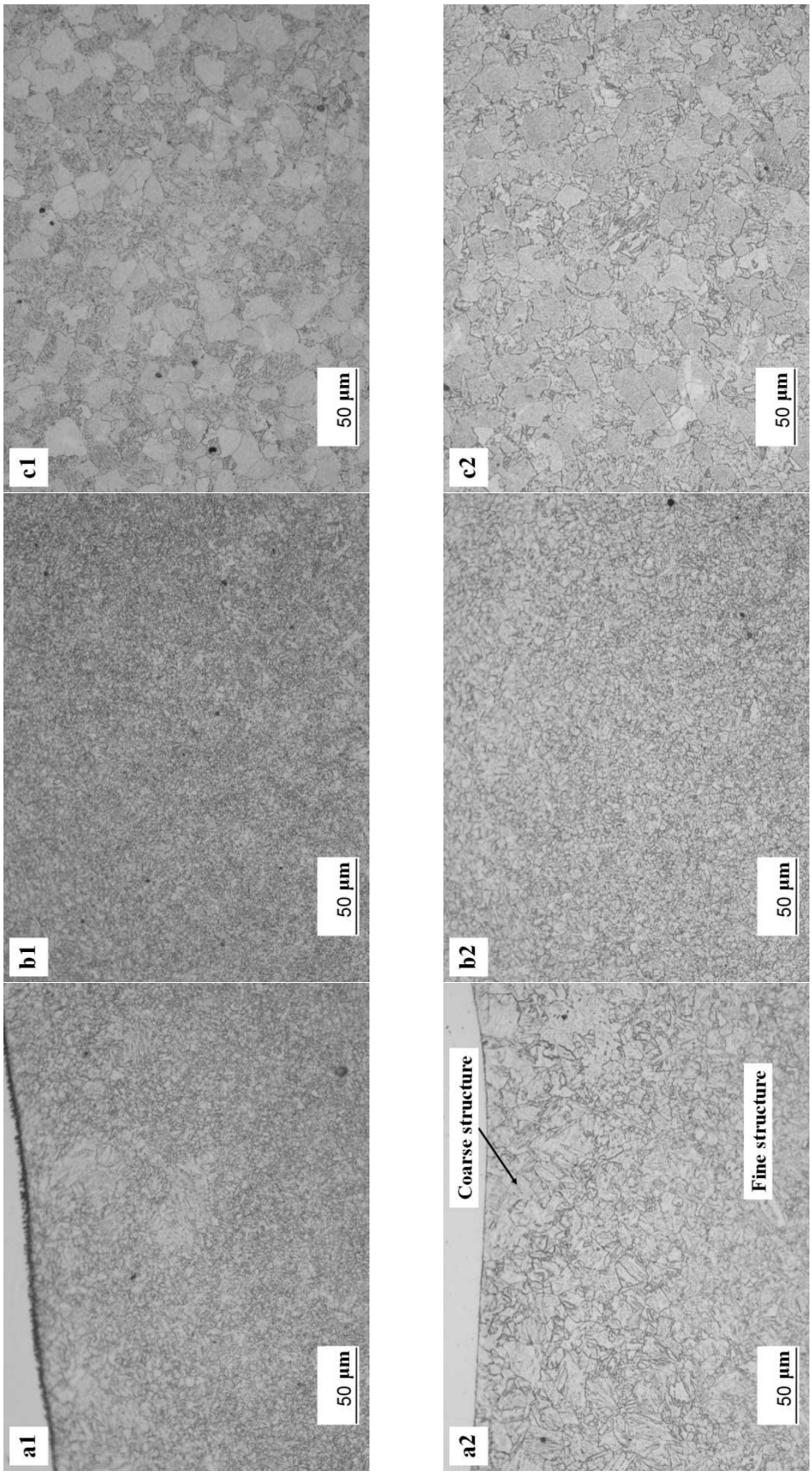

Figure 5-25. Showing higher magnification optical microscope images from the D1 (1) and the D8 (2) samples; (a1, a2) the near-HAZ region microstructure, (b1, b2) microstructure in the far-HAZ region and (c1, c2) bimodal microstructure in the central zone.

Higher magnification optical microscope images of the main regions in both samples are presented in Figure 5-25. The near-HAZ region in the D1 sample is shown in Figure 5-25(a1) and indicates a fine and uniform microstructure in this region. Figure 5-25(a2) shows the same region in the D8 sample which is not uniform, and adjacent to the interface, exhibits a coarser microstructure compared to other regions. The far-HAZ region in the D1 and the D8 samples are presented in Figure 5-25(b1) and (b2) respectively. The fine grains are observed in this region of both samples. Finally, the higher magnification optical microscope images from the central zone of the D1 and the D8 samples are shown in Figure 5-24(c1) and (c2) respectively. The bimodal microstructure (ferrite grains and TM/B) of the central zone is seen in both samples.

SE micrographs of the main regions in the etched condition for these samples are presented in Figure 5-26. Figure 5-26(a1) shows the near-HAZ region microstructure in the D1 sample and indicates uniform tempered structure. The near-HAZ region microstructure in the as-welded sample is shown in Figures 4-6(b) and (c) which exhibits a lath-like structure. After one day exposure at 650˚C, the structure was changed to a tempered structure with fine precipitates. The near-HAZ region in the D8 sample shown in Figure 5-26(a2) indicates larger grains with fine precipitates. Figure 5-26(b1) shows the microstructure of the far-HAZ region in the D1 sample which contains two different types of precipitates named as coarse and fine precipitates. As mentioned in section 4-3-4, in the as-welded sample, the far-HAZ region microstructure is non-uniform with un-dissolved carbides.

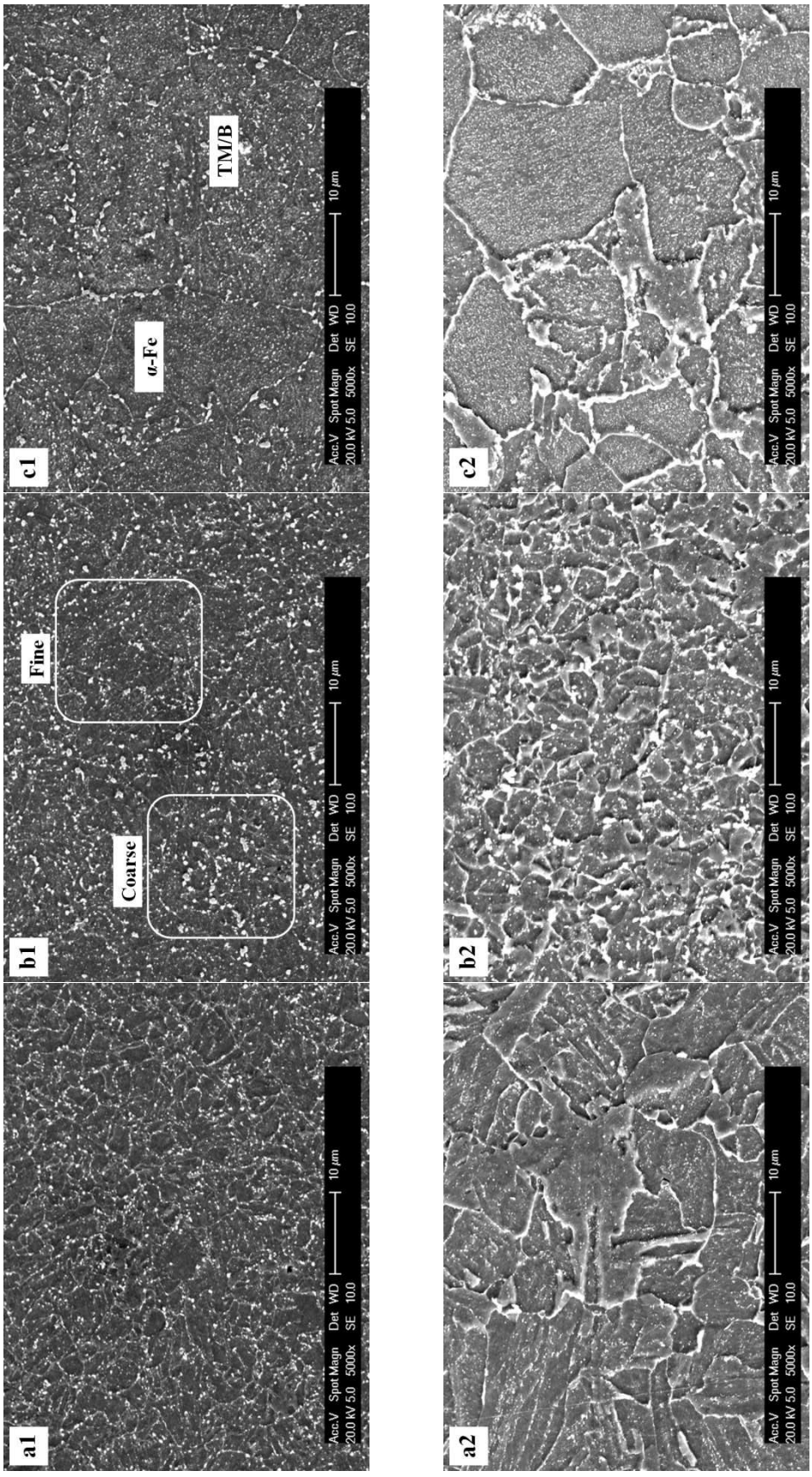

Figure 5-26. Showing higher magnification SE micrographs for different regions in the D1 (1) and the D8 (2) samples; (a1, a2) the near-HAZ region, (b1, b2) the far-HAZ region and (c1, c2) the central zone.

After 1 day exposure, the tempered non-uniform microstructure is observed in the far-HAZ region. Those regions with coarse carbides are related to the former TM/B areas while the fine carbide dispersed in the matrix are related to the former ferrite grains. Figure 5-26(b2) shows a SE micrograph from the far-HAZ region in the D8 sample and indicates fine grains in this region. Moreover, some carbides in this sample are coarser than to those observed in the D1 sample. The microstructural evolution in the far-HAZ region is carbide coarsening between the ferrite fine grains.

SE micrographs of the central zone in the D1 and the D8 samples are presented in Figure 5-26(c1) and (c2) which are similar to the as-welded sample. The bimodal microstructure is visible in these samples. However, the grain boundaries are more distinct in the D8 sample compared to those of the D1 sample. Moreover, some fine precipitates are seen within the ferrite grains in the D8 sample.

Higher magnification BSE micrographs of the near-HAZ region in the D1 and the D8 samples are shown in Figure 5-27(a1) and (a2). There are a few bright acicular precipitates in the D8 sample. Figure 5-27(b1) shows a BSE micrograph of the far-HAZ region in the D1 sample and there are some regions where a few fine round precipitates are present which shows non-uniform precipitation in the far-HAZ region after a day exposure. Figure 5-27(b2) shows the far-HAZ region in the D8 sample and there are more and coarser bright precipitates compared to the D1 sample. The BSE micrographs of the central zone in these samples are presented in Figure 5-27(c1) and (c2) and show some precipitates on the ferrite grain boundaries in the D8 sample.

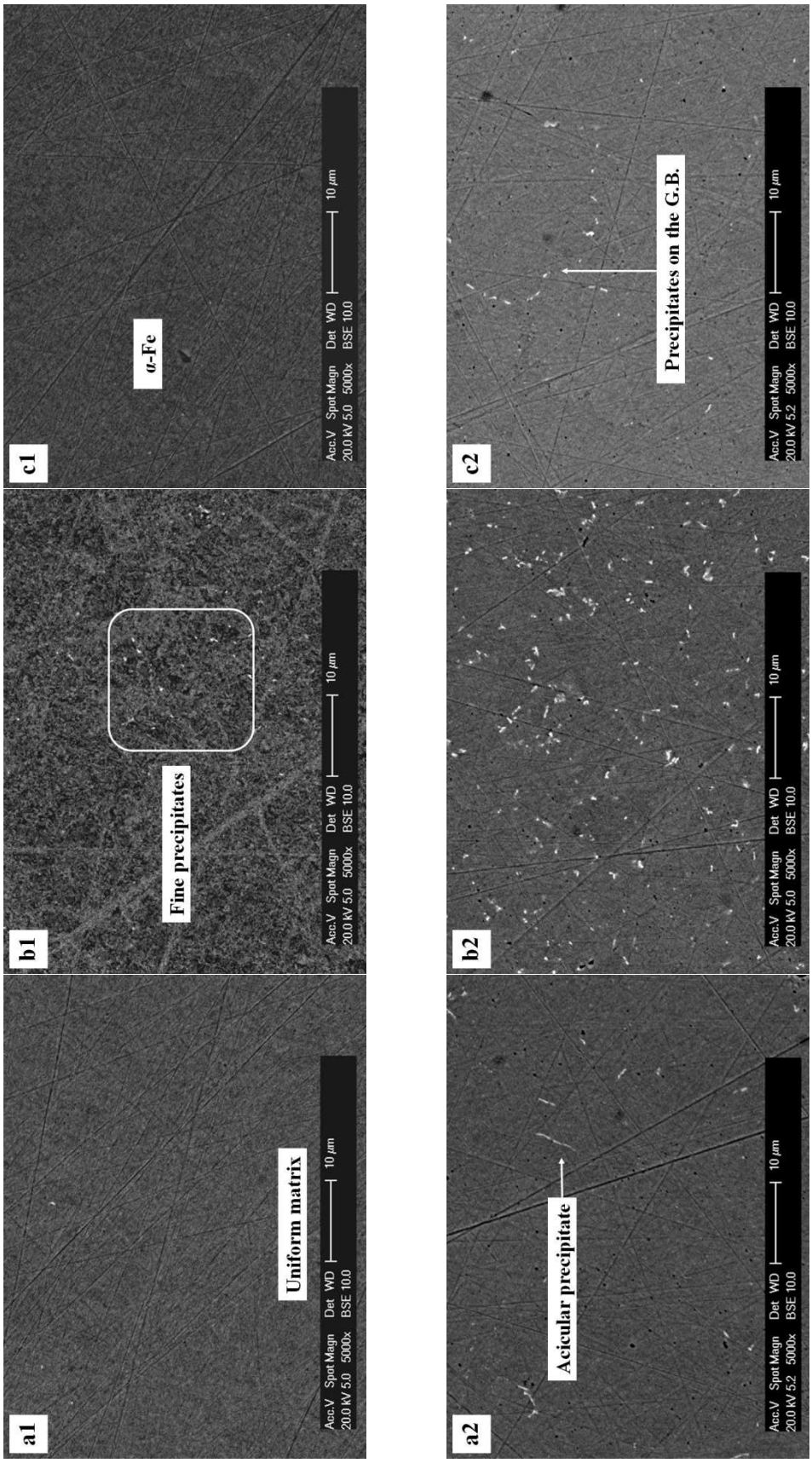

Figure 5-27. Showing higher magnification BSE micrographs for different regions in the D1 (1) and the D8 (2) samples; (a1, a2) the near-HAZ region, (b1, b2) precipitates in the far-HAZ regions and (c1, c2) fine precipitates on the grain boundaries in the central zone of D8 sample.

5-4-2-2- Formation of soft zone

Microstructural analysis of thermally exposed samples reveals that after 12 days exposure, a soft zone with low hardness and a large grain structure has formed adjacent to the interface. A soft zone was observed in samples aged up to 32 days. In this section only the microstructures of the D16 and the D32 samples are presented. Figure 5-28(a1) shows an optical microscope image of the interfacial region in the D16 sample in the etched condition where a white zone ~300 μm wide is seen adjacent to the interface. Based on the hardness test results (see section 5-3), this region has lower hardness values compared to the other regions. The optical microscope image of the D32 sample in the etched condition is shown in Figure 5-28(a2) which is similar to that of the D16 sample.

Figure 5-28(b1) and (b2) show SE micrographs of the interfacial region in the etched condition in these samples and indicate large grain structures with fine precipitates. The soft zone in the D32 sample contains fewer and coarser precipitates in the interfacial region compared to those of the D16 sample. BSE micrographs of these samples in the un-etched condition shown in Figure 5-28(c1) and (c2), revealed a noticeable change in the microstructure. The D16 sample microstructure is similar to the D8 sample. However, in the D32 sample some bright precipitates are visible which are non-uniformly distributed in the near-HAZ region. The Mo-rich phase (possibly M_6C carbide) has a higher mean atomic number compared to that of the matrix (Fe). Therefore bright precipitates can be attributed to the formation of the Mo-rich carbide precipitates.

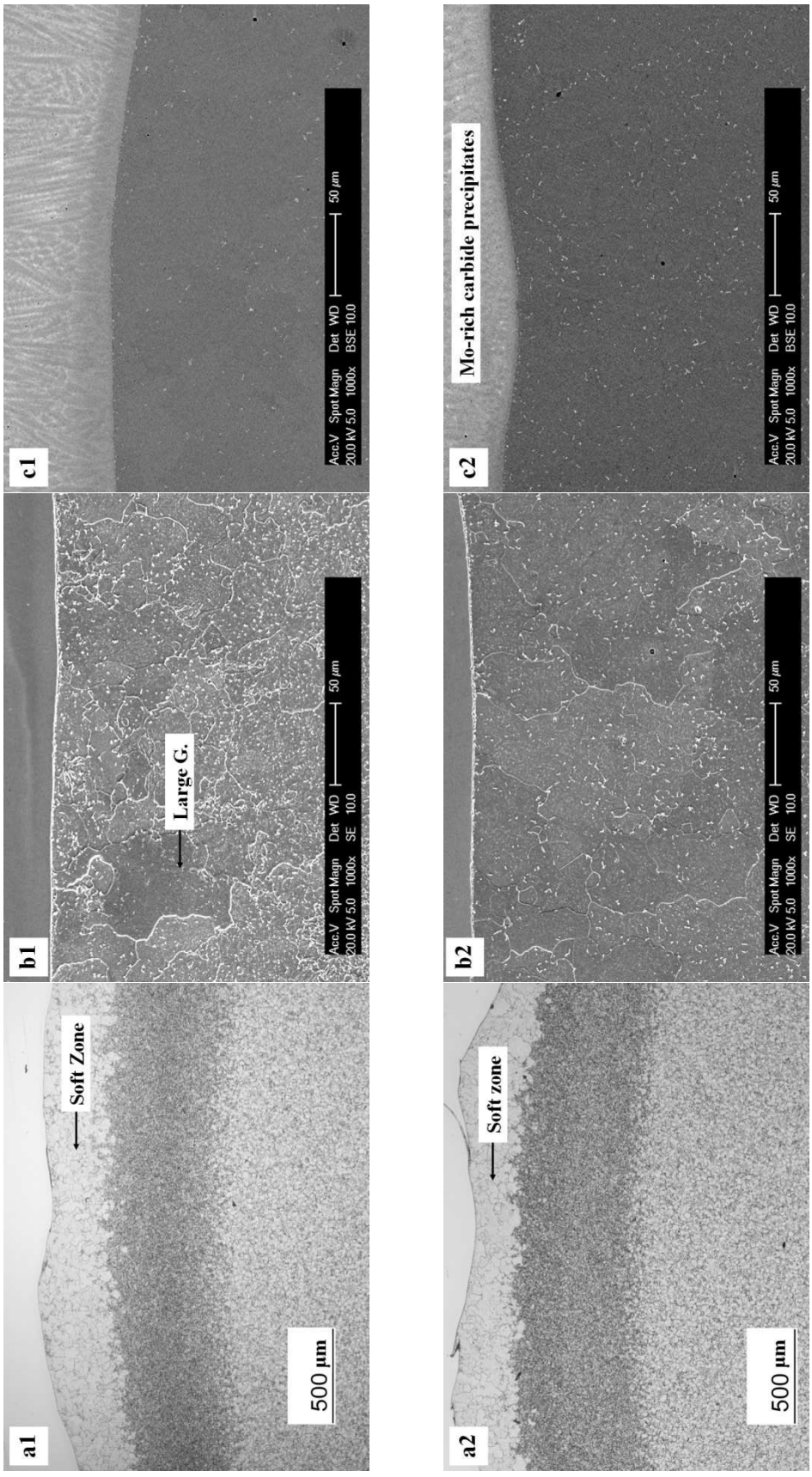

Figure 5-28. Showing different images of the D16 (1) and the D32 (2) samples; (a1, a2) optical microscope images indicate the soft zone, (b1, b2) SE micrographs indicate the large grains in the soft zone and (c1, c2) BSE micrographs indicate fine bright Mo-rich carbide precipitates in the D32 sample.

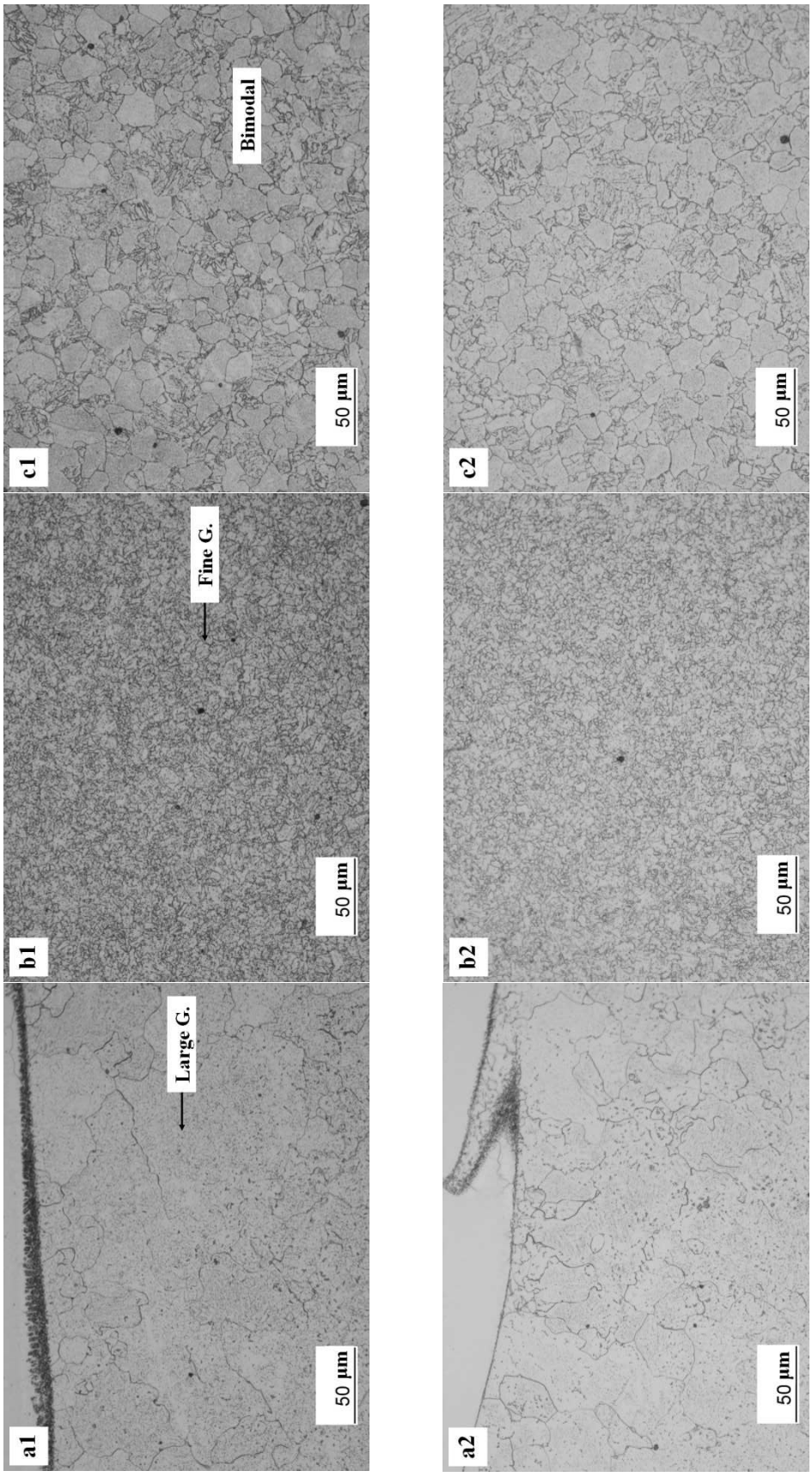

Figure 5-29. Showing higher magnification optical microscope images from different regions in the D16 (1) and D32 (2) samples in the etched condition; (a1, a2) show the soft zone adjacent to the interface, (b1, b2) indicate fine grains in the far-HAZ region and (c1, c2) the bimodal microstructure in the central zone.

Higher magnification optical microscope images of the D16 and the D32 samples are presented in Figure 5-29. The soft zones in these samples are shown in Figure 5-29(a1) and (a2) which are seen to contain large grains (up to several hundred microns in size). The microstructures of the far-HAZ region are presented in Figure 5-24(b1) and (b2). The grain size in this region is less than 10 μm and its microstructure is similar to that of the D8 sample. The bimodal microstructure in the central zone of these samples is shown in Figure 5-29(c1) and (c2) respectively.

SE images of the D16 and the D32 samples in the etched condition are shown in Figure 5-30. SE micrographs of the soft zones in these samples are presented in Figure 5-30(a1) and (a2) which show some fine precipitates uniformly dispersed within the large grains. There are some coarse precipitates in this region too. Grain boundaries in these samples are not delineated by precipitates. There are more coarse precipitates in the D32 than in the D16 sample. Moreover, the coarse precipitates are dispersed more uniformly on the grain boundaries and within the grains in the D32 sample.

The far-HAZ region microstructures of these samples are presented in Figure 5-30(b1) and (b2) respectively. It seems that these images are similar to that of the D8 sample and contain fine grains and some precipitates. Figure 5-30(c1) and (c2) show the microstructure of the central zone in these samples. The bimodal microstructure is clearly seen in these images too. However, the precipitates on the ferrite grain boundaries are coarser in the D32 sample compared to those in the D16 sample. Moreover, fine precipitates within the ferrite grains are fewer and coarser in the D32 sample.

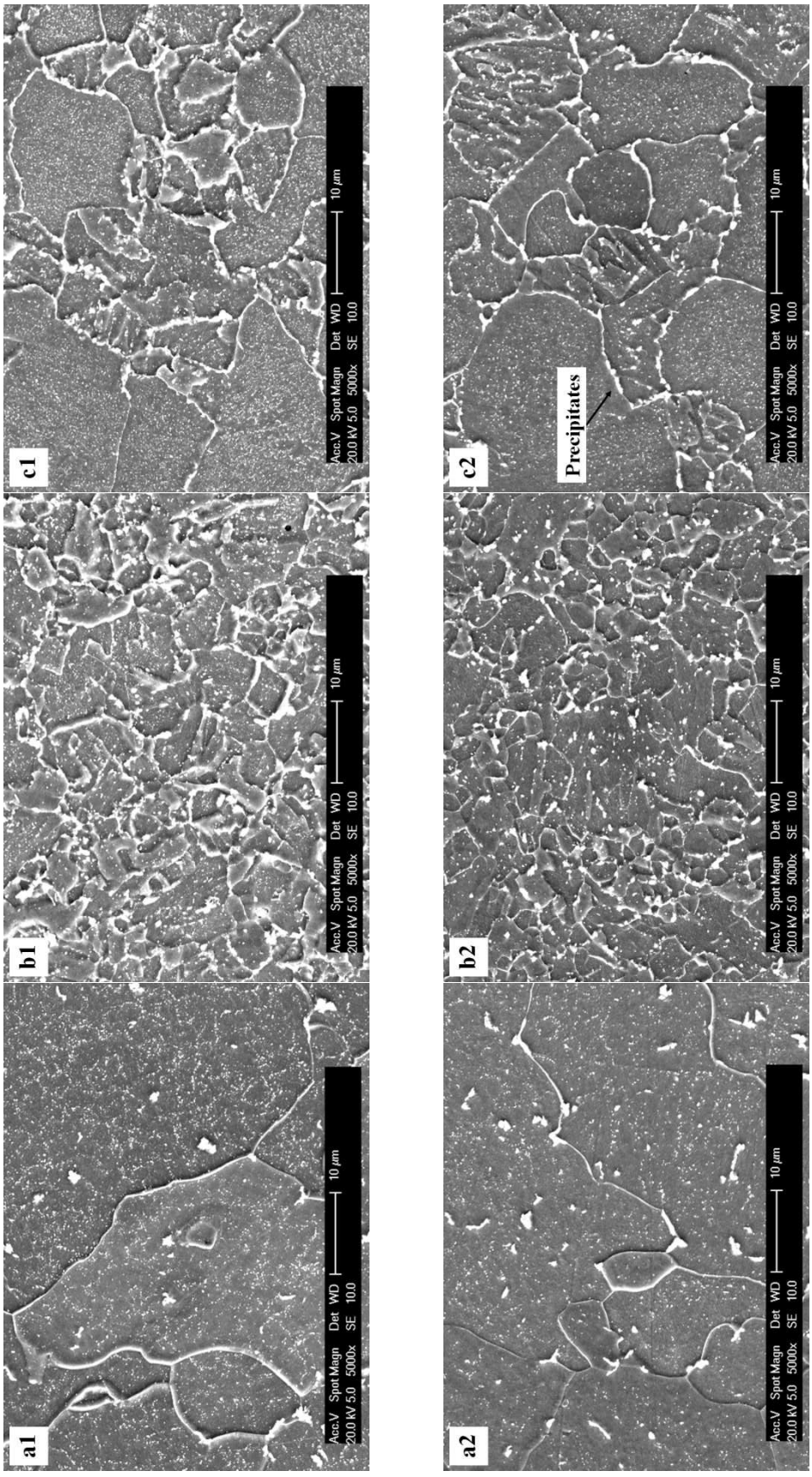

Figure 5-30. Showing higher magnification SE micrographs from different regions in the D16 (1) and the D32 (2) samples in the etched condition; (a1, a2) precipitates in the near-HAZ region, (b1, b2) microstructure in the far-HAZ region and (c1, c2) precipitates on ferrite grain boundaries in the central zone.

BSE micrographs of the soft zone in the D16 and D32 samples are shown in Figure 5-31(a1) and (a2). As seen, there are more bright precipitates and fewer dark precipitates in the D32 sample compared to those of the D16 sample. A comparison between the D8 sample (see Figure 5-27(a2)) and the D32 sample (see Figure 5-31(a2)) shows that number and size of bright precipitates increases with increasing exposure time. These elongated precipitates in the near-HAZ region have higher mean atomic number compared to the matrix. This indicates that Mo-rich precipitates (possibly M_6C carbides) have grown in the near-HAZ after 32 days exposure. The distribution of these precipitates is not uniform in the matrix. In contrast, the dark precipitates in the D32 sample are fewer compared to those in the D16 sample. This indicates that other types of carbides i.e. (Fe and/or Cr) carbides were dissolved in the matrix with increasing exposure time.

Figure 5-31(b1) and (b2) show BSE micrographs of the far-HAZ regions in these samples. Two different types of precipitates (bright and dark) are present in these images. There is no significant difference between these micrographs. It seems that the far-HAZ region microstructure did not change significantly with increasing exposure time up to 32 days. The morphology of the bright precipitates in the far-HAZ region is different compared to that of the near-HAZ region in both samples. The size of elongated particles is up to several microns in the near-HAZ region while in the far-HAZ region blocky precipitates are very smaller in size. It seems that the fine precipitates in the far-HAZ region did not grow with increasing exposure time, as their quantity and size in the D32 sample is similar to those in the D16 sample.

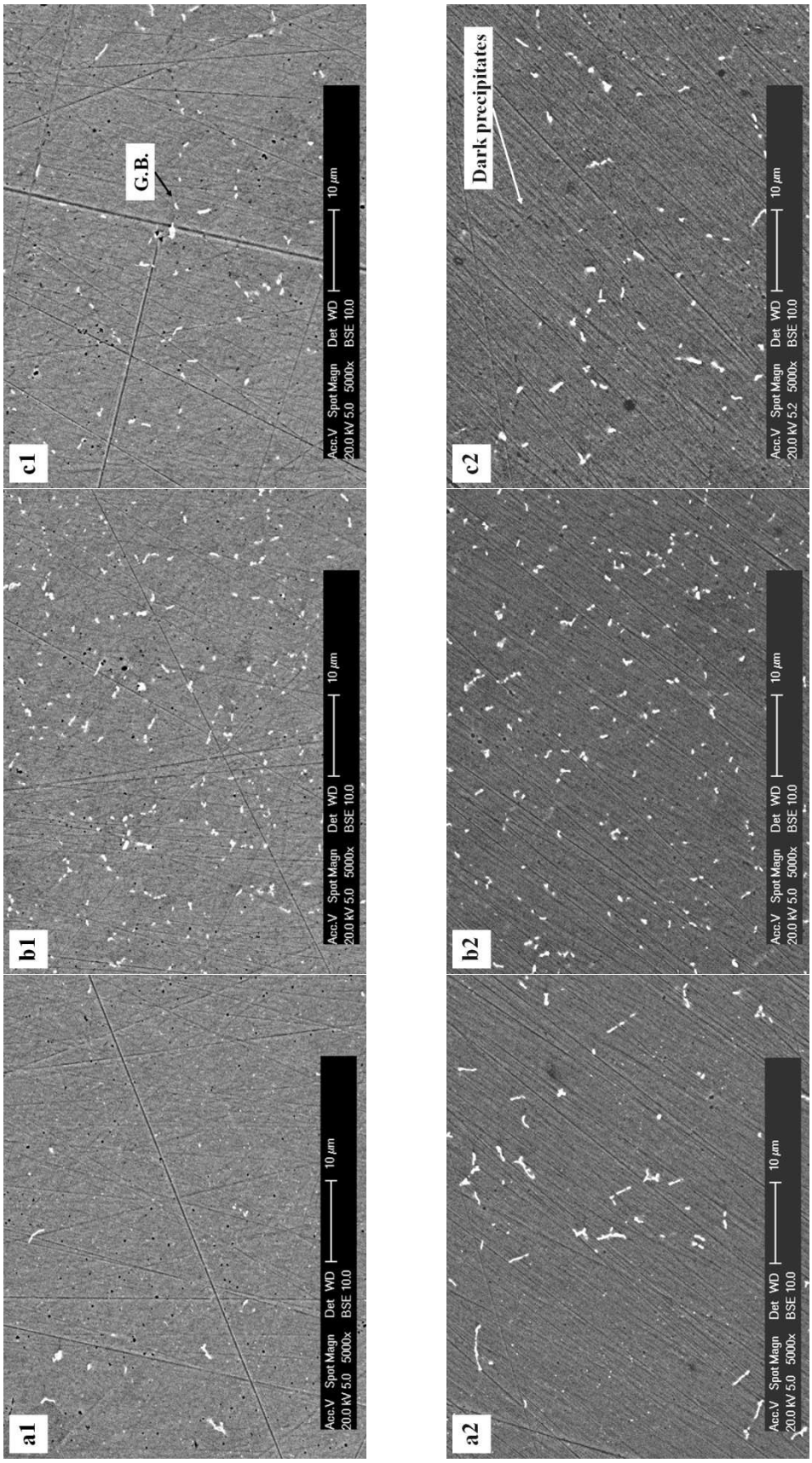

Figure 5-31. Showing higher magnification BSE micrographs from different regions in the D16 (1) and the D32 (2) samples; (a1, a2) precipitates in the near-HAZ region, (b1, b2) indicate similar microstructure in the far-HAZ region and (c1, c2) dark precipitates on the ferrite grain boundaries.

Finally, BSE micrographs of the central zone in these samples are seen in Figure 5-31(c1) and (c2). It seems that some bright precipitates (possibly Mo-rich M_6C carbide) and some dark precipitates (possibly Fe/Cr-rich carbides) are present along the ferrite grain boundaries in both samples. However, these precipitates in the D32 sample are coarser compared to those of the D16 sample.

Further investigations were carried out on the D16 sample using EPMA to examine the differences between the near-HAZ and the far-HAZ regions. The elemental colour maps for these regions are presented in Figure 5-32. It should be noted that the average of Cr and Mo in both regions are in the same level. The Cr distribution in the soft zone is more uniform compared to that of the far-HAZ region (see Figure 5-32(a1) and (a2)). However, the Mo map in the far-HAZ region (see Figure 5-32(b2)) shows highly concentrated regions while in the soft zone (see Figure 5-32(b1)), the Mo concentration is almost uniform. The C maps for both points are presented in Figure 5-32(c1) and (c2) and do not show any significant features due to its low concentration.

The elemental maps for the alloying elements indicate that Cr and Mo in the far-HAZ region are concentrated in the precipitates. These maps confirm that Mo-rich precipitates (possibly M_6C carbide) are present in the far-HAZ region of the D16 sample. However, considering the fully Tγ structure in the near-HAZ region of the as-welded sample, the uniform Cr and Mo maps in the soft zone of the D16 sample must be related to smaller precipitates after tempering in this region. In other words, it is suggested that these did not grow significantly even after 16 days exposure.

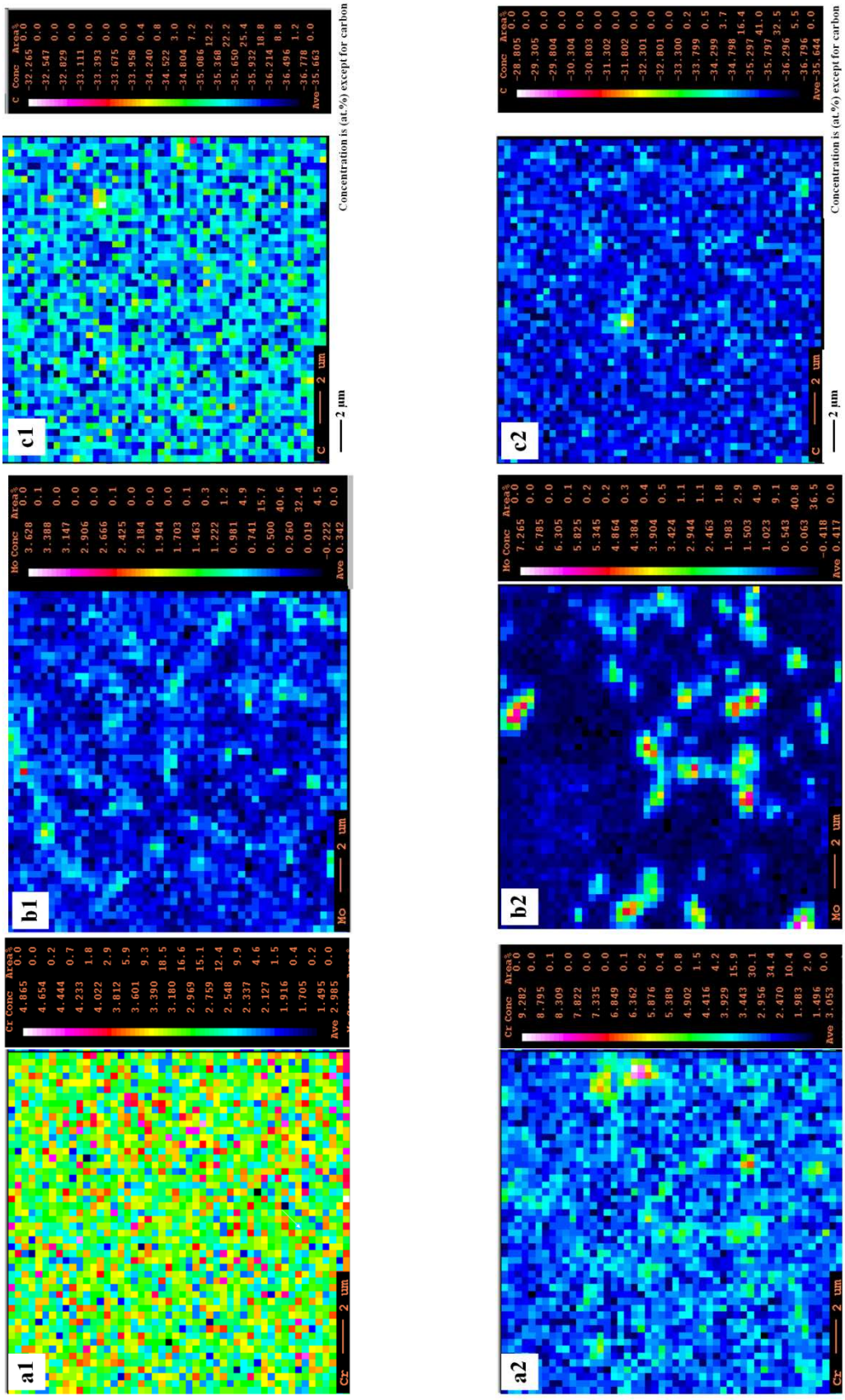

Figure 5-32. Showing EPMA elemental colour maps for alloying elements in the near-HAZ region (1) and the far-HAZ region (2) of the D16 sample; (a1, a2) relatively uniform Cr distribution in both regions, (b1, b2) Mo-rich points in the far-HAZ region and (c1, c2) the C distribution maps which are not valid due to negative concentrations.

EDX analyses were performed on the different precipitates in the interfacial region of the D32 sample and the results are presented in Figure 5-33(a). As seen in this image, two different precipitates are present in this region. There are some Mo-rich precipitates in the near-HAZ region (soft zone) and some (Cr, Mo)-rich precipitates adjacent to the interface. Figure 5-33(b) shows EDX results in the far-HAZ region and shows there are some (Cr)-rich precipitates in this region, in addition to (Mo)-rich precipitates.

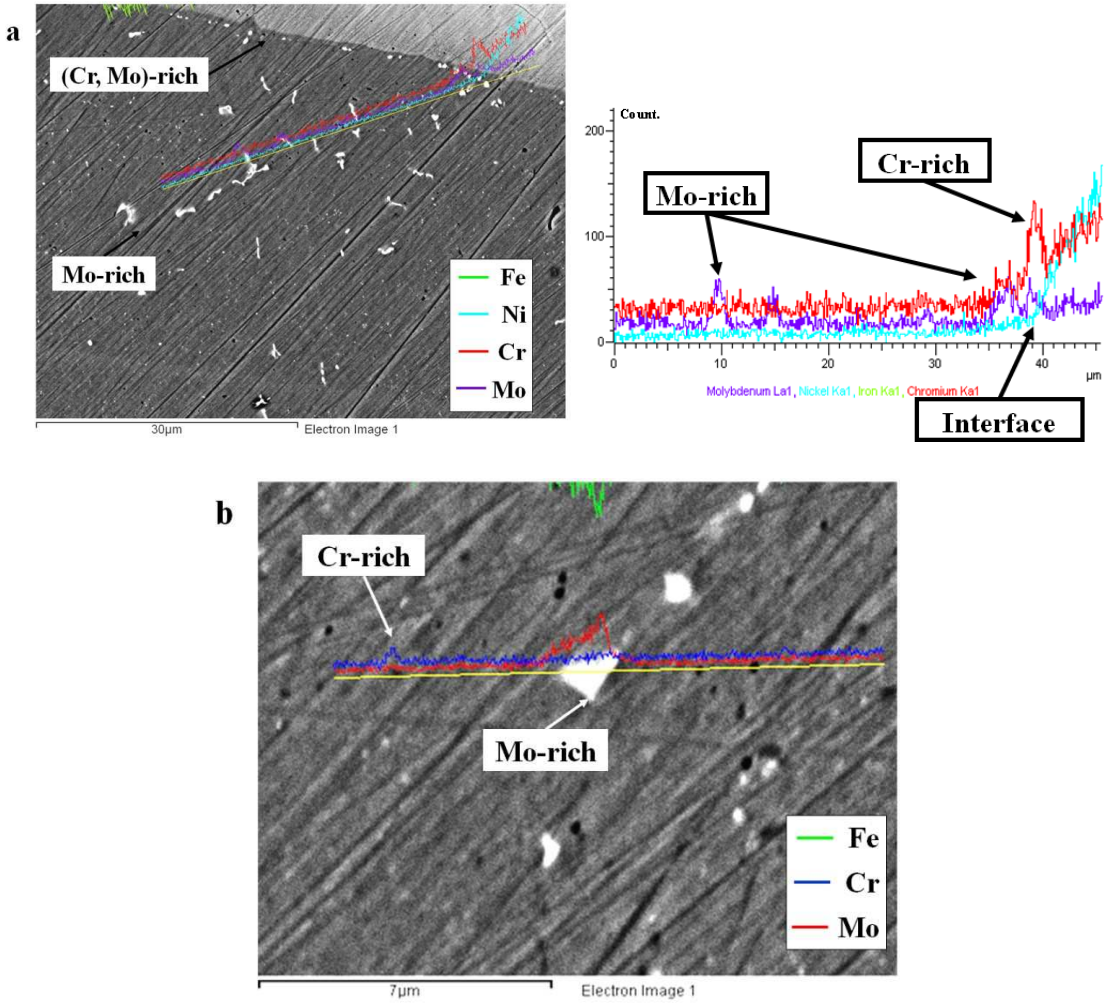

Figure 5-33. Showing EDX analysis results in different regions of the D32 sample; (a) the Mo-rich elongated precipitates in the near-HAZ region (soft zone) and (Cr, Mo)-rich precipitates adjacent to the interface which is shown in higher magnification too, (b) the Mo-rich and the Cr-rich precipitates in the far-HAZ region.

Further investigations were carried out on the D32 sample using EBSD in the Oxford Instrument laboratory. The small grains in the far-HAZ region and TM/B areas in the central zone can be easily observed with this process. The large grains in the near-HAZ region (soft zone) and the fine grains in the far-HAZ region are shown in Figure 5-34(a) and (b). The central zone is shown in Figure 5-34(c) which indicates ferrite sub grains in the TM/B areas.

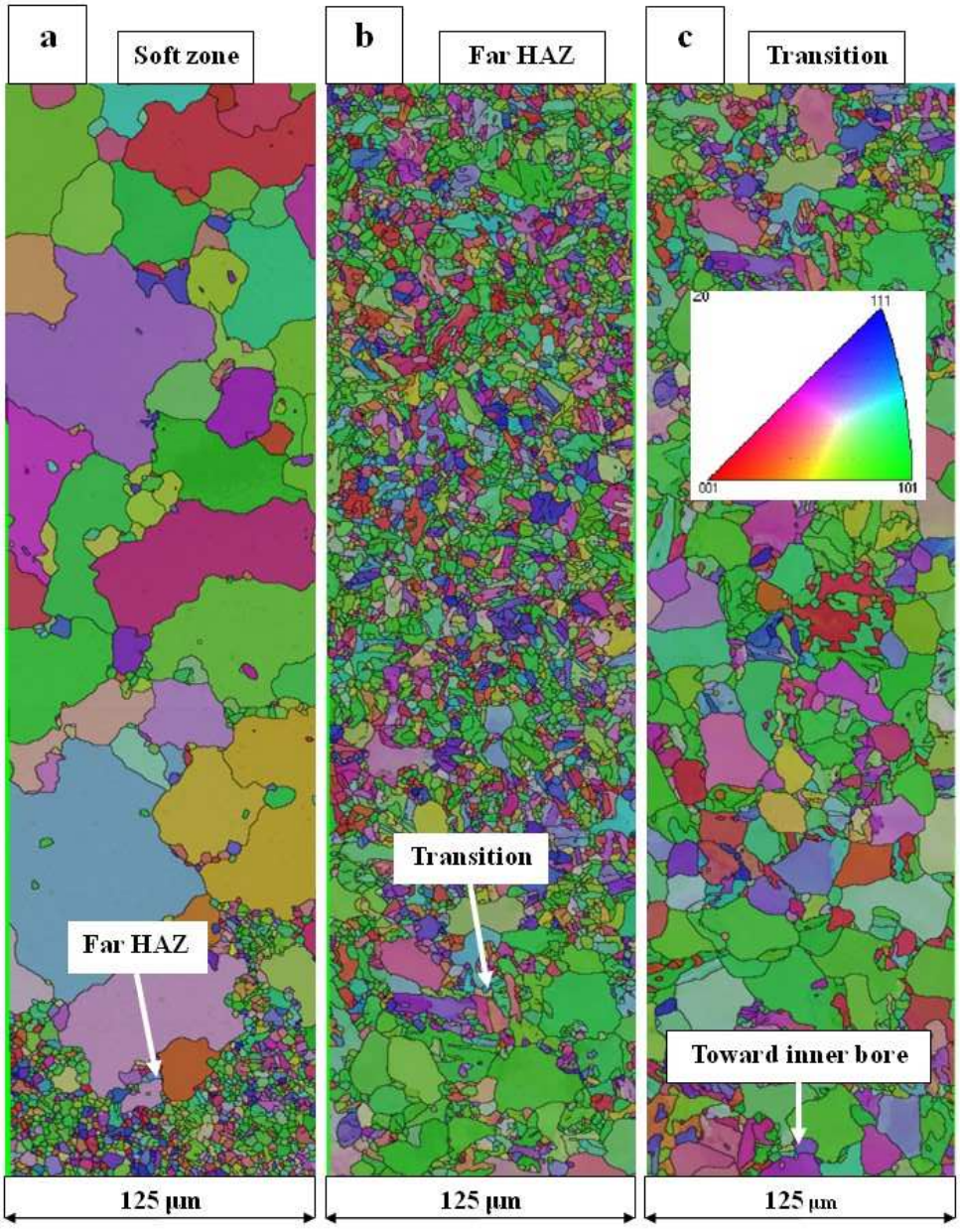

Figure 5-34. Showing EBSD results for the D32 sample indicates; (a) large grains in the soft zone (b) fine grains in the far-HAZ region and (c) ferrite sub grains in TM/B areas.

5-4-2-3- Re-hardening and fine grain formation in the near-HAZ region

Microstructural investigations were carried out on the D64 and the D128 samples and the results are presented in this section. Based on the hardness test results shown in Figure 5-7(b), these samples have a similar hardness profile. As mentioned in section 5-3, the soft zone which was formed in the near-HAZ region in the mid-term thermally exposed sample was found to be re-hardened in the D64 sample. Moreover, a little change was observed in the D128 sample hardness compared to that of the D64 sample. This fact is related to some changes in the microstructure which are shown schematically in Figure 5-3.

The overall view images from the interfacial region in these samples are shown in Figure 5-35. The optical microscope image of the interfacial region in the D64 sample is presented in Figure 5-35(a1). As seen, the microstructure in this sample is similar to that of the mid-term thermally exposed samples (see Figure 5-28(a1) and (a2)). Although the hardness values of this region are significantly increased, large grains are still seen in this image.

The optical microscope image of the interfacial region in the D128 sample is shown in Figure 5-35(a2) and revealed a significant change in the microstructure. As observed, the large ferrite grains were not seen in the near-HAZ region after a long term thermal exposure which is a very unusual. SE micrographs of the interfacial region in the etched condition in both samples are shown in Figure 5-35(b1) and (b2) respectively.

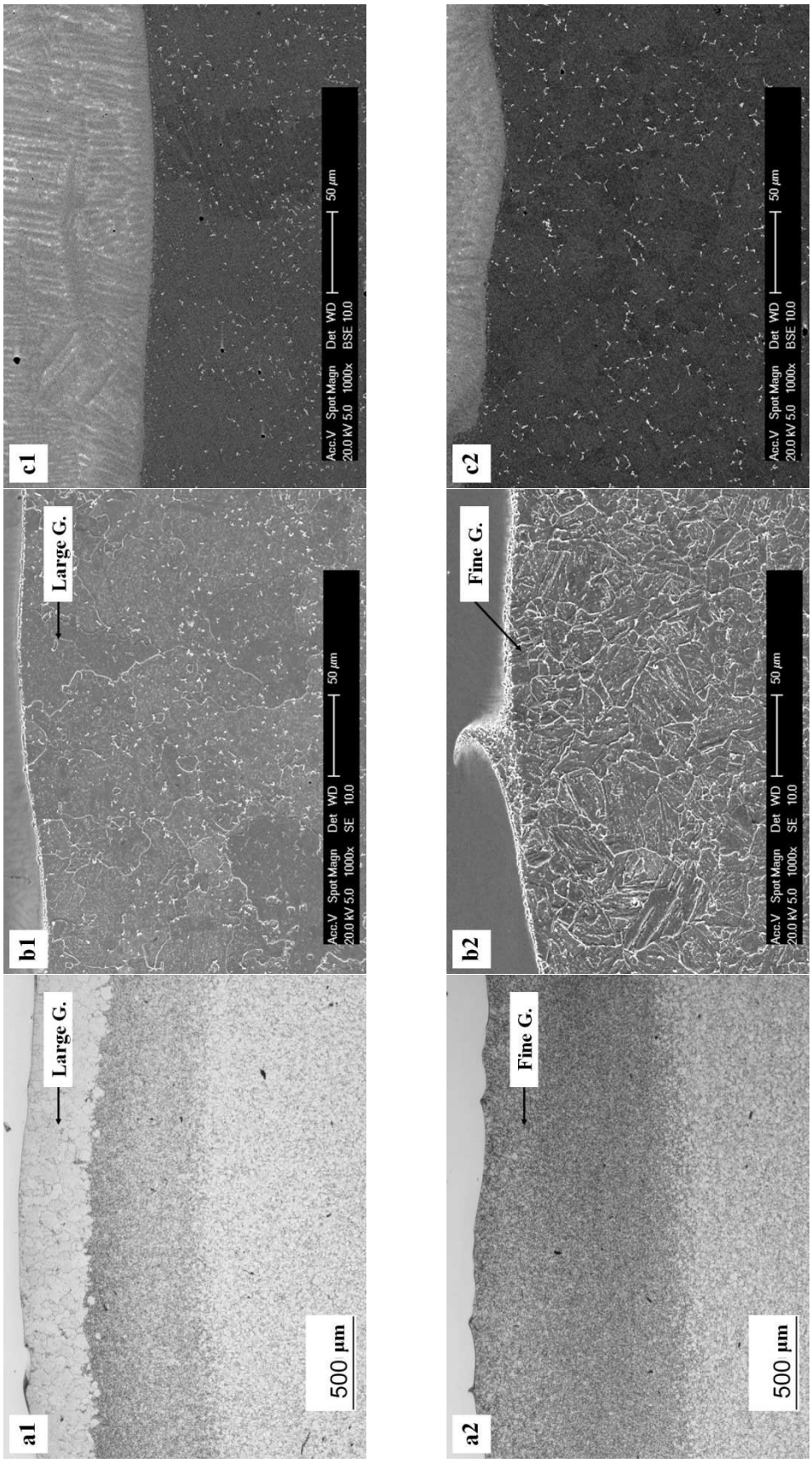

Figure 5-35. Showing different images of the D64 (1) and the D128 (2) samples; (a1, a2) optical microscope images indicate significant change in the near-HAZ region, (b1, b2) SE micrographs indicate the grain size changing and (c1, c2) BSE micrographs indicate different morphologies for bright precipitates in the near-HAZ region.

The SE micrograph of the D64 sample in the etched condition contains large grains with some coarse and fine precipitates dispersed in the matrix. However, the interfacial region in the D128 sample (see Figure 5-35(b2)) is similar to the tempered structure of the D8 sample (see Figure 5-24(b2)). In other words, the D128 sample microstructure contains fine grains and some precipitates.

The BSE micrograph of the interfacial region of the D64 sample is presented in Figure 5-35(c1) and is similar to that of the D32 sample (see Figure 5-28(c2)). As previously shown, the Mo-rich precipitates (possibly M_6C carbide) are present in the matrix. However, the morphology of these precipitates in the D64 sample is different compared to those of the D32 sample. Moreover, the population and size of these precipitates did not increase significantly. The BSE micrograph of the interfacial region in the D128 sample in the un-etched condition contains Mo-rich precipitates (see Figure 5-35(c2)). However, their morphology and distribution are significantly different compared to those of the D64 sample.

Figure 5-36 shows higher magnification optical microscope images of the main regions in these samples in the etched condition. It seems that all images of the D64 sample presented in Figure 5-36 (a1), (b1) and (c1) are similar to those of the mid-term thermally exposed samples. Nevertheless, higher magnification optical microscope image of the near-HAZ region in the D128 sample (see Figure 5-36(a2)) shows a very unusual feature. It is seen that grain size in this region is less than 10 μm which are very smaller compared to that of the D64 sample. (i.e. there has been a substantial grain size reduction)

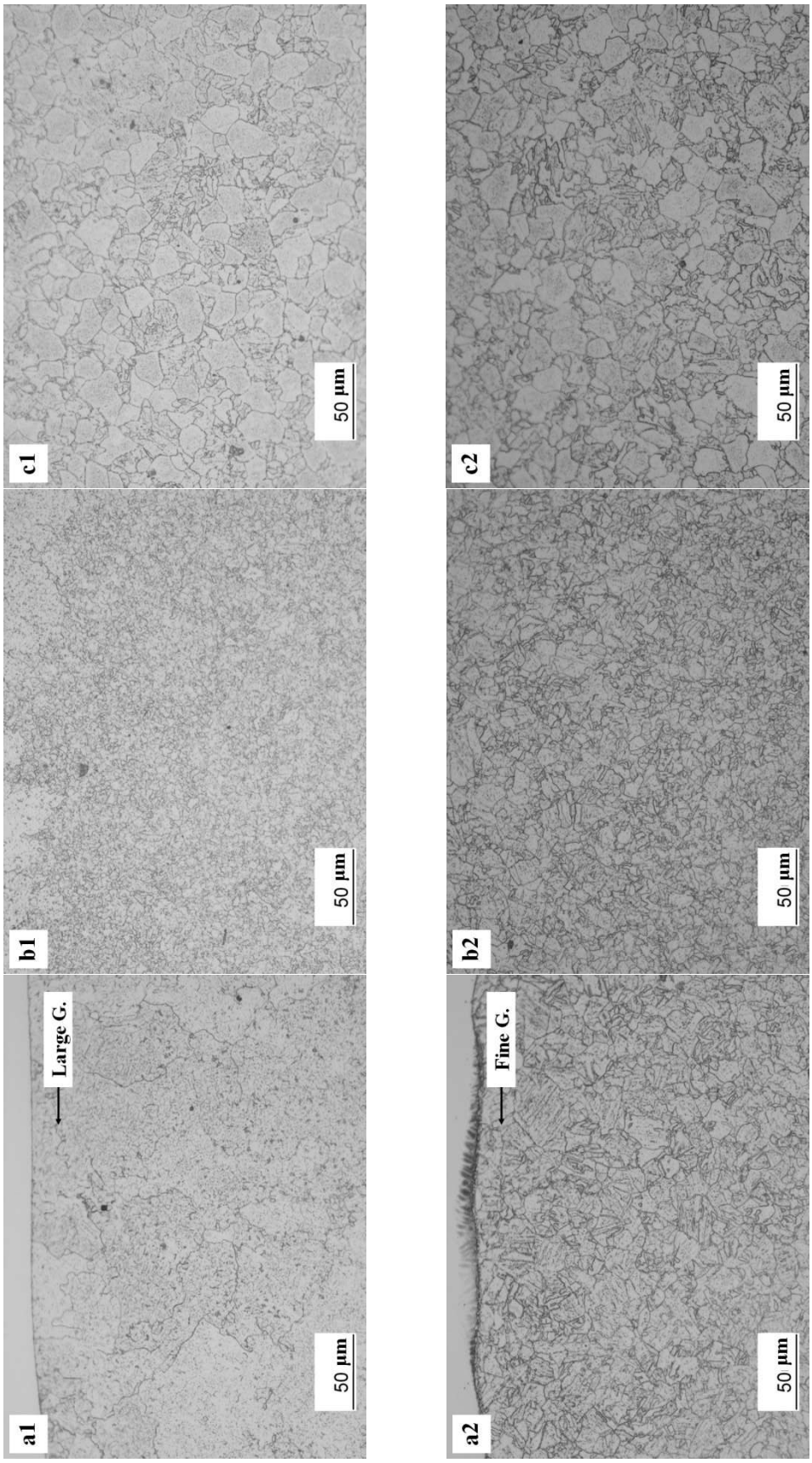

Figure 5-36. Showing higher magnification optical microscope images from different regions in the D64 (1) and D128 (2) samples in the etched condition; (a1, a2) indicate the grain size reduction in the near-HAZ region, (b1, b2) indicate similar far-HAZ regions and (c1, c2) indicate the bimodal microstructure in the central zone.

Figure 5-36(b2) and (c2) show the far-HAZ region and the central zone microstructures in the D128 sample respectively. There is no significant difference between these images and those of the mid-term thermally exposed samples. It is suggested that the bimodal microstructure remained largely unchanged during these later stages of thermal exposure up to 128 days.

High magnification SE micrographs of the main regions in the etched condition are presented in Figure 5-37. The first row shows the D64 sample micrographs and they did not reveal any significant difference compared to those of the D32 sample (see Figure 5-30(a2), (b2) and (c2)). The near-HAZ region microstructure (see Figure 5-37(a1)) contains large grains with some coarse and fine precipitates which are dispersed in the matrix. The far-HAZ region microstructure is presented in Figure 5-37(b1) and shows fine grains. Finally, the central zone microstructure is shown in Figure 5-37(c1) which exhibits the bimodal microstructure. However, there are fewer and coarser precipitates within the ferrite grains and larger precipitates along grain boundaries in this sample compared to the D32 sample.

High magnification SE micrographs from the different regions of the D128 sample in the etched condition are presented in Figure 5-37(a2), (b2) and (c2). The near-HAZ region microstructure is shown in Figure 5-37(a2) and contains fine grains with some precipitates. This structure is similar to tempered structure of the D8 sample (see Figure 5-27(a2)). There are no significant differences between this sample and the D64 sample regarding the microstructure of other regions. However, precipitates in the central zone have grown with increasing exposure time.

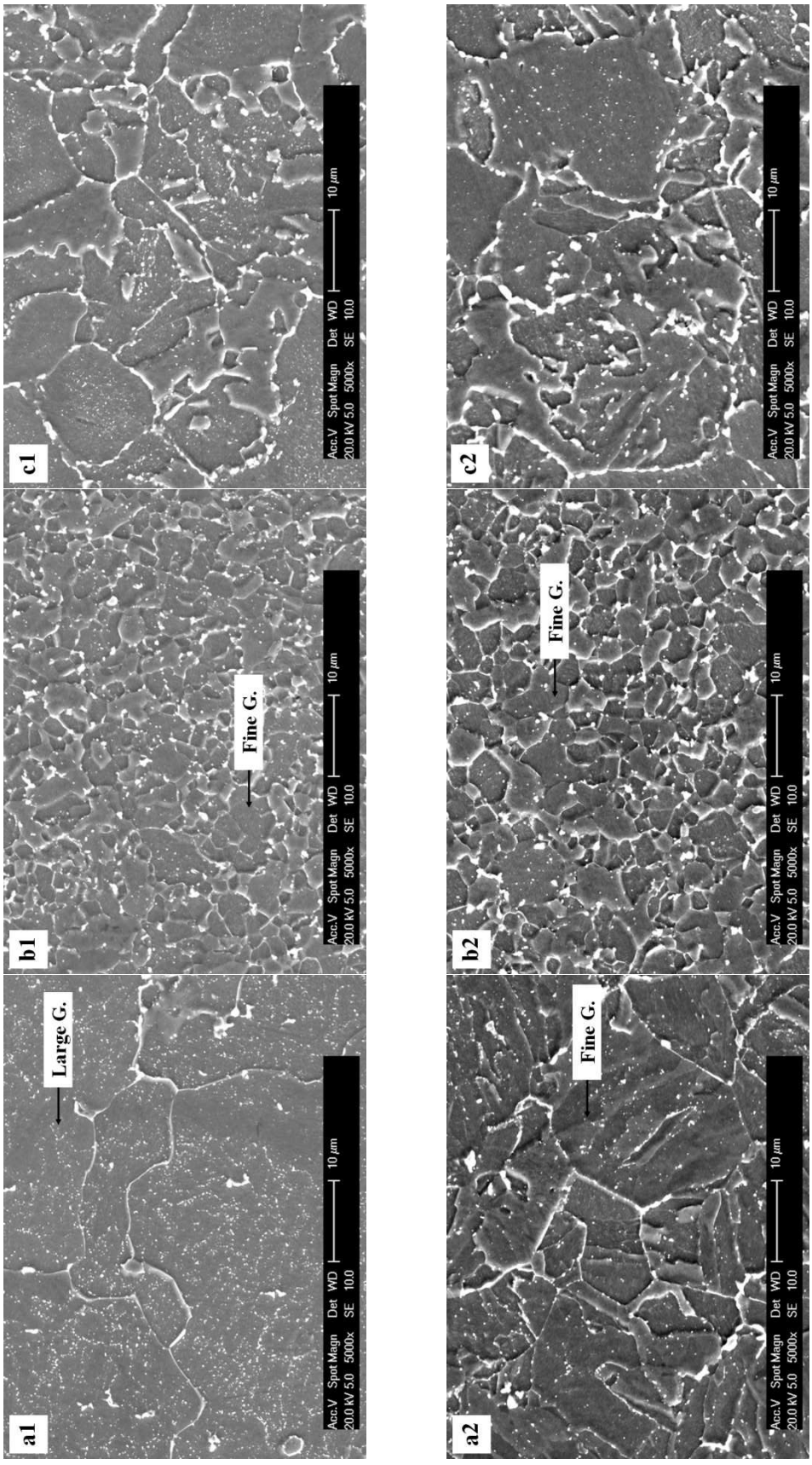

Figure 5-37. Showing higher magnification SE micrographs from different regions in the D64 (1) and the D128 (2) samples in the etched condition; (a1, a2) indicate the near-HAZ region, (b1, b2) indicate the far-HAZ region and (c1, c2) indicate precipitates growth in the central zone.

High magnification BSE micrographs from these regions in the D64 sample are presented in Figure 5-38(a1), (b1) and (c1). In all of these micrographs, fine dark precipitates are visible in the microstructure in addition to Mo-rich bright precipitates. It is suggested that the dark precipitates are related to the formation of Cr-rich precipitates (possibly M_7C_3 and $M_{23}C_6$) with lower mean atomic number compared to the matrix. Moreover, the morphology of the bright precipitates is different in these regions. The bright precipitates are coarser in the near-HAZ region compared to those of the far-HAZ region (see Figure 5-38(b1)). Moreover, these precipitates are present on the ferrite grain boundaries in the central zone (see Figure 5-38(c1)).

The BSE micrographs from different regions of the D128 sample in the polished condition are shown in Figure 5-38(a2), (b2) and (c2). The near-HAZ region micrograph in the D128 sample (see Figure 5-38(a2)) is different compared to that of the D64 sample and shows some chains of coarse bright precipitates in some locations and some fine bright precipitates which are dispersed in the matrix. Moreover, there are fewer coarse bright and fine dark precipitates in the near-HAZ region of the D128 sample compared to those of the D64 sample. The far-HAZ region and the central zone micrographs in the D128 sample (see Figure 5-38(b2) and (c2)) contain similar features (bright and dark precipitates). However, morphologies and distribution of these precipitates are different compared to those of the near-HAZ region. Generally, it is seen that dark precipitates are fewer in the D128 sample compared to those of the D64 sample. This can be related to formation of (Cr, Mo)-rich carbides with a mean atomic number close to that of the matrix.

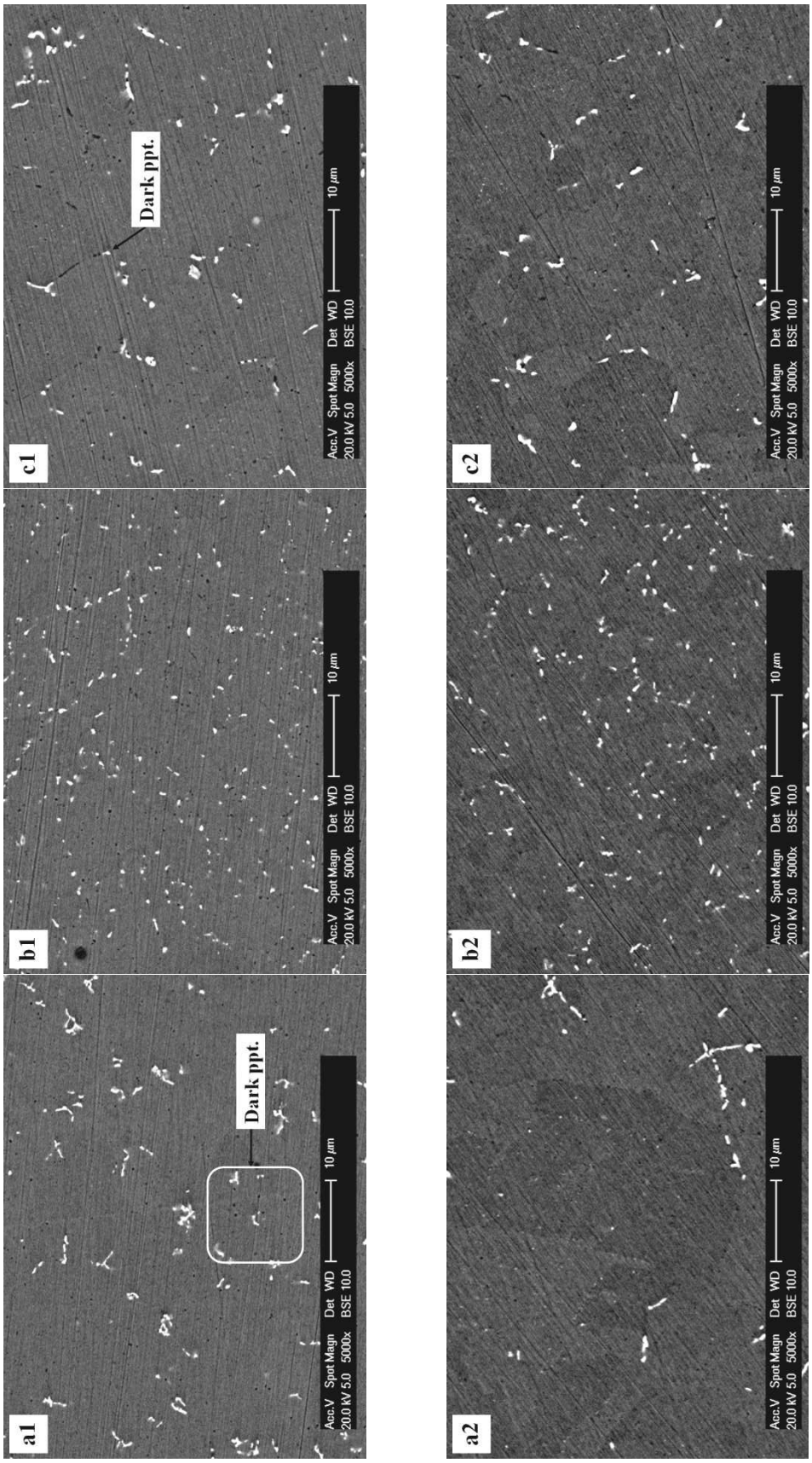

Figure 5-38. Showing higher magnification BSE micrographs from different regions in the D64 (1) and the D128 (2) samples; (a1, a2) indicate precipitates in the near-HAZ region, (b1, b2) indicate the far-HAZ region precipitates and (c1, c2) indicate fewer dark precipitates on the ferrite grain boundaries with increasing exposure time.

Comparison between BSE micrographs of the near-HAZ region in the D32 (see Figure 5-31(a2)) and the D64 (see Figure 5-38(a1)) samples shows that the bright precipitates morphology changes from elongated to coarser irregular particles. This means further growth of these precipitates with increasing exposure time. Moreover, there are a lot of fine dark precipitates which are uniformly dispersed in the matrix of the D64 sample which are related to Cr-rich carbides and attributed to re-hardening of this region.

The presence of dark precipitates observed in the BSE micrographs of the near-HAZ region is complex. In the D64 sample, there are more dark precipitates compared to those in the D32 sample. However, these features are fewer in the D128 sample than those observed in the D64 sample. It seems that increasing exposure time results in precipitation of Cr-rich $M_{23}C_6$ in addition to the former Cr-rich M_7C_3. However, these carbides convert to (Cr, Mo)-rich $M_{23}C_6$ with a mean atomic number close to matrix which are not seen in the BSE micrographs.

In order to identify these precipitates, further investigations were carried out on the D128 sample using EBSD and the results are shown in Figure 5-39. The fine grains in the steel region adjacent to interface are clearly visible in the IPF (Inverse Pole Figure) map of this region (see Figure 5-39(a)). The phase discrimination map of the interfacial region is shown in Figure 5-39(b) and shows many mismatched (black) points. The precipitates contain some points which match with $Cr_{23}C_6$ while other points match with Mo_2Fe_4C. Both of these phases i.e. $Cr_{23}C_6$ and Mo_2Fe_4C have FCC structure; therefore it is suggested that (Cr, Mo)-rich precipitates were formed in this region.

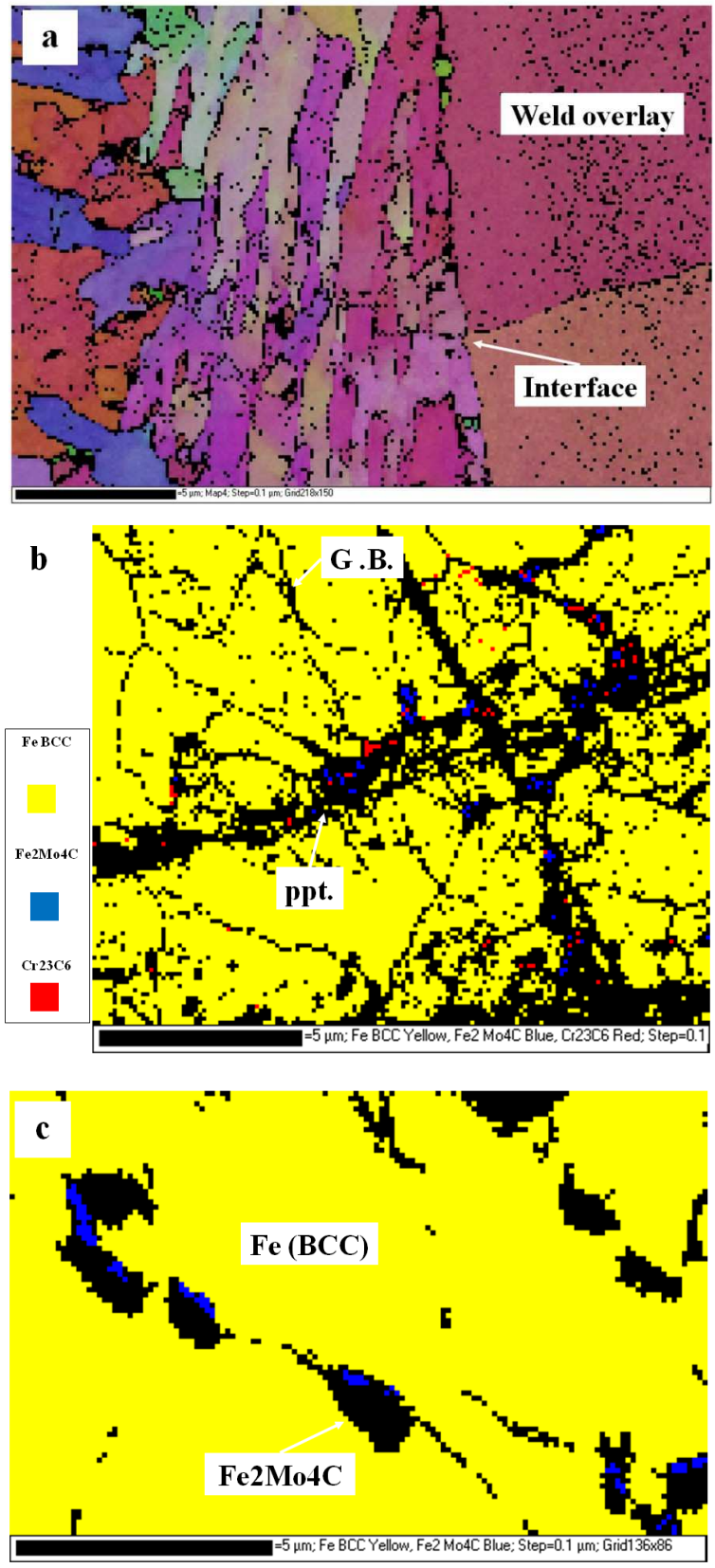

Figure 5-39. Showing EBSD results from different regions of the D128 sample; (a) IPF map from the interfacial region indicates the interface and fine grain in this region, (b) higher magnification phase discrimination map of the near-HAZ region indicates two different phases in the precipitates and (c) higher magnification phase discrimination map of the far-HAZ region indicates only M_6C phase in the precipitates.

Figure 5-39(c) shows the phase discrimination map in the far-HAZ region, and it is clear from BSE micrographs that finer precipitates are present in this region. The precipitates in the far-HAZ region are mainly M_6C with no evidence for $M_{23}C_6$ phase. This issue is related to limitation of W filament electron gun in producing phase discrimination maps.

Advanced microstructural examination

Based on the above observations, it was deemed necessary to identify the bright and dark contrast precipitates of BSE images in the near-HAZ region of the D64 and the D128 samples. Moreover, the unusual grain size reduction in this region from the D64 to the D128 samples should be investigated; specifically how this might be related to changes in the precipitates. Therefore further analyses were carried out using ion beam imaging and FIB/TEM (see section 3-5-4 and 3-5-5) on these samples in the Loughborough University.

The ion beam induced secondary electron (ISE) images of these samples are presented in Figure 5-40. The interfacial regions in the D64 and D128 samples are shown in Figure 5-40(a1) and (a2) respectively. A comparison of these images shows a significant change in the grain size of the near-HAZ region. Figure 5-40(b1) and (b2) show higher magnification ISE images from the near-HAZ region after 1 raster in the D64 and the D128 samples respectively. It is observed that there are a lot of fine precipitates in the D64 sample (see Figure 5-40(b1)) and that these have grown with increasing exposure time to 128 days (see Figure 5-40(b2)). It is clear that further raster results in a changing in channelling of ISE images. Therefore it is possible to observe the grain boundaries.

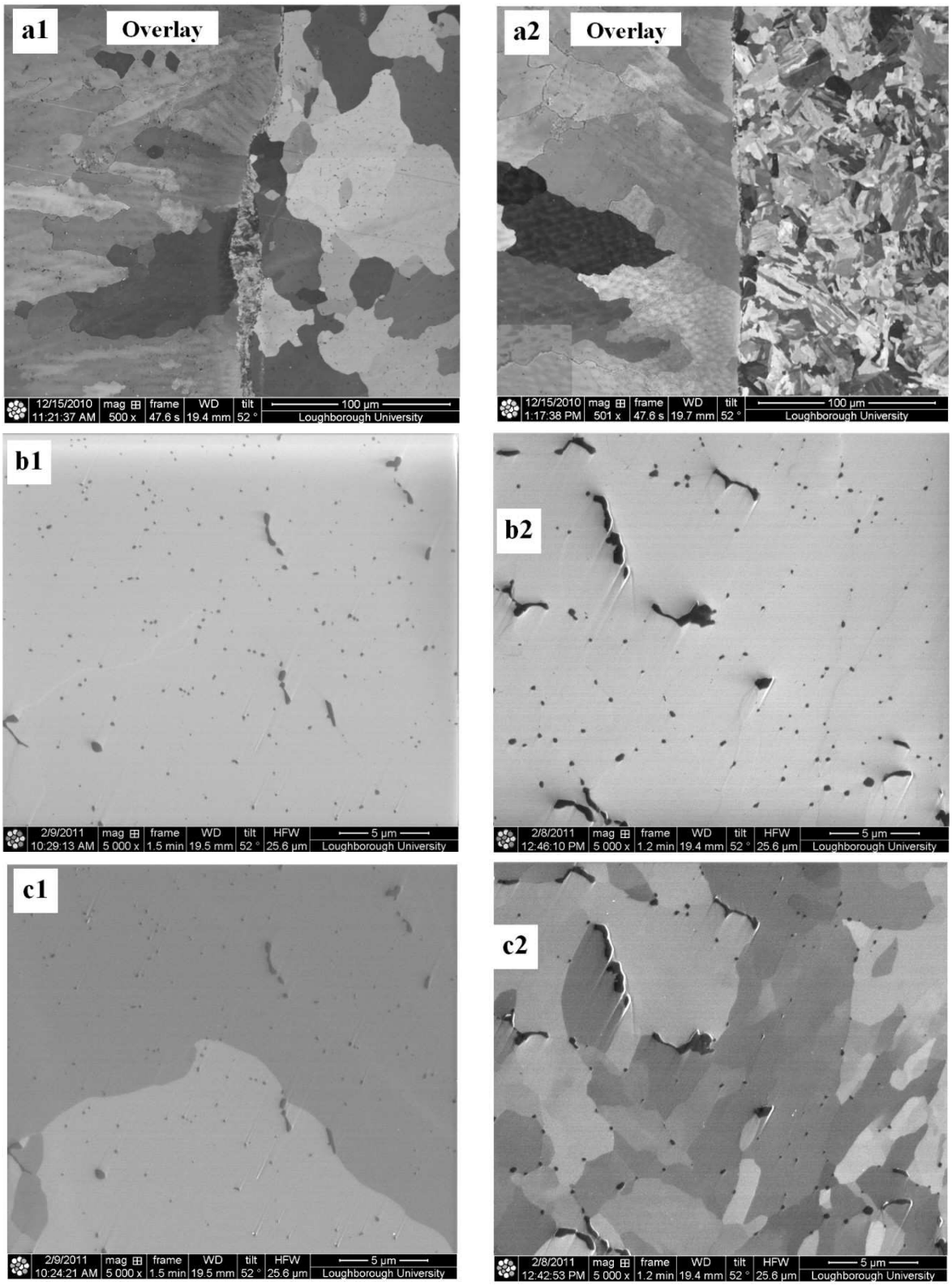

Figure 5-40. Showing ion beam induced secondary images of the D64 (1) and the D128 (2) samples; (a1, a2) low magnification ISE images from the interfacial region indicate grain size difference in the near-HAZ region, (b1, b2) higher magnification ISE images of near-HAZ after 1 raster indicate precipitate growth with increasing exposure time and (c1, c2) higher magnification ISE images of the same region after 3 raster indicate precipitates along the grain boundaries in the D128 sample.

Higher magnification ISE images from the same regions after 3 raster in both samples are presented in Figure 5-40(c1) and (c2). It is observed that the fine precipitates in the D64 sample are scattered in the matrix. However, the precipitates in the D128 sample are mostly along the grain boundaries in the near-HAZ region.

Further investigation using FIB-TEM was carried out and the high angle annular dark field (HAADF) scanning transmission electron microscope (STEM) micrographs from two regions of these samples are presented in Figure 5-41. The far-HAZ region of the D64 sample is shown in Figure 5-41(a1) and indicates fine grains and precipitates in this region. The near-HAZ region of this sample are shown in Figure 5-41(b1) and (c1) with different magnifications. It is observed that the grain boundaries are not visible in the near-HAZ region of the D64 sample. However, the fine precipitates (nano-particles) are clearly visible in both images.

Similarly the HAADF-STEM micrographs of the D128 sample are presented in Figure 5-41(a2), (b2) and (c2). Figure 5-41(a1) shows the far-HAZ region and indicates that it is similar to that of D64 sample. However, the low magnification image of the near-HAZ region in the D128 sample (see Figure 5-41(b2) indicates grain boundaries. Moreover, the higher magnification image of this region shows only one coarse precipitate (see Figure 5-41(c2)). The EDS maps of the main elements (Fe, Cr and Mo) for Figure 5-41(c1) and (c2) are presented in Figure 5-42. The Fe maps indicate the location of precipitates in these regions and their size. Figure 5-42(a1) shows precipitate size is less than 50 nm while Figure 5-42(a2) shows a ~200 nm particle.

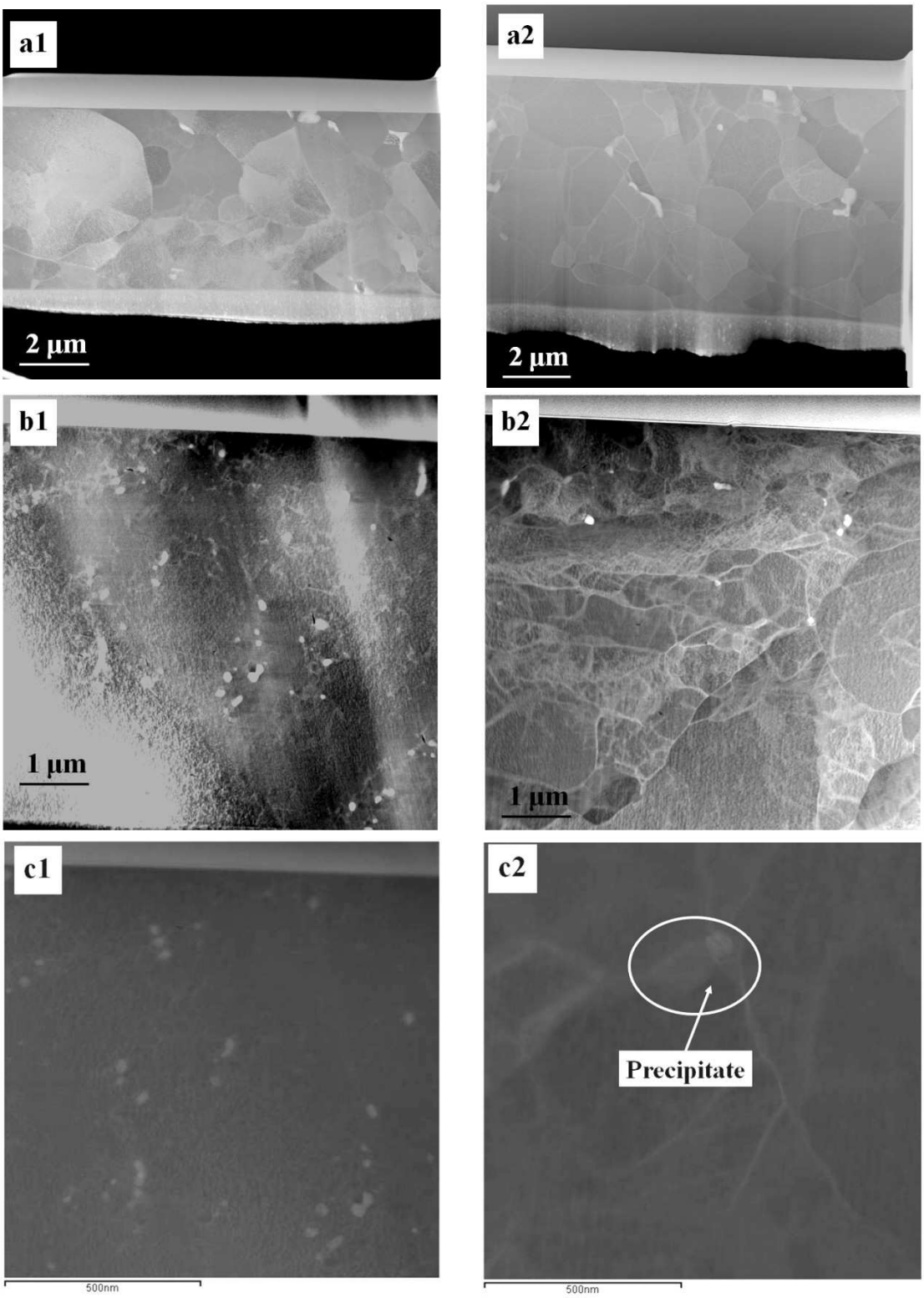

Figure 5-41. Showing HAADF STEM micrographs of the D64 (1) and the D128 (2) samples; (a1, a2) low magnification images from the far-HAZ region indicate similar microsructure, (b1, b2) low magnification images from the near-HAZ region indicate fine grain formation with increasing exposure time and (c1, c2) higher magnification images from the near-HAZ region indicates precipitate growth with increasing exposure time.

Comparison between Cr maps in the D64 (see Figure 5-42(b1)) and the D128 (see Figure 5-42 (b2)) samples indicates that Cr-rich precipitates grow in size with increasing exposure time. It is observed that many fine Cr-rich precipitates (less than ~50 nm size) are present in the D64 sample while there is only one coarse Cr-rich precipitate (~200 nm size) in the D128 sample.

A comparison of Mo maps in both samples (see Figure 5-42(c1) and (c2)), indicates the growth of Mo-rich precipitates with increasing exposure time. Moreover, it is observed that coarse precipitate in the D128 sample is a (Cr, Mo)-rich phase. It should be noted that Mo-rich part of this precipitate is different from the Cr-rich part.

A comparison between the Cr and Mo maps in the D64 sample (Figure 5-42(b1) and (c1)) reveals that there are 3 types of precipitates in this sample. It is seen that a number of precipitates are (Cr, Mo)-rich. However, there are some precipitates which are either Cr-rich or Mo-rich precipitates. As such, it is suggested that in the near-HAZ region of the D64 sample, fine Cr-rich and (Cr, Mo)-rich precipitates are present in the microstructure in addition to coarse Mo-rich precipitates in BSE micrographs (see Figure 5-38(a2)).

The fine (Cr, Mo)-rich precipitates are likely to be $M_{23}C_6$ carbide and their presence causes re-hardening of the near-HAZ region (former soft zone) in the D64 sample. Moreover, these precipitates have grown with increasing exposure time and in the D128 sample only a coarser (Cr, Mo)-rich precipitate (possibly $M_{23}C_6$ carbide) is present in the microstructure. It is observed that these precipitates are present mainly on ferrite grain boundaries (see Figure 5-40 (c2)).

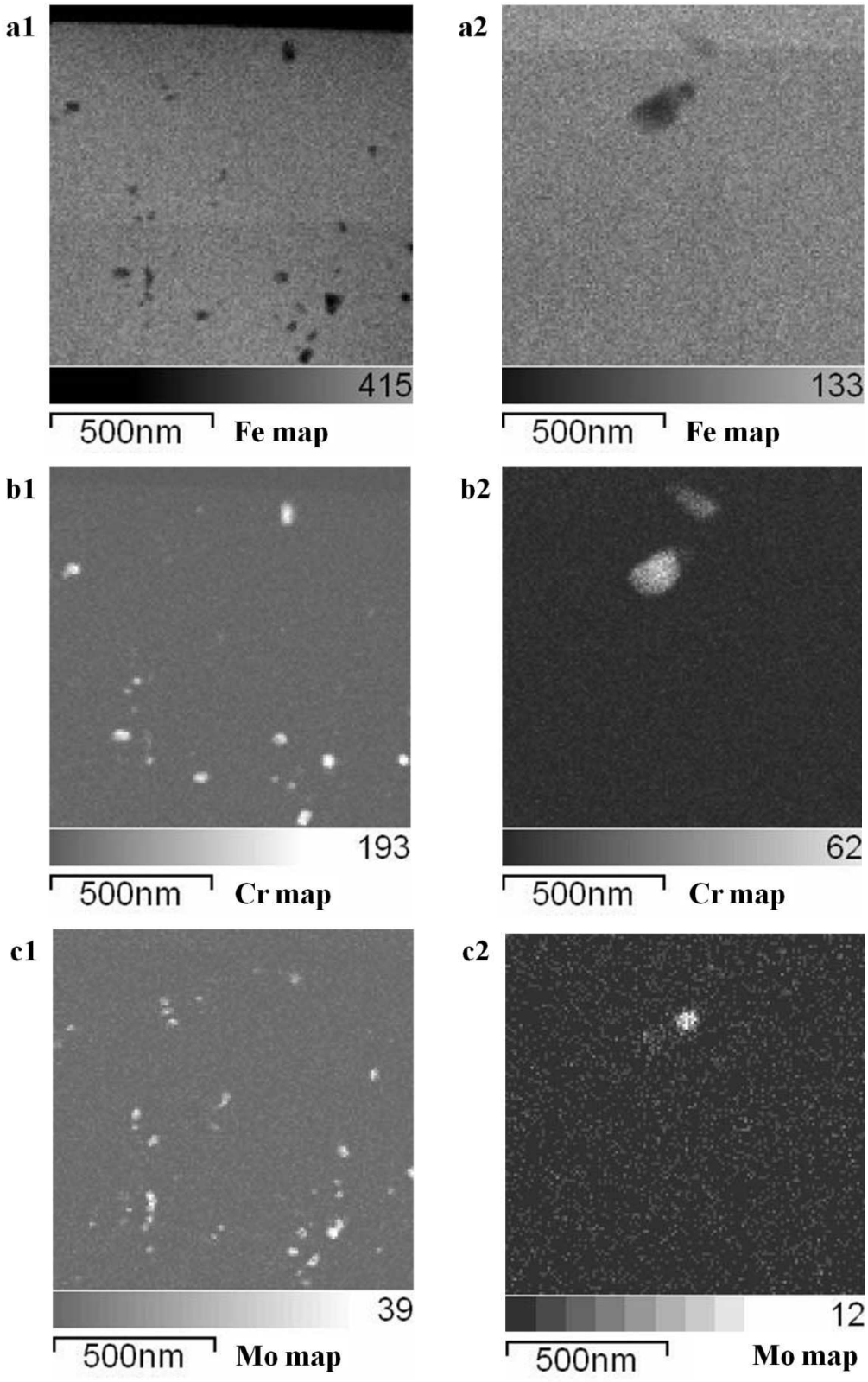

Figure 5-42. Showing EDS maps for key elements for the D64 (1) and the D128 (2) samples with reference to Figures 5-42(c1) and (c2); (a1, a2) Fe maps indicate location of precipitates and their growth with increasing exposure time, (b1, b2) Cr map for precipitates and (c1, c2) Mo map for precipitates.

5-4-2-4- Formation of carbides at interface

The interfacial regions of the D32 and the D64 samples were analysed in the Oxford Instruments labratory in order to identify the precipitates at the interface and the results are shown in Figure 5-43. The low magnification BSE micrographs of the interfacial region in these samples are presented in Figure 5-43(a1) and (a2) respectively. A comparison of these images shows that more bright contrast precipitates exist at the interface of the D64 sample compared to those of the D32 sample. Moreover, higher magnification micrographs from the interface region indicate coarser precipitates in the D64 sample (Figure 5-43(b2)) compared to those of the D32 sample (Figure 5-43(b2)).

Further analyses were carried out using EBSD and EDS on the D64 sample. The superimposed results of EBSD with the EDS for one precipitate adjacent to the interface is presented in Figure 5-43(c) and shows a F.C.C structure which is related to the $Cr_{23}C_6$ carbide. However, it is seen that some parts of this precipitate did not match with the $Cr_{23}C_6$ structure. Analysis of the mismatched parts with EDS shows a higher Mo concentration. Therefore, it is suggested that these precipitates are (Cr, Mo)-rich carbide, possibly $M_{23}C_6$ carbide. Moreover, the carbide precipitates at the interface have grown with increasing exposure time.

The precipitates at the interface in the D64 sample are easily identified by the Cr and Mo peaks in the EDX line scans across the interface in this sample. Figure 5-44(a) shows a BSE micrograph from the interfacial region in the D64 sample with Cr and Mo peaks adjacent to interface.

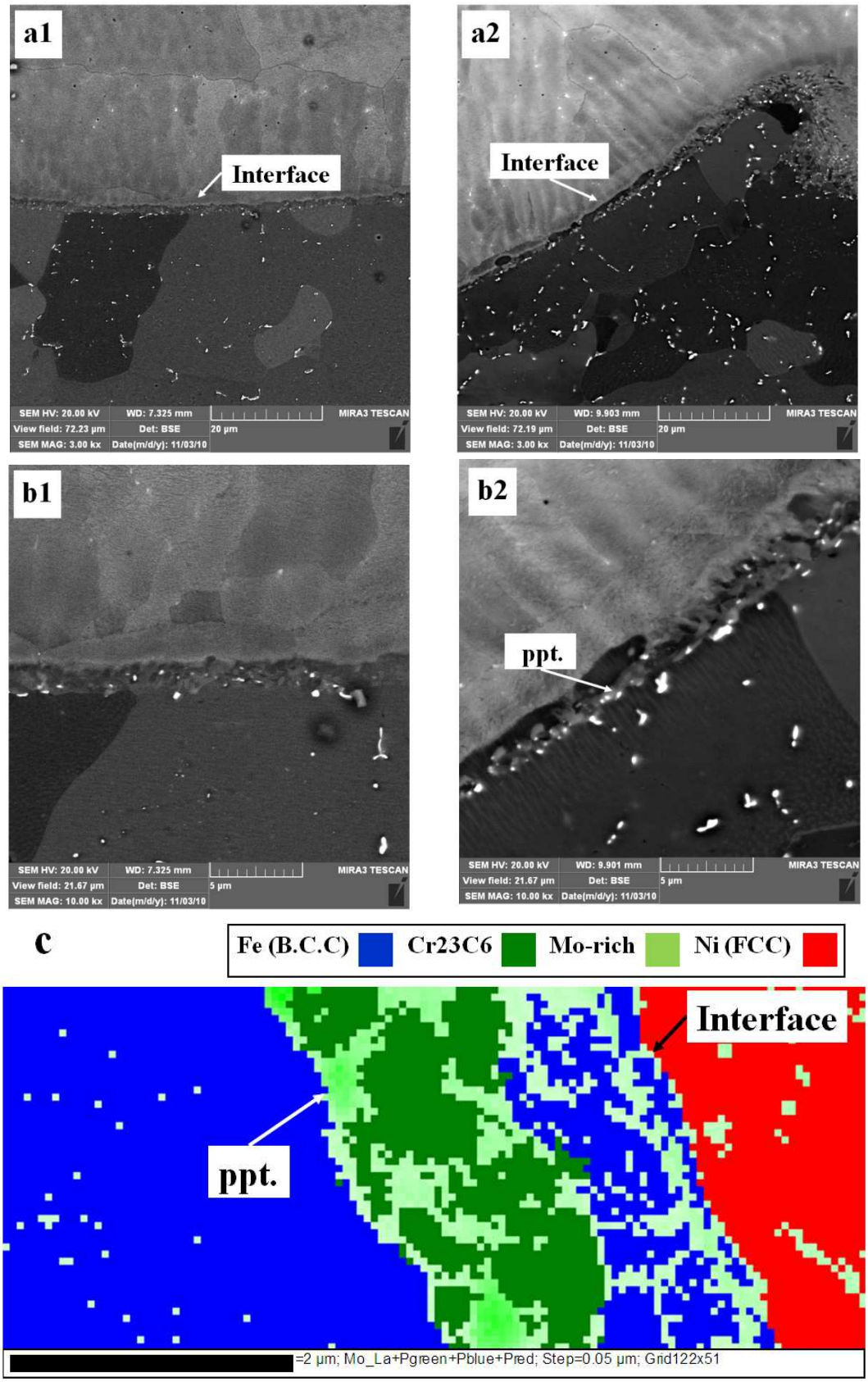

Figure 5-43. Showing precipitates at the interface region of the D32 (1) and the D64 (2) samples; (a1, a2) low magnification BSE micrographs indicate precipitates growth with increasing exposure time, (b1, b2) higher magnification BSE micrographs and (c) EBSD analysis with EDS maps for one precipitate in the D64 sample.

Similar EDX analyses were carried out on the interfacial region of the D128 sample in the etched condition. The results confirm the presence of the (Cr, Mo)-rich carbides adjacent to the interface (see Figure 5-44(b)). Moreover, the SE micrograph in the etched condition indicates a network of these carbides formed at the interface. A comparison of these images shows that Cr-rich region width increased with extending exposure time.

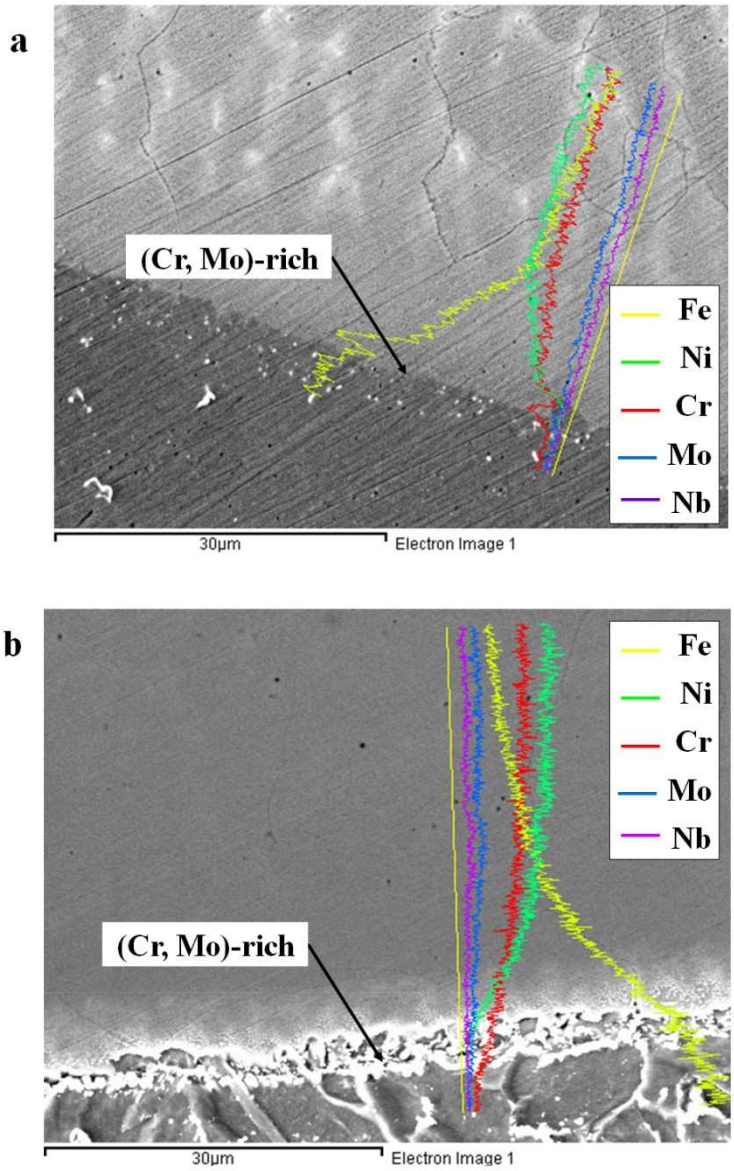

Figure 5-44. Showing (Cr, Mo)-rich carbides in the D64 and the D128 samples; (a) BSE micrograph indicate higher Cr and the Mo concentrations in the region adjacent to interface in the D64 sample (b) SE micrograph in the etched condition indicates a network of particles adjacent to the interface in the D128 sample in the Cr-rich region.

Advanced microstructural examination

Based on the above presented results, it was deemed that further analyses were required for characterization of carbide precipitates at the interface region in the D64 and the D128 samples. Therefore, further analyses were carried out using FIB/TEM (see section 3-5-4) on these samples in the Loughborough University. The HAADF STEM micrographs from the interface region in the D64 and the D128 samples are presented in Figure 5-45(a1) and (a2) respectively.

These dark field images show a chain of precipitates in both samples. The EDS maps for the main elements in the carbide phase i.e. Cr and Mo in the D64 sample are presented in Figure 5-45(b1) and (c1) and confirm that these precipitates are (Cr, Mo)-rich and possibly are $M_{23}C_6$. The similar maps for the D128 sample (see Figure 5-45(b2) and (c2)) indicate similar results for this sample. These results are in accord with former results obtained with the SEM.

Considering the EDS maps in both samples, it is clear that generally the Mo-rich regions correspond to the Cr-rich regions; however, there are some points in the precipitates that the Mo concentration is higher compared to other points. A comparison of the EDS maps in theses samples shows that there are slightly larger precipitates (~110 nm) in the D128 sample compared to (~90 nm) precipitates in the D64 sample. This fact could be related to the growth of these precipitates with increasing exposure time. Moreover, these (Cr, Mo)-rich precipitates are likely to be $M_{23}C_6$, as shown in the EBSD results of the D64 sample (see Figure 5-43(c)).

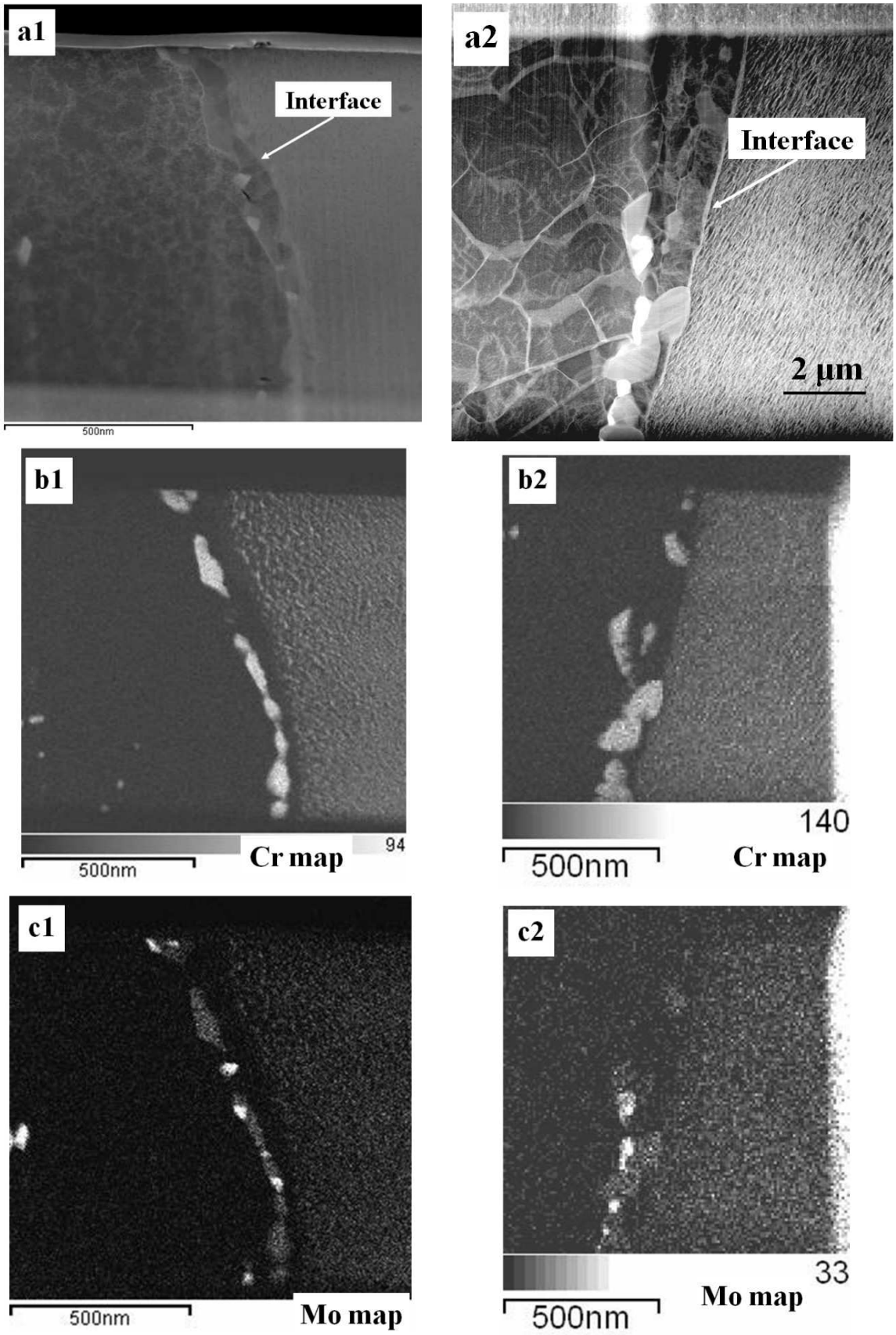

Figure 5-45. Showing precipitates at the interface region in the D64 (1) and the D128 (2) samples; (a1, a2) HAADF STEM micrographs from the interface, (b1, b2) the EDS map for Cr indicate the growth of precipitates and (c1, c2) the EDS map for Mo.

In summary, the following transformations were observed during the ageing of the weld overlaid tube at 650˚C:

1) In the weld overlay region:

   a) Carbide particle formation and growth along grain boundaries within a region ~100 μm wide adjacent to the interface. The width of this region remained constant during thermal exposure.

   b) Formation of a hard band ~30 μm wide adjacent to interface. The hardness of this region may affect the tube service behaviour.

   c) Precipitation and growth of TCP phases is different in different regions of this material.

2) In the steel substrate:

   a) Tempering of all regions of this material occurs at different rates which could be related to the as-welded microstructure.

   b) Decarburization of the steel occurs (formation of soft zone in the near-HAZ region) which could affect the service behaviour.

   c) Re-hardening of the near-HAZ region and fine grain formation in this region is observed after 128 days. This unusual phenomenon may be related to carbide transformation and carbon concentration in the matrix.

   d) Carbides precipitate at the interface and possibly cause a barrier to carbon migration.

Chapter 6

Calculation of phase equilibria in Ni-based alloys and 2.25Cr1Mo steel using Thermo-Calc software

6-1- Introduction

Thermo-Calc is a software package for multi-component phase diagram calculation and, when combined with a suitable critically assessed thermodynamic database, it can be used to predict equilibrium phase formation in complex alloys such as those investigated in the present work. Thermo-Calc is now available with a Windows interface and this version was employed in this work which is referred to as TCW (Thermo-Calc Windows).

In this research, TCW was used to investigate the equilibrium phases in the wrought IN625, weld overlay material and 2.25Cr1Mo steel. In the next section, the principles of computer calculation of phase diagrams (CALPHAD) will be presented and the implementation of this approach in TCW will be reviewed. In the following section, the focus is on Thermo-Calc software, the methodology employed and the available databases. A study of the wrought IN625 composition is presented in the next section and then, based on this section, the weld overlay material will be compared to the wrought IN625. In the weld overlay section, both regions of the weld overlay material (i.e. the bulk and the mixing zone) will be assessed separately.

A further application of the TCW software was to investigate non-equilibrium solidification of the weld overlay based on the well known Scheil solidification model. This was undertaken to have a better understanding of phases likely to be present in the weld overlay material in the as-deposited condition. The different regions of the weld overlay will be analysed in this section too.

In the final section, the equilibrium stable and metastable phases are predicted for the 2.25Cr1Mo steel. Based on these calculations, the carbide transformations and changes in the co-existing ferrite will be described. Finally, the effect of carbon content on the stable carbide will be introduced in order to provide underpinning understanding of the carbide phase changes which occur during decarburization of the near-HAZ region.

6-2- CALPHAD principles

The usual (temperature versus composition) phase diagram is a graphical representation of the most stable phases in a certain chemical composition at a given temperature as well as constant pressure. With these conditions these stable phases correspond to a minimum of the system Gibbs free energy. The Gibbs free energy of a system is defined by the equation as follow:

$$G = H - TS$$

where H is the enthalpy (heat content), T the absolute temperature, and S the entropy (measure of randomness) of the system. It is suitable to choose G as the basic thermodynamic modelling function because a system at constant temperature and pressure has the lowest possible value of the Gibbs free energy if it is in stable equilibrium or phases are the most stable ones.

Phase transformations occur when one or more phases in an alloy system change into a new phase or mixture of phases. This occurs because the initial state of the alloy is unstable relative to the final one. This phenomena is related to diffusion of atoms from one state to another one which occurs in order to decrease the system Gibbs free energy [175]. Therefore, calculation of stable phases in a system or its phase diagram is achieved by achieving the minimum Gibbs free energy. If the Gibbs energies of all competing phases in a system are known as a function of temperature and composition, this calculation can be done numerically.

Practically, the thermodynamic functions can be determined from experiments only for observable phases and these are valid only for their stability regions

in terms of temperature and composition ranges [176]. Therefore, choosing a suitable mathematical expression is important for the thermodynamic functions. These equations must be based on realistic physical models while the interpolation of the experimental data as well as extrapolation outside the experimentally ranges is being allowed.

A simple power series can represent the Gibbs energy of a system. There is no natural zero point for the Gibbs free energy and it must always be given relative to one reference. For example, it is expressed as following popular equation:

$$\Delta G^0 = G^0(T) - H^0(298.15) + TS^0(0)$$

The S^0 is set to zero and then the last term is omitted. H^0 (298.15) is indicated by H_{SER} for enthalpy of a stable element reference. Different states of a stoichiometric compound can be shown with unary data. As their compositions are defined, a mathematical formula is used for presenting their fundamental properties such as enthalpy and entropy. These type of data are expressed as a function of temperature in the form of the following equation:

$$G - H_{SER} = a + bT + cTlnT + dT^2 + e\,T^3 + fT^{-1}$$

Critical analyses and computer optimisation of experimental results and Gibbs free energy as well as information from phase equilibria studies are needed for calculation of the coefficients of this equation. Moreover, some theoretical methods may also be used in this regard [161].

Where phases exist over a wide range of chemical compositions (for example, solid solution phases in metallic materials) other mathematical models are

used to show the effect of composition changes on free energy. The ideal solution is the simplest description of a solid solution phase which means that the constituents are non-interacting and only mixed randomly together. The free energy of a solution phase with two elements is described as follows:

$$\Delta G = \Delta G^0 + \Delta G_{mix}^{ideal} \quad \text{where} \quad \Delta G^0 = x_A \Delta G_A^0 + x_B \Delta G_B^0$$

$$\Delta G_{mix}^{ideal} = RT(x_A \ln x_A + x_B \ln x_B)$$

The first term in this equation is related to the unary data of each element and shows the free energy change because of presence of pure A and B atoms together. Mixing of x_A and x_B mole fractions of atoms A and B in the solution causes changes in the entropy of system. The second term is associated with the configurational entropy and its effect on the Gibbs energy of system.

In practice, most binary systems are non-ideal and interactions between the elements within the lattice should be considered. This difference from ideal is expressed by the excess Gibbs energy which is shown in the following equation by ΔG^{xs}_{mix}:

$$\Delta G = \Delta G^0 + \Delta G_{mix}^{ideal} + \Delta G_{mix}^{xs}$$

A large number of thermodynamic models have been developed for crystalline phases and related systems such as the substitutional type and the multiple sublattice models [155, 161] based on this general equation for free energy. The main differences in these models are based on the definition of the excess Gibbs free energy term. There are different sites for atoms in the crystalline structure which cause an increase in the entropy of system. The free energy of

the substitutional model (ΔG_m) for a multi-component system can be represented by the following equation:

$$\Delta G_m = \sum_i x_i \, \Delta G_i^0 + RT \sum_i x_i \, ln x_i + \sum_i \sum_{j>i} x_i \, x_j \sum_v \Omega_v \, (x_i - x_j)^v$$

where x_i is the mole fraction of component i, ΔG^0_i is the free energy of the pure component i based on the unary data, T is the temperature and R is the gas constant. Ω_v is an interaction coefficient dependent on the value of v. In the regular solution model, v=0 and in the sub-regular model v=0 and 1. In practice v does not go up above 2 [155]. The ΔG^{xs}_{mix} term is associated with interaction between the different elements on the first sublattice.

In real systems, there are two and/or more crystallographic sublattices and interaction between these sublattices must be considered. The multiple sublattice model is significantly complex because the ΔG^{xs}_{mix} term is related to the interaction between components on the sublattice and between sublattices themselves. These interactions must be considered in calculation of the ΔG^0 and the ΔG^{ideal}_{mix} terms in addition to the ΔG^{xs}_{mix} term. Details of calculation of these terms for a phase with two sublattices and two species in each of them are presented elsewhere [177].

Once thermodynamic properties of various phases are defined, phase equilibria can be calculated using software packages such as Thermo-Calc or MTDATA which perform free energy minimization routines with the aid of thermodynamic databases. All types of models require input of coefficients which uniquely describe the properties of the various phases and these coefficients are held in databases.

6-3- Thermo-Calc software

6-3-1- Methodology

Calculation of equilibrium phase fractions in a system and their compositions as a function of temperature for multi-component materials is the main application of Thermo-Calc software. The Windows version of Thermo-Calc software (TCW) has a graphical user interface which makes calculations of multi-component phase diagrams easy to perform. The calculation of stable phases where temperature is varied can easily be shown by a single axis diagram. In this diagram, mole fraction or mass fraction of each phase is shown versus temperature. This is termed a multiphase diagram in this work.

Moreover, it is possible to analyse the effects of changing the chemical composition on the stable phases at a given temperature in a single axis diagram. For example, the effect of Fe content on the stable phases in the wrought IN625 can be shown in this type of diagram. Different types of "multiphase" diagrams were calculated for the wrought IN625, the weld overlay material and 2.25Cr1Mo steel.

Diagrams for the equilibrium phases can be generated by the Thermo-Calc software using a diagram map which contains two axes. In these phase diagrams, the effect of chemical composition and temperature on the stable phases can be plotted. By generating the diagram for equilibrium phases in a material versus one specified element content, the phase formation at a given temperature could be predicted. This data can be used for analysis of experimental observations during the high temperature exposure experiments.

For example, the diagram for the equilibrium phases in the 2.25Cr1Mo steel with carbon content and temperature can help in evaluation of the stable phases in the steel resulting from changing carbon concentration. In other words, the effects of the steel decarburizing on its stable phases can be investigated.

Another application of the Thermo-Calc software is the calculation of phases arising from non-equilibrium solidification using the Scheil-Gulliver model. TCW contains a Scheil module for calculating the effect of microsegregation on the solidification process in a multi-component alloy such as the weld overlay material. The basic assumptions in the Scheil-Gulliver model are:

1) Fast diffusion in the liquid phase (homogenous composition in this phase)

2) No diffusion of solute elements in the solid phase [160]

In this type of calculation, the chemical composition of the liquid and the solid phases at the start of solidification are computed from the equilibrium calculation. Then, for the next step, the resultant liquid composition is used for the calculation of new liquid and solid phases using thermodynamic equations in order to minimize the free energy of system. Therefore, the effect of enrichment of alloy elements in the remaining liquid phase is considered for calculation of the coexisting solid phase composition as temperature is changed.

6-3-2- Multicomponent Databases

A thermodynamic software package is dependent upon accurate and validated databases. There are many critically-assessed and high quality databases available which cover a wide spectrum of materials including steels and nickel-based alloys. An important step in using Thermo-Calc is choosing the right database. The general database is SSOL4 which covers a large number of elements whereas the TTNI7 database is suitable only for nickel-based alloys and the TCFE6 database is designed for steels. The data sheets of these databases are presented in Appendix 3.

The TCFE6 database was released in March 2008 by Thermo-Calc and includes many new critical assessments of the thermodynamic data for multicomponent system of various steel/Fe alloys. This database covers complete and critical assessment of binary and ternary systems as well as the iron corner of some higher order systems, within a 21 element framework.

Table 6-1.TCFE6 alloying elements and their maximum wt.%

Element	*Max (wt.%)*	*Element*	*Max (wt.%)*
Al	5.0	N	5.0
B	Trace	Nb	5.0
C	7.0	Ni	20.0
Ca	Trace	O	Trace
Co	20.0	P	Trace
Cr	30.0	S	Trace
Cu	5.0	Si	5.0
Mg	Trace	Ti	3.0
Mn	20.0	V	15.0
Mo	10	W	15.0

The database is applicable to various types of steels/Fe alloys with a minimum 50 wt.% Fe and for the alloying elements, the recommended composition limits in weight percent are as Table 6-1. Sensible calculations cannot be expected if all alloying elements are at their highest limits but considering the 2.25Cr1Mo steel composition (presented in Table 6-8), this database can be used for equilibrium calculations in this material.

The TTNI7 database was specially created by Saunders [155-157] to answer the requirements of dealing with Ni-based superalloys including IN718 and IN625. This database has proved to provide excellent agreement with experimental observations in a range of nickel based alloys [178]. Furthermore, it has also been used successfully in solidification modelling of these alloys [156]. The database contains following 22 elements:

Ni, Al, Ca, Co, Cu, Fe, Hf, Mn, Mo, Nb, Re, Ru, Si, Ta, Ti, V, W, Zr, B, C, N and O.

Considering the chemical composition of the wrought IN625 presented in Table 6-2 and the weld overlay material (bulk and mixing zones) presented in Table 6-4 and Table 6-6 respectively, the TTNI7 is an appropriate database for them. Data sheets of these databases are presented in appendix No.3.

6-4- Calculation of phase equilibria in wrought IN625

The results of calculations for the equilibrium phases in the wrought IN625 using Thermo-Calc software are presented in this section. As it is a well

known material, the Thermo-Calc results can be compared with the experimental results. Moreover, it gives a good baseline for the calculation of stable phases in the weld overlay material. The composition of wrought IN625 as obtained by spark emission spectroscopy is given in Table 6-2.

Table 6-2.Chemical composition of the wrought IN625 material

Element	*wt.%*	*at.%*
C	0.005	0.025
Al	0.1	0.22
Ti	0.21	0.26
Cr	21.9	25.2
Fe	3.18	3.4
Co	0.1	0.1
Ni	Balance	Balance
Cu	0.17	0.16
Nb	3.5	2.3
Mo	9.2	5.7

In this work, the "Elements" module was chosen for entering the initial conditions (temperature, pressure and chemical composition). By choosing the TTNI7 database for the wrought IN625, the chemical composition presented in Table 6-2 was entered in the software. Moreover, referring to the thermal exposure tests at 650˚C, additional conditions (T=650˚C, P=1 Bar) were entered in software too. The equilibrium molar fractions of the phases at 650˚C are calculated as follows (in mol.%):

1) FCC-A1#1(γ) : Austenite (Ni solid solution) - 81.95

2) DELTA#1 (δ) : $Ni_3 (Nb_{0.88} Ti_{0.08} Mo_{0.04})$ - 8.97

3) Mu_PHASE#1 (μ) : Mo $(Cr_{0.52} Ni_{0.47} Fe_{0.01})_2$ - 8.95

4) Carbide ($M_{23}C_6$): $(Cr_{0.82} Mo_{0.13} Ni_{0.05})_{23}C_6$ - 0.13

As expected for the wrought IN625 at 650˚C, the main phase is the austenite (γ) or FCC-A1#1 which is the matrix and other phases are precipitates. Because of the low (0.005 wt.%) carbon content, the stable Cr-rich $M_{23}C_6$ carbide phase has the lowest fraction in system. Two other phases in this material can be classified as interemetallics. The (μ) is a Mo-rich phase, while the (δ) is a Nb-rich phase.

The multiphase (molar fraction of phases) diagram versus temperature is a convenient presentation of the changes in the stable phases. Figure 6-1(a) shows a multiphase diagram of phase fraction (NPM) versus temperature for the wrought IN625 alloy in the range of 500 to 1500˚C. This figure indicates the temperature range for the equilibrium solidification in this material. Moreover, the temperature range for precipitation of minor phases in the γ can also be seen in this diagram.

It is clear that above 1000˚C and under equilibrium conditions, only austenite (γ) phase exists in this material and below 1000˚C, (MC) precipitates from the austenite (γ) phase. As seen in Figure 6-1(b) with decreasing temperature other phases become stable in this material. The (δ) becomes stable at temperatures below 900˚C while the (μ) is stable at temperatures below 850˚C. These phases are formed at the expense of matrix (γ) and so it can be shown by following reaction:

$$\gamma \rightarrow \gamma + ppt.$$

where ppt. represents different secondary phases such as (MC), (δ) and (μ).

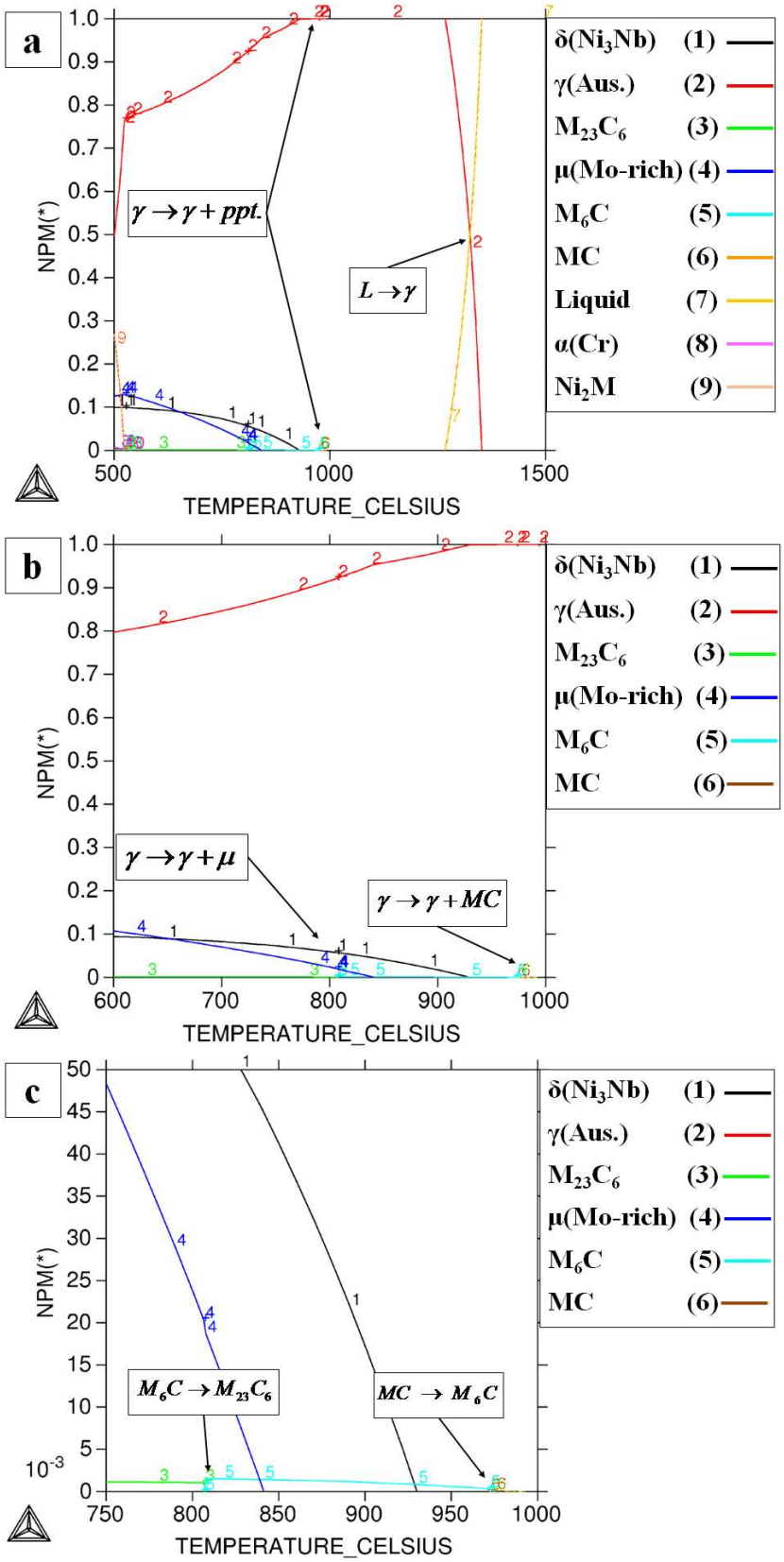

Figure 6-1. Showing plots of mole-fraction of phase (NPM) versus temperature for the equilibrium phases in wrought IN625 (Table 4-2); (a) indicates equilibrium solidification and precipitation, (b) indicates temperature range for precipitation of different phases and (c) indicates carbide transformation temperature range .

Based on former experimental observations (see section 2-4-2-2), carbide transformation occurs in the IN625 alloy and as seen in Figure 6-1(c) above 950˚C, the (MC) phase (line No.6) converted to the M_6C carbide (line No.5). In order to determine the chemical composition of the MC and M_6C phases, two separate single equilibrium calculations were carried out at 990˚C and 950˚C respectively. The results of the calculation at 990˚C show the following equilibrium phases are present (in mole %):

1) FCC_A1#1 (γ) : Ni solid solution - 99.99

2) FCC_A1#1 (MC): $(Nb_{0.96}\,Ti_{0.04})C$ - 0.01

While at 950˚C the equilibrium phases are as follows:

1) FCC_A1#1 (γ) : Ni solid solution with 99.99

2) Carbide (M_6C): $(Mo_{0.37}\,Ni_{0.33}Cr_{0.24}\,Ti_{0.06})_6\,C$ with 0.01

The above results clearly indicate that the Nb-rich MC carbide transforms to the Mo-rich M_6C carbide. Moreover, the diagram shows that the Mo-rich M_6C molar fraction increased with decreasing temperature and finally transforms to Cr-rich $M_{23}C_6$ at temperatures around ~800˚C.

As seen in Figure 6-1(b), in the temperature range of 500-800˚C four equilibrium phases are present in this material. However, the mole fractions of (δ) and (μ) phases increased while the mole fraction of the (γ) phase decreases with equilibrium cooling. This behaviour can be attributed to the growth of these phases. At a temperature just above 500˚C the Ni_2M phase is predicted to precipitate from the (γ) phase and its molar fraction increases with cooling.

There is evidence from published research (see section 2-4-2-3) that at temperatures below 600˚C, the Ni_2M phase precipitates and grows at the expense of the (γ) phase by the following reaction:

$$\gamma \rightarrow \gamma + Ni_2M$$

The effect of changes in the chemical composition on the equilibrium phases at a specified temperature can be investigated by a diagram which shows the mole fractions of phases versus mass percent of one element. For example, the effect of changing carbon and iron contents on the stable phases at 650˚C was investigated by these diagrams. In these calculations, the carbon or iron contents are changed by treating nickel as the balancing element and keeping all other element contents constant.

The multiphase diagram of stable phases in the wrought IN625 versus carbon mass percent at 650˚C is presented in Figure 6-2(a). The composition of wrought IN625 contains 0.005 wt.% C; however, at the zero point of this diagram, the composition contains zero percent carbon. The maximum of carbon content was chosen for relevance to the experimental work. This diagram shows that increasing the carbon content results in more $M_{23}C_6$ carbide at the expense of (γ) and (μ) phases. Increasing the carbon content has negligible effect on the (δ) fraction while the (μ) phase is reduced due to formation of the $M_{23}C_6$ carbide which contains a higher fraction of the Mo atoms. Therefore it is suggested that increasing the carbon content at 650˚C decreases the stability of the (μ) phase in the wrought IN625.

The effect of iron level was explored because this is relevant to intermixing in the experimental samples due to weld deposition. The maximum iron level

was chosen for relevance to the experimental work. The multiphase diagram of mole fraction of phases versus iron mass percent at 650˚C is presented in Figure 6-2(b). Increasing the iron content to about 25 wt.% has no effect on the carbide type and minimal effect on its molar fraction. However, above that level the carbide transforms to MC with a little change in its molar fraction. Increasing the Fe content up to 8 wt.% increases the mole fraction of (μ) but at this level, the (σ) phase starts to appear and its fraction increases at the expense of the (μ) phase, eventually replacing the latter above 13 wt.% Fe

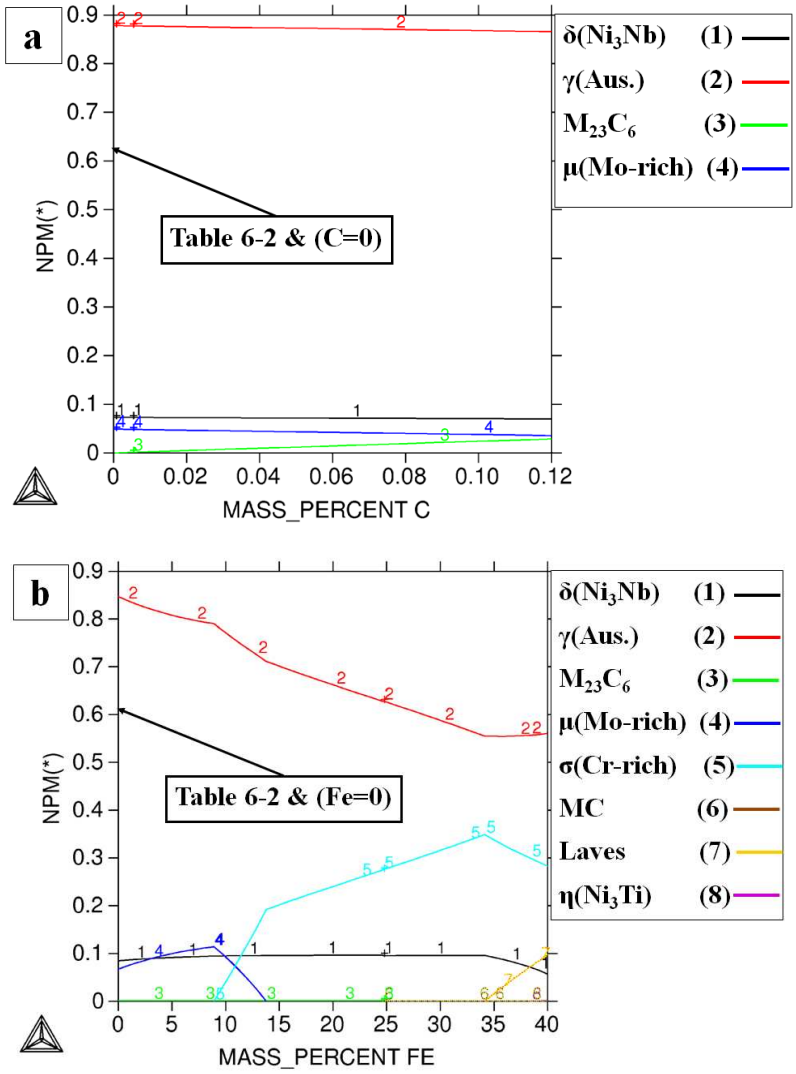

Figure 6-2. Showing plots of mole-fraction of phases (NPM) versus composition for the equilibrium phases in wrought IN625 (Table 6-2) at 650˚C; (a) multiphase diagram for varying the carbon (b) multiphase diagram for varying the iron content.

The results of calculation of equilibrium phases at 650˚C with different Fe levels are shown in Table 6-3 and indicate changes in the stable phases and the chemical composition of (μ) and (σ) phases. The mole fraction of (σ) phase increases with increasing Fe content; however, above 33 wt.% Fe, the Laves phase become stable and its mole fraction increases at the expense of (σ) phase.

Table 6-3. Stable phases in the wrought IN625 with different Fe content at 650˚C.

Phase	*IN625 with 10 wt.% Fe*		*IN625 with 15 wt.% Fe*	
	Composition	*mol.%*	*Composition*	*mol.%*
γ	-	77.13	-	70.13
δ	$Ni_3 (Nb_{0.88} Ti_{0.08} Mo_{0.04})$	9.48	$Ni_3 (Nb_{0.88} Ti_{0.09} Mo_{0.03})$	9.58
μ	$Mo (Cr_{0.52}Ni_{0.43}Fe_{0.05})_2$	9.26	-	0.00
σ	$Cr_{0.45} Ni_{0.25} Mo_{0.19} Fe_{0.11}$	4.01	$Cr_{0.42} Ni_{0.22} Mo_{0.21} Fe_{0.15}$	20.17
$M_{23}C_6$	$(Cr_{0.82} Mo_{0.13} Ni_{0.05})_{23}C_6$	0.12	$(Cr_{0.82} Mo_{0.13} Ni_{0.05})_{23}C_6$	0.12

The effects of chemical composition and temperature on the stable phases can be investigated simultaneously with phase diagrams. Figure 6-3(a) shows the phase diagram of the wrought IN625 with carbon while an enlarged diagram is presented in Figure 6-3(b). The stability regions of stable phase are shown by different lines. For example, the line No.2 shows the stability region of the MC phase and its curvature indicates solid solution of carbon in the IN625 at temperatures above 950˚C. Line No.4 shows the stability region of M_6C phase and indicates that increasing the carbon content results in stability of this type of carbide at higher temperature. Finally, line No.3 shows the stability region of $M_{23}C_6$ carbide and indicates that at carbon content more than 0.06 wt.%, it becomes stable at higher temperatures.

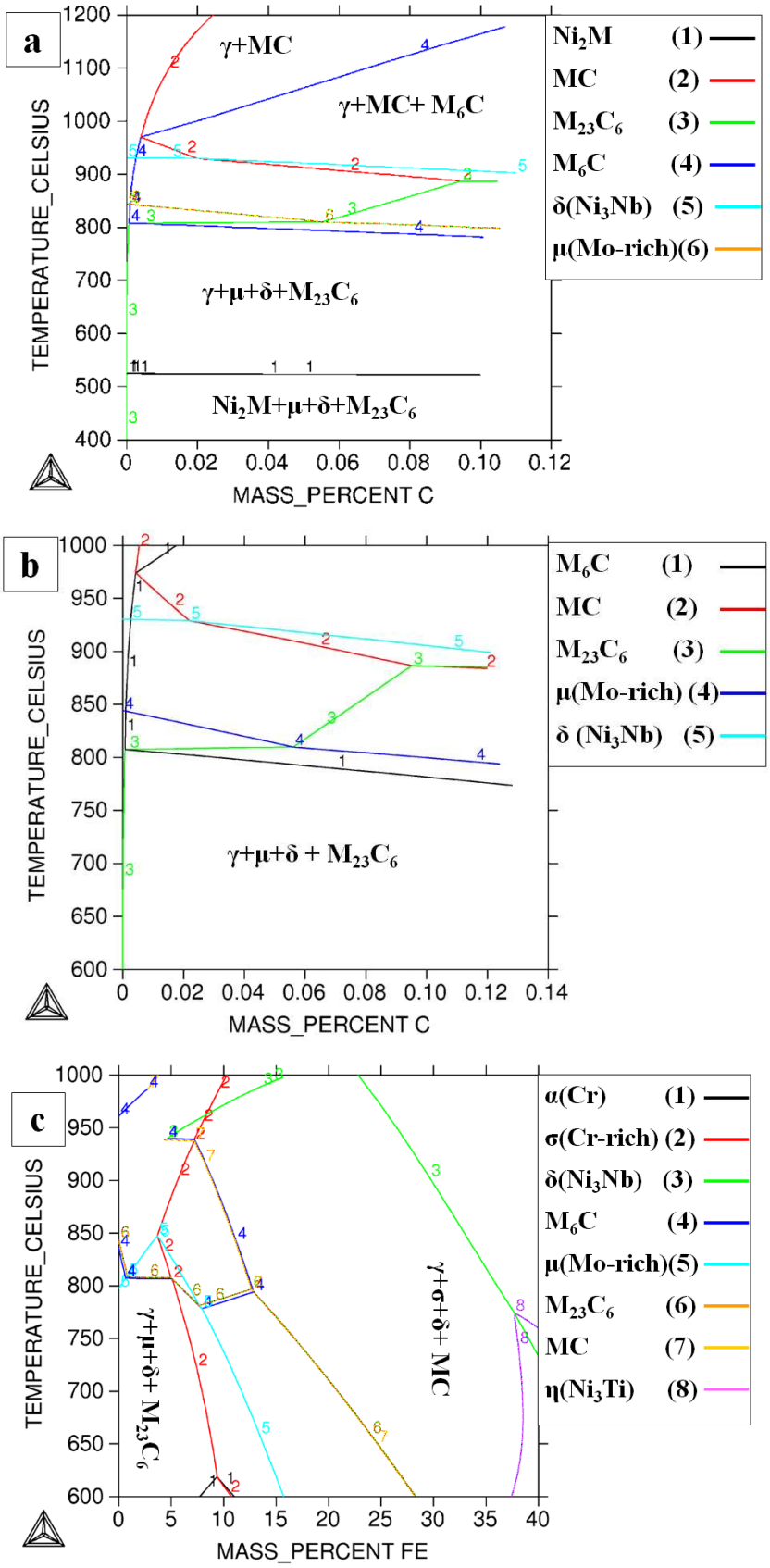

Figure 6-3. Showing different phase diagrams for the wrought IN625 material (Table 6-2); (a) phase diagram of IN625 and carbon between 400˚C and 1200˚C, (b) phase diagram of IN625 and carbon between 600˚C and 1000˚C, (c) phase diagram of IN625 and iron between 600˚C and 1000˚C.

As shown in Figure 6-3(a) and (b) below 800˚C, the stable carbide is $M_{23}C_6$ and there is little solid solution of carbon in the IN625 alloy. The stability regions of three different intermetallic phases in this material are shown by the straight lines because carbon content does not have any significant effect on these minor phases. The Ni_2M phase (line No.1) is stable at temperatures below 500˚C; however, line No.5 shows the stability region of (δ) phase whereas line No.6 is related to the (μ) phase.

The phase diagram for the IN625 alloy with iron is presented in Figure 6-3(c) and shows that above 850˚C, the (μ) phase is not stable while the (σ) phase is stable. However, at 650˚C and iron content less than 8 wt.%, the (μ) phase is stable. Between 8 and 13 wt.% iron, the (σ) phase becomes stable in addition to the (μ) phase and at higher Fe content (>13 wt.%), the (μ) phase is not stable.

6-5- Calculation of phase equilibria in the weld overlay material

The weld overlay is a nickel based similar on composition to alloy IN625 but because of inter-mixing with the steel substrate during deposition, its chemical composition is significantly different from that of the wrought IN625. Based on the experimental observations presented in chapter 4, there are two different regions in this material with different composition which have been termed the bulk and the mixing zones. In this section, the effect of chemical composition and temperature on the stable phases under equilibrium will be described for these regions separately.

6-5-1- Stable phases in the Bulk zone

The chemical composition of the bulk zone in the weld overlay material as obtained by spark emission spectroscopy is given in Table 6-4. The results of calculations for the equilibrium phases using Thermo-Calc are presented in this section. As the composition contains more Fe and C compared to those of the wrought IN625, the Thermo-Calc results for this material can be compared with the phases of the wrought IN625. The composition of stable phases and their mole fractions in the weld overlay and the wrought IN625 at 650˚C are presented in Table 6-5.

Table 6-4. Chemical composition of the weld overlay material in the bulk zone.

Element	*wt.%*	*at.%*
C	0.02	0.1
Ti	0.18	0.22
Cr	20.9	23.9
Fe	8.0	8.5
Ni	Balance	Balance
Nb	3.2	2.0
Mo	8.2	5.1

Table 6-5. Stable phases in the bulk zone of the weld overlay and the IN625 at 650˚C

Phase	*IN625*		*Weld overlay*	
	Composition	*mol.%*	*Composition*	*mol.%*
γ	-	81.95	-	83.36
δ	$Ni_3 (Nb_{0.88} Ti_{0.08} Mo_{0.04})$	8.97	$Ni_3 (Nb_{0.87} Ti_{0.07} Mo_{0.06})$	8.12
μ	$Mo (Cr_{0.52}Ni_{0.47} Fe_{0.01})_2$	8.95	$Mo (Cr_{0.49} Ni_{0.48} Fe_{0.03})_2$	8.04
$M_{23}C_6$	$(Cr_{0.82} Mo_{0.13} Ni_{0.05})_{23}C_6$	0.13	$(Cr_{0.82} Mo_{0.13} Ni_{0.05})_{23}C_6$	0.48

A comparison between the phases in the weld overlay and IN625 at 650˚C shows that the chemical composition of the intermetallic phases and their molar fractions are almost similar. For example, the (μ) phase in weld overlay contains more Fe atoms. The carbide molar fraction in the weld overlay is almost four times that predicted in the wrought material; this ration is approximately the same as the ratio of their carbon levels.

Figure 6-4(a) shows the multiphase diagram of (NPM) versus temperature for the bulk zone in the range of 500 to 1500˚C. This figure indicates that the temperature range for equilibrium solidification is approximately the same as that of the wrought IN625 (see Figure 6-1(a)). However, the precipitation of MC carbide occurs at temperatures above 1100˚C. The carbide transformation process in this material is similar to that of the IN625 but the temperature ranges of their stability are different as indicated in the following equations:

$$MC\ (stable\ at\ T > 930) \rightarrow M_6C(stable\ at\ T < 910)$$

$$M_6C\ (stable\ at\ T > 770) \rightarrow M_{23}C_6(stable\ at\ T < 750)$$

Figure 6-4(b) shows that higher carbon and iron contents in the weld overlay material result in some changes in the stability of different phases compared to those of the wrought IN625 (see Figure 6-1(b)). For example, the MC becomes stable at higher temperature while M_6C carbide transformation temperature is lower compared to that of the wrought IN625 alloy. Nevertheless, there is no significant difference between the precipitation behaviour of the intermetallic phases i.e. (δ) and (μ) in these materials.

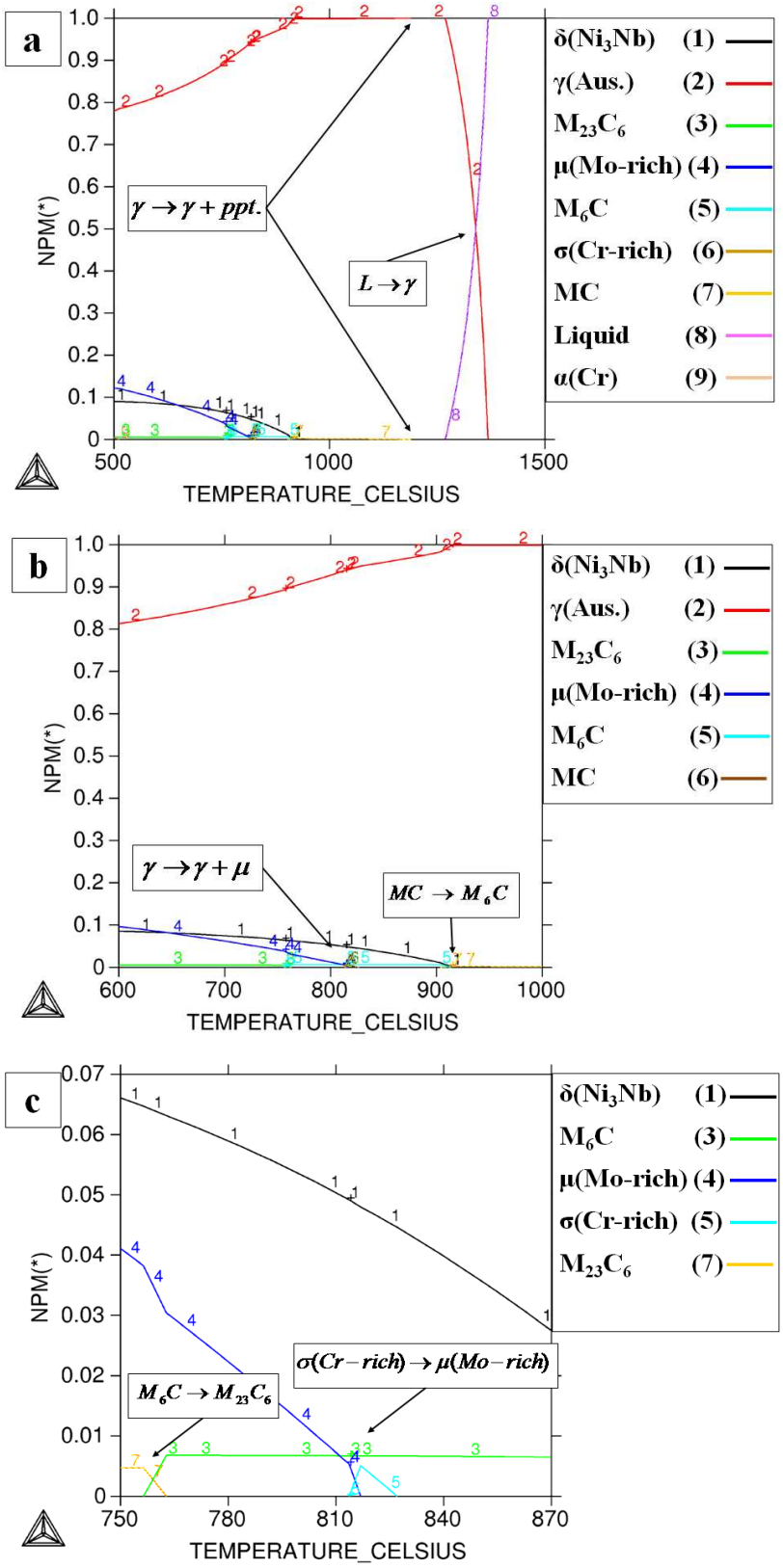

Figure 6-4. Showing plots of mole-fraction of phase (NPM) versus temperature for the equilibrium phases in the bulk zone of the weld overlay material (Table 6-4); (a) indicates equilibrium solidification and precipitation, (b) indicates temperature range for carbide transformation and precipitation of intermetallic phases, (c) indicates carbide transformation temperature at (~760˚C) and (σ) phase transformation to (μ) phase at (~820˚C).

Moreover, the precipitation of the Ni_2M phase is not seen in this range of temperature. However, two different Cr-rich phases i.e. (σ) and α (Cr) phases precipitate at temperatures ~830˚C and ~500˚C respectively. Figure 6-4(c) shows the stability temperature range of the (σ) phase and as seen, it transforms to the (μ) phase at ~820˚C.

6-5-1-1- Effect of carbon on phase equilibria

As seen in the experimental observations, high temperature exposure of the overlaid tube at 650˚C results in microstructural changes due to carbon diffusion. Therefore the effect of carbon content on the stable phases was examined. To show this effect, a multiphase diagram involving changes in carbon content at 650°C along with a temperature – wt.% C phase diagram were calculated. The multiphase diagram of stable phases in the bulk zone versus carbon mass percent at 650˚C is presented in Figure 6-5(a). At the zero point of this diagram, the composition is the same as Table 6-4 but with zero percent carbon. This diagram shows that increasing the carbon content results in an increase of carbide mole fraction at the expense of the (γ) and the (μ) phases. Calculation of equilibrium phases at 650˚C with 0.12 wt.% carbon indicates that the carbide mol.% increases to 2.85 while (μ) phase mol.% decreases to 6.98 compared to values in Table 6-5.

Figure 6-5(b) shows the phase diagram of this material with varying carbon level. Although the phases are similar to those of the wrought IN625 (see Figure 6-3(b)), their stability regions are different. In this diagram there is a stability region for the (σ) phase which is shown with line No.6 and increasing the carbon content results in a reduction in the stability of this phase.

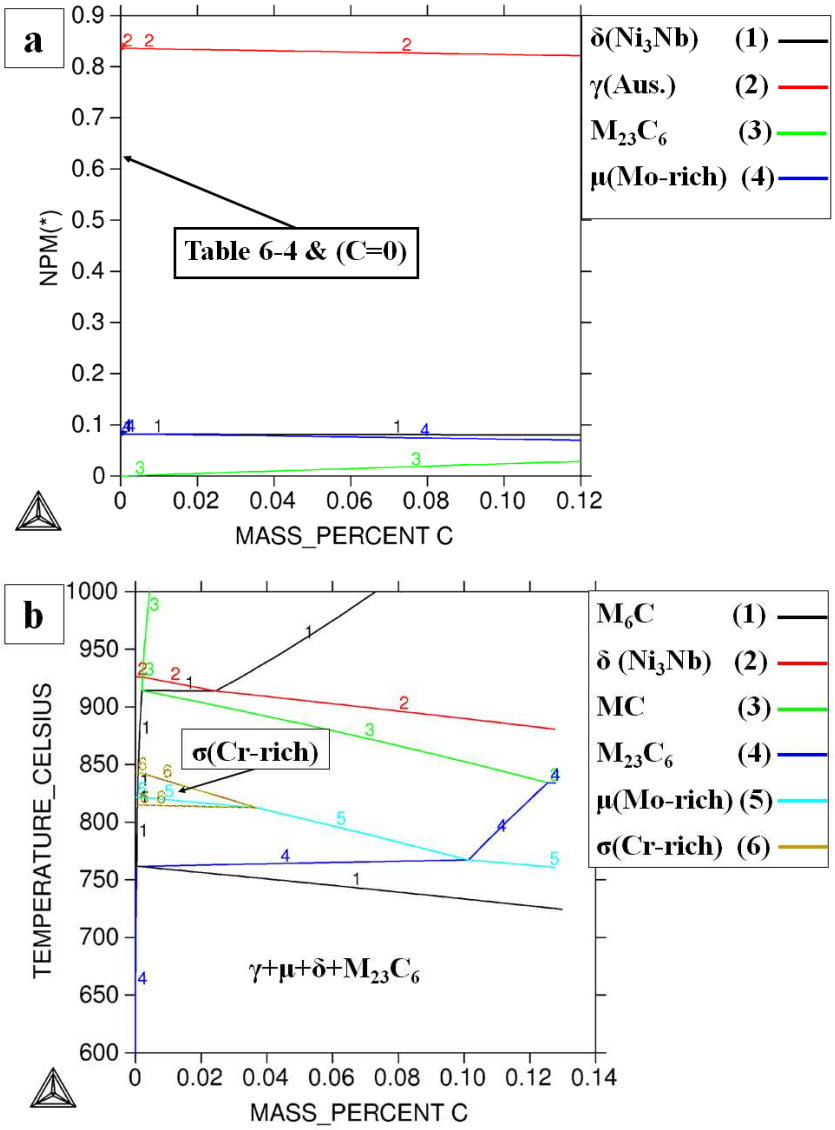

Figure 6-5. Showing different diagrams for the bulk zone of the weld overlay material (Table 6-4); (a) the multiphase diagram versus carbon content at 650˚C indicates increasing the carbide mole fraction at the expense of the (γ) and the (μ) phases, (b) the phase diagram with carbon between 600˚C and 1000˚C indicates stability region of the Cr-rich (σ) phase.

6-5-2- Stable phases in the mixing zone

The Fe content in the mixing zone is higher compared to that of the bulk zone. The definition of chemical composition in the mixing zone is complicated because of a three dimensional interface between the steel and this zone. The EDX results for elements (excluding C) in this region from several analyses at

a distance of ~10 μm from the interface were collected and their mean values are presented in Table 6-6.

Table 6-6. Mean chemical composition of the weld overlay material in the mixing zone as determine by EDX (excluding carbon)

Element	*wt.%*	*at.%*
C	0.02<x<0.1	0.1<x<0.5
Cr	17.4	19.7
Fe	24.8	26.1
Ni	Balance	Balance
Nb	3.1	2.0
Mo	7.0	4.3

Although the Fe level in this zone is greater than in standard nickel alloys, it is believed that TTNI7 database is suitable for high Fe content nickel alloys [178]. To allow simulation of interdiffusion of carbon into the mixing zone during welding, a range of carbon levels is explored in the calculations. The carbon content in this region is investigated in a range between the carbon content of bulk zone (0.02wt.%) and steel (0.1wt%). The Thermo-Calc calculation results for phase equilibria with different carbon content at 650˚C are presented in Table 6-7.

Table 6-7. Stable phases in the mixing zone of the weld overlay at 650˚C with different carbon content.

Phase	*C=0.02 wt.%*		*C= 0.1wt.%*	
	Composition	*mol.%*	*Composition*	*mol.%*
γ	-	81.6	-	82.4
δ	$Ni_3(Nb_{0.97}Mo_{0.03})$	7.4	$Ni_3(Nb_{0.97}Mo_{0.03})$	7.3
σ	$Cr_{0.37}Ni_{0.21}Mo_{0.24}Fe_{0.18}$	10.3	$Cr_{0.37}Ni_{0.21}Mo_{0.24}Fe_{0.18}$	7.1
M_6C	$(Mo_{0.48}Cr_{0.17}Ni_{0.17}Fe_{0.16}Nb_{0.02})_6C$	0.7	$(Mo_{0.48}Cr_{0.17}Ni_{0.17}Fe_{0.16}Nb_{0.02})_6C$	2.7
$M_{23}C_6$	-	0.00	$(Cr_{0.8}Mo_{0.13}Ni_{0.04}Fe_{0.03})_{23}C_6$	0.5

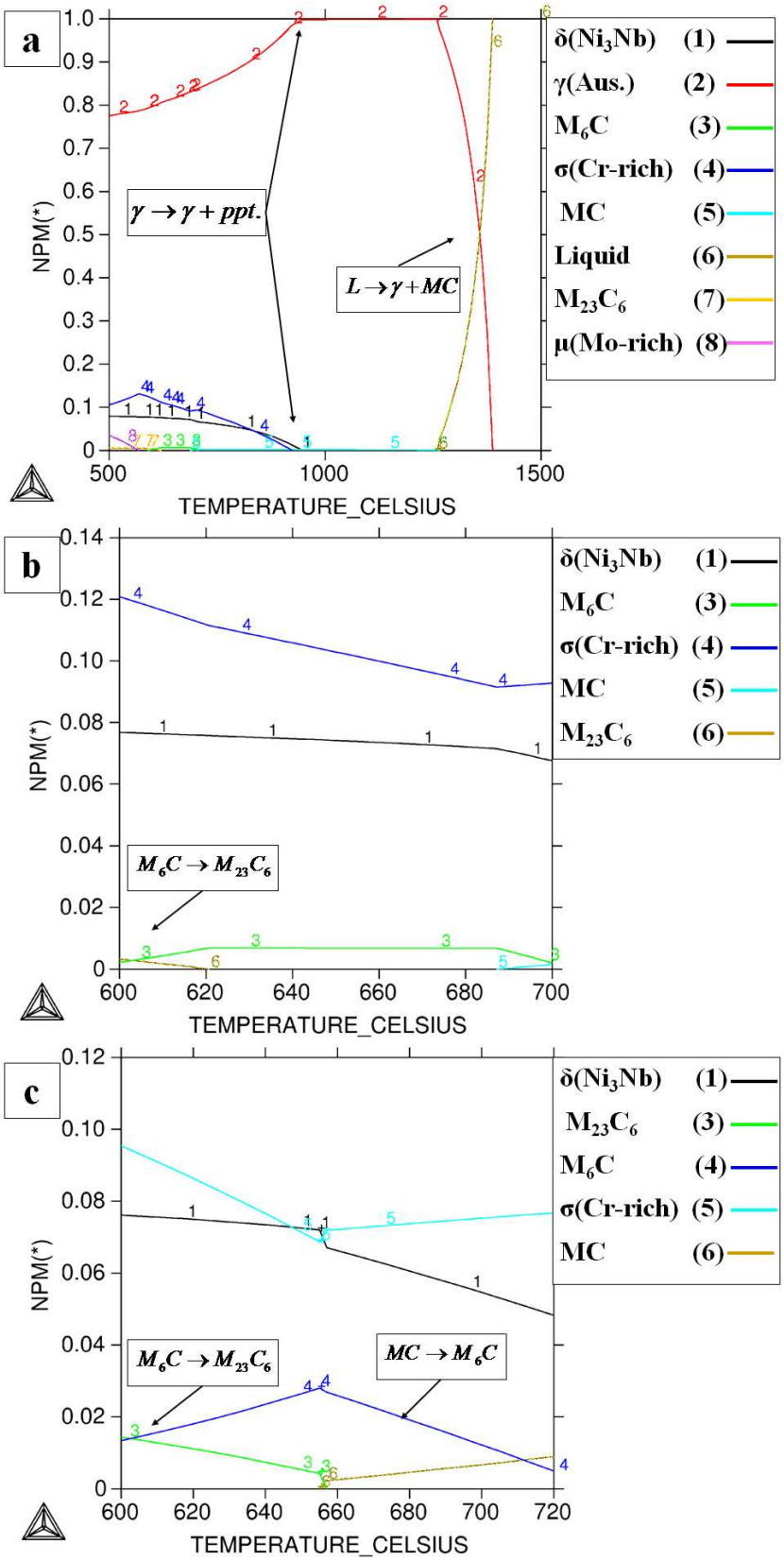

Figure 6-6. Showing plots of mole-fraction of phase (NPM) versus temperature for the equilibrium phases in the mixing zone of the weld overlay material (Table 6-6); (a) indicates equilibrium phases for 0.02 wt.% C, (b) indicates temperature range for carbide transformation for 0.02 wt.% C and (c) indicates stable carbides and transformation temperature for 0.1 wt.% C.

A comparison of the mole fraction of phases in Table 6-7 indicates that increasing the carbon content in the mixing zone results in a higher carbide content, with two different types forming at expense of the (σ) phase. The Cr-rich $M_{23}C_6$ carbide becomes stable in addition to the Mo-rich M_6C carbide.

The multiphase diagrams of NPM versus temperature for the mixing zone with different carbon contents are presented in Figure 6-6. The multiphase diagram with 0.02 wt.% carbon is shown in Figure 6-6(a). The equilibrium solidification behaviour in this material is different compared to that of the bulk zone (see Figure 6-4(a)). As seen in this diagram, at the final stages of solidification, the MC phase becomes stable. It is suggested that equilibrium solidification terminates with following eutectic reaction:

$$L \rightarrow \gamma + MC$$

Considering 0.02 wt.% carbon (see Figure 6-6(b)), the M_6C carbide is the stable carbide at the temperature range of 620 to 690˚C while with 0.1 wt.% carbon (see Figure 6-6 (c)), MC and M_6C are stable above 660˚C and the M_6C and $M_{23}C_6$ carbides are stable below this temperature. The effect of carbon content on the stable phases in the mixing zone can be easily shown using multiphase diagram versus carbon content along with the phase diagram. The multiphase diagram for stable phases versus carbon content at 650˚C in the mixing zone is presented in Figure 6-7(a). An enlarged diagram presented in Figure 6-7(b) indicates that with increasing carbon content, the mole fraction of M_6C carbide increases at the expense of the (σ) phase. Moreover, above 0.06 wt.% C, the $M_{23}C_6$ carbide becomes stable.

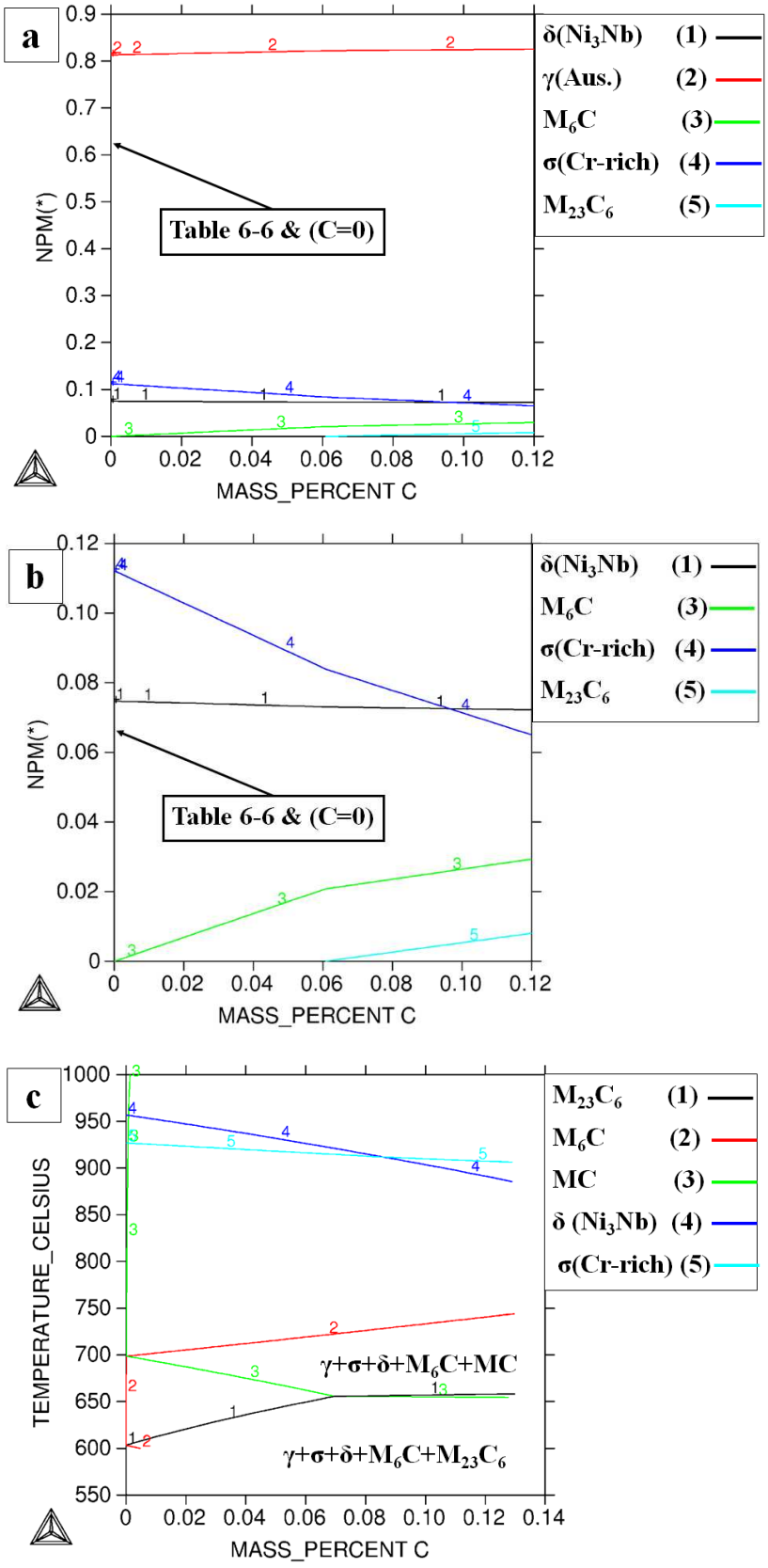

Figure 6-7. Showing different diagrams for the mixing zone of the weld overlay material (Table 6-6); (a) the multiphase diagram NPM versus carbon content at 650˚C, (b) a enlarged diagram indicates increasing the carbide mole fraction at the expense of (σ) phase and (c) phase diagram with carbon mass percent between 600 and 1000˚C indicates the stability regions of different carbides.

Figure 6-7(c) shows the phase diagram for the mixing zone with carbon content. Although the carbide types in this diagram are similar to those of the bulk zone, their stability regions are different (see Figure 6-5(b)). Moreover, the stability region for the (σ) phase (line No.5) is significantly larger than that in the bulk zone.

6-6- Non-equilibrium solidification of weld overlay material

Rapid cooling after welding results in non-equilibrium solidification of weld overlay material which affects phase formation at the final stages of solidification. The Thermo-Calc Scheil module enables a diagram to be plotted which shows mole fraction of all solid phases versus temperature.

6-6-1- Bulk zone

The non-equilibrium and equilibrium solidification behaviours for the composition of the bulk zone (Table 6-4) are shown in Figure 6-8(a) and (b) respectively. In non-equilibrium condition, the temperature range for solidification is between 1370˚C and 1140˚C. In contrast, in the equilibrium condition (Figure 6-8(b)) the temperature range of solidification is between 1370˚C and 1270˚C. Moreover, there are more secondary phases predicted to form during non-equilibrium solidification than under equilibrium freezing. The Scheil model shows that solidification starts at 1370˚C with following reaction:

$$L \rightarrow L + \gamma \qquad \text{Along the Line No.2}$$

This reaction causes enrichment of alloying elements in the remaining liquid and at 1207˚C, the MC carbide starts to form with a eutectic-like reaction (as follows) and therefore the solid phases are γ and MC along the Line No.3

$$L \rightarrow L + \gamma + MC \qquad \text{Along the Line No.3}$$

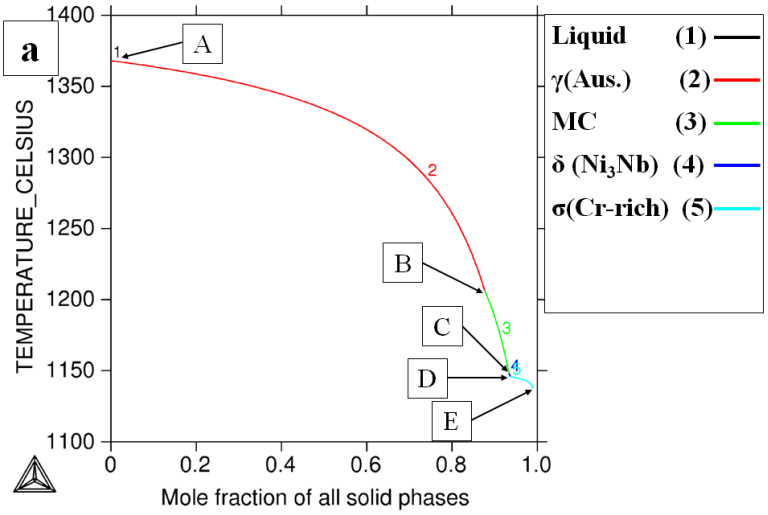

Point	*Temperature(˚C)*	*Liquid mol.%*	*Solid phases*
A	1370	100	-
B	1207	12	γ
C	1148	7	γ + MC
D	1147	6	γ + MC+ δ
	1137	0	γ + MC + δ +σ

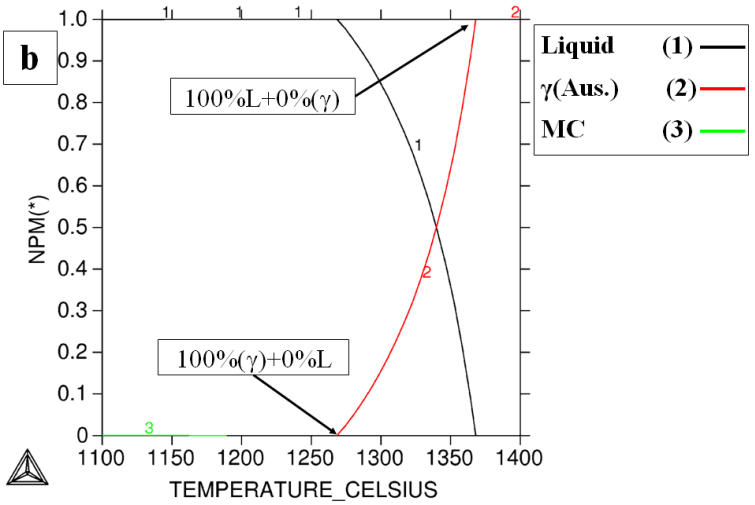

Figure 6-8. Showing different diagrams for the bulk zone of the weld overlay material (Table 6-4); (a) diagram indicates formation of different phases during final stages of the solidification based on the Scheil model, (b) equilibrium solidification diagram.

Further non-equilibrium cooling results in Nb enrichment in the remaining liquid and causes formation of the Nb-rich (δ) at ~1148˚C with the following reaction:

$$L \rightarrow L + \gamma + MC + \delta \qquad \text{Along the Line No.4}$$

Finally, at ~1147˚C, the composition of the remaining liquid is capable for formation of the Cr-rich (σ) phase which is shown with point D. Therefore the final reaction is:

$$L \rightarrow \gamma + MC + \delta + \sigma \qquad \text{Along the Line No.5}$$

Therefore, in the final state, different phases like (γ), (MC), (δ) and (σ) are present in the as-solidified microstructure under non-equilibrium condition (no diffusion in the solid state) while under equilibrium solidification, only (γ) phase is stable. There is an option in the Scheil calculation for the elements to be considered as fast diffusing elements in the solid state. Carbon is the only element that can be considered as fast diffuser. However, calculation in this conditon did not change the predicted phases in the Scheil model.

6-6-2- Mixing zone

The Scheil model calculation results for the mixing zone (Table 6-6) with low carbon content (0.02 wt%) are shown in Figure 6-9(a). As seen in this diagram, the temperature range for non–equilibrium solidification in this material is similar, but secondary phases are different compared to those of the bulk zone. In this composition, MC, Laves and (δ) were firstly formed and the solidification terminates with formation of the (σ) and the (μ) phases.

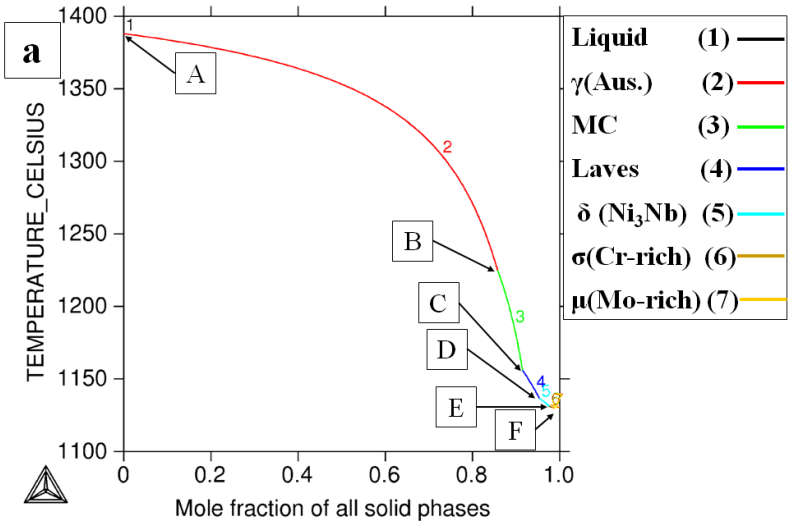

Point	*Temperature(˚C)*	*Liquid mol.%*	*Solid phases*
A	1370	100	-
B	123	15	γ
C	1155	9	γ + MC
D	1147	5	γ + MC + Laves
E	1135	1	γ + MC + Laves + δ
F	1130	0	γ +□M□ + Laves + δ +σ +μ

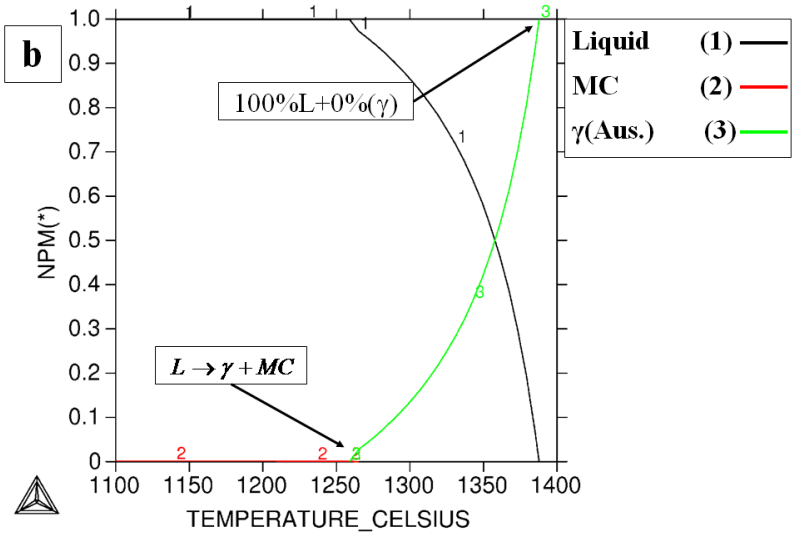

Figure 6-9.Showing different diagrams for the mixing zone of the weld overlay material (Table 6-6) with 0.02 wt.% C; (a) diagram indicates formation of different phases during final stages of the solidification based on the Scheil model, (b) equilibrium solidification diagram.

The equilibrium solidification diagram presented in Figure 6-9(b) shows that MC carbide is predicted to form at the final stages of solidification by a eutectic like reaction. As seen in this diagram, at the final stages of

solidification, the mole fraction of liquid suddenly decreases to zero while (γ) and (MC) carbide phases increase. Therefore, it is suggested that under equilibrium conditions, the solidification terminates with following eutectic reaction:

$$L \rightarrow \gamma + MC$$

Considering carbon as a fast diffuser element has no effect on the results of the Scheil model.

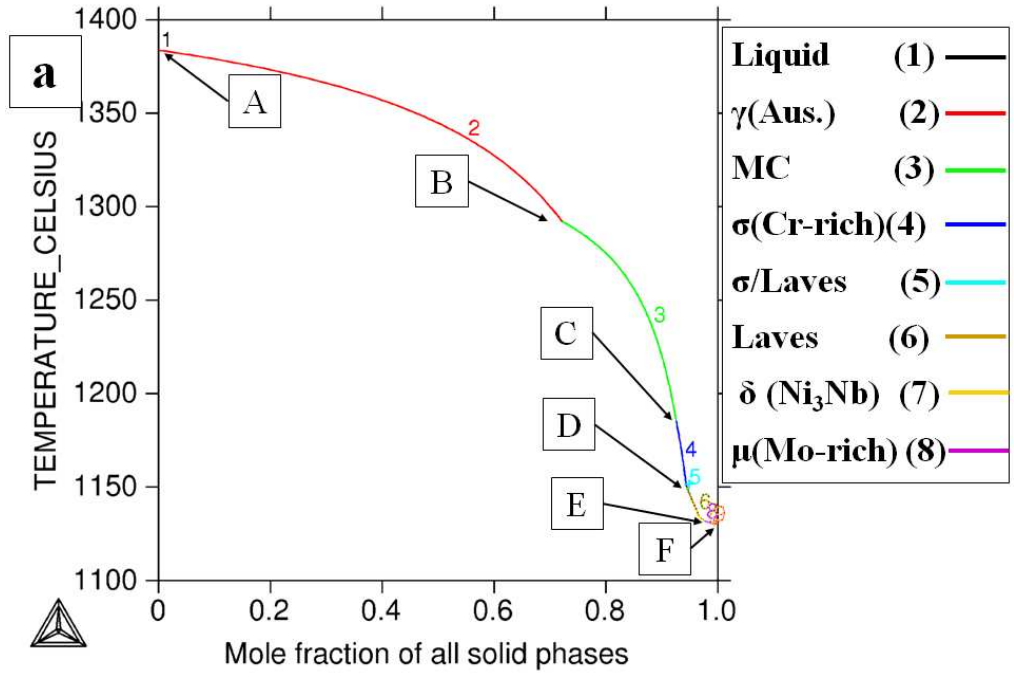

Point	*Temperature(˚C)*	*Liquid mol.%*	*Solid phases*
A	1370	100	
B	1290	28	γ
C	1185	7	γ + MC
D	1150	5	γ + MC + σ
E	1135	3	γ + MC + σ + Laves
F	□130	0	γ + MC +σ + Laves + δ +μ

Figure 6-10. Showing a diagram indicates formation of different phases during final stages of the solidification based on the Scheil model for the mixing zone of the weld overlay material (Table 6-6) with 0.1wt.% carbon .

Although the equilibrium solidification behaviour of the mixing zone is the same for different carbon contents, the Scheil model results are different. The Scheil model results for the mixing zone (Table 6-6) with a high (0.1 wt.%) carbon content are shown in Figure 6-10. It is seen that secondary phases during solidification under non-equilibrium condition are different compared to those of the low carbon material. Increasing the carbon content causes formation of (σ) phase after (MC) phase. At point D (point No.5), formation of σ phase stopped and Laves phase formed from the remaining liquid which is shown by line No.6.

6-7- Calculation of stable and metastable phase equilibria in 2.25Cr1Mo steel

Analysis of the stable phases in the 2.25Cr1Mo steel (the substrate material of the weld overlaid tube) is presented in this section. The chemical composition of this steel is shown in Table 6-8. The thermodynamic calculations were carried out using the TFEC6 database.

Table 6-8.Chemical composition of 2.25Cr1Mo steel substrate as determined by spark emission spectroscopy

Element	*wt.%*	*at.%*
C	0.10	0.46
Si	0.24	0.48
Cr	2.33	2.5
Mn	0.43	0.43
Fe	Balance	Balance
Cu	0.11	0.1
Ni	0.1	0.1
Mo	0.92	0.53

6-7-1- Effect of temperature on the stable phases

Thermo-Calc calculations for stable phases at 650˚C results in the following phases being predicted to form (in mol. %):

1) BCC_A2#1 (α) : Ferrite - 97.77
2) M23C6#1 ($M_{23}C_6$ Carbide) : $(Cr_{0.50}Fe_{0.39}Mo_{0.11})_{23}C_6$ - 2.23

Referring to section 2-3-2, the stable carbide in this steel is dependent upon the temperature. Therefore, a multiphase diagram of phase fraction versus temperature is an appropriate method to display carbide type. The multiphase diagrams of phase mole fraction (NPM) versus temperature with different temperature ranges are presented in Figure 6-11. The equilibrium solidification in low carbon steels terminates with the following peritectic reaction:

$$L + \delta \rightarrow \gamma$$

Figure 6-11(a) shows this reaction in the temperature range between 1450 to 1470˚C. Moreover, the eutectoid transformation (as follows) at temperature below 800˚C is indicated in this diagram.

$$\gamma \rightarrow \alpha + carbide$$

Based on the experimental results, it is clear that this diagram shows the effect of heating up during welding. In other words, the extent of HAZ can be related to the stability region of the (γ) phase which is between ~ 850˚C and ~1450˚C.

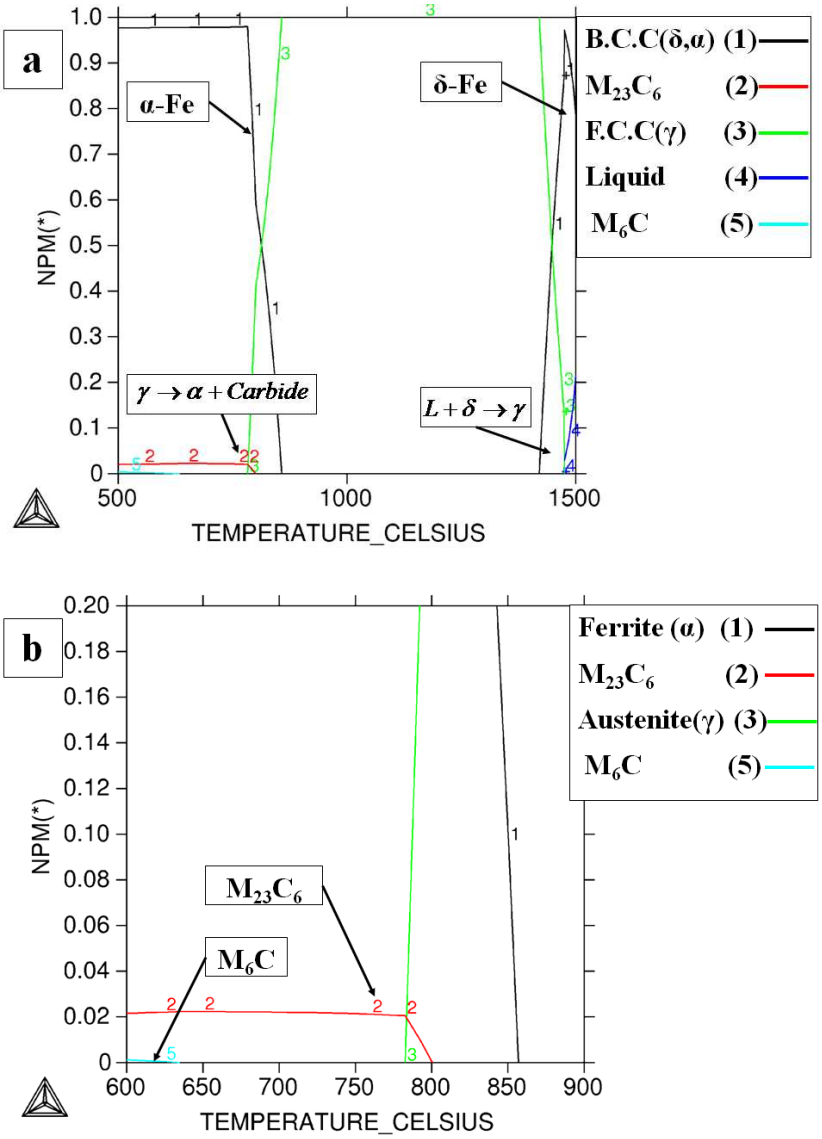

Figure 6-11. Showing plots of mole-fraction of phase (NPM) versus temperature for the equilibrium phases in the 2.25Cr1Mo steel (Table 6-8); (a) indicates equilibrium peritectic solidification transformation and eutectoid carbide formation, (b) indicates temperature range for stability of different carbides in the microstructure of steel.

6-7-2- Metastable phase equilibria

It is well known that the microstructure of the 2.25Cr1Mo steel in industrial applications and after normalization is bainitic (see section 2-3-1) which is a metastable structure. Moreover, as shown in section 2-3-2, the carbide type in this steel changes during the ageing process and ageing at temperatures above 630˚C results in precipitation of the Cr-rich $M_{23}C_6$ carbide.

Based on the experimental observations of the as-welded sample (see section 4-3-4), the lath-like microstructure of the HAZ contains metastable carbide. Therefore, it suggested that the initial carbide in this state is cementite. In order to establish which metastable carbides could potentially form in the microstructure, the stable carbide should be suspended from the calculation at a specified temperature and this procedure repeated for all available carbides in the database.

Thermo-calc software results show that in the 2.25Cr1Mo steel at 650˚C; when Cr-rich $M_{23}C_6$ is not stable, the M_7C_3 and M_6C are stable and instability of M_7C_3 leads to stability of Cr-rich M_2C. Moreover, instability of Cr-rich M_2C carbide results in the stability of (Cr, Fe)-rich M_3C [CEMENTITE#1] and (Fe, Mo)-rich M_3C [KSI CARBIDE]. Finally, when KSI is not stable, it transforms to CEMENTITE#1. Nevertheless, instability of M_6C causes stability of Mo-rich M_2C; and instability of this carbide have a similar result.

Considering the chemical composition of these carbides from Thermo-Calc calculations, the carbide transformation process can be related to the enrichment of alloying elements (Cr and Mo) in the carbide phase. The carbide transformation process can be summarized in the following reactions where alpha represents coexisting B.C.C. iron.

$$\alpha_1 + (Cr_{0.53}Fe_{0.44}Mn_{0.02}Mo_{0.01})_3C$$

$$\rightarrow \alpha_2 + (Cr_{0.55}Fe_{0.42}Mn_{0.02}Mo_{0.01})_3C + (Fe_{0.58}Mo_{0.29}Cr_{0.13})_3C$$

$$\rightarrow \alpha_3 + (Cr_{0.63}Mo_{0.35}Fe_{0.02})_2C$$

$$\rightarrow \alpha_4 + (Mo_{0.8}Cr_{0.2})_2C + (Cr_{0.7}Fe_{0.23}Mo_{0.07})_7C_3$$

$$\rightarrow \alpha_5 + (Mo_{0.54}Fe_{0.37}Cr_{0.06}Si_{0.03})_6C + (Cr_{0.7}Fe_{0.23}Mo_{0.07})_7C_3$$

$$\rightarrow \alpha_6 + (Cr_{0.49}Fe_{0.39}Mo_{0.12})_{23}C_6$$

It is known that at 650˚C, the Cr-rich M_3C is not stable and above reactions indicate how it transforms to different types of the Cr-rich and the Mo-rich metastable carbides. It is clear that the Cr-rich carbides have different metastable states compared to those of the Mo-rich carbides. Moreover, changing the carbide type from the (Cr, Fe)-rich M_3C to the equilibrium $M_{23}C_6$ affects the coexisting ferrite composition as well as the molar fraction of carbide which are shown in Table 6-9.

Table 6-9.Ferrite compositional changes with carbide transformation

Ferrite type	*Cr(wt.%)*	*Mo(wt.%)*	*Carbide type*	*Carbide mol.%*
α_1	1.68	0.91	(Cr-rich)M_3C	1.83
α_2	1.85	0.66	(Cr-rich)M_3C+(Mo-rich)M_3C	1.83
α_3	1.81	0.38	(Cr-rich)M_2C	1.37
α_4	1.73	0.66	M_7C_3+(Mo-rich)M_2C	1.52
α_5	1.72	0.54	M_7C_3+M_6C	1.72
α_6	1.55	0.57	$M_{23}C_6$	2.23

6-7-3- Effect of carbon content on the stable phase equilibria

The experimental results (Chapter 5) show that the near-HAZ region decarburized during high temperature exposure at 650˚C. Thermo-Calc was used to explore the effect of changing carbon content on the stable phases.

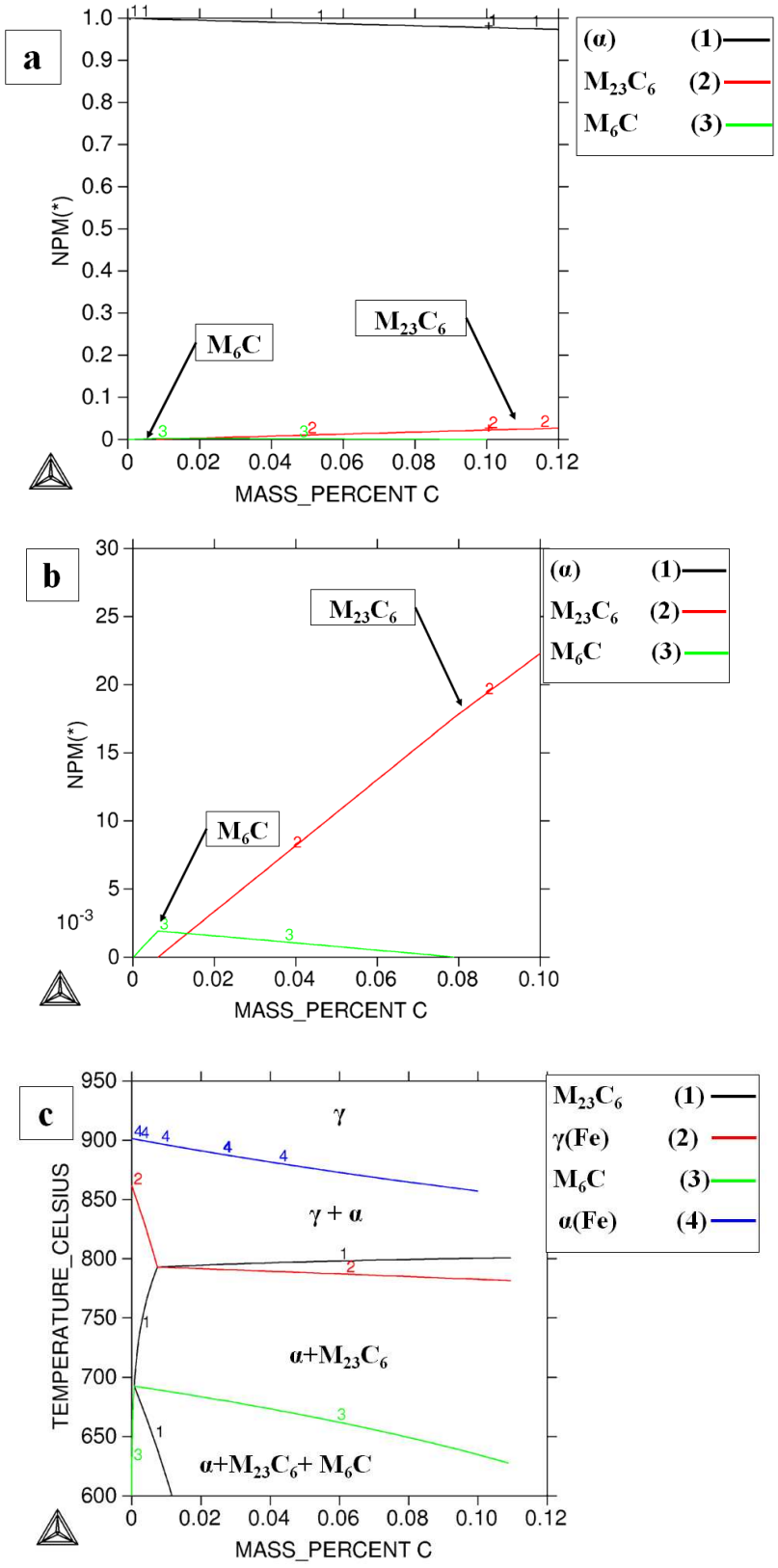

Figure 6-12. Showing different diagrams for the 2.25Cr1Mo steel (Table 6-8); (a) the multiphase diagram versus carbon content at 650˚C, (b) indicates changing carbide type and increasing the $M_{23}C_6$ carbide molar fraction with carbon content at 650˚C and (c) phase diagram with carbon between 600˚C and 950˚C indicates the stability regions of different carbides types.

The multiphase diagram of NPM versus carbon content at 650 °C is shown in Figure 6-12(a) and (b) which indicate that at low carbon levels, the stable carbide is M_6C which changes to the $M_{23}C_6$ with increasing carbon content. The phase diagram of 2.25Cr1Mo steel with carbon is shown in Figure 6-12(c). It is seen that decarburizing of steel in the near-HAZ region results in a changing in the carbide type and stability of M_6C carbide at 650˚C. It is clear that stability of M_6C carbide affects the composition of coexisting ferrite.

A calculation was carried out with a similar composition but very low (0.005 wt.%) carbon content to analyse the ferrite composition. The results are as follows in mol.%:

1) Ferrite : (α) [Mo: 0.79 wt.%, Cr: 2.32 wt.%]- 99.84

2) M_6C Carbide : $(Mo_{0.55}Fe_{0.37}Cr_{0.06}Si_{0.02})_6C$ - 0.16

In summary, Thermo-calc software is a useful tool for understanding of equilibrium phases in different materials. Thermodynamic calculations can be used to indicate the stability regions of interesting phases and the effects of chemical composition and temperature on these regions. Moreover, the Scheil module show solidification behaviour under non-equilibrium conditions and phase formation during final stages of this process.

Chapter 7

Discussion and conclusions

7-1- Introduction

In this chapter, the main aspects concerning the microstructural evolution following high temperature exposure in the weld overlay and steel substrate are discussed. The microstructural evolution in different regions (presented in chapter 5) is discussed with reference to the as-welded condition. The size, shape and type of precipitates in both materials are discussed in detail. Emphasis is given to the carbon migration across the interface and its effect on the phase transformation in both materials. The kinetics and thermodynamics relating to nucleation, growth and phase transformation in both the weld overlay and the steel are considered. The precipitate transformations in different regions of the steel and the weld overlay and their effects on the matrix microstructure are discussed.

This chapter is divided into four main sections; in the first section microstructural changes in the steel region are discussed. In this section, a model for carbon supply which considers formation of a carbide network at the interface will be presented. The following section is related to the microstructural evolution in the weld overlay and finally a summary will be presented.

7-2- Microstructural evolution in the steel substrate

As shown in section 2-3-2, the microstructure of 2.25Cr1Mo steel in the normalized and tempered condition consists of almost equal portions of bainite/tempered bainite and proeutectoid ferrite grains [66, 179]. During ageing or service at high temperature, the morphology, distribution and type of carbides in this steel will change depending on the time and temperature. There are different arguments regarding equilibrium carbide and transformation sequences during ageing. In this work, the equilibrium carbide is considered to be $M_{23}C_6$ for both bainitic regions (as presented by Race [58]) and for ferrite grains (as presented by Yang [43]).

In this system, two essential issues should be considered for understanding the microstructural evolution in the steel region following the high temperature exposure.

1) Welding of the nickel alloy material on the steel substrate causes microstructural changes in the HAZ region. Therefore, based on the work of Thomson and Bhadeshia [60, 61], carbide transformation rates

in the HAZ following high temperature exposure is different to those of the central zone.

2) The steel has a fusion bond to a nickel alloy with higher Cr and Mo contents and carbon migration occurs across the interface during the high temperature exposure experiments. The carbon migration may cause further modifications to the carbide transformation process.

In this work, carbide transformation and carbon migration occurs simultaneously. In following section, the carbide transformations in the central zone and HAZ region are presented and effect of carbon migration is discussed later with a carbon supply model.

7-2-1- Carbide transformation in the central zone

The observations of the central zone reveal that there are some blocky precipitates present in the TM/B areas and fine precipitates within the ferrite grains. Although the hardness and etched micrographs of samples with different ageing times are the same in this zone, there are significant differences between precipitates in the BSE micrographs. The BSE micrograph did not reveal any precipitates in the D1 sample. However, in the D8 sample, some coarse blocky particles along grain boundaries with brighter contrast were observed (see Figure 5-27). Increasing exposure time to 32 days resulted in precipitation of some dark precipitates in addition to these bright precipitates along grain boundaries (see Figure 5-30).

Referring to Figure 5-38, it is clear that dark and bright precipitates have grown with increasing exposure time to 64 days. However, a comparison of the BSE micrographs of the D64 and the D128 samples indicates that the population of dark and bright precipitates have decreased with increasing exposure time. Moreover, a comparison of the SE micrographs in the D8 (Figure 5-36) and the D128 samples (see Figure 5-37) indicates transformation of a large number of needle shape precipitates to a few precipitates with more rounded shapes within the ferrite grains.

Thermodynamic calculation for stable phases were used to predict carbide transformation sequence in a similar manner to the work of Saroja [153]. Successively less stable carbides and their mole fraction (mol.%) were determined using Thermo-Calc and TCFE6 database. The calculation results for this steel in section 6-7 shows that the equilibrium carbide is $(Cr_{0.49}Fe_{0.39}Mo_{0.12})_{23}C_6$ with 2.22 mol.% at 650˚C, and Figure 7-1(a) shows the less stable carbides which are predicted with their mole fraction with the least stable carbide being Cr-rich M_3C.

These facts should be considered with the following important observations concerning the carbide transformation process:

1) The M_2C precipitates have an acicular shape and are very small in size [53, 180].

2) It is reported that thermal ageing at 580 to 630˚C for durations less than 10,000 hours could not lead the transformation of metastable carbides to the equilibrium carbide [56]. Moreover, based on TTT

diagram of this steel presented by Robson and Bhadeshia [169, 181] the $M_{23}C_6$ carbide is not seen before 1000 hours at 650˚C.

3) There are different arguments about stable carbides in the mid-term aged samples (up to 500 hours at temperatures between 630˚C to 650˚C). Some argued that the stable carbide is Mo-rich M_6C [44, 53, 130, 180]. However, others [43, 60, 170, 181] argued that Cr-rich M_7C_3 and $M_{23}C_6$ carbides are the dominant carbides. Moreover, metastable carbides formation affects the composition of the coexisting ferrite [153, 170].

4) Some researchers believe that the Mo content in precipitates increases with exposure time at 540˚C [44] while there are other reports that stated that the Mo content in precipitates first increased with ageing time and then decrease with long term ageing [46, 153] which caused Mo replenishment in the coexisting ferrite [48].

Based on calculation in appendix No.2, the Mo-rich carbides (M_2C and M_6C) have a higher mean atomic number than the matrix and are thus brighter in BSE micrographs, while the Cr-rich carbides (M_7C_3 and $M_{23}C_6$) are darker than matrix in BSE imaging. However, the mean atomic number of the alloyed $M_{23}C_6$ carbide is close to that of matrix and therefore this carbide is not visible in BSE micrographs. Moreover, due to presence of Mo atoms in (M_3C) carbides, these are not visible in BSE micrographs.

Bright precipitates with a blocky shape in the D8 sample are attributed to the Mo-rich M_6C carbide; fine acicular precipitates within ferrite grains are suggested to be M_2C carbide. Increasing the exposure time promotes

formation of Cr-rich M_7C_3 and Mo-rich M_6C carbides. These carbides have grown with increasing exposure time up to 64 days. However, in the D128 sample Cr-rich M_7C_3 carbides and Mo-rich M_6C dissolved in the matrix and the equilibrium alloyed $M_{23}C_6$ is formed at their expense.

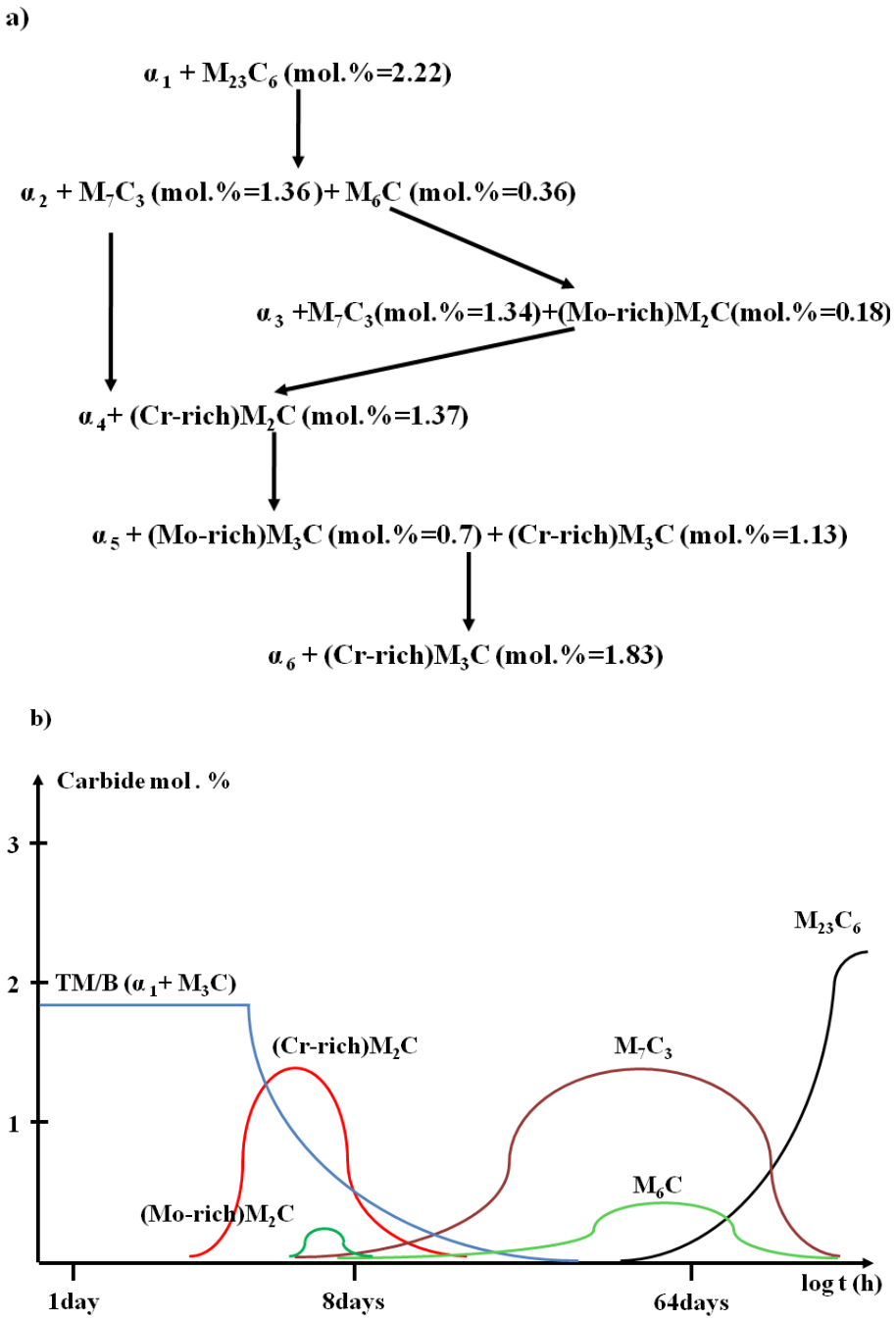

Figure 7-1. Showing schematic diagrams for the carbide transformation in the central zone; (a) indicates carbide transformation prediction using Thermo-Calc, (b) indicates carbide transformation in TM/B areas with exposure time based on experimental observations of the central zone.

The transformation of carbides within the ferrite grains is different and M_2C carbides transform directly to the $M_{23}C_6$ with increasing exposure time. A new model considering both Cr-rich and Mo-rich carbides as metastable and $M_{23}C_6$ as the equilibrium carbide for TM/B areas is presented in Figure 7-1(b) and it is clear that these sequences are not seen in the ferrite grains.

7-2-2- Carbide transformation in the HAZ region

It is known that welding processes alter the microstructure in the heat affected zone (HAZ) and generate a complex microstructure which results in a significant variation in ageing behaviour [62]. Therefore, carbide transformation in this region has different sequences compared to that of the central zone. The microstructure of the HAZ is dependent on the heat input, the welding procedure and the post weld heat treatment. The state of the HAZ affected by welding process is shown schematically in Figure 7-2.

Bhadeshia reported that normalization (cooling form the austenite) in the bulk material results in formation of bainite in this steel [42]. Moreover, Race [58] and Bergquiest [64] and Laha [182] indicated that the weld metal of 2.25Cr1Mo has a fully bainitic microstructure. Nevertheless, it is reported that metallographic analysis of the HAZ adjacent to the fusion boundary in the dissimilar weld joints [63, 65] revealed a bainitic structure consisting of laths of ferrite with aligned carbide precipitates between the laths with no pro-eutectoid ferrite. There is a report which mentioned that the Mo-rich carbides (M_2C and M_6C) are not seen in the HAZ after long term service [66].

The experimental observations of the as-welded sample confirmed that bainite was formed in the HAZ region (Figure 4-7). The hardness profile can be related to the carbon content in the new bainite which was formed in this region after welding and is dependent upon austenitisation temperature.

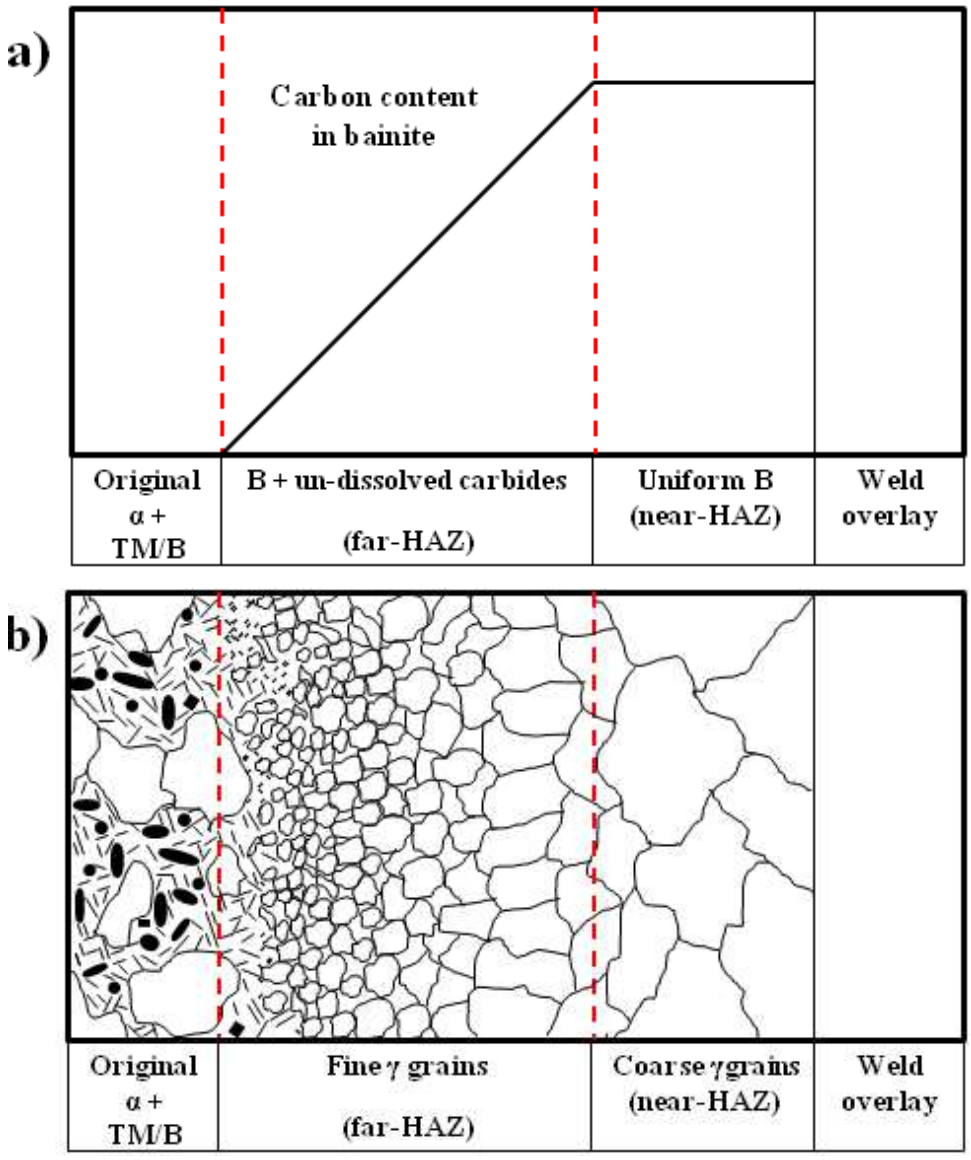

Figure 7-2. Showing schematic diagrams for the HAZ microstructure affected by welding; (a) indicates carbon content in the new bainite based on the hardness survey, (b) different γ grains in the near-HAZ and the far-HAZ regions during welding process (i.e. at elevated temperatures).

Figure 7-2(a) shows the carbon content in bainite based on hardness values and the width of the near-HAZ region (Figure 5-4(b)). Referring to results on TIG welding of 2.25Cr1Mo steel [62, 65], the fully bainitic region hardness is

about ~450 kgf mm^{-2} and the width of this region is about 300 μm in both studies. However, the width of non-uniform bainite is reported to be from about 300 μm [62] to zero[65].

Figure 7-2(b) is based on former research introducing prior coarse grain austenite region adjacent to interface and prior fine grain austenite region away from the weld interface [63, 149]. Moreover, it is reported that number of carbides in the fine grain zone is higher than coarse grain zone and tend to be coarser [63]. This diagram indicates differences in the HAZ region in the as-welded sample. Therefore, it is suggested that a metastable structure of bainite with different levels of carbon will vary in their decomposition. Moreover, the presence of carbides in the far-HAZ region results in different sequences in the carbide transformation.

The hardness profiles of the D1 and the D8 samples are comparable with other research on 2.25Cr1Mo steel with an Inconel 182 nickel alloy filler. Nicholson [140] reported the hardness after ageing at 630˚C decreased to a range of 220 to 230 kgf mm^{-2} within 200 h. Moreover, Bhaduri [143] mentioned that the hardness values decreased to 200 ~ 210 kgf mm^{-2}after 10 h ageing at 630˚C.

In the HAZ region of the D1 sample, the SE micrographs show a large number of fine precipitates and very small ferrite grains (less than 2 μm). However, BSE micrographs indicate that a few bright precipitates are present only in the far-HAZ region. SE micrographs of the D8 sample indicate growth of ferrite grains (about 10 μm) in the near-HAZ region and coarsening of precipitates in the far-HAZ region. Moreover, BSE micrographs of the D8 sample show a few acicular bright and fine dark precipitates in the near-HAZ region. The

number of these precipitates in the far-HAZ region is significantly higher. It should be noted that some regions adjacent to the interface decarburized in the D8 sample which will be discussed later.

The near-HAZ region decarburized very quickly between 8 days and 12 days of exposure but changes in the far-HAZ region were not noticeable. The hardness profile and microscopic observation of the D16 and the D32 samples indicate that the decarburization width is equal to the near-HAZ region and did not change with exposure time. The optical microscope and SE micrographs of these samples in the far-HAZ region are similar to the D8 sample. However, BSE micrographs of the near-HAZ region in the D16 and the D32 samples indicates that bright precipitates have grown and the dark precipitates have become less with increasing exposure time.

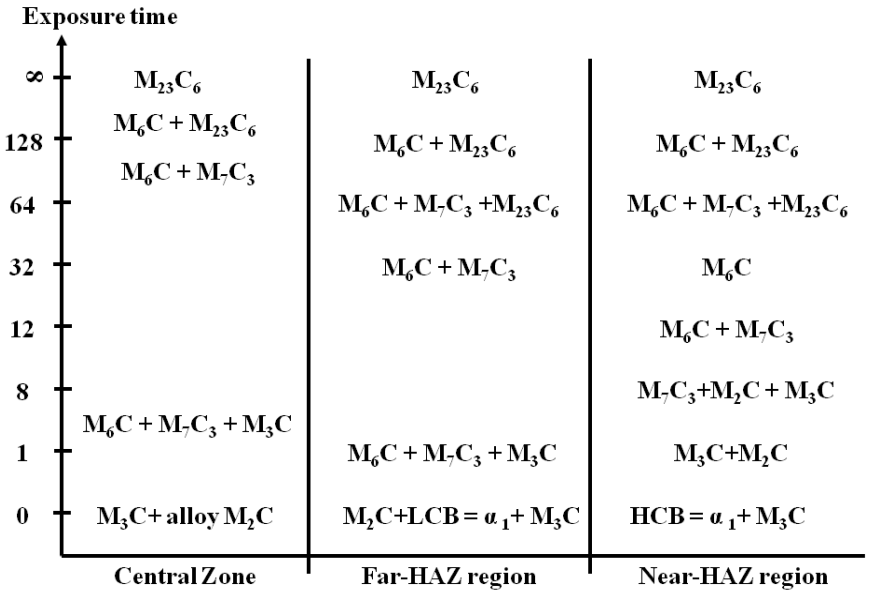

Figure 7-3. Showing stable carbides in different regions of the steel with increasing exposure time indicates different sequences in carbide transformation.

Finally, hardness surveys indicated that the near-HAZ region re-hardened in the D64 sample and little changes occurs in the hardness profile with

increasing exposure time. Moreover, many fine dark and coarse bright precipitates were observed in the BSE micrographs of this region in the D64 sample which become fewer in the D128 sample. These evidence confirmed that carbide transformation sequences in the HAZ region are similar to those of the central zone.

However, there are different rates in these sequences which are shown in Figure 7-3. This diagram shows stable carbides for the different regions and their transformation with exposure time based on observations and is in accord agreed with the following former research:

1) Parameswaran [46] found that bainite dissolution rate is related to its carbon content and higher carbon content shows more resistance to dissolution.

2) There is a report that carbide transformation occurs at a slower rate in a mixed microstructure of bainite and allotrimorphic ferrite compared to that of a fully bainitic microstructure [60, 61].

3) The type of carbides in equilibrium is agreed with the Wada report [168]. However, carbon content [46, 180] is an important factor in the carbide transformation. For example, Thomson found that in low carbon content, M_7C_3 carbide is stable at the expense of M_3C [60]. Moreover, Natesan [180] reported that in low carbon content the Mo-rich M_6C carbide is stable.

It is known that these different carbides are affected by carbon migration process and in the next section a new model is developed to explain experimental results for decarburization of steel region.

7-2-3- Carbon migration

It is known that carbon migration occurs across the weld interface in the dissimilar weld joint from the low alloy steel to the high Cr material [67, 128, 139, 143, 183, 184]. The temperature range of 500 to 700˚C results in depletion of carbon in the area adjacent to the interface in the low alloy steel which is called soft zone or carbon depleted zone (CDZ) [129, 131, 139]. The soft zone is characterized by lower hardness and its width is varied depending on the composition of materials as well as temperature and time of exposure. Many researchers argued that growth of decarburized zone width (η_α) between austenitic and ferritic steels joints [67, 128, 134, 139] follow parabolic kinetic with time (t) according to following equation:

$$\eta_\alpha \propto \sqrt{t}$$

However, Race [58] reported that in ferritic steels joints, the decarburized zone width growth is not a parabolic function of the time. The carbon migration is a diffusion process and occurs according to the profile of chemical potential of carbon [185] and is not related to the carbon concentration. However, carbon concentration profile in the steel region, $C_{(X, t)}(s)$ is used for showing of the decarburization process. Haung [67] approximated the carbon concentration profile in the steel region by following equation in a ferritic steel/nickel alloy system:

$$C_{(X,\ t)}(s) - C_f(s) = \left[C_0(s) - C_f(s)\right] \mathrm{erf}\left(\frac{X}{2\sqrt{D_C\, t}}\right)$$

where $C_0(s)$ and $C_f(s)$ are carbon concentrations in the initial and the decarburized states and D_C is the carbon diffusion coefficient and t is exposure time. The flux of carbon out of the steel is equal the carbon flux into the weld overlay (i.e. changes in both sides must satisfy following equation):

$$D_C\ [C_0(s) - C_f(s)]^2 = D_W\ [C_0(w) - C_f(w)]^2$$

where $C_0(w)$ and $C_f(w)$ are carbon concentration in the initial state and carburized zone in the nickel alloy and D_W is the carbon diffusion coefficient in this material.

Carbon diffusion coefficient is an important parameter and is dependent upon its concentration [185] and the presence of other alloying elements and temperature [67]. The carbon diffusion coefficient (D_C^0) in ternary Fe-Cr-C is reported as $1.05X10^{-11}$ m^2/s while for the 2.25Cr1Mo steel is reported to be $1.58X10^{-11}$ m^2/s. The apparent D_C increased to $2.85x10^{-9}$ m^2/s in the soft zone with carbon concentration less than 0.002 at.% at 750˚C [185]. Pavlovsky [127] reported experimental values for carbon diffusion coefficient in a specific ferritic/austenitic steel dissimilar joint as a function of temperature which is $3.16X10^{-14}$ m^2/s at 650˚C. These different values of D_C^0 in this system will be used to describe carbon supply model.

7-2-3-1- Thermodynamic prediction

Thermo-Calc calculation results show that the chemical potential of carbon in the steel depends upon the carbide type and carbon content. These data are

shown schematically in Figure 7-4(a). As shown in the initial state where the (Fe, Cr)-rich M_3C is stable, carbon chemical potential is $\mu_0(s)$= -2.5E+04 while in the equilibrium state with alloyed $M_{23}C_6$ is $\mu_e(s)$= -3.3E+04. Moreover, in the low carbon content (0.005 wt.%) with M_6C is $\mu_f(s)$= -4.1E+04. Nevertheless, the chemical potential of carbon in the bulk zone of weld overlay region is $\mu_0(w)$= -8.26E+04 while in the mixing zone with the same carbon content is -7.97E+04. Increasing the carbon content of mixing zone to about 0.1 wt.% rises carbon chemical potential to $\mu_e(w)$= -7.9E+04.

The carbon migration during welding is not considered and carbon concentration profile in the as-welded condition is shown in Figure 7-4(b). Since the carbon activity in the steel is higher than that of the weld overlay, it is predicted that carbon atoms will diffuse from steel into this material. Moreover, decarburization should continue indefinitely due to higher chemical potential.

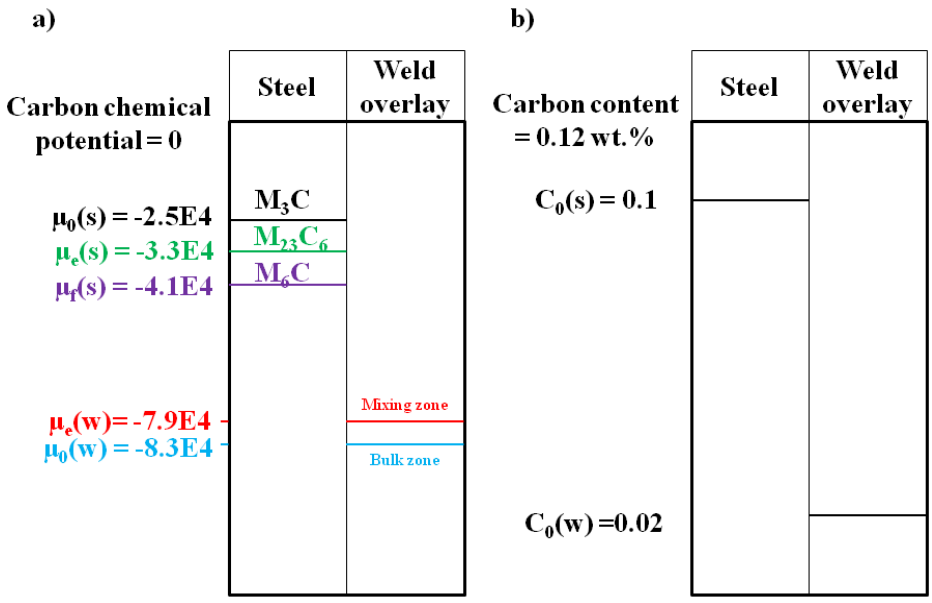

Figure 7-4. Showing schematic diagrams indicates carbon chemical potential and carbon concentration in the as-welded sample.

7-2-3-2- Carbon supply model

Based on the experimental observation, the decarburized region growth in this system has different rates. Moreover, there is a carbon migration across the interface and the carburized zone includes a narrow region of the steel. After a period of time, the carbon migration stopped at the interface while redistribution of carbon within the steel region continued. In order to explain the apparent inconsistencies between experimental results for decarburization and the thermodynamic predictions and previously published research a new model is developed based on the present carbides in different regions of steel microstructure which is called the carbon supply model. The hardness profile is considered to represent the carbon content in the steel and variation of carbon chemical potential in this steel is shown schematically with correlation to the carbide type.

Hardness surveys indicate that in the D8 sample, the hardness of the near-HAZ region is still higher than that of the far-HAZ region and decarburization is limited to small regions. However, it has been reported that exposure at 650˚C for times over 100 hours [168, 186] causes instability of M_3C and M_2C carbides in this steel. This difference can be explained by nucleation of alloyed M_2C carbide in the near-HAZ region. Precipitation of this type of carbide causes higher hardness values and prevents carbon migration in this region.

In this condition decarburization occurs by dissolution of present coarse M_3C carbides and growth of metastable carbides in other regions. This process is

considered in the other models [169, 181, 187] and the rate of carbon supply is low. The carbon concentration profile did not change significantly compared to the as-welded condition (see Figure 7-5(a)). The calculated D_C in this condition is about 10^{-16} m^2/s which in the range of the diffusivity of C in this steel reported in previous researches [127, 180].

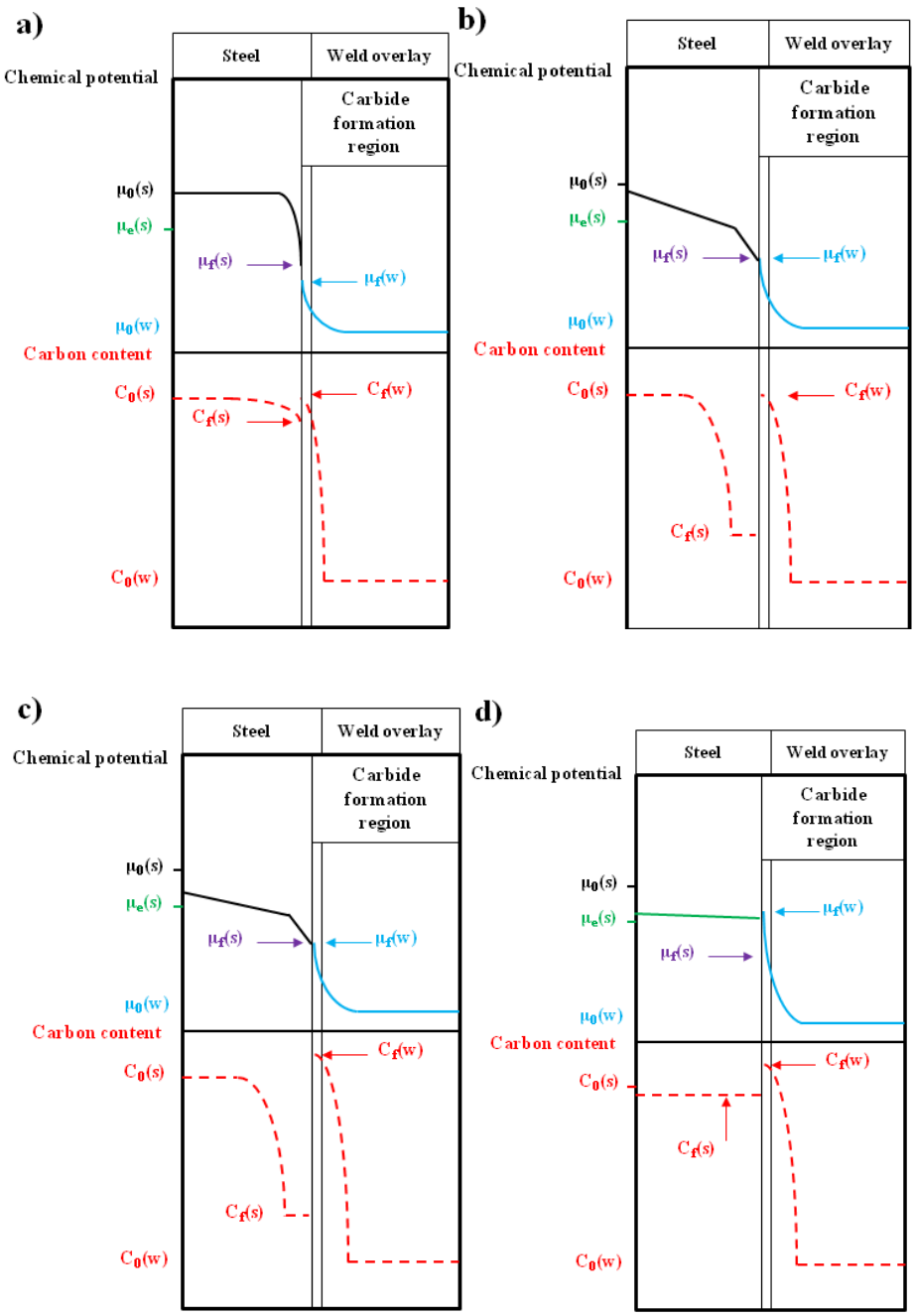

Figure 7-5. Showing schematic diagrams indicates carbon chemical potential variation and carbon concentration in different states; (a) in the D8 sample, (b) in the D12 sample, (c) in the D32 sample and (d) in the D64 and the D128 samples. (Values are same as the Figure 7-4)

The carbon concentration changes rapidly in the D12 sample (see Figure 7-5(b)). The nuclei of alloyed carbides in the near-HAZ region have formed in the neighbourhood of other carbides. Therefore carbon supply is governed by this region with $D_C = 10^{-8}$ m^2/s which is in the range of the diffusivity of C in ferrite and the soft zone [185].

The chemical potential of carbon at the interface is $\mu_f(s)$ and there are different slopes in the carbon potentials to ensure carbon diffusion. The decarburized region width is equal to the near-HAZ region and carbon supply continues until all M_2C carbides transformed to other metastable carbides. The chemical potential of carbon in other regions changes with increasing exposure time to 32 days (see Figure 7-5(c)).

D_C in this condition is about 10^{-16} m^2/s which means that carbon supply is governed by other regions again. Figure 7-5(d) shows the carbon potential and concentration in the D64 and D128 sample and chemical potential at border is higher than steel region. This is related to formation of carbide network at the interface which is shown schematically in Figure 5-3. EDX line scans over the interface in these sample reveal that these particles are (Mo, Cr)-rich and EBSD results indicate their structure is $M_{23}C_6$. The TEM work indicates that increasing exposure time causes a little coarsening of the $M_{23}C_6$ carbides at the interface.

Formation of carbides at interface is reported in former works of the aging of dissimilar weld joints between 2.25Cr1Mo steel and different nickel alloys [6, 143, 149, 188, 189]. Moreover, it was reported [9, 143, 149] that an austenite band formed parallel to interface which is related to diffusion of Ni and Cr

from the nickel alloy during bonding. The nickel rich austenite band has different precipitation behaviour compared to that of other regions in the steel.

Interruption of carbon migration across the interface and carbon chemical potential differences in the steel result in carbon supply to the soft zone from the bulk steel and carbon concentration becomes even through the steel region. The re-hardening of the near-HAZ region is related to formation of Cr-rich carbides in this region which indicates that carbon content is increasing. Based on thermodynamic calculations, the $M_{23}C_6$ carbide is the equilibrium carbide in this steel and therefore increasing the exposure time results in stability of alloyed $M_{23}C_6$ carbide in all regions. The slope of chemical potential line in the steel region at equilibrium state will be zero.

7-2-4- Formation of fine ferrite grains in the near-HAZ region of the D128 sample

Although the carbon depleted zone (CDZ) formation has been reported in previous research on dissimilar welds, there is no information about the microstructural evolution in this region after long term exposure. Albert [129] reported that in the dissimilar welds between Cr-Mo steels and austenitic stainless steels, the soft zone re-crystallized during the thermal exposure. Moreover, Foret [139] analysed a dissimilar weld between two Cr-Mo-V steels, and found that the re-crystallization of ferrite was observed in the CDZ at temperatures above 700˚C.

Experimental observations of the near-HAZ region in the D64 and D128 samples indicates $M_{23}C_6$ carbides are formed at the expense of coarse Mo-rich M_6C carbides which indicates dissolution of Mo into the matrix. Moreover,

the IES images confirmed that in the D128 sample, precipitates in the near-HAZ region are along the grains boundaries.

Thermodynamic calculation of the stable phases in this steel revealed that Mo content (wt.%) in the coexisting ferrite with $M_{23}C_6$ in equilibrium $5.7X10^{-3}$ while it is $5.4X10^{-3}$ with metastable M_6C and M_7C_3 carbides. Therefore, fine grain ferrite formation could be related to the carbide transformation and the related Mo replenishment in the coexisting ferrite, with new ferrite grains being formed between carbide particles with following reaction.

$$\alpha(low\ Mo) + M_3C_7 + M_6C \rightarrow \alpha'(high\ Mo) + M_{23}C_6$$

Bhadeshia and Fujita [170] have shown similar reactions in the modelling of alloy carbide sequence in power plant steels. Although there are disagreements about the changes in Mo content in the carbides with exposure time, the proposed reaction is in accord with the work of Jayan [48].

7-3- Microstructural evolution in the weld overlay

Based on spark analysis, the weld overlay region is a nickel based alloy similar to IN625 but which contains higher iron and carbon contents compared to the standard IN625. The microstructural development in this nickel alloy weldment can be significantly influenced by microsegregation and phase transformation during non-equlibrium solidification because the dendritic structure results in formation of intermetallic secondary solidification constituents in the interdendritic regions.

The intermixing between substrate and the overlay material during welding results in a variation of Fe and C contents in the weld overlay material. Therefore, solidification and ageing behaviour of different regions are various. Finally, there is a metallurgical bond to the steel which has a higher carbon activity and carbon migration from the steel substrate causes further changes in the microstructure of this material.

7-3-1- Microstructure in the as-welded sample

Phase formation during solidification in the nickel based alloys including IN625 [69, 85] in the bulk solidification [69, 71, 85] and in weld metal [33, 74, 77, 79, 81-83, 150, 190, 191] have been thoroughly investigated in previoius research. It is reported that the dominating solidification reaction is the enrichment of the remaining interdendritic liquid in niobium, and the consequent formation of Laves phase and/or (Nb, Ti)-rich MC carbide during final stages of solidification [71]. It is reported that the residual liquid solidifies with a eutectic-like reaction [84] and that the phase formation is strongly influenced by the C/Nb ratio.

Cieslak [70] showed that carbon addition causes formation of more MC carbide at the expense of Laves phase. The solidification of the nickel alloy weldment is generally similar to the above mentioned process. Although the welding wires or electrodes are produced with no intermetallic phases, after welding TCP phases appear in the microstructure [74, 81, 192]. The size and type of the terminal eutectic-like constituents in IN625 weldments is affected

by heat input during welding [33] and cooling rate; however, the amount of carbide present remains at constant level [83].

The experimental observations indicate that weld overlay material has a rapidly solidified microstructure and consists of columnar grains originating from the substrate (see Figure 4-9). Within the grains are finely spaced dendrites which indicate a general loss of homogeneity (Figure 4-10). Moreover, EPMA results (Figure 4-13) confirmed the formation of (Nb, Ti)-rich points in the bulk zone. There is no evidence for formation of phases in the mixing zone.

Thermodynamic calculations reveal that phase formation during non-equilibrium solidification of the weld overlay depends on Fe and C content. In the bulk zone, MC, (δ) and (σ) phases are predicted to form (see Figure 6-8). The MC and δ are Nb-rich while the σ is a (Cr, Mo)-rich phase. Increasing the Fe content with the same level of carbon in the mixing zone causes formation of Laves phase (see Figure 6-9).

However, addition of carbon delays formation of Laves phase by formation of σ phase (see Figure 6-10). These phases must be present in the interdendritic regions of the as-welded sample. The (Nb, Ti)-rich points are related to the MC and/or δ phases, and cooling rate has a critical affect on formation of these phases. Higher cooling rate in the mixing zone will result in the absence of δ phase in this region. However, it is believed that there are some fine carbide precipitates in this region.

7-3-2- Microstrcutral evolution following high temperature exposure

7-3-2-1- Bulk zone hardening

Different studies have dealt with the effects of aging at temperatures in the range of 600 to 750°C on the wrought IN625 microstructure [87, 88, 90, 98, 101, 103, 104, 106-108, 114, 115, 117, 118] and weld overlay material [95, 119, 150]. In this condition, strengthening is brought about by precipitation of the metastable (γ'') phase with a body centred tetragonal DO_{22} structure [69, 97, 98]. It is reported that (γ'') phase transform to orthorhombic (δ) phase with DO_a structure on prolonged aging [99].

Experimental observation indicates that hardening of the bulk zone in the D1 sample (Figure 5-4) continues with increasing exposure time (Figure 5-5). However, exposure times of more than 8 days causes little change in the bulk zone hardness. The hardness values in the as-welded condition are well matched with those of the weld metal [119] and rapidly solidified IN625 [82] from previous research. The hardness values after 8 days of thermal exposure are also well matched with those of the weld metal [95] and wrought IN625 [69].

As such, it may be argued that the hardening of the bulk zone with thermal exposure at 650˚C occurs by precipitation of (γ'') phase. This phase has a coherent structure and cannot be seen in this study. However, needles of the (δ) phase become visible after prolong ageing in the D128 sample in some regions which can related to transformation of (γ'') to (δ) phase.

7-3-2-2- Mixing zone hardening

Formation of a narrow hard band adjacent to the interface in the weld metal, after heat exposure in the range of 600˚C to 700˚C has been reported in previous research in dissimilar weld joints between steels and Ni alloys [6, 7, 9, 66]. It has been argued that the increasing in hardness is related to the precipitation of carbides on the higher Cr side of the interface.

Observations of the D8 sample in this work indicates hardening of the mixing zone and increasing exposure time to 16 days results in formation of a hard band ~30 μm wide. Increasing exposure time causes only small changes, both in hardness values or hard band wide. Nevertheless, it is notable that the hard band was also formed in the free standing weld overlay sample (WD128).

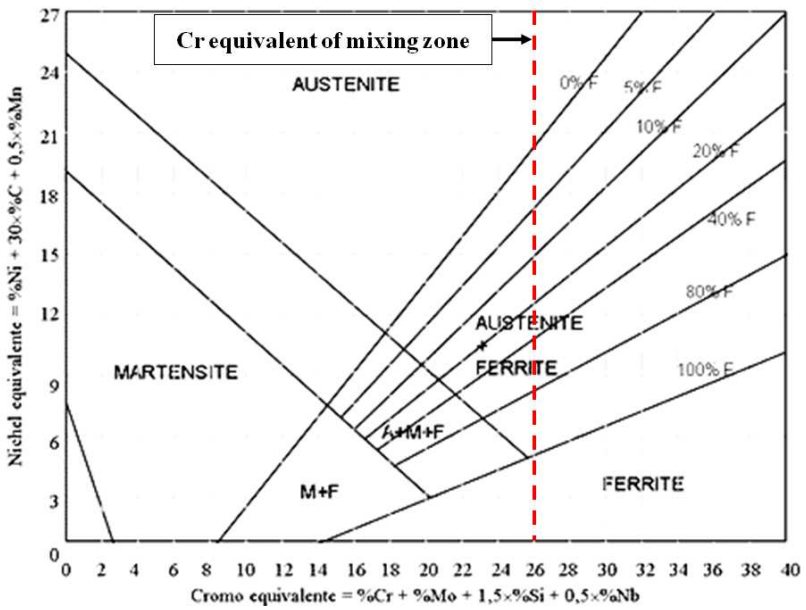

Figure 7-6. Showing Schaeffler diagram and indicating Cr equivalent for the mixing zone composition and stability of austenite in this region.

Therefore it is suggested that carbon migration has no effect on hard band formation, which indicates that it is not related to formation of carbides. The Schaeffler diagram (see Figure 7-6) indicates that (γ) austenite is stable in the

mixing zone. Thermodynamic calculation indicates that the (σ) phase is stable at 650˚C in this region (Figure 6-6). Therefore it is suggested that hard band formation is related to the precipitation of the hard intermetallic (σ) phase in this zone

7-3-2-3- Phase precipitation in the interfacial region

It is known that some carbides and intermetallic phases are normally precipitated in the IN625 alloy during either aging or service at temperatures in the range of 600˚C to 750˚C in wrought [93, 193, 194] and as-solidified conditions [91, 96, 97, 99, 102, 195]. It is reported [104, 119] that below 700˚C, the $M_{23}C_6$ carbide is the most stable type of carbide in the IN625 alloy. Moreover, precipitation of Mo-rich (μ) phase in this alloy has also been reported [92].

Observations indicate that some veins were formed in the interfacial region following thermal exposure tests. These veins are ~100 μm in length and increasing exposure time has a little effect on the length of them. BSE micrographs indicated that these veins are associated with carbides in the microstructure and that the carbide population increased with increasing exposure time around the grain boundaries. The EPMA results of the D64 and the D128 samples confirm that in the interfacial region, (Cr, Mo)-rich carbide precipitates are present. Analysis of the WD128 sample reveals that precipitation of carbides in this region is related to carbon migration from the steel.

Thermodynamic calculations for the bulk zone show that at 650˚C, the (Cr, Mo)-rich $M_{23}C_6$ carbide is stable. However, there are different stable carbides with changing Fe content, and in the mixing zone the Mo-rich M_6C is stable. Increasing the carbon content results in a higher carbide mol.% at the expense of other phases in the bulk zone while in the mixing zone causes the stability of (Cr, Mo)-rich $M_{23}C_6$. These results are similar to those reported in other works based on thermodynamic calculations [103, 142].

Therefore, it is suggested that MC carbides formed during the final stage of solidification transform to the (Cr, Mo)-rich $M_{23}C_6$ in the neighbourhood of grain boundaries in the interfacial region. Carbon migration across the interface results in growth of these carbide precipitates. However, the constant length of the carbide precipitation region in the weld overlay (veins) can be related to the formation of other phases.

Evaluation of the weld overlay region microstructure in different samples indicates that some intermetallic precipitates are present at the grain boundaries which were identified as TCP phases. These precipitates are (Mo, Nb)-rich and were formed in the interdendritic regions. However, EPMA results reveal that the Nb-rich areas are different from the Mo-rich areas.

Thermodynamic calculations show that although (μ) phase is not formed during non-equilibrium solidification, this phase is stable at 650˚C with Fe contents of less than 8 wt.% (in addition to Nb-rich (δ) phase). Increasing the Fe content results in formation of (σ) phase at the expense of the (μ) phase and above 15wt.%, (σ) phase is stable with Nb-rich (δ) phase.

Therefore, beyond the ~100 μm distance and due to lower Fe content, the (Mo, Cr)-rich (μ) phase becomes stable and formation of this phase decreases the chemical potential of Cr and Mo and prevents carbide formation in this area. However, this phase formed very close to the Nb-rich (δ) in the interdendritic regions and so it is difficult to distinguish these phases from each other. It can be said that both these phases are co-exist in these regions.

In the D128 sample some acicular bright precipitates become visible in the microstructure very close to carbides which are suggested to be the (δ) phase. In this region, the Cr and Mo atoms formed carbides and as such, the Nb atoms are free to form the Ni_3Nb phase. The (δ) phase was also seen in the WD128 sample along the grain boundaries close to interface because (μ) phase is not stable at this region due to high Fe content.

7-4- Summary

The precipitation behaviour following thermal exposure, in various regions of the weld overlaid tube, are different due to variation of as-welded microstructure and composition. Moreover carbon migration causes further changes in the interfacial region due to wide differences in its chemical potential in the 2.25Cr1Mo steel and the nickel alloy.

The main process in the early stages of thermal exposure is dissolution of metastable carbides in the steel region and formation of carbides at the interface and along the grain boundaries of the interfacial region. However, different microstructures in the steel region cause different rates of dissolution and precipitation sequences which are considered in a new model to explain microstructural evolution in the different regions of steel. It is clear that the

width of the HAZ zone is related to heat input during welding. Therefore choosing a welding process with a narrower HAZ could be useful in changing the width of the soft zone during service.

Formation of a carbide network at the interface interrupts carbon supply across the interface. However, there is carbon redistribution in the steel region which causes further changes in the microstructure of the near-HAZ region. The re-hardening of this region and the formation of fine ferrite grains is explained by formation of fine Cr-rich carbides and Mo replenishment in the coexisting ferrite. Due to the above observations, carbon migration cannot continue indefinitely and it is observed that the mechanical properties and microstructure of the central and the far-HAZ zones remain almost unchanged at 650˚C. Therefore, it is suggested that increasing the steam temperature to above 450˚C in the power plants is possible. However, the technical issues in this regard should be considered.

The Fe/Mo ratio is the major parameter in formation of different phases in the microstructure of weld overlay region. Increasing distance from the interface with lower Fe/Mo ratio results in formation of the (μ) intermetallic phase at the expense of carbide precipitates which are stable at higher ratio along the grain boundaries. This fact indicates that the steel substrate has some effect on the first 100 μm of the weld overlay material. Therefore, it is suggested that by consideration of corrosion rate and it relation to the thickness, the weld overlay thickness can be reduced which means reduction of costs for manufacturing of the bimetallic tube.

Based on the results of this research, it is clear that formation of the hard band is not related to the carbide formation as it also formed in the WD128 sample. Although formation of this hard band layer has not a significant effect on the hook stress, due to the temperature fluctuation and 3 dimensional forces in the tube, the presence of a hard band adjacent to the soft zone could degrade mechanical properties of the tube during its service life.

7-5- Future work

The first important issue is to determine the realistic temperature profile in the wall thickness of a super heater tube in the service condition. This thermal analysis helps to understand the effect of increasing service temperature on the different regions of this tube especially at interface.

The second issue is that the aim of applying a weld overlay on ferritic steel is to increase the corrosion resistance in the severe operating conditions such as WtE boilers. The corrosion resistance is related to the microstructure and it is necessary to analyse this property of the weld overlay. It is clear that the weld overlay material contains about 9 wt% Fe which may cause different corrosion behaviour compared to that of the standard wrought Inconel 625 with less than 5 wt% Fe content.

The third issue is to understand the affects of the hard band and the soft zone on the mechanical properties under service conditions. Therefore mechanical tests need to be done on different samples.

References

1. Adamiec, J., "*High temperature corrosion of power boiler components cladded with nickel alloys"* Materials Characterization, **2009**. **60**(10): p. 1093-1099.

2. Lee, S.H. ; Themelis, N.J. ; Castaidi, M.J., "*High-temperature corrosion in waste-to-energy boilers"* Journal of Thermal Spray Technology, **2007**. **16**(1): p. 104-110.

3. Kawahara, Y., "*Development and application of high-temperature corrosion-resistant materials and coatings for advanced waste-to-energy plants"* Materials at High Temperatures, **1997**. **14**(3): p. 261-268.

4. Cane, B.J. ; Fidler, R.S., "*The Effect of Microstructure and Grain Size on the Creep and Rupture Properties of 2.25Cr--Mo and 9Cr--Mo Steels"*, in *International Conference on Ferritic Steels for Fast Reactor Steam Generators*. **1978**: London. p. 193-199.

5. Orr, J. ; Beckitt, F.R. ; Fawkes, G.D., "*The Physical Metallurgy of Chromium--Molybdenum Steels for Fast Boilers"*, in *International Conference on Ferritic Steels for Fast Reactor Steam Generators*. **1978**: London. p. 91-109.

6. Nicholson, R.D., "*Effect of aging on interfacial structures of nickel-based transition joints"* Metals Technology, **1984**. **11**(MAR): p. 115-124.

7. Lopez, B. ; Gutierrez, I. ; Urcola, J.J., "*Microstructural analysis of steel nickel alloy clad interfaces"* Materials Science and Technology, **1996**. **12**(1): p. 45-55.

8. Uusitalo, M.A. ; Vuoristo, P.M.J. ; Mantyla, T.A., "*High temperature corrosion of coatings and boiler steels in oxidizing chlorine-containing atmosphere"* Materials Science and Engineering A-Structural Materials Properties Microstructure and Processing, **2003**. **346**(1-2): p. 168-177.

9. Lopez, B. ; Gomez, X. ; Echeberria, J. ; Gutierrez, I. ; Urcola, J.J., "*Interface analysis on diffusion bonded bimetallic composites .1. Extended solid solubility"*, in *Cmmc 96 - Proceedings of the First International Conference on Ceramic and Metal Matrix Composites, Pts 1 and 2*, M. Fuentes, J.M. MartinezEsnaola, and A.M. Daniel, Editors. **1997**, Trans Tech Publications: Clausthal Zellerfe. p. 695-702.

10. Lai, G.Y. ; Blogg, N., "*Unifuse overlay cladding for surface protection against corrosion and erosion/corrosion in power boilers and waste heat recovery"*, in *OMMI*. **2004**. p. 1-19.

11. Kawahara, Y., "*Application of high temperature corrosion-resistant materials and coatings under severe corrosive environment in waste-to-energy boilers"* Journal of Thermal Spray Technology, **2007**. **16**(2): p. 202-213.

12. www.wte.org. [cited.

13. Kiser, S.D. ; Hinshaw, E.B. ; Orsini, T., "*Extending the life of fossil fired boiler tubing with cladding of nickel based alloy materials"*, in *NACE International CORROSION/2006, 61st Annual Conference & Exposition*. **2006**, NACE International, P.O. Box 218340, Houston, TX, 77218, USA,: San Diego, CA; USA.

14. Sidky, P.S. ; Hocking, M.G., "*Review of inorganic coatings and coating processes for reducing wear and corrosion"* British Corrosion Journal, **1999**. **34**(3): p. 171-183.

15. Stringer, J., "*Coatings in the electricity supply industry: past, present, and opportunities for the future"* Surface & Coatings Technology, **1998**. **108**(1-3): p. 1-9.

16. Wyatt, L.M., "*Materials tchnology in power generation in UK"* Materials Science and Engineering, **1971**. **7**(5): p. 237-&.

17. Viswanathan, R. ; Henry, J.F. ; Tanzosh, J. ; Stanko, G. ; Shingledecker, J. ; Vitalis, B. ; Purgert, R., "*US program on materials technology for ultra-supercritical coal power plants"* journal of Materials Engineering and Performance, **2005**. **14**(3): p. 281-292.

18. Viswanathan, R. ; Purgert, R. ; Rao, U., "*Materials technology for advanced coal power plants"*, in *1st International Conference on Super-High Strength Steels*. **2005**: Rome, Italy.

19. Uusitalo, M. ; Kaipiainen, M. ; Vuoristo, P. ; Mantyla, T., "*High temperature erosion-corrosion of superheater materials and coatings in chlorine containing environments"*, in *High Temperature Corrosion and Protection of Materials 5, Pts 1 and 2*, R. Streiff, et al., Editors. **2001**, Trans Tech Publications Ltd: Zurich-Uetikon. p. 475-482.

20. Uusitalo, M.A. ; Vuoristo, P.M.J. ; Mantyla, T.A., "*High temperature corrosion of coatings and boiler steels in reducing chlorine-containing atmosphere"* Surface & Coatings Technology, **2002**. **161**(2-3): p. 275-285.

21. Uusitalo, M.A. ; Vuoristo, P.M.J. ; Mantyla, T.A., "*High temperature corrosion of coatings and boiler steels below chlorine-containing salt deposits"* Corrosion Science, **2004**. **46**(6): p. 1311-1331.

22. Montgomery, M. ; Biede, O. ; Larsen, O.H., "*Experiences with Inconel 625 in biomass and waste incineration plants"*, in *High-Temperature Oxidation and Corrosion 2005*, S. Taniguchi, et al., Editors. **2005**, Trans Tech Publications Ltd: Stafa-Zurich. p. 523-530.

23. Cha, S.C. ; Wolpert, P., "*High-temperature erosion and corrosion measurement of thermally sprayed materials"* Advanced Engineering Materials, **2003**. **5**(4): p. 213-217.

24. Vollertsen, F. ; Partes, K. ; Meijer, J., "*State of the art of laser hardening and cladding"*, in *Third International WLT-conference on Lasers in Manufacturing*, E. Beyer, et al., Editors. **2005**: Munich, Germany.

25. Lai, G. ; Hulsizer, P., "*Corrosion control by modern weld overlay technology"*, in *14th International Corrosion Congress (ICC)*. **1999**: Cape Town; South Africa.

26. Thornton, C.E. ; Cooper, C., "*Welding and corrosion performance of INCO-WELD 686CPT filler metal in Waste-To-Energy power plants"*. **2003**, Special Metals Welding Products Co.

27. Deacon, R.M. ; DuPont, J.N. ; Marder, A.R., "*High temperature corrosion resistance of candidate nickel-based weld overlay alloys in a low NO_x environment"* Materials Science and Engineering A-Structural Materials Properties Microstructure and Processing, **2007**. **460**: p. 392-402.

28. Amador, P. ; Lai, G. "*Application of unifuse overlay tubes in the convection section of waste-to-energy boilers*." in *11th Annual North American Waste to Energy Conference*. **2003**. New York: Amer. Soc. Mechanical Engineers.

29. Ganesan, P. ; Renteria, C.M. ; Crum, J.R., "*Versatile corrosion resistance of INCONEL alloy 625 in various aqueous and chemical processing environments"*, in *Superalloys 718, 625 and Various Derivatives*, E.A. Loria, Editor. **1991**, The Minerals, Metals and Materials Society (TMS): Pittsburgh, PA. p. 663-680.

30. Capitamescu, D., "*Alloy 625 weld overlays for offshore and onshore projects"*, in *Superalloys 718, 625 and Various Derivatives*, E.A. Loria, Editor. **1991**, The Minerals, Metals and Materials Society (TMS): Pittsburgh, PA. p. 821-835.

31. Smith, G.D. ; Tillack, D.J. ; Patel, S.J., "*Alloy 625 - Impressive past/significant presence/awesome future"*, in *Superalloys 718, 625, 706 and Various Derivatives*, E.A. Loria, Editor. **2001**, The Minerals, Metals and Materials Society (TMS): Warrendale, PA. p. 35-46.

32. Lai, G. ; Van Lienden, C. ; Hou, P.Y., "*Erosion/corrosion behavior of weld overlays in HCl containing atmospheres"*, in *Corrosion/2001*. **2001**, NACE International: Houston, TX.

33. Wilson, I.L.W. ; Gourley, R.G. ; Walkosak, R.M. ; Bruck, G.J., "*The effect of heat input on microstructure and cracking in alloy 625 weld overlays"*, in *Superalloys 718, 625 and Various Derivatives*, E.A.

Loria, Editor. **1991**, The Minerals, Metals and Materials Society (TMS): Pittsburgh, PA. p. 735-747.

34. Oh, Y.K. ; Devletian, J.H. ; Chen, S.J., "*Low-dilution electrosalg cladding for shipbuilding"* Welding Journal, **1990**. **69**(8): p. 37-44.

35. Bates, D., "*Cost effective maintenance by spiral welding"* Welding and Metal Fabrication, **1983**. **51**(8): p. 440.

36. Wang, X.L. ; Payzant, E.A. ; Taljat, B. ; Hubbard, C.R. ; Keiser, J.R. ; Jirinec, M.J., "*Experimental determination of the residual stresses in a spiral weld overlay tube"* Materials Science and Engineering A-Structural Materials Properties Microstructure and Processing, **1997**. **232**(1-2): p. 31-38.

37. Siman, A. ; Shelton, J., "*Feedwater heater application of T-22 tubing"*, Bobcockpower Thermal Engineering International Inc. .

38. Xu, H. ; Huang, X.K. ; Yang, Z. ; Pan, J.T., "*Property changes of 12Cr1MoV with 10CrMo910 main steam piping after long-term high-temperature service"* Engineering Failure Analysis, **2003**. **10**(2): p. 245-250.

39. Matsumoto, I. ; Wignarajah, S. ; Shinoda, T. ; Yamada, S., "*Microstructure and Mechanical Properties of 2.25Cr1Mo and 0.50Mo Heat Resisting Steels After Long Service"* Transaction of the Japan Welding Society, **1983**. **14**(1): p. 34-39.

40. Song, S.H. ; Faulkner, R.G. ; Flewitt, P.E.J., "*Quenching and tempering-induced molybdenum segregation to grain boundaries in a 2.25Cr-1Mo steel"* Materials Science and Engineering A-Structural Materials Properties Microstructure and Processing, **2000**. **281**(1-2): p. 23-27.

41. Gojic, M. ; Kosec, L. ; Matkovic, P., "*The effect of tempering temperature on mechanical properties and microstructure of low alloy Cr and CrMo steel"* Journal of Materials Science, **1998**. **33**(2): p. 395-403.

42. Bhadeshia, H.K.D.H., "*Bainite in steels : transformations, microstructure and properties "*. **2001**, London: Institute of Materials.

43. Yang, J.R. ; Huang, C.Y. ; Yang, C.N. ; Horng, J.L., "*Microstructural examination of 2.25Cr-1Mo steel steam pipes after extended service"* Materials Characterization, **1993**. **30**(2): p. 75-88.

44. Mitchell, D.R.G. ; Small, R., "*Microstructural evolution in seven 2.25Cr-1Mo superheater outlet headers resulting from service exposure"* Science and Technology of Welding and Joining, **2001**. **6**(3): p. 168-176.

45. Chang, H.J. ; Kai, J.J., "*The effects of thermal treatment on the microstructure and tensile properties of 2.25Cr1Mo Steel"* Scripta Metallurgica et Materialia, **1990**. **24**(11): p. 2101-2106.

46. Parameswaran, P. ; Vijayalakshmi, M. ; Shankar, P. ; Raghunathan, V.S., "*Influence of carbon content on microstructure and tempering behaviour of 2-1/4Cr1Mo steel"* Journal of Materials Science, **1993**. **28**(20): p. 5426-5434.

47. Mitchell, D.R.G. ; Ball, C.J., "*A quantitative X-ray diffraction and analytical electron microscopy study of service-exposed 2.25Cr-1Mo steels"* Materials Characterization, **2001**. **47**(1): p. 17-26.

48. Jayan, V. ; Khan, M.Y. ; Hussain, M., "*X-ray investigation of solid solution partitioning in 2.25Cr-1Mo steel after extended elevated temperature service in power station"* Materials Science and Technology, **2003**. **19**(11): p. 1546-1552.

49. Yang, H.T. ; Kim, S., "*A study on the mechanical strength change of 2.25Cr-1Mo steel by thermal aging"* Materials Science and Engineering A-Structural Materials Properties Microstructure and Processing, **2001**. **319**: p. 316-320.

50. Lonsdale, D. ; Flewitt, P.E.J., "*Damage accumulation and microstructural changes occurring during the creep of a 2 1/4%Cr1%Mo steel"* Materials Science and Engineering, **1979**. **39**(2): p. 217-229.

51. Ahila, S. ; Radhakrishnan, V.M. ; Iyer, S.R., "*Effect of temperature on the microstructure of 2.25Cr1Mo steel during creep testing"* Journal of Materials Science Letters, **1993**. **12**(16): p. 1296-1298.

52. Gope, N. ; Chatterjee, A. ; Mukherjee, T. ; Sarma, D.S., "*Influence of long-term aging and superimposed creep stress on the microstructure of 2.25Cr1Mo steel"* Metallurgical Transactions A-Physical Metallurgy and Materials Science, **1993**. **24**(2): p. 315-326.

53. Abdellatif, A.M. ; Corbett, J.M. ; Taplin, D.M.R., "*Analysis of carbides formed during accelerated aging of 2-25Cr-1Mo steel"* Metal Science, **1982**. **16**(2): p. 90-96.

54. Cheruvu, N.S., "*Degradation of mechanical properties of Cr-Mo-V and 2.25Cr-1Mo steel components after long-term service at elevated temperatures"* Metallurgical Transactions A-Physical Metallurgy and Materials Science, **1989**. **20**(1): p. 87-97.

55. Baker, R.G. ; Nutting, J., "*The tempering of a 2.25%Cr–1%Mo steel after quenching and normalizing"* Journal of the Iron and Steel Institute., **1959**. **208**: p. 257-268.

56. Jones, W.B. ; Vandeavyle, J.A., "*Substructure and strengthening in 2.25Cr1Mo steel at elevated temperatures"* Metallurgical Transactions

A-Physical Metallurgy and Materials Science, **1980**. **11**(8): p. 1275-1286.

57. Pigrova, G. ; Sedov, V. ; Archakov, Y., "*Carbide transformations in Cr-Mo steels in the process of long-term ageing and operation"* Metal Science and Heat Treatment **1997**. **39**(9): p. 371-375.

58. Race, J.M.,"*Carbon diffusion across dissimilar steel welds"*,**1992**,Ph.D.,Materials Science and Metallurgy St. John's College

59. Klueh, R.L. ; Swindeman, R.W., "*Thw microstructure and mechanical properties of a modified 2.25Cr1Mo steel"* Metallurgical Transactions A-Physical Metallurgy and Materials Science, **1986**. **17**(6): p. 1027-1034.

60. Thomson, R.C. ; Bhadeshia, H.K.D.H., "*Changes in chemical composition of carbides in 2.25Cr-1Mo power plant steel. part 1. Bainitic microstructure"* Materials Science and Technology, **1994**. **10**(3): p. 193-203.

61. Thomson, R.C. ; Bhadeshia, H.K.D.H., "*Changes in chemical composition of carbides in 2.25Cr-1Mo power plant steel. part 2. Mixed microstructure"* Materials Science and Technology, **1994**. **10**(3): p. 205-208.

62. Parameswaran, P. ; Paul, V.T. ; Vijayalakshmi, M. ; Raghunathan, V.S., "*Microstructural evolution in a single pass autogenously welded 2.25Cr-1Mo steel"* Transactions of the Indian Institute of Metals, **2004**. **57**(3): p. 253-264.

63. Miranda, R.M. ; Fortes, M.A., "*Austenite grain growth, microstructure and hardness in the heat-affected-zone of a 2.25Cr1Mo steel"* Materials Science and Engineering A-Structural Materials Properties Microstructure and Processing, **1989**. **A108**(1-2): p. 1-8.

64. Bergquist, E.L. ; Karlsson, L. ; Thuvander, M. ; Keehan, E., "*Microstructure and properties of post weld heat treated 2.25Cr1Mo weld metal"*, in *7th International Conference: Trends in Welding Research*. **2005**, ASM International: Pine Mountain, GA; USA. p. 963-968.

65. Rao, R.V.S. ; Parameswaran, P. ; Dayal, R.K., "*Microstructural modification in a laser-treated 2.25Cr-1Mo steel"* Journal of Materials Engineering and Performance, **2001**. **10**(5): p. 515-520.

66. Laha, K. ; Chandravathi, K.S. ; Rao, K.B.S. ; Mannan, S.L. ; Sastry, D.H., "*An assessment of creep deformation and fracture behavior of 2.25Cr-1Mo similar and dissimilar weld joints"* Metallurgical and Materials Transactions A-Physical Metallurgy and Materials Science, **2001**. **32**(1): p. 115-124.

67. Buchmayer, B. ; Cerjak, H. ; Witwer, M. ; Kiekaldy, J.S., "*Carbon diffusion and microstructure in dissimilar Cr-Mo-V welds and their influence on the mechanical properties*", in *Recent Trends in Welding Science and Technology*. **1989**, ASM International, Materials Park, Ohio 44073, USA Gatlinburg, Tennessee; USA. p. 237-242.

68. Pilling, J. ; Ridley, N., "*Tempering of 2.25%Cr1%Mo low-carbon steels*" Metallurgical Transactions A-Physical Metallurgy and Materials Science, **1982**. **13**(4): p. 557-563.

69. Eiselstein, H.L. ; Tillack, D.J., "*The invention and definition of alloy 625*", in *Superalloys 718, 625 and Various Derivatives*, E.A. Loria, Editor. **1991**, The Minerals, Metals and Materials Society (TMS): Pittsburgh, PA. p. 1-13.

70. Cieslak, M.J. ; Headley, T.J. ; Kollie, T. ; Romig, A.D.J., "*A melting and solidification study of alloy 625*" Metallurgical Transactions A-Physical Metallurgy and Materials Science., **1988**. **19A**(9): p. 2319-2331.

71. Floreen, S. ; Fuchs, G.E. ; Yang, W.J., "*The metallurgy of alloy 625*", in *Superalloys 718, 625, 706 and Various Derivatives*, E.A. Loria, Editor. **1994**, The Minerals, Metals and Materials Society (TMS): Warrendale, PA. p. 13-37.

72. Atamert, S. ; Bhadeshia, H.K.D.H., "*Nickel based hardfacing alloys for high-temperature applications*" Materials Science and Technology, **1989**. **5**(12): p. 1220-1228.

73. Luer, K. ; DuPont, J. ; Marder, A. ; Skelonis, C., "*Corrosion fatigue of alloy 625 weld claddings in combustion environments*" Materials at High Temperatures, **2001**. **18**(1): p. 11-19.

74. Cieslak, M.J. ; Knorovsky, G.A. ; Headley, T.J. ; Romig, A.D., "*The use of new PHACOMP in understanding the solidification microstructure of nickel-base alloy weld metal*" Metallurgical Transactions A-Physical Metallurgy and Materials Science, **1986**. **17**(12): p. 2107-2115.

75. Thompson, R.G. ; Mayo, D.E. ; Radhakrishnan, B., "*The relationship between carbon content, microstructure, and intergranular liquation in cast nickel alloy-718*" Metallurgical Transactions A-Physical Metallurgy and Materials Science, **1991**. **22**(2): p. 557-567.

76. Cieslak, M.J. ; Headley, T.J. ; Romig, A.D., "*The welding metallurgy of hastelloy alloy-C-4, alloy-C-22, and alloy-C-276*" Metallurgical Transactions A-Physical Metallurgy and Materials Science, **1986**. **17**(11): p. 2035-2047.

77. Cieslak, M.J., "*The welding and solidification metallurgy of alloy 625*" Welding Journal., **1991**. **70**(2): p. 49s-56s.

78. Cieslak, M.J. ; Headley, T.J. ; Frank, R.B., "*The welding metallurgy of custom age 625 Plus alloy"* Welding Journal, **1989**. **68**(12): p. S473-S482.

79. Yoon, B.H. ; Ahn, Y.S. ; Lee, C.H., "*The effect of dilution on HAZ liquation cracking in PTAW Ni-base superalloys overlay deposit"* The Iron and Steel Institute of Japan International, **2002**. **42**(2): p. 178-183.

80. Cooper, K.P. ; Slebodnick, P. ; Thomas, E.D., "*Seawater corrosion behavior of laser surface modified Inconel 625 alloy"* Materials Science and Engineering A-Structural Materials Properties Microstructure and Processing, **1996**. **206**(1): p. 138-149.

81. Ogborn, J.S. ; Olson, D.L. ; Cieslak, M.J., "*Influence of solidification on the microstructural evolution of nickel base weld metal"* Materials Science and Engineering A-Structural Materials Properties Microstructure and Processing, **1995**. **203**(1-2): p. 134-139.

82. Dey, G.K. ; Albert, S. ; Srivastava, D. ; Sundararaman, M. ; Mukhopadhyay, P., "*Microstructural studies on rapidly solidified INCONEL-625"* Materials Science and Engineering A-Structural Materials Properties Microstructure and Processing, **1989**. **119**: p. 175-184.

83. Tinoco, J. ; Fredriksson, H., "*Solidification of a modified Inconel 625 alloy under different cooling rates"* High Temperature Materials and Processes, **2004**. **23**(1): p. 13-24.

84. Hojerslev, C. ; Tiedje, N. ; Hald, J., "*Segregation effects and phase developments during solidification of alloy 625"*, in *Solidification and Gravity Iv*, R. Roosz, M. Rettenmayr, and Z. Gacsi, Editors. **2006**, Trans Tech Publications Ltd: Zurich-Uetikon. p. 373-378.

85. Barker, J.F. ; Cox, J.D. ; Margolin, E., "*INCONEL 625 - An alloy for steam and gas turbines"* Metal Progress, **1968**. **93**(4): p. 91-&.

86. Matthewss, S.J., "*Thermal Stability of Solid solutioned Strengthened High Performance Alloys"*, in *3rd International Superalloy Symposium*. **1976**: Seven Springs, PA.

87. Radavich, J.F. ; Fort, A., "*Effects of long-time exposure in alloy-625 at 1200°F, 1400°F and 1600°F"*, in *Superalloys 718, 625, 706 and Various Derivatives*, E.A. Loria, Editor. **1994**, The Minerals, Metals and Materials Society (TMS): Warrendale, PA. p. 635-647.

88. Kohler, M., "*Effect of the elevated-temperature-precipitation in alloy 625 on preoperites and microstructure"*, in *Superalloys 718, 625, 706 and Various Derivatives*, E.A. Loria, Editor. **1991**, The Minerals, Metals & Materials Society(TMS): Pittsburgh, PA. p. 363-374.

89. Heubner, U. ; Kohler, M., "*Effect of carbon content and other variables on the yield strength, ductility and creep preoperties of*

alloy-625", in *Superalloys 718, 625, 706 and Various Derivatives*, E.A. Loria, Editor. **1994**, The Minerals, Metals and Materials Society (TMS): Pittsburgh, PA. p. 479-488.

90. Kohler, M. ; Heubner, U., "*Time-Temperature-Sensitization and Time-Temperature-Precipitation behavior of alloy 625"*, in *CORROSION 96*. **1996**, NACE International: Denver, Co. p. 427/1-427/10.

91. Tawancy, H.M. ; Allam, I.M. ; Abbas, N.M., "*Effect of Ni_3Nb precipitation on the corrosion resistance of INCONEL alloy 625"* Journal of Materials Science Letters, **1990**. **9**(3): p. 343-347.

92. Tawancy, H.M., "*Precipitation characteristics of mu-phase in wrought nickel-base alloys and its effect on their properties"* Journal of Materials Science, **1996**. **31**(15): p. 3929-3936.

93. Ferrer, L. ; Pieraggi, B. ; Uginet, J.F., "*Microstructural evolution during thermomechanical processing of alloy 625"*, in *Superalloys 718, 625 and Various Derivatives*, E.A. Loria, Editor. **1991**, The Minerals, Metals and Materials Society (TMS): Pittsburgh, PA. p. 217-229.

94. Comprelli, F.A. ; Wolff, U.E., "*Stability of high nickel alloys in superheated steam"*. **1963**, General Electric: san jose.

95. Cortial, F. ; Corrieu, J.M. ; Vernotloier, C., "*Heat treatments of weld alloy 625 - Influence on the microstructure, mechanical properties and corrosion resistance"*, in *Superalloys 718, 625, 706 and Various Derivatives*, E.A. Loria, Editor. **1994**, The Minerals, Metals and Materials Society (TMS): Pittsburgh, PA. p. 859-870.

96. Kirman, I., "*Precipitation in Fe-Ni-Cr-Nb system"* Journal of the Iron and Steel Institute, **1969**. **207**: p. 1612-1618.

97. Bohm, H. ; Ehrlich, K. ; Kramer, K.H., "*Precipitation behaviour of Nickel-alloy INCONEL-625"* Metall, **1970**. **24**(2): p. 139-.

98. Sundararaman, M. ; Kishore, R. ; Mukhopadhyay, P., "*Some aspects of the heterogeneous precipitation of the metastable-gamma" phase in alloy 625"*, in *Superalloys 718, 625, 706 and Various Derivatives*, E.A. Loria, Editor. **1994**, The Minerals, Metals and Materials Society (TMS): Pittsburgh, PA. p. 405-418.

99. Sundararaman, M. ; Mukhopadhyay, P. ; Banerjee, S., "*Precipitation of the delta-Ni_3Nb phase in 2 nickel-base superalloys"* Metallurgical Transactions A-Physical Metallurgy and Materials Science, **1988**. **19**(3): p. 453-465.

100. Mittra, J. ; Dubey, J.S. ; Kulkarni, U.D. ; Dey, G.K., "*Role of dislocation density in raising the stage II work-hardening rate of Alloy 625"* Materials Science and Engineering A-Structural Materials Properties Microstructure and Processing, **2009**. **512**(1-2): p. 87-91.

101. Sundararaman, M. ; Mukhopadhyay, P. ; Banerjee, S., "*Carbide precipitation in nickel base superalloys 718 and 625 and their effect on mechanical properties"*, in *Superalloys 718, 625, 706 and Various Derivatives*, E.A. Loria, Editor. **1996**, The Minerals, Metals and Materials Society (TMS): Pittsburgh, PA. p. 367-378.

102. Dahlen, M. ; Fischmister, H., "*Carbide precipitation in superalloys"*, in *Superalloys* **1980**, Metals Park, OH, American Society for Metals.

103. Evans, N.D. ; Maziasz, P.J. ; Shingledecker, J.P. ; Yamamoto, Y., "*Microstructure evolution of alloy 625 foil and sheet during creep at 750 degrees C"* Materials Science and Engineering A-Structural Materials Properties Microstructure and Processing, **2008**. **498**(1-2): p. 412-420.

104. Rai, S.K. ; Kumar, A. ; Shankar, V. ; Jayakumar, T. ; Rao, K.B.S. ; Raj, B., "*Characterization of microstructures in Inconel 625 using X-ray diffraction peak broadening and lattice parameter measurements"* Scripta Materialia, **2004**. **51**(1): p. 59-63.

105. Muzyka, D.R., "*Controlling microstructures and properties of superalloys via use of precipitated phases"* Metals Engineering Quarterly, **1971**. **11**(4): p. 12-&.

106. Shankar, V. ; Rao, K.B.S. ; Mannan, S.L., "*Microstructure and mechanical properties of Inconel 625 superalloy"* Journal of Nuclear Materials, **2001**. **288**(2-3): p. 222-232.

107. Mathew, M.D. ; Rao, K.B.S. ; Mannan, S.L., "*Creep properties of service-exposed Alloy 625 after re-solution annealing treatment"* Materials Science and Engineering A-Structural Materials Properties Microstructure and Processing, **2004**. **372**(1-2): p. 327-333.

108. Mathew, M.D. ; Parameswaran, P. ; Rao, K.B.S., "*Microstructural changes in alloy 625 during high temperature creep"* Materials Characterization, **2008**. **59**(5): p. 508-513.

109. Vernotloier, C. ; Cortial, F., "*Influence of heat treatment on microstructure, mechanical properties and corrosion behaviour of alloy-625 forged rod"*, in *Superalloys 718, 625, 706 and Various Derivatives*, E.A. Loria, Editor. **1991**, The Minerals, Metals and Materials Society (TMS): Pittsburgh, PA. p. 409-422.

110. Corrieu, J.M. ; Vernotloier, C. ; Cortial, F., "*Influence of heat treatments on corrosion behaviour of alloy-625 forged rod"*, in *Superalloys 718, 625, 706 and Various Derivatives*, E.A. Loria, Editor. **1994**, The Minerals, Metals and Materials Society (TMS): Pittsburgh, PA. p. 795-806.

111. Vandervoort, G.F. ; Bowman, J.W. ; Frank, R.B., "*Microstructural characterization of custom age 625-PLUS(R) alloy"*, in *Superalloys*

718, 625, 706 and Various Derivatives, E.A. Loria, Editor. **1994**, The Minerals, Metals and Materials Society (TMS): Pittsburgh, PA. p. 489-498.

112. Edris, H.,"*Studies on high-velocity oxy-fuel sprayed coating of Inconel 625 and Ni-Cr3C2"*,**1997**,Ph.D.,M3 School,University of nottingham

113. Jones, R.H., "*Stress-corrosion cracking"*. **1992**: ASM International.

114. Sundararaman, M. ; Kumar, L. ; Prasad, G.E. ; Mukhopadhyay, P. ; Banerjee, S., "*Precipitation of an intermetallic phase with Pt_2Mo-type structure in alloy 625"* Metallurgical and Materials Transactions A-Physical Metallurgy and Materials Science, **1999**. **30**(1): p. 41-52.

115. Sundararaman, M. ; Mukhopadhyay, P. ; Banerjee, S., "*Influence of intermetallic phase precipitation during prolonged service in Alloy 625 on its properties"*, in *Superalloys 718, 625, 706 and Various Derivatives*, E.A. Loria, Editor. **2001**, The Minerals, Metals and Materials Society (TMS): Pittsburgh, PA. p. 367-378.

116. alloys, U.P.-C.-r.n.-c.-m.

117. Palanichamy, P. ; Mathew, M.D. ; Latha, S. ; Jayakumar, T. ; Bhanu, K. ; Rao, S.K. ; Mannan, S.L. ; Raj, B., "*Assessing microstructural changes in alloy 625 using ultrasonic waves and correlation with tensile properties"* Scripta Materialia, **2001**. **45**(9): p. 1025-1030.

118. Mittra, J. ; Dubey, J.S. ; Banerjee, S., "*Acoustic emission technique used for detecting early stages of precipitation during aging of Inconel 625"* Scripta Materialia, **2003**. **49**(12): p. 1209-1214.

119. Cortial, F. ; Corrieu, J.M. ; Vernotloier, C., "*Influence of heat treatments on microstructure, mechanical propeties, and corrosion resistance of weld alloy 625"* Metallurgical and Materials Transactions A-Physical Metallurgy and Materials Science, **1995**. **26**(5): p. 1273-1286.

120. Savage, W.F. ; Nippes, E.F. ; Szekeres, E.S., "*Study of weld interface phenomena in a low-alloy steel"* Welding Journal, **1976**. **55**(9): p. S260-S268.

121. Cui, Y. ; Xu, C.L. ; Han, Q., "*Effect of ultrasonic vibration on unmixed zone formation"* Scripta Materialia, **2006**. **55**(11): p. 975-978.

122. Sopousek, J. ; Million, B., "*Carbon profile analysis of Fe-Cr-C/Fe-Cr-Ni-C diffusion joints"* Kovove Materialy-(Metallic Materials), **2003**. **41**(2): p. 118-126.

123. Li, G.F. ; Charles, E.A. ; Congleton, J., "*Effect of post weld heat treatment on stress corrosion cracking of a low alloy steel to stainless steel transition weld"* Corrosion Science, **2001**. **43**(10): p. 1963-1983.

124. Diez, F.M. ; Liu, S., "*Compositional boundary between primary austenitic and ferritic Mn-Cr and Ni-Cr steel weld metals"* Materials Science and Engineering A-Structural Materials Properties Microstructure and Processing, **2007**. **452**: p. 1-7.

125. Gómez, X. ; Echeberría, J., "*Microstructure and mechanical properties of low alloy steel T11-austenitic stainless steel 347H bimetallic tubes"* Materials Science and Technology, **2000**. **16**: p. 187-193.

126. Barnhouse, E.J. ; Lippold, J.C., "*Microstructure/property relationships in dissimilar welds between duplex stainless steels and carbon steels"* Welding Journal, **1998**. **77**(12): p. 477S-487S.

127. Pavlovsky, J. ; Million, B. ; Ciha, K. ; Stransky, K., "*Carbon redistribution between an austenitic cladding and a ferritic steel for pressure-vessels of a nuclear-reactor"* Materials Science and Engineering A-Structural Materials Properties Microstructure and Processing, **1991**. **149**(1): p. 105-110.

128. Huang, M.L. ; Wang, L., "*Carbon migration in 5Cr-0.5Mo/21Cr-12Ni dissimilar metal welds"* Metallurgical and Materials Transactions A-Physical Metallurgy and Materials Science, **1998**. **29**(12): p. 3037-3046.

129. Albert, S.K. ; Gill, T.P.S. ; Tyagi, A.K. ; Mannan, S.L. ; Kulkarni, S.D. ; Rodriguez, P., "*Soft zone formation in dissimilar welds between two Cr-Mo steels"* Welding Journal, **1997**. **76**(3): p. S135-S142.

130. Race, J.M. ; Bhadeshia, H.K.D.H., "*Precipitation sequences during carburization of Cr-Mo steel"* Materials Science and Technology, **1992**. **8**(10): p. 875-882.

131. Sudha, C. ; Paul, V.T. ; Terrance, A.L.E. ; Saroja, S. ; Vijayalakshmi, M., "*Microstructure and microchemistry of hard zone in dissimilar weldments of Cr-Mo steels"* Welding Journal, **2006**. **85**(4): p. 71S-80S.

132. Kozeschnik, E. ; Polt, P. ; Brett, S. ; Buchmayr, B., "*Dissimilar 2.25Cr/9Cr and 2Cr/0.5CrMoV steel welds - Part 1: Characterisation of weld zone and numerical simulation"* Science and Technology of Welding and Joining, **2002**. **7**(2): p. 65-68.

133. Kozeschnik, E. ; Warbichler, P. ; Letofsky-Papst, I. ; Brett, S. ; Buchmayr, B., "*Dissimilar 2.25Cr/9Cr and 2Cr/0.5CrMoV steel welds - Part 2: Identification of precipitates"* Science and Technology of Welding and Joining, **2002**. **7**(2): p. 69-76.

134. Laha, K. ; Latha, S. ; Rao, K.B.S. ; Mannan, S.L. ; Sastry, D.H., "*Comparison of creep behaviour of 2.25Cr-1Mo/9Cr-1Mo dissimilar weld joint with its base and weld metals"* Materials Science and Technology, **2001**. **17**(10): p. 1265-1272.

135. Sudha, C. ; Terrance, A.L.E. ; Albert, S.K. ; Vijayalakshmi, M., "*Systematic study of formation of soft and hard zones in the dissimilar weldments of Cr-Mo steels"* Journal of Nuclear Materials, **2002**. **302**(2-3): p. 193-205.

136. Kozeschnik, E. ; Polt, P. ; Warbichler, P. ; Letofsky-Papst, I. ; Brett, S. ; Buchmayr, B., "*The microstructure of dissimilar chromium steel welds during PWHT and inservice exposure"*, in *Mathematical Modelling of Weld Phenomena 6*, H. Cerjak, Editor. **2002**, Maney Publishing: Leeds. p. 323-336.

137. Moorthy, V. ; Vaidyanathan, S. ; Laha, K. ; Jayakumar, T. ; Bhanu Sankara Rao, K. ; Raj, B., "*Evaluation of microstructures in 2.25Cr-1Mo and 9Cr-1Mo steel weldments using magnetic Barkhausen noise"* Materials Science and Engineering A-Structural Materials Properties Microstructure and Processing, **1997**. **231**(1-2): p. 98-104.

138. Luo, G.M. ; Wu, J.S. ; Meng, Q.S., "*Microstructural evolution on the T91 dissimilar metal joints during creep rupture tests"* Journal of Materials Science & Technology, **2004**. **20**(4): p. 383-386.

139. Foret, R. ; Zlamal, B. ; Sopousek, J., "*Structural stability of dissimilar weld between two Cr-Mo-V steels - Results are presented of an experimental study and modeling of the structural stability of 6Cr-Mo-V 8-3-2 and X12Cr-Mo-Nb 10-1 steels in a temperature interval from 600 to 900C"* Welding Journal, **2006**. **85**(10): p. 211S-217S.

140. Nicholson, R.D., "*Effect of post weld heat teatment on development of interfacial structures in nickel-based transition joints"* Materials Science and Technology, **1985**. **1**(3): p. 227-233.

141. Naffakh, H. ; Shamanian, M. ; Ashrafizadeh, F., "*Influence of artificial aging on microstructure and mechanical properties of dissimilar welds between 310 stainless steel and INCONEL 657"* Metallurgical and Materials Transactions A-Physical Metallurgy and Materials Science, **2008**. **39A**(10): p. 2403-2415.

142. Lippold, J.C. ; Sowards, J.W. ; Murray, G.M. ; Alexandrov, B.T. ; Ramirez, A.J., "*Weld solidification cracking in solid-solution strengthened Ni-base filler metals"*, in *Hot Cracking Phenomena in Welds II*, T. Bollinghaus, et al., Editors. **2008**, Springer-Verlag Berlin: Berlin. p. 147-170.

143. Bhaduri, A.K. ; Seetharaman, V. ; Venkadesan, S., "*Effect of aging on the interfacial microstructure and mechanical properties of a alloy 800/2.25Cr1Mo steel joint"* Zeitschrift fur Metallkunde, **1989**. **80**(9): p. 630-634.

144. Gómez, X. ; Echeberria, J., "*Microstructure and mechanical properties of carbon steel A210-superalloy Sanicro 28 bimetallic tubes"* Materials

Science and Engineering A-Structural Materials Properties Microstructure and Processing, **2003**. **348**(1-2): p. 180-191.

145. Sireesha, M. ; Albert, S.K. ; Sundaresan, S., "*Metallurgical changes and mechanical behaviour during high temperature aging of welds between Alloy 800 and 316LN austenitic stainless steel"* Materials Science and Technology, **2003**. **19**(10): p. 1411-1417.

146. Sireesha, M. ; Albert, S.K. ; Sundaresan, S., "*Influence of high-temperature and mechanical properties of exposure on the microstructure dissimilar metal welds between modified 9Cr-1Mo steel and alloy 800"* Metallurgical and Materials Transactions a-Physical Metallurgy and Materials Science, **2005**. **36A**(6): p. 1495-1506.

147. Naffakh, H. ; Shamanian, M. ; Ashrafizadeh, F., "*Microstructural evolutions in dissimilar welds between AISI 310 austenitic stainless steel and Inconel 657"* Journal of Materials Science, **2010**. **45**(10): p. 2564-2573.

148. Sireesha, M. ; Albert, S.K. ; Sundaresan, S., "*Thermal cycling of transition joints between modified 9Cr-lMo steel and Alloy 800 for steam generator application"* International Journal of Pressure Vessels and Piping, **2002**. **79**(12): p. 819-827.

149. Ayer, R. ; Mueller, R.R. ; Leta, D.P. ; Sisak, W.J., "*Phase transformations at steel-IN625 clad interfaces"* Metallurgical Transactions A-Physical Metallurgy and Materials Science, **1989**. **20**(4): p. 665-681.

150. DuPont, J.N., "*Solidification of an Alloy 625 weld overlay"* Metallurgical and Materials Transactions A-Physical Metallurgy and Materials Science, **1996**. **27**(11): p. 3612-3620.

151. Schmid-Fetzer, R. ; Andersson, D. ; Chevalier, P.Y. ; Eleno, L. ; Fabrichnaya, O. ; Kattner, U.R. ; Sundman, B. ; Wang, C. ; Watson, A. ; Zabdyr, L. ; Zinkevich, M., "*Assessment techniques, database design and software facilities for thermodynamics and diffusion"* Calphad, **2007**. **31**(1): p. 38-52.

152. Engstrom, A. ; Hoglund, L. ; Agren, J., "*Computer-simulation of diffusion in multiphase systems"* Metallurgical and Materials Transactions a-Physical Metallurgy and Materials Science, **1994**. **25**(6): p. 1127-1134.

153. Saroja, S. ; Parameswaran, P. ; Vijayalakshmi, M. ; Raghunathan, V.S., "*Prediction of microstructural states in Cr-Mo steels using phase evolution diagrams"* Acta Metallurgica et Materialia, **1995**. **43**(8): p. 2985-3000.

154. Schneider, A. ; Inden, G., "*Simulation of the kinetics of precipitation reactions in ferritic steels"* Acta Materialia, **2005**. **53**(2): p. 519-531.

155. Saunders, N., "*Phase diagram calculations for Ni-based superalloys"*, in *Superalloys 1996*, R.D. Kissinger, et al., Editors. **1996**, The Minerals, Metals & Materials Society(TMS): Warrendale, PA. p. 101-110.

156. Saunders, N. ; Fahrmann, M. ; Small, C.J., "*The application of CALPHAD calculations to Ni-based superalloys"*, in *Superalloys 2000*, T.M. Pollock, et al., Editors. **2000**, Minerals, Metals & Materials Soc: Warrendale. p. 803-811.

157. Saunders, N. ; Guo, Z. ; Li, X. ; Miodownik, A.P. ; Schille, J.P., "*Modelling the material properties and behaviour of Ni-based superalloys"*, in *Superalloys 2004*, K.A. Green, et al., Editors. **2004**, The Minerals, Metals and Materials Society (TMS): Warrendale, PA. p. 849-858.

158. Warnken, N. ; Ma, D. ; Drevermann, A. ; Reed, R.C. ; Fries, S.G. ; Steinbach, I., "*Phase-field modelling of as-cast microstructure evolution in nickel-based superalloys"* Acta Materialia, **2009**. **57**(19): p. 5862-5875.

159. Turchi, P.E.A. ; Kaufman, L. ; Liu, Z.K., "*Modeling of Ni-Cr-Mo based alloys: Part I-phase stability"* Calphad, **2006**. **30**(1): p. 70-87.

160. Andersson, J.O. ; Helander, T. ; Hoglund, L.H. ; Shi, P.F. ; Sundman, B., "*THERMO-CALC & DICTRA, computational tools for materials science"* Calphad, **2002**. **26**(2): p. 273-312.

161. Butler, C.J.,"*The solidification characteristics of titanium aluminides "*,**1995**,Ph.D.,M3 School,University of Nottingham

162. Sundman, B. ; Jansson, B. ; Andersson, J.-O., "*The Thermo-Calc databank system"* Calphad, **1985**. **9**(2): p. 153-190.

163. Borgenstam, A. ; Engstrom, A. ; Hoglund, L. ; Agren, J., "*DICTRA, a tool for simulation of diffusional transformations in alloys"* Journal of Phase Equilibria, **2000**. **21**(3): p. 269-280.

164. Miller, M.K. ; Babu, S.S. ; Burke, M.G., "*Comparison of the phase compositions in Alloy 718 measured by atom probe tomography and predicted by thermodynamic calculations"* Materials Science and Engineering A-Structural Materials Properties Microstructure and Processing, **2002**. **327**(1): p. 84-88.

165. Tancret, F., "*Thermo-Calc and Dictra simulation of constitutional liquation of gamma prime (gamma') during welding of Ni base superalloys"* Computational Materials Science, **2007**. **41**(1): p. 13-19.

166. Million, B. ; Bacilek, K. ; Kucera, J. ; Michalicka, P. ; Rek, A. ; Stransky, K., "*Carbon diffusion and thermodynamic characteristics in chromium steels"* Zeitschrift fur Metallkunde, **1995**. **86**(10): p. 706-712.

167. Million, B. ; Kucera, J. ; Michalicka, P., "*The influence of silicon on carbon redistribution in steel weldments"* Materials Science and Engineering A-Structural Materials Properties Microstructure and Processing, **1995**. **190**(1-2): p. 247-252.

168. Wada, H., "*Thermodynamic properties of carbides in 2.25Cr1Mo steel at 985K"* Metallurgical Transactions A-Physical Metallurgy and Materials Science, **1986**. **17**(9): p. 1585-1592.

169. Robson, J.D. ; Bhadeshia, H.K.D.H., "*Modelling precipitation sequences in power plant steels .2. Application of kinetic theory"* Materials Science and Technology, **1997**. **13**(8): p. 640-644.

170. Fujita, N. ; Bhadeshia, H.K.D.H., "*Modelling simultaneous alloy carbide sequence in power plant steels"* The Iron and Steel Institute of Japan International, **2002**. **42**(7): p. 760-769.

171. Helander, T. ; Agren, J. ; Nilsson, J.O., "*An experimental and theoretical investigation of diffusion across a joint of two multicomponent steels"* The Iron and Steel Institute of Japan International, **1997**. **37**(11): p. 1139-1145.

172. Engstrom, A. ; Hoglund, L. ; Agren, J., "*Computer-simulation of carburization in multiphase systems"*, in *Proceedings of the Second Asm Heat Treatment and Surface Engineering Conference in Europe, Pts 1 and 2*, E.J. Mittemeijer, Editor. **1994**, Transtec Publications Ltd: Zurich-Uetikon. p. 725-730.

173. Reed, S.J.B., "*Electron microprobe analysis"*. **1997**: Cambridge University Press.

174. McCartney, D.G.,"*Studies on cellular and dendritic growth"*,**1982**,DPhill,University of Oxford

175. Porter, D.A. ; Easterling, K.E., "*Phase transformations in metals and alloys"*. **1992**: Nelson Thornes.

176. Guttmann, V., "*Phase stability in high temperature alloys"*. **1981**: Applied Science Publishers.

177. Dupin, N. ; Sundman, B., "*A thermodynamic database for Ni-base superalloys"* Scandinavian Journal of Metallurgy, **2001**. **30**(3): p. 184-192.

178. Saunders, N. ; Guo, Z. ; Miodownik, A.P. ; Schille, J.P., "*Modelling the material properties and behaviour of Ni- and NiFe-based superalloys"*, in *Superalloys 718, 625, 706 and Derivatives, Proceedings*. **2005**, Minerals, Metals & Materials Soc: Warrendale. p. 571-580.

179. Bueno, L.D., "*Effect of oxidation on creep data: Part 1-Comparison between some constant load creep results in air and vacuum on*

21/4Cr-1Mo steel from 600 to 700 C" Materials at High Temperatures, **2008**. **25**(3): p. 213-221.

180. Natesan, K. ; Chopra, O.K. ; Kassner, T.F., "*Compatibility of Fe-2 1/4 wt%Cr-1 wt%Mo steel in a sodium environment"* Nuclear Technology, **1976**. **28**(3): p. 441-451.

181. Robson, J.D. ; Bhadeshia, H.K.D.H., "*Kinetics of precipitation reactions in ferritic power plant steels"*, in *Microstructural Stability of Creep Resistant Alloys for High Temperature Plant Applications*, A. Strang, J. Cawley, and G.W. Greenwood, Editors. **1998**, Inst Materials: London. p. 395-404.

182. Laha, K. ; Chandravathi, K.S. ; Rao, K.B.S. ; Mannan, S.L. ; Sastry, D.H., "*Prediction of creep deformation and rupture behaviour of 2.25Cr-1Mo weld joint"* International Journal of Pressure Vessels and Piping, **2000**. **77**(12): p. 761-769.

183. Chopra, O.K. ; Natesan, K. ; Kassner, T.F., "*Carbon and nitrogen transfer in Fe-9Cr-Mo ferritic steels exposed to a sodium environment"* Journal of Nuclear Materials, **1981**. **96**(3): p. 269-284.

184. Kucera, J. ; Million, B. ; stransky, K., "*Stationary and quasistationary models of carbon redistribution in austenitic steel weldments. I. Ternary systems"* Czechoslovak Journal of Physics B, **1985**. **35**: p. 1355-1361.

185. Sudha, C. ; Anand, R. ; Saroja, S. ; Vijayalakshmi, M., "*Evaluation of concentration dependant diffusion coefficients of carbon in a dissimilar joint of ferritic steels"* Transactions of the Indian Institute of Metals, **2010**. **63**(4): p. 739-744.

186. Robson, J.D. ; Bhadeshia, H.K.D.H., "*Kinetics of precipitation in power plant steels"* Calphad, **1996**. **20**(4): p. 447-460.

187. Robson, J.D. ; Bhadeshia, H.K.D.H., "*Modelling precipitation sequences in power plant steels .1. Kinetic theory"* Materials Science and Technology, **1997**. **13**(8): p. 631-639.

188. Bhaduri, A.K. ; Venkadesan, S. ; Rodriguez, P. ; Mukunda, P.G., "*Combined effects of post-weld heat-treatment and aging on alloy 800/2.25Cr1Mo steel joint"* Materials Science and Technology, **1991**. **7**(11): p. 1051-1056.

189. Bhaduri, A.K. ; Ray, S.K. ; Rodriguez, P., "*New toughness parameters from tensile test for optimizing post weld heat treatment of alloy 800/2.25Cr1Mo steel joint"* Materials Science and Technology, **1993**. **9**(12): p. 1133-1136.

190. Ojo, O.A. ; Richards, N.L. ; Chaturvedi, M.C., "*Microstructural study of weld fusion zone of TIG welded IN 738LC nickel-based superalloy"* Scripta Materialia, **2004**. **51**(7): p. 683-688.

191. Gurumoorthy, K. ; Kamaraj, M. ; Rao, K.P. ; Venugopal, S., "*Microstructure and wear characteristics of nickel based hardfacing alloys deposited by plasma transferred arc welding"* Materials Science and Technology, **2006**. **22**(8): p. 975-980.

192. Thompson, R.G., "*Microfissuring of alloy-718 in the weld heat-affected-zone"* Journal of Metals, **1988**. **40**(7): p. 44-48.

193. Tawancy, H.M., "*Thermal-stability of an Ni-Cr-Mo-Nb alloy"* Materials Characterization, **1992**. **28**(3): p. 221-240.

194. Thomas, C. ; Tait, P., "*The performance of alloy 625 in long-term intermediate temperature applications"* International Journal of Pressure Vessels and Piping, **1994**. **59**(1-3): p. 41-49.

195. Tawancy, H.M., "*Precipitation of NiMo in a Ni-Mo Base alloy"* Journal of Materials Science, **1980**. **15**(10): p. 2597-2604.

Appendix No.1: Optical emission spectroscopy

Optical emission spectroscopy for the steel (page 1)

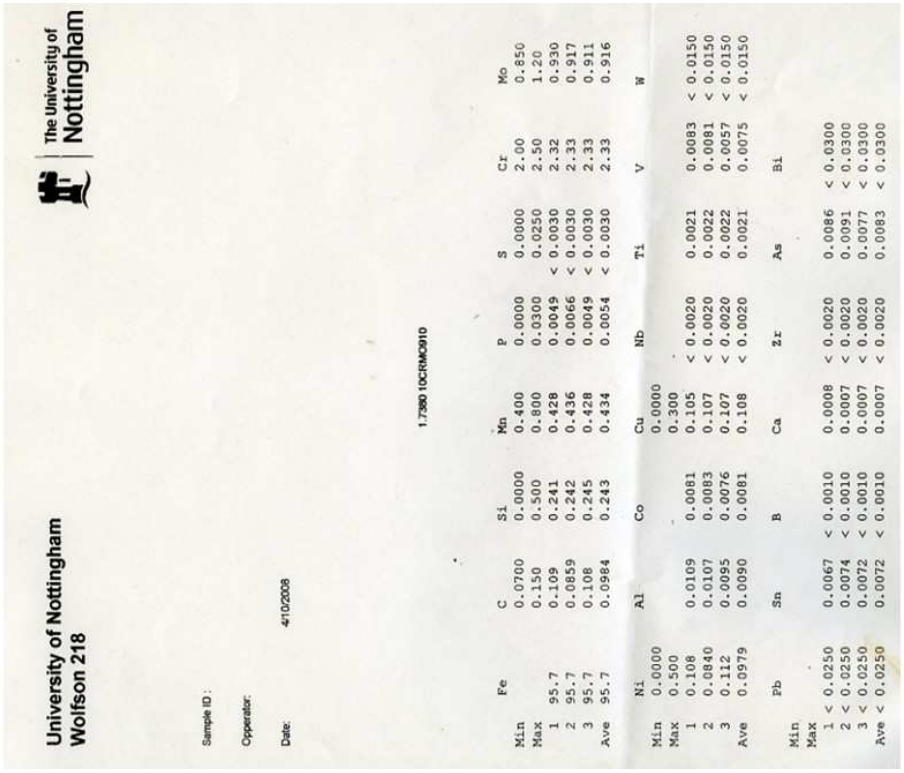

University of Nottingham
Wolfson 218

The University of Nottingham

Sample ID :

Opperator:

Date: 4/10/2008

1.7380 10CRMO910

	Fe	C	Si	Mn	P	S	Cr	Mo
Min		0.0700	0.0000	0.400	0.0000	0.0000	2.00	0.850
Max		0.150	0.500	0.800	0.0300	0.0250	2.50	1.20
1	95.7	0.109	0.241	0.428	0.0049	< 0.0030	2.32	0.930
2	95.7	0.0859	0.242	0.436	0.0066	< 0.0030	2.33	0.917
3	95.7	0.108	0.245	0.428	0.0049	< 0.0030	2.33	0.911
Ave	95.7	0.0984	0.243	0.434	0.0054	< 0.0030	2.33	0.916

	Ni	Al	Co	Cu	Nb	Ti	V	W
Min	0.0000			0.0000				
Max	0.500			0.300				
1	0.108	0.0109	0.0081	0.105	< 0.0020	0.0021	0.0083	< 0.0150
2	0.0840	0.0107	0.0083	0.107	< 0.0020	0.0022	0.0081	< 0.0150
3	0.112	0.0095	0.0076	0.107	< 0.0020	0.0022	0.0057	< 0.0150
Ave	0.0979	0.0090	0.0081	0.108	< 0.0020	0.0021	0.0075	< 0.0150

	Pb	Sn	B	Ca	Zr	As	Bi
Min							
Max							
1	< 0.0250	0.0067	< 0.0010	0.0008	< 0.0020	0.0086	< 0.0300
2	< 0.0250	0.0074	< 0.0010	0.0007	< 0.0020	0.0091	< 0.0300
3	< 0.0250	0.0072	< 0.0010	0.0007	< 0.0020	0.0077	< 0.0300
Ave	< 0.0250	0.0072	< 0.0010	0.0007	< 0.0020	0.0083	< 0.0300

Optical emission spectroscopy for the steel (page 2)

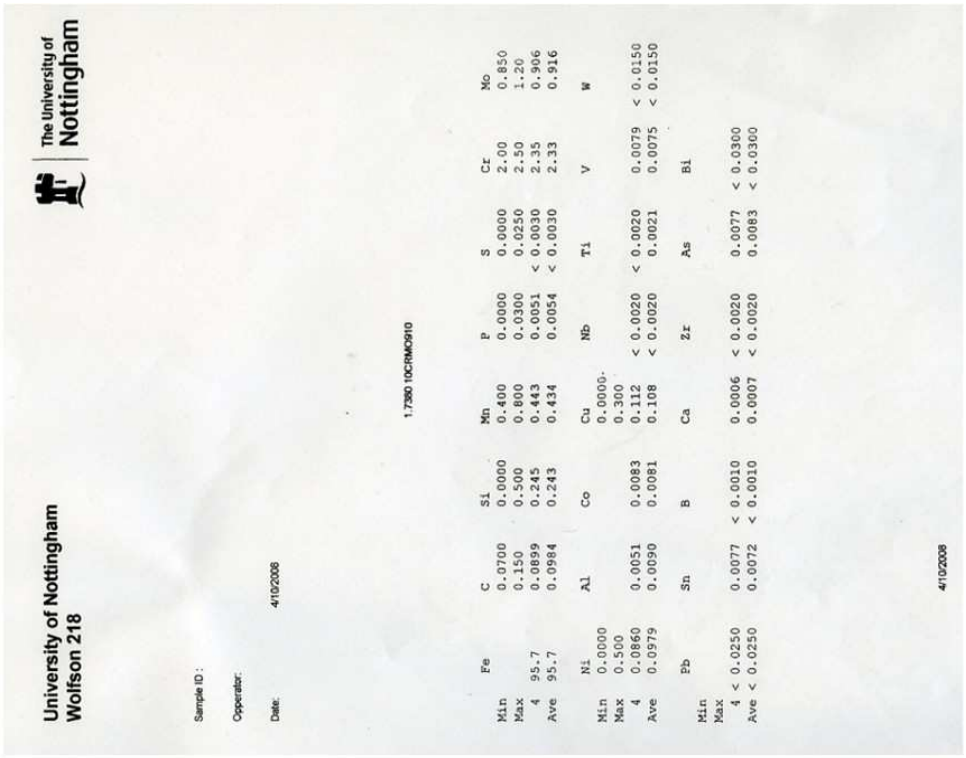

University of Nottingham
Wolfson 218

The University of Nottingham

Sample ID :

Opperator:

Date: 4/10/2008

1.7380 10CRMO910

	Fe	C	Si	Mn	P	S	Cr	Mo
Min		0.0700	0.0000	0.400	0.0000	0.0000	2.00	0.850
Max		0.150	0.500	0.800	0.0300	0.0250	2.50	1.20
4	95.7	0.0899	0.245	0.443	0.0051	< 0.0030	2.35	0.906
Ave	95.7	0.0984	0.243	0.434	0.0054	< 0.0030	2.33	0.916

	Ni	Al	Co	Cu	Nb	Ti	V	W
Min	0.0000			0.0000				
Max	0.500			0.300				
4	0.0860	0.0051	0.0083	0.112	< 0.0020	0.0020	0.0079	< 0.0150
Ave	0.0979	0.0090	0.0081	0.108	< 0.0020	0.0021	0.0075	< 0.0150

	Pb	Sn	B	Ca	Zr	As	Bi
Min							
Max							
4	< 0.0250	0.0077	< 0.0010	0.0006	< 0.0020	0.0077	< 0.0300
Ave	< 0.0250	0.0072	< 0.0010	0.0007	< 0.0020	0.0083	< 0.0300

4/10/2008

Optical emission spectroscopy for the weld overlay at 500 µm

University of Nottingham
Wolfson 218

The University of Nottingham

Sample ID :

Operator:

Date: 6/26/2008

	Ni	Si	Mn	Cr	Mo	Cu	Fe	Co
1	58.9	0.0618	0.0490	21.2	8.31	0.0123	7.70	0.0465
2	59.6	0.0720	0.0613	21.1	8.17	0.0104	7.31	0.0405
3	59.2	0.0665	0.0554	21.0	8.09	0.0104	7.95	0.0453
Ave	59.2	0.0668	0.0553	21.1	8.19	0.0110	7.66	0.0441

	Ti	Al	Nb	W	V	C	S	Hf
1	0.189	0.0701	3.30	< 0.0200	0.0283	0.0142	< 0.0040	< 0.0200
2	0.187	0.0696	3.20	< 0.0200	0.0284	0.0130	< 0.0040	< 0.0200
3	0.182	0.0696	3.12	< 0.0200	0.0289	0.0106	< 0.0040	< 0.0200
Ave	0.186	0.0695	3.21	< 0.0200	0.0285	0.0126	< 0.0040	< 0.0200

	Mg	Ta	Zr
1	0.0032	< 0.0500	0.0236
2	0.0030	< 0.0500	0.0217
3	0.0030	< 0.0500	0.0219
Ave	0.0031	< 0.0500	0.0224

6/26/2008

Optical emission spectroscopy for the weld overlay at 700 µm

University of Nottingham
Wolfson 218

The University of Nottingham

Sample ID :

Operator:

Date: 4/16/2008

	Ni	Si	Mn	Cr	Mo	Cu	Fe	Co
1	58.7	0.0590	0.0606	20.7	8.26	0.0146	8.37	0.0414
2	58.8	0.0656	0.0569	20.7	8.11	0.0139	8.69	0.0459
3	59.1	0.0666	0.0598	20.6	7.88	0.0127	8.71	0.0414
Ave	59.1	0.0680	0.0600	20.6	8.17	0.0139	8.40	0.0425

	Ti	Al	Nb	W	V	C	S	Hf
1	0.186	0.0778	3.28	< 0.0200	0.0254	0.0599	< 0.0040	< 0.0200
2	0.178	0.0727	3.06	< 0.0200	0.0289	0.0253	< 0.0040	< 0.0200
3	0.179	0.0720	3.06	< 0.0200	0.0283	0.0190	< 0.0040	< 0.0200
Ave	0.182	0.0749	3.15	< 0.0200	0.0278	0.0351	< 0.0040	< 0.0200

	Mg	Ta	Zr
1	0.0030	< 0.0500	0.0189
2	0.0029	< 0.0500	0.0191
3	0.0026	< 0.0500	0.0193
Ave	0.0029	< 0.0500	0.0189

4/16/2008

Optical emission spectroscopy for the wrought IN625

University of Nottingham
Wolfson 218

The University of Nottingham

Sample ID :

Operator:

Date: 5/9/2008

	Ni	Si	Mn	Cr	Mo	Cu	Fe	Co
1	61.4	0.0694	0.0601	22.0	9.08	0.173	3.09	0.0994
2	61.3	0.0697	0.0648	21.8	9.23	0.174	3.28	0.0989
3	61.2	0.0680	0.0572	21.9	9.25	0.169	3.17	0.100
Ave	61.3	0.0690	0.0607	21.9	9.19	0.172	3.18	0.0997

	Ti	Al	Nb	W	V	C	S	Hf
1	0.216	0.103	3.52	< 0.0200	0.0295	0.0056	< 0.0040	< 0.0200
2	0.208	0.101	3.48	< 0.0200	0.0335	0.0054	< 0.0040	< 0.0200
3	0.213	0.0994	3.53	0.0222	0.0333	0.0052	< 0.0040	< 0.0200
Ave	0.212	0.101	3.51	< 0.0200	0.0321	0.0054	< 0.0040	< 0.0200

	Mg	Ta	Zr
1	0.0159	< 0.0500	0.0227
2	0.0172	< 0.0500	0.0228
3	0.0167	< 0.0500	0.0236
Ave	0.0166	< 0.0500	0.0230

5/9/2008

Appendix No.2: Mean atomic number calculations

1) Steel

$$\alpha : (Fe) = 26$$

$$(Cr_{0.53}Fe_{0.44}Mn_{0.02}Mo_{0.01})_3C = 20.31$$

$$(Fe_{0.58}Mo_{0.29}Cr_{0.13})_3C = 24.3$$

$$(Cr_{0.63}Mo_{0.35}Fe_{0.02})_2C = 22.227$$

$$(Mo_{0.8}Cr_{0.2})_2C = 27.6$$

$$(Cr_{0.7}Fe_{0.23}Mo_{0.07})_7C_3 = 19.8$$

$$(Mo_{0.54}Fe_{0.37}Cr_{0.06}Si_{0.03})_6C = 30.14$$

$$(Cr_{0.49}Fe_{0.39}Mo_{0.12})_{23}C_6 = 23.00$$

2) Weld overlay

$$\gamma : (Ni_{0.62}Cr_{0.25}Fe_{0.1}Mo_{0.03}) = 27.22$$

$$\delta : Ni_3(Nb_{0.87}Ti_{0.07}Mo_{0.06}) = 30.93$$

$$\mu : Mo(Cr_{0.49}Ni_{0.48}Fe_{0.03})_2 = 31.33$$

$$\sigma : (Cr_{0.37}Ni_{0.21}Mo_{0.24}Fe_{0.18}) = 29.52$$

$$(Cr_{0.82}Mo_{0.13}Ni_{0.05})_{23}C_6 = 22.29$$

$$(Mo_{0.48}Cr_{0.17}\,Ni_{0.17}Fe_{0.16}Nb_{0.02})_6C = 30.0$$

Appendix No.3: Database description forms

Thermo-Calc Database Description Form

SSOL4

SGTE Solutions Database

(Version 4.10, 2004/2005/2008)

Producer: SGTE, Scientific Group Thermodata Europe

Contact persons: Pingfang Shi, Thermo-Calc Software AB, Stockholm, Sweden

Description: The SSOL4 Solutions Database is a sophisticated important thermochemical database for many non-ideal multicomponent solution phases within a chemical framework of 78 elements (compared with the SSOL2 solutions database, F-Cl-Br-I-H are excluded). The contents of this database (sub-version of SSOL4.10) have been greatly expanded from that of its previous version SSOL2, and extensively improved from its earlier sub-versions SSOL4.7 (of 2003), SSOL4.8 (of 2004) and SSOL4.9 (2005).

Combinations of several critically-assessed systems can calculate and extrapolate higher-order multicomponent systems. Such extrapolations require experience and understanding and the producer or vendor should be contacted if problems occur.

The descriptions of the elements are identical to the descriptions in PURE4, the SGTE Pure Elements Database (version 4). The SSOL4 database is compatible, among others, with PURE4 and SSUB4 databases.

Status of the SGTE Solutions Database: This database was originally created by SGTE in 1992 and first released in TCC in November 1993. It was completely revised by SGTE in 1997, 1999 and later on. The actual systems included in a distribution may be different due to various updates and removal of inconsistencies. The previous version SSOL2 commercially distributed with Thermo-Calc is the updated version of 1999 (with some minor modifications made by Bo Sundman and Pingfang Shi in April 2002).

This current version SSOL4 has been further developed on the basis of SSOL2, but mainly focused on alloy solution phases and important intermetallic compound phases. It was released as version 4.74B by SGTE in Sept. 2003, but converted into the Thermo-Calc database format and further modified by TCS during Nov. 2003 – Feb. 2004 (and formally released as to SSOL4.8 in Feb. 2004, and SSOL4.9 in Apr. 2005). ***In the fall of 2008, a further sub-version SSOL4.10 will be released, which includes the unique on-line reference lists and many greatly-improved/modified descriptions.*** Continuous developments of this database have been planned within the SGTE community.

Systems: SSOL4 covers the following 78 elements:

Ag	**Al**	**Am**	**As**	**Au**	**B**	**Ba**	**Be**	**Bi**	**C**
Ca	**Cd**	**Ce**	**Co**	**Cr**	**Cs**	**Cu**	**Dy**	**Er**	**Eu**
Fe	**Ga**	**Gd**	**Ge**	**Hf**	**Hg**	**Ho**	**In**	**Ir**	**K**
La	**Li**	**Lu**	**Mg**	**Mn**	**Mo**	**N**	**Na**	**Nb**	**Nd**
Ni	**Np**	**O**	**Os**	**P**	**Pa**	**Pb**	**Pd**	**Pr**	**Pt**
Pu	**Rb**	**Re**	**Rh**	**Ru**	**S**	**Sb**	**Sc**	**Se**	**Si**
Sm	**Sn**	**Sr**	**Ta**	**Tb**	**Tc**	**Te**	**Th**	**Ti**	**Tl**
Tm	**U**	**V**	**W**	**Y**	**Yb**	**Zn**	**Zr**		

Included thermodynamic data that have been critically assessed are available for many binary, ternary and higher-order subsystems in various multicomponent solution phases, as well as for many important intermetallic compound phases. **The total number of solution phases and intermetallic compound phases has been greatly increased from 222 (in SSOL2) to more than 600 (in SSOL4.10).**

Applications: Alloy design and engineering; Inorganic materials.

Availability: Commercially available for uses with TCC and TCW. *It can also be upgraded from its older versions (SSOL1 of 1992/1998 or SSOL2 of 1999/2002) to SSOL4, at a certain database upgrade fee. It is freely upgradeable from sub-versions SSOL4.7, 4.8 and 4.9 to SSOL4.10, when there is a valid TCC/TCW Software M&SS Subscription.*

Thermo-Calc Database Description Form

TCFE6

TCS Steels/Fe-Alloys Database

(Version 6.0, Apr. 2008)

Producer: Thermo-Calc Software AB, Stockholm, Sweden

Contact person: Pingfang Shi, Thermo-Calc Software AB, Stockholm, Sweden

Description: The TCFE6 Steels/Fe-Alloys Database was released by TCS in March 2008. Its development was based on TCFE5 (2007) & TCFE4 (2006), and it includes many new critical assessments on thermodynamic data for multi-component systems of interests for various steels/Fe-alloys.

Systems: TCFE6 covers complete and critical assessments of binary and some ternary systems, as well as the iron-rich corner of some higher order systems, within the 21-element framework:

Al B C Ca Co Cr Cu Fe Mg Mn
Mo N Nb Ni O P S Si Ti V W

The database is applicable for various types of steels/Fe-alloys with a Fe-minimum of 50wt%, and for alloying elements the recommended composition limits (in weight percent) are as follows:

Element	max	Element	max	Element	max	Element	max
Al	5.0	Cr	30.0	N	5.0	S	*trace*
B	*trace*	Cu	5.0	Nb	5.0	Si	5.0
C	7.0	Mg	*trace*	Ni	20.0	Ti	3.0
Ca	*trace*	Mn	20.0	O	*trace*	V	15.0
Co	20.0	Mo	10.0	P	*trace*	W	15.0
Fe	*min* 50						

The update was based on complete reassessments of binary and many ternary systems. Many intermediate compounds that do not occur in steels have been deleted from the database. Therefore, it is not suitable to calculate complete systems, but rather only in the iron rich corner. Each parameter in the database has a reference to its origin.

Sensible calculations cannot be expected if all alloying elements are at their highest limits. Some combinations of elements at high values will not give reasonable results; but, some alloying elements can exceed their limits considerably and the calculations will still give good results. Critical calculations must always be verified by equilibrium experimental data; it is the user's responsibility to verify the calculations but TCS is interested to know about any significant deviations in order to improve any future release.

In version TCFE4, all necessary volume data (including molar volume and thermal expansivity) for various alloy phases were incorporated; such volume data has been updated in TCFE6.

Results from the CCT-Applied Stainless Steel Project were incorporated into the TCFE5 version. The CCT (Centre of Computational Thermodynamics) is a collaboration among Thermo-Calc Software, KTH (Royal Institute of Technology), Swerea KIMAB and Swedish industries. In order to further increase the predictive capability of the database, many significant assessments and modifications have been performed by TCS and are introduced in TCFE6. The element Ca has been added and the alloying ranges for the elements C, Co, Cu, N, Ti and V have been extended. For details of all the major improvements, refer to the document "***TCFE6 Database Description Form***".

All the major improvements that have been implemented in TCFE6 make this database suitable to predict different thermodynamic properties with accurate results. It can be used with satisfying results for several types of alloys *e.g.* stainless steels, high-speed steels, tool steels, HSLA steels, cast iron and corrosion-resistant high strength steels and more.

The TCFE6 database contains a simple GAS mixture phase (Ar, O2, N2 and S2) only for the main purpose of considering oxygen/nitrogen-gas controls in steel-making processes; however, it can be replaced by a large GAS phase appended from a compatible database (*e.g.* SSUB4, SLAG2 or TCMP2).

Applications: Steel /Fe-alloys design and engineering.

Availability: Commercially available for uses with TCC and TCW.

It is highly recommended to upgrade from the older versions (TCFE1 of 1992, FEDAT of 1996, TCFE2 of 1999, TCFE3 of 2002), TCFE4 (of 2006) or TCFE5 (of 2007) to TCFE6 (upon a certain database upgrade fee).

Thermo-Calc Database Description Form

TTNi7

TT Ni-based Superalloys Database

(Version 7.0, Jan. 2006)

Producer: ThermoTech Ltd., Surrey Technology Center, Guildford ,UK

Contact person: Pingfang Shi, Thermo-Calc Software AB, Stockholm, Sweden

Description: This database has been developed by ThermoTech for commercial Ni-based superalloys, high Fe-containing Ni-based superalloys, single crystal Ni-based superalloys, and so on. Using the SCHEIL module in the TCC and TCW software, it is also possible to make solidification simulations that provide predictions for non-equilibrium micro-segregation, like f_s *vs* T plots and heat evolution. For more complex modeling, the calculations provide critical information that can otherwise only be found by expensive experimental techniques.

During validation process of the TTNi database, extensive comparison has been made between the simulated results and available experimental data for superalloys (*Figures 1* and *2*). The database performs at an accuracy close to the level expected of the experiments themselves. The database can be used for predictions of all types of equilibria, such as γ/γ', γ' solvus, solidus/liquidus relations (*Figure 3* for U720 alloy as an example).

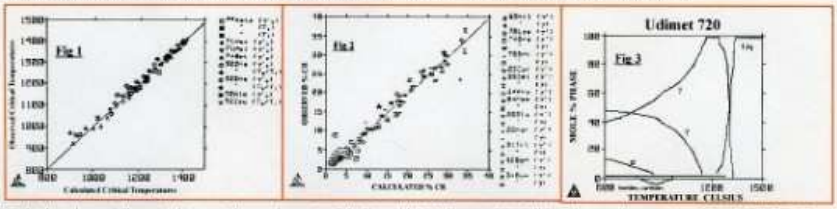

The TTNF database is specially created to meet the requirements of dealing with high Fe-containing Ni-based superalloys such as 706 and 718. NiFe-based superalloys can behave in a more complex fashion than predominantly Ni-based alloys. For example, the hardening mechanism often involves γ', the metastable form of Ni3Nb. The TTNiFe database has proved capable of handling these very complex alloys providing excellent answers for both stable and metastable equilibrium. Furthermore, it has been used with excellent success in solidification modelling of such alloys. It also provides an accelerated route by which certain elements that are important to such alloys can be pursued. Further additions such as Si, P and S will be added. The figures on the right side show a phase% plot for a 718 alloy showing the stable behaviour where Ni3Nb is formed and its behaviour under more usual hardening conditions where sluggish kinetics cause γ' to form in preference to Ni3Nb. In these circumstances the alloy is hardened by a duplex precipitation of γ' and γ".

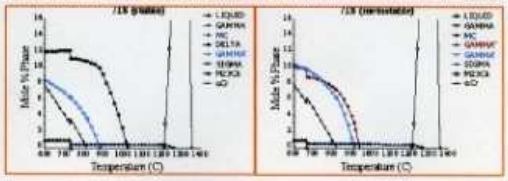

From TTNi6 to TTNi7, extensive new work done on Si containing alloys to improve modelling of higher Si containing alloys. Also new modelling work undertaken for the Pt2Mo type ordered phase in NiCrMo based superalloys, which forms at low temperatures. Extensive new work on oxides based around the Ni-Al-Cr-Fe-Si-Ti-O system. Gamma' solvus temperatures improved for recently developed High Refractory Element Ni-based superalloys.

Systems: The database (Version 7.0) contains the following 22 elements (from TTNi6 to TTNi7, Ca-V-O are added):

Ni Al Co Cr Cu Fe Hf Mn Mo Nb
Re Ru Si Ta Ti V W Zr B C N O

The TTNi database is currently designed as the following two individual database versions:

Name	*Description*	*Elements*
TTNi7	V7, complete, 22 elements	Ni-Al-Co-Cr-Cu-Fe-Hf-Mn-Mo-Nb-Re-Ru-Si-Ta-Ti-V-W-Zr-B-C-N-O
TTNF5	V5, NiFe-based, 14 elements	Ni-Fe-Al-Co-Cr-Mn-Mo-Nb-Si-Ti-Zr-B-C-N

Note that they are originally called as Ni-DATA and NiFe-Super, respectively.

The phases covered by the TTNi6 version are: **Liquid, γ, γ', γ'', η, σ, μ, α-(Cr,Mo,W), NiAl, Ni_3Nb, Ni_4Mo, δ-NiMo, Laves_C14, Laves_C15, P_phase, R_phase, M(C,N), $M_{23}(B,C)_6$, M_6C, $M_7(B,C)_3$, M_2N, M_3B, M_3B_2_tetragonal, MB_2_tetragonal, MB_2_orthorhombic, MB_orthorhombic, Cr_5B_3, TiB_2, $Ni_3Si(h)$, Ni_5Si_2, $Cr_2Ni_3Si_2$, B2_BCC, A4B_D1, Cub_A15. From TTNi6 to TTNi7, added new phases are: Silicon rich G_phase, Z and Pi nitrides, SiO2, MO_B2, M3O4, M2O3, M2SiO4, Mullite, Spinel.**

The phases covered by the TTNF5 version are: **Liquid, γ, γ', γ'', η, σ, μ, α-(Cr,Mo,W), NiAl, Ni_3Nb, Ni_4Mo, δ-NiMo, Laves, P_phase, M(C,N), $M_{23}(B,C)_6$, M_6C, $M_7(B,C)_3$, M_2N, M_3B_2_tetragonal, TiB_2, $Ni_3Si(h)$, Ni_5Si_2, Cub_A15**

Applications: Ni-based superalloy design and engineering.

Availability: Commercially available for uses with TCC and TCW.

References: Saunders N. and Miodownik A.P. (1998) *CALPHAD (Calculation of Phase Diagrams): A Comprehensive Guide.* Cambridge.